LEABHARLANN CHOLÁISTE NA TRÍONÓIDE, BAILE ÁTHA CLIATH | TRINITY COLLEGE LIBRARY DUBLIN
Ollscoil Átha Cliath | The University of Dublin

Terms and Conditions of Use of Digitised Theses from Trinity College Library Dublin

Copyright statement

All material supplied by Trinity College Library is protected by copyright (under the Copyright and Related Rights Act, 2000 as amended) and other relevant Intellectual Property Rights. By accessing and using a Digitised Thesis from Trinity College Library you acknowledge that all Intellectual Property Rights in any Works supplied are the sole and exclusive property of the copyright and/or other IPR holder. Specific copyright holders may not be explicitly identified. Use of materials from other sources within a thesis should not be construed as a claim over them.

A non-exclusive, non-transferable licence is hereby granted to those using or reproducing, in whole or in part, the material for valid purposes, providing the copyright owners are acknowledged using the normal conventions. Where specific permission to use material is required, this is identified and such permission must be sought from the copyright holder or agency cited.

Liability statement

By using a Digitised Thesis, I accept that Trinity College Dublin bears no legal responsibility for the accuracy, legality or comprehensiveness of materials contained within the thesis, and that Trinity College Dublin accepts no liability for indirect, consequential, or incidental, damages or losses arising from use of the thesis for whatever reason. Information located in a thesis may be subject to specific use constraints, details of which may not be explicitly described. It is the responsibility of potential and actual users to be aware of such constraints and to abide by them. By making use of material from a digitised thesis, you accept these copyright and disclaimer provisions. Where it is brought to the attention of Trinity College Library that there may be a breach of copyright or other restraint, it is the policy to withdraw or take down access to a thesis while the issue is being resolved.

Access Agreement

By using a Digitised Thesis from Trinity College Library you are bound by the following Terms & Conditions. Please read them carefully.

I have read and I understand the following statement: All material supplied via a Digitised Thesis from Trinity College Library is protected by copyright and other intellectual property rights, and duplication or sale of all or part of any of a thesis is not permitted, except that material may be duplicated by you for your research use or for educational purposes in electronic or print form providing the copyright owners are acknowledged using the normal conventions. You must obtain permission for any other use. Electronic or print copies may not be offered, whether for sale or otherwise to anyone. This copy has been supplied on the understanding that it is copyright material and that no quotation from the thesis may be published without proper acknowledgement.

Spin transport in magnetic nanostructures

by

Oscar Céspedes Boldoba

A thesis submitted for the degree of
Doctor of Philosophy
in the University of Dublin

Department of Physics
Trinity College Dublin

December 2004

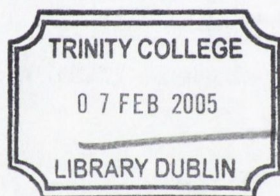
TRINITY COLLEGE
0 7 FEB 2005
LIBRARY DUBLIN
THESIS
7393

DECLARATION

This thesis is submitted by the undersigned for examination for the degree of Doctor of Philosophy at the University of Dublin. It has not been submitted as an exercise for a degree at any other university.

This thesis, apart from the advice, assistance and joint effort mentioned in the acknowledgements and in the text, is entirely my own work.

I agree that the library may lend or copy this thesis freely on request.

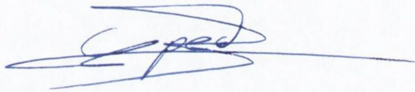

Oscar Céspedes Boldoba

December 2004

Summary

The study presented in this thesis is concerned with the spin dependent transport and spin transfer in magnetic nanostructures.

The first two chapters are dedicated to introduce spin-electronics, electrical transport and the experimental techniques commonly used in this work. Chapters three and four present the results obtained in the measurement of electronic transport in Ni, Fe_3O_4 (magnetite) and $(La_{0.7}Sr_{0.3})MnO_3$ (LSMO) nanostructures. The idea examined in chapter five is to place a multi-walled carbon nanotube (MWCNT) in contact with a ferromagnet and measure the spin transfer associated with the alignment of their chemical potentials. In chapter six the results obtained will be discussed and chapter seven contains the conclusion and proposed further work.

During this work, a technique to fabricate nickel nanocontacts on a thin film geometry by combining UV lithography and electrodeposition has been developed. The transport properties of the structures fabricated using this technique are found to be very similar to those of samples fabricated by e-beam lithography and focussed ion beam milling, with non-linear, asymmetric I-V characteristics when the samples are patterned on SiO_x/Si substrates. The asymmetry will be associated with tunnel transport through the SiO_x substrate and/or through an insulating NiO_x layer present in the nanoconstriction. The later will play a fundamental role in the magneto-transport of the samples.

The magnetic field effect in nickel nanoconstrictions can be sorted in three groups depending on the MR values obtained. The first one, obtained for samples with high conductance well above G_0, represents an increase of the resistance of a few %, which we will associate to the AMR generated by a domain wall. The second one, with an increase of re-

sistance of a few % followed by a drop of 30-50 %, is present in samples with a resistance of 1 to 5 kΩ. This behaviour could be attributed to the annihilation of a domain wall, and the change of a surrounding NiO_x layer from antiferromagnetic-insulating to ferromagnetic-conducting at higher fields due to the magnetic interaction of the NiO_x layer with the nickel electrodes via exchange energy. Finally, the huge drops of resistance up to 50000 % obtained for samples with a conductance below G_0 are attributed to the constrictions being completely covered by a NiO_x layer which behaviour is also changed from insulating to conducting, opening conduction paths that were not present previously. This metal-insulator transition explanation will be supported by other noise and transport measurements. Other explanations, as domain wall magnetoresistance and magnetostriction will also be considered.

A new method to fabricate in-plane edge junctions to measure spin polarization by Andreev reflection will be described. The success ratio is very low (~ 5 %) and the fabrication method needs to be optimized, but it has proved to be useful to measure the polarization P of $Ni/NiO_x/Nb$ junctions and their transport characteristics. The polarization P is defined as the difference in the electron population of a conducting ferromagnet at the Fermi level depending if the electrons are spin up or down. In a half-metal, the spin of all the conduction electrons is either up or down, which gives a spin-polarization for a half metal of 100 %. The Andreev reflection measurements give values for P in Ni/NiO_x nanoconstrictions up to 70 %, with high scattering at the $Ni/NiO_x/Nb$ interface.

Fe_3O_4 and LSMO are half-metallic ferromagnets with high spin polarization at room temperature. This makes of magnetite and LSMO two of the best candidates as sources and analysers of spin-polarized currents for spin-electronic devices. Measurements carried out on

Fe_3O_4 and LSMO nanostructures patterned by focussed ion beam (FIB) milling on films 50-150 nm thick will be presented. The study of the transport through these structures can give us a better knowledge of the mechanism followed by a highly spin-polarised current to cross very narrow domain walls and the subsequent origin of the huge MR measured in point and electrodeposited nanocontacts. On the other hand, these patterned nanostructures are stable with time and bounded to a substrate, thus eliminating (or reducing to subatomic levels) possible magnetostrictive effects and making feasible their use in technological applications.

The transport through nanoconstrictions, nanobridges and nanogaps fabricated by FIB milling in LSMO and magnetite thin films exhibits a behaviour that can be metallic or semiconductor-like with temperature, with ohmic, tunnelling or field-emission behaviour depending of the structure and the applied voltage. Electromigration will play an essential role in the transport properties of our nanostructures, with changes in the transport characteristics and the samples physical structure after high currents are applied. We will use these effects to achieve different sample geometries and transport regimes (e.g., from tunnelling to field-emission).

Finally, molecular and spin-electronics are combined in the study of the spin transfer from a ferromagnetic substrate into a carbon nanotube. We will need to detect a tiny spin transfer against the huge background magnetic moment of the ferromagnet, and this will be resolved by taking a smooth ferromagnetic thin film as a substrate and looking for a stray field around the nanotube. Cobalt and magnetite are chosen as magnetic substrates. Cobalt forms a rather strong chemical bond involving Co $3d_z^2$ and graphite pz electrons, and Fe_3O_4 is a half-metal with a high magnetic ordering temperature (860 K), where the spin transfer should be equal to the charge transfer. Si and Cu substrates are used for control purposes.

In order to estimate the magnitude of the induced magnetization of the carbon nanotube, we will compare our images with those obtained from hard and floppy disks. From bits of 1 x 10 μm recorded on γ-Fe_2O_3, we obtain signals that are approximately one order of magnitude greater than those coming from carbon nanotubes. The medium has magnetization M 200 kA m^{-1}, and it produces a stray field of order 2 kA m^{-1} around each bit. The dimensions of the recorded bits and nanotubes are similar, so the stray field gradients are expected to scale similarly. The weak dependence on lift height allows us to compare the stray fields generated by the tubes and the bits. The stray field close to the tube will be of order of 0.2 M if it behaves like a bar magnet, so we estimate a tube magnetization of order 1 kA m^{-1}, corresponding to an average carbon moment of order 0.001 μ_B. Finally, allowing for the fact that no more than 1% of the carbon atoms are likely to be in contact with the substrate, the observed magnetization corresponds to a moment of order 0.1 μ_B per contact atom. This experimental evidence of spin transfer to molecules can be used to obtain spin currents without the limitations imposed by the resistance mismatch of ferromagnet-semiconductor devices.

Acknowledgements

First and foremost, thanks to my supervisor, J.M.D. Coey, for giving me the opportunity to join his lab, for the interest he has shown in this work, and for the supervision and encouragement throughout.

In order of appearance: thanks Mazhar for all your help, especially the first hard days, Venki for always having time to answer my silly questions and for all those afternoons at Bewleys and Govindas, Janko for introducing me into spin electronics, AFM and the IFC, Katie for her friendliness, Cora for giving out to Mazhar, Treasa for most cinema nights and all those songs, Gareth for making the proper connections, Guenole for sharing his knowledge in electronics and his desk, Ciara for being near when I needed (even if it was to pull someone's hair), Adrielle for finding me a place first and almost drowning me later, Jiang for his Chinese lessons, Alex for being a coffee mate, Fernando for being always so friendly and for his expertise in electrochemistry, Rob for shielding the storms and being ready to help, Emma for her patience and the Wicklish tutorials, Eoin for taking me to dodgy parties and for his calculations in the Andreev model, Sonia for shaking the world and all her work with electrodeposited nanocontacts, Han for his professional advice, Sebastian for his optimism, Steve for taking it easy and depositing magnetite films for this work, Sebastiaan and Marjo for their introduction to the eastern cultures and a few advices (spin electronics), Plamen for always sharing his broad

knowledge and work power, Kentaro for sharing his experience, Richard for his introduction to FIB milling, Catherine for changing the tide at the SFI, Nandu for coming for coffee and for all the electrochemical advices, Jerome for a sort night, Lucio for not letting me be the only bald one and Aurore for her dedication and patience.

Thanks also to all the summer students who have passed by the group during the past years and made it so internationally French.

Thanks to Tom, John, Jacquie, Mick, Jemmer, Dave, Joe, Ken, Pat, Gunilla, Michele, Susan and Sandra for taking care of the orders, the paperwork and all your friendly assistance.

Thanks to Mathieu Kociack for his expertise in carbon nanotubes, Michel Viret (CEA, Saclay) for his help with the theory of domain wall magnetoresistance, e-beam lithography and the nickel nanostructures microsimulations, and thanks to Claude Fermon for letting me use the e-beam lithography system in his laboratory at the CEA in Saclay.

Yuko, domo arigato kimi-san, omae irodoru maiwee.

Y, por supuesto, gracias a mi familia, papá, Toni, Natalie, Luis, Jose, Alex, Edu, Lola, Jesús y, muy especialmente, a mamuchi. Gracias por las llamadas, los paquetes, los viajes a Madrid y Barcelona, y por apoyarme siempre sin importar lo que hiciera. Gracias también a Juanjo, Cris, Gus, Tere, Dani, Marta y Alex por encontrar tiempo para mí cada vez que os llamaba. Sin todos vosotros esta tesis no hubiera sido posible.

Table of Contents

List of figures.. 4

1 Introduction.. **10**

1.1 Spin electronics.. 11
1.1.1 Spin polarization and half metals.. 13
1.1.2 Measurements of spin polarization.. 16
1.1.3 Spin currents and spin transfer.. 17

1.2 Electric transport.. 20
1.2.1 Diffusive and hopping transport.. 21
1.2.2 Ballistic transport, quantum conductance and quantum interference.... 25
1.2.3 Magnetoresistance and domain wall scattering.......................... 30
1.2.4 Tunnelling and field emission.. 36
1.2.5 Heating and capacitive effects, breakdown and electromigration......... 41

1.3 Noise measurements.. 43
1.3.1 White noise.. 44
1.3.2 1/f noise.. 47
1.3.3 Non-Gaussian and random telegraph noise.......................... 55

Bibliography.. 60

2 Experimental method.. **67**

2.1 Sample preparation and characterization.. 67
2.1.1 Thin film deposition.. 67
2.1.2 Atomic and magnetic force microscopy.. 69
2.1.3 Scanning electron microscope imaging.. 75
2.1.4 SQUID.. 80
2.1.5 Transport measurements.. 81

2.2 Nanofabrication.. 85
2.2.1 U-V lithography, wet and dry etching.. 85
2.2.2 Electrodeposition of nanostructures.. 92

2.2.3 e-beam lithography........ 97
2.2.4 Focussed ion beam milling........ 100
2.2.5 Patterning of in-plane Andreev reflection samples........ 104

Appendix: Comparative table........ 106

Bibliography........ 107

3 Transport measurements in nickel nanostructures........ 108

3.1 I-V characteristic and magnetoresistance........ 111
3.1.1 Fabrication and I-V characteristic........ 111
3.1.2 Magnetic field effect and relaxation........ 115
3.1.3 Electrical switching........ 123

3.2 Noise measurements of nickel nanostructures........ 126
3.2.1 Noise characteristic........ 126
3.2.2 Asymmetric behaviour and electromigration........ 128
3.2.3 Random telegraph noise........ 131

3.3 Spin polarization of nickel nanoconstrictions measured by planar Andreev reflection........ 135

Appendix: Micromagnetic simulations........ 144

Bibliography........ 145

4 Transport measurements in Fe_3O_4 and $La_{0.7}Sr_{0.3}MnO_3$ nanostructures........ 149

4.1 Sample fabrication........ 151

4.2 Electric transport........ 155
4.2.1 Electric transport in LSMO and magnetite nanoconstrictions........ 155
4.2.2 Electric transport in magnetite nanobridges........ 160
4.2.3 Electric transport in the field emission regime........ 163

4.3 Magnetic field effect........ 167
4.3.1 Magnetic field effect in LSMO and magnetite nanoconstrictions........ 167

4.3.2 Magnetic field effect in magnetite nanobridges 172
4.3.3 Magnetic field effect in the field emission regime 174
Bibliography 177

5 Contact induced magnetism in carbon nanotubes 178

5.1 Atomic force imaging of MWCNTs: artefacts and other issues 180

5.2 Magnetic measurements and imaging 186

Appendix: Theoretical calculations 197

Bibliography 201

6 Discussion 203

6.1 Transport in nickel nanoconstrictions 203

6.2 Transport in LSMO and magnetite nanostructures 222
6.2.1 LSMO and Fe_3O_4 nanoconstrictions 222
6.2.2 Magnetite nanobridges 231
6.2.3 Magnetite nanogaps 234

6.3 Contact induced magnetism in carbon nanotubes 237

Bibliography 240

7 Conclusion and further work 242

List of publications 247

List of figures:

Chapter 1: Introduction

1.1. Density of states for Co and CrO_2 (p. 15)

1.2. Different experiments for the measurement of spin polarization (p. 17)

1.3. Three terminal device for pure spin-current generation (p.18)

1.4. Method for the detection of a pure spin-current via a double nanoconstriction (p. 19)

1.5. Characteristic length scales for electronic transport in cobalt (p. 21)

1.6. Magnetic domain walls schematics (p. 32)

1.7. Energy diagram for a square metal-insulator-metal barrier (p. 39)

1.8. I-V and Fowler-Nordheim plots for a tunnel junction at the different transport regimes of tunnelling, field emission and electromigration (p. 40)

1.9. AFM image showing the effect of the Towsend avalanche (p. 41)

1.10. SEM images of a Fe_3O_4 nanobridge before and after a measurement (p. 42)

1.11. White and 1/f noise spectra in the real and Fourier space (p. 48)

1.12. Noise spectra obtained when applying high currents (p.50)

1.13. Temperature dependence of the α parameter in $1/f^{\alpha}$ (p. 54)

1.14. Random telegraph noise in a LSMO film (p. 56)

Chapter 2: Experimental method

2.1. SEM image of an evaporated gold film (p. 69)

2.2. AFM image of a Co doped ZnO thin film deposited by PLS (p. 70)

2.3. Schematic of the tapping and lift modes in AFM (p. 72)

2.4. Response of the MFM to a magnetic field (p. 74)

2.5. MFM image of a Co doped SnO_2 grain (p. 75)

2.6. Schematic of an electron microscope (p. 76)

2.7. Raster and vector scan of a SEM (p. 77)

2.8. SEM image of a magnetite nanobridge with magnification 800 k (p. 79)

2.9. Schematic of the 4 point DC noise measurements set-up (p. 83)

2.10. Schematic and measurement of the Andreev reflection (p. 84)

2.11. Schematic types of nanostructures (p. 85)

2.12. UV lithography schematic (p. 87)

2.13. Lithographed micro-track with a mirror-like artefact (p. 89)

2.14. Continuous and radio-frequency Ar milling schematics (p. 90)
2.15. Reactive ion etching schematic (p. 90)
2.16. Electrodeposition of nanocontacts departing from a gap (p. 92)
2.17. Schematic of *ele*ctrochemical *na*nodeposition, ELENA (p. 94)
2.18. Three different ways to fabricate a nanocontact by electrodeposition (p. 95)
2.19. SEM images of nanowires: while inside of a cut membrane, attached to the metallic electrode and isolated laying on a substrate (p. 96)
2.20. Mechanism of radiation-induced chain scission in PMMA (p. 98)
2.21. Schematic of three different e-beam lithography processes (p. 99)
2.22. Operation of a focussed ion beam (p. 100)
2.23. Steps for the fabrication of FIB-milled nanostructures (p. 101)
2.24. SEM images of FIB-patterned structures (p. 103)
2.25. Fabrication of in-plane edge junctions (p. 105)

Chapter 3: Transport measurements in nickel nanostructures

3.1. I-V characteristic of nickel nanostructures on SiO_x substrates (p. 112)
3.2. Variation of dV/dI with the temperature (p. 113)
3.3. I-V characteristic of the control samples (p. 114)
3.4. Magnetoresistance measurements on low resistance, electrodeposited samples (p. 115)
3.5. Magnetic switching effect on an electrodeposited sample (p. 116)
3.6. Magnetic switch in the I-V, dV/dI and R (H) plots (p. 117)
3.7. I-V characteristics of two nickel on SiO_x samples fabricated by FIB and electrodeposition before and after a field. Effects of 50000 and 5000 % (p. 118)
3.8. Highest magnetoresistance ratio and its dependence with the voltage (p. 119)
3.9. Relaxation process after a field is applied (p. 120)
3.10. Changes in the I-V for different magnetic fields (p. 121)
3.11. Micromagnetic simulations for a double nanoconstriction (p. 122)
3.12. Electrical switching and hysteresis (p. 123)
3.13. Instabilities on the I-V characteristic (p. 124)
3.14. Magnetic field effect on the electrical hysteresis (p.125)
3.15. Fit of the noise data to the $1/f^{\alpha}$ dependence (p. 126)
3.16. Deduce fluctuator volume from the noise spectra (p. 127)
3.17. Asymmetries and bursts on the noise characteristic (p. 129)

3.18. Effect of a high current on the I-V and its relaxation (p. 130)
3.19. Magnetic field effect on the $1/f^{\alpha}$ noise (p. 131)
3.20. Noise spectra after a high current is applied, showing a bump on the $1/f^{\alpha}$ characteristic. Magnetic field effect (p. 132)
3.21. Random telegraph fluctuations in the real time domain (p. 133)
3.22. Dependence of the random fluctuations with the temperature (p. 134)
3.23. Milling process and R(T) for two superconducting Nb films (p. 136)
3.24. SEMs of the steps for the preparation of edge junctions (p. 137)
3.25. Milling damage on edge junctions (p. 138)
3.26. R(T) for bad interfaces showing a transition to insulating (p. 139)
3.27. SEM of Cu-Nb and Ni-Nb junctions (p. 140)
3.28. DC Andreev measurements (p. 141)
3.29. Andreev measurement of a sample with an oxidised interface (p. 142)
3.30. AC measurements on Cu-Nb and Ni-Nb junctions and fitting to BTK theory (p. 143)
3.31. Micromagnetic simulations for a field parallel to the track (p. 144)
3.31. Micromagnetic simulations for a field perpendicular to the track (p. 144)

Chapter 4: Transport measurements in Fe_3O_4 and $La_{0.7}Sr_{0.3}MnO_3$ nanostructures

4.1. Effect of a high current on a magnetite nanobridge (p. 151)
4.2. SEMs of magnetite nanobridges milled at different currents (p. 152)
4.3. SEMs of the different milled-patterned geometries (p. 153)
4.4. SEM image and the R vs. current characteristic of a magnetite nanobridge showing evidence for electromigration with the sample going from 1 MΩ to 6 kΩ (p. 154)
4.5. SEM and I-V of Fe_3O_4 and LSMO nanoconstrictions (p. 155)
4.6. Dependence between the barrier height and width (p. 156)
4.7. RTN on the I-V of a LSMO nanoconstriction (p. 157)
4.8. R(T) for two LSMO nanoconstrictions (p. 158)
4.9. SEMs and MFM of magnetite thin films with anti-phase boundaries (p. 160)
4.10. R(T) characteristic for a magnetite nanoconstriction and a nanobridge (p. 161)
4.11. I-V characteristic of a magnetite nanoconstriction after a high voltage (p. 162)
4.12. I-V characteristic of a magnetite nanoconstriction at three different transport regimes: tunnelling, field emission and electromigration (p. 163)
4.13. Transport in a magnetite nanoconstriction before and after a 500 μA current (p. 164)

4.14. SEMs of a magnetite nanoconstriction before and after 500 μA are applied (p. 165)
4.15. SEM of a FIB-milled gap between Fe_3O_4 electrodes (p. 166)
4.16. Transport characteristic of a FIB-milled nanogap (p. 166)
4.17. Scaling of the MR ratios with the conductance (p. 167)
4.18. I-V and MR vs. V for Fe_3O_4 and LSMO nanoconstrictions (p. 169)
4.19. Variation of the Simmons coefficients β and γ for a LSMO nanoconstriction at high magnetic fields up to 5 T (p. 170)
4.20. Electrical hysteresis and MR for LSMO and magnetite nanoconstriction (p. 171)
4.21. MR for a magnetite nanobridge across an anti-phase boundary (p. 172)
4.22. Variation of the Simmons coefficients and MR vs. V for a magnetite nanobridge across an anti-phase boundary (p. 173)
4.23. MR vs. V at different magnetic fields (p. 174)
4.24. Magnetic field effect in an induced nanogap (p. 175)
4.25. Fowler-Nordheim plot with and without a magnetic field (p. 176)

Chapter 5: Contact induced magnetism in carbon nanotubes

5.1. Typical AFM of multi-walled carbon nanotubes spread on a film (p. 180)
5.2. Stripped pattern artefact (p. 181)
5.3. AFM-MFM images of an attached nanotube with different scan heights (p. 182)
5.4. Images when the lift height is small compared with the scan amplitude (p. 184)
5.5. AFM-MFM artefacts for the amplitude mode (p. 185)
5.6. Susceptibility of multiwalled carbon nanotubes (p. 186)
5.7. AFM-MFM images of carbon nanotubes on Si and Cu (p. 187)
5.8. AFM-MFM images of a carbon nanotube laid on a 20 Gb hard disk (p. 188)
5.9. AFM-MFM images of a MWCNT on cobalt showing magnetic contrast (p.189)
5.10. AFM-MFM images of two MWCNTs on a cobalt film, the signal is stronger at the end of the tube (p. 190)
5.11. MFM image of a nanotube with contrast at the lateral edges of the tube (p. 191)
5.12. MFM signal for different substrate magnetization directions (p. 192)
5.13. MFM image of different magnetite thin films (p. 193)
5.14. MFM images of a MWCNT on magnetite with different domain structures (p. 194)
5.15. AFM-MFM images of a nanotube on a Si substrate while a magnetic field of a few mT is applied (p. 195)

5.16. Band structure obtained for a Co/C superlattice (p. 198)

5.17.Charge transfer and energy gain between a CNT and a metallic substrate (p. 200)

Chapter 6: Discussion

6.1. I-V and R(V) for Ni nanoconstrictions on insulating substrates (p. 203)

6.2. Magnetic field effects on Ni nanostructures (p. 204)

6.3. Schematic for domain wall induced transport asymmetry (p. 206)

6.4. Schematic for transport across SiO_x and/or NiO_x (p. 207)

6.5. R (V) and dR (V) vs. T for Ni nanoconstrictions on a SiO_x substrate (p. 209)

6.6. Andreev reflection, band schematic and MR vs. G for Ni nanoconstrictions (p. 210)

6.7. Schematic and magnetic field effect for high resistance Ni nanoconstrictions (p. 211)

6.8. R(T) before (exponential increase of resistance as the temperature is decreased) and after (linear increase) a magnetic field is applied (p. 213)

6.9. Schematic for the mixed magnetic effect (small increased followed by big drop) in medium resistance (2-10 x G_0) Ni nanoconstrictions (p. 215)

6.10. Noise characteristic of a nickel nanoconstriction and the magnetic field effect (p. 216)

6.11. Change of resistance and noise characteristic after a high current is applied (p. 216)

6.12. SEM image and schematic explaining the changes of resistance in Ni nanoconstrictions as due to electromigration (p. 218)

6.13. RTN in Ni nanoconstrictions and its temperature dependence (p. 219)

6.14. Electrical switching and hysteresis in Ni nanoconstrictions; schematic of the two possible explanations: domain wall and geometry distortion (p. 221)

6.15. Heating and breakdown effects on LSMO and Fe_3O_4 nanoconstrictions (p. 222)

6.16. Deduced barrier height and width for LSMO and Fe_3O_4 nanoconstrictions (p. 223)

6.17. Chemical mapping and gallium doping levels on Fe_3O_4 nanostructures (p. 224)

6.18. MR of a LSMO nanoconstriction and scaling of the MR with the conductance of LSMO and Fe_3O_4 nanoconstrictions (p. 226)

6.19. R vs. current for a LSMO nanoconstriction before (non-linear, hysteretical I-V) and after a magnetic field is applied and the hysteresis disappears (p. 227)

6.20. Highest magnetic effect found in a (hysteretical) half-metallic nanostructure (p. 228)

6.21. Changes on the Simmons coefficients of a LSMO nanoconstriction (p. 229)

6.22. Changes on the Simmons coefficients of a magnetite nanobridge (p. 229)

6.23. Bias dependence of the current and TMR for a MTJ (p. 232)

6.24. Calculated oscillations of the TMR (p. 233)

6.25. SEM image and schematic explaining the oscillations of the γ parameter (p. 234)

6.26. Magnetic field effect in the field emission regime (p. 235)

6.27. Schematic of the variation in the field-emission threshold with the magnetic field, with changes up to 1V at 0.6 T (p. 236)

6.28. MFM images of a carbon nanotube on magnetite and of a 20Gb hard disk (p. 237)

6.29. AFM image section analysis of a carbon nanotube (p. 238)

6.30. SQUID magnetization measurements of a Co substrate with and without MWCNTs laying on it (p. 239)

Chapter 7: Conclusion and further work

7.1. AFM image of a nano-hole punctured by the AFM tip itself (p. 246)

Abbreviations employed in this list:

AFM → Atomic Force Microscopy

FIB → Focussed Ion Beam

LSMO → $La_{0.7}Sr_{0.3}MnO_3$

MFM→ Magnetic Force Microscopy

MTJ → Magnetic Tunnel Junction

MWCNT → Multi-Walled Carbon NanoTube

SEM → Scanning Electron Microscope

TMR → Tunnel MagnetoResistance

Chapter 1

Introduction

The size of electronic devices and data storage elements has been reducing exponentially during the last fifty years, allowing for smaller, lighter and faster instruments and computers. But with this reduction in size, quantum effects become more and more relevant, and we are reaching the limit where they will be restricted by the very principles that allow those devices to work. This downturn in electronic progress is not far in the future. Conception and implementation of nano-scaled devices which make use of these limiting quantum effects rather than neglect them is required.

Spin-electronics is the field of condensed matter that for the past fifteen years has integrated the spin of the electron, previously mostly ignored, into conventional electronics. For this effect, materials with higher spin polarization and magnetic moments have been intensely, and effectively, researched. Half-metals due to their full spin polarization and magnetic semiconductors thanks to the combination of well investigated semiconductor properties and the added degree of freedom of magnetic properties, are at the centre of this research.

But the need for new switching devices and transistors which take into account the quantum mechanics-related problems due to their nanometric size, has also brought back old and well-known materials, such as nickel and magnetite, with renewed interest for their use in novel devices which could be combined with, or even replace, conventional electronic elements.

Research on ferromagnetic point contacts with quantum conductance where magnetic domains and spin polarised currents play an important role, opened new perspectives. However, the miniaturisation of device dimensions and the application in communication and information technology requires fabrication methods able to produce stable nano-scaled structures with reproducible properties, such as patterned or lithographed devices. But together with the fabrication of these structures, is essential to understand their magnetic and transport properties, and the role of the spin transport, which is the purpose of this work

This thesis is therefore mainly concerned on the investigation of spin transport and spin transfer in nano-scaled materials. Several experimental setups using different fabrication methods and detailed characterization have been used to study transport through ferromagnetic nanocontacts, nanoconstrictions (single and multiple), nanobridges, nanogaps and the spin transfer from ferromagnetic thin films to carbon nanotubes. Section 1.1 outlines the emerging field of spin electronics, and introduces a few important concepts. Section 1.2 gives an account of the different transport mechanisms in nanostructures. Section 1.3 introduces the different types of electric noise and the physics behind each of them.

1.1 Spin electronics

Electronic instruments are present in almost every aspect of our life. Equipment like computers, radio, television and the nowadays omnipresent mobile phone are the product of fifty years of materials and device research.

Electronics, with its transistors and the other components which integrate those instru-

ments, is based on manipulating and controlling a flow of electrons generated by an electric field, which generates movement of these charged particles. But the magnetic field, which interacts with the spin of the particles itself, has been put to use only in a few devices, like reed switches and Hall probes. The fact that electrons have a magnetic moment (they are either spin-up or spin-down) as well as a charge was widely recognised but mostly ignored until recently: "Conventional electronics has hitherto ignored the spin of the electron" [1]. Electrons are magnets in their own right, with a tiny but measurable magnetic moment, μ_B. Distinguishing and manipulating the spin as well as the charge of the electron, adds a new degree of freedom to the handled information.

As early as the 1930's, Mott [27] already glimpsed in the relevance of the spin for electric transport and modelled the electric conduction in a ferromagnetic material by postulating that the current is carried via two distinct conduction channels, with the carriers consisting of the spin-up electrons and the spin-down electrons respectively, each with different transport properties. At the initial stage, this two channels were considered independent, spin-up and spin-down remained as such during the scattering process without mixing. This implied that the characteristic spin flip time has to be much longer than the scattering of the electrons, so they conserve their spin even after many collisions, which we know now is not quite correct.

A conventional electronic device would ideally provide an extra-functionallity by differentiating between the flow of spin up and spin down electrons that form the electric current, and a magnetic field could manipulate this added information. Spin electronics, also known as spintronics or magnetoelectronics, is the branch of condensed matter where the electron spin, so far altogether inseparable from the electronic charge, is the active element manipulated in transport processes. This new field ([2],[3]) combines two well established

areas of research: magnetism and electronics. Devices based on spin electronics can potentially complement or replace various conventional electronic devices exploiting the same tunnelling effects that tend to damage the performance of the latest devices, especially now that size-related problems doom the future of semiconductor-based transistors [4]. Experimental applications of this new way to understand electronic transport started in 1988, with the discovery of the giant magnetoresistance (GMR) effect, which has been successfully implemented in magnetic read heads [5].

As happens with any other new branch of science, broad interest and much effort is dedicated to a wide domain of issues that range from the fundamental concepts of spin-dependent transport and length scales to the feasibility and implementation of novel devices structures. Spin electronics is a combined product of physicists, chemists and materials researchers that look for the ideal combination of spin, charge, size and structure which outperforms any of the commonly used actual devices.

1.1.1 Spin polarization and half metals

Basic for the differential study of spin-up and spin-down flow of electrons is the concept of spin polarization. When an electrical current passes, there is a flow of spin-up and spin-down electrons, but for spin electronics to work one needs a source of spins, not charge, to manipulate. Ferromagnetic materials have a spin dependent band structure, where the majority subband contains electrons with spin parallel to the magnetization direction, and the minority subband spins are antiparallel. The spin polarization, P, is a measure of the ratio between spin-up and spin-down electrons 'available' at the Fermi level. Several definitions

are possible, depending on which physical process is being considered. If we just consider the number of electrons with spin-up or spin-down this leads to the definition:

$$P_n = \frac{n_\uparrow - n_\uparrow}{n_\downarrow + n_\downarrow} \tag{1}$$

where P_n is now defined as the normalized difference between spin-up and spin-down density of states ($n_\uparrow$ and $n_\downarrow$ respectively) at the Fermi level.

But this is valid only at zero temperature. At non-zero temperatures, P is reduced by spin-flip processes. As a first approximation, P should vary as the reduced magnetization m, dropping to zero at the Curie temperature, T_C.

Half-metals are ferromagnets with the unusual property of having a Fermi surface in one spin band, and a spin gap for the opposite spin direction, which gives them a metallic behaviour for one spin orientation and semiconducting or insulating behaviour for the other. By definition, the resultant polarization is $P = 100\%$ at zero temperatures when there is no spin mixing.

We can compare the polarization of a half-metal with that of a normal ferromagnet, such as cobalt and nickel for example (see figure 1.1), which have fully spin-polarized d-bands, but where the Fermi level also crosses the 4s band, which is almost unpolarized. This gives a total polarization for these 3d ferromagnets around 40 % at low temperatures both for bulk and thin film samples. The concept of half-metallicity can be extended to cover narrow bands, where the electrons are localized [6].

Half-metallicity is not easy to detect experimentally because there is no intrinsic behaviour that constitutes the unmistakable signature of a half-metal. A classification of half metals has been proposed in function of their conductivity and the transport properties of the majority and minority electrons at the Fermi level [6], [7]:

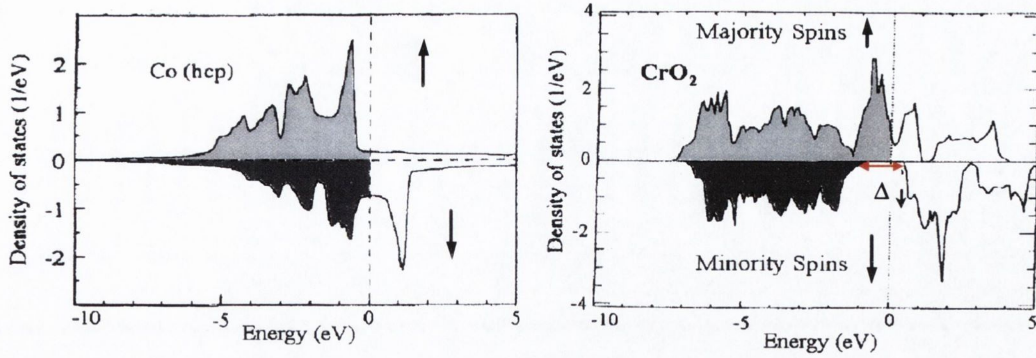

Figure 1.1. (Co) and a half-metallic ferromagnet (CrO_2): the red arrow marks the energy gap between the spin up and down bands, after [6].

Type	Density of states	Conductivity	↑ e^- at E_F	↓ e^- at E_F
$\mathbf{I}_A$	half-metal	metallic	itinerant	none
$\mathbf{I}_B$	half-metal	metallic	none	itinerant
$\mathbf{II}_A$	half-metal	non-metallic	localized	none
$\mathbf{II}_B$	half-metal	non-metallic	none	localized
$\mathbf{III}_A$	metal	metallic	itinerant	localized
$\mathbf{III}_B$	metal	metallic	localized	itinerant
$\mathbf{IV}_A$	semimetal	metallic	itinerant	localized
$\mathbf{IV}_B$	semimetal	metallic	localized	itinerant
$\mathbf{V}_A$	semiconductor	semiconducting	few, intinerant	none
$\mathbf{V}_B$	semiconductor	semiconducting	none	few, itinerant

Table 1: Classification of half-metallic materials according to [6]

Using this classification, some half-metallic materials used in spin-electronics and their properties are [6] (with $(n_\uparrow - n_\downarrow)^2$ the spin wave amplitude):

Material	Type	↑ electrons	↓ electrons	T_C (K)	$(n_\uparrow - n_\downarrow)^2$	Ref.
CrO_2	I_A	Cr (t_{2g})	-	396	2	[8]
Sr_2FeMoO_6	I_B	-	Mo (t_{2g})	421	4	[9]
$(Co_{1-x}Fe_x)S_2$	I_A	Co (e_g)	-	≈ 100	(1 − x)	[10]
NiMnSb	I_A	-	Ni (e_g)	730	4	[11]
Mn_2VAl	I_B	Mn (t_{2g})	-	760	2	[12]
Fe_3O_4	II_B	-	Fe (t_{2g})	860	4	[13]
$(La_{0.7}Sr_{0.3})MnO_3$	III_A	Mn (e_g)	Mn (t_{2g})	390	< 3.7	[14]
$Tl_2Mn_2O_7$	IV_B	Mn (t_{2g})	Tl (6s)	120	6	[15]

Table 2: Some half-metallic materials, their classification and properties.

1.1.2 Measurements of spin polarization

Measuring P presents not only experimental, but also conceptual problems. Although the idea of polarization as the ratio of majority versus minority electrons is simple, almost all the methods of measuring it necessitate either the removal of electrons or from the material or transport measurements. Methods available include spin-polarized photoemission, and transport measurements in point contacts and tunnel junctions, either with two ferromagnetic electrodes, or with one ferromagnetic and one superconducting electrode, as summarized in Fig. 1.2, but none of these methods provide a direct measurements for the ratio of the densities of states.

In the photoemission experiment, the polarization is normalised by the probability of escape in photoemission, which is generally different for $\uparrow$and $\downarrow$ electrons.

In experiments involving ballistic or diffusive transport, P must be normalised by the Fermi velocity of the electrons, or its square, respectively [16]. In the case of tunneling transport, the normalization must be done by using spin-dependent tunneling matrix elements, which vary as v_F^2, for a specular barrier with low transparency. P can then be defined in function of the transport experiment employed as:

$$P_{nv^2} = \frac{\langle nv^n \rangle_\uparrow - \langle nv^n \rangle_\downarrow}{\langle nv^n \rangle_\uparrow + \langle nv^n \rangle_\downarrow} \quad (2)$$

With v the wave velocity and $n = 0, 1$ or 2 [16]. For a type I or II half-metal, P_n is 100 % whatever the weighting, but for a type III or IV half-metal, different experiments may yield quite different values of polarization (table 1). Although solid state physicists use the

notion of a degree of spin polarization of a ferromagnet rather often, it is not well defined. While the total magnetization is uniquely defined as the difference between the number of spin up and spin down electrons, it tells us little about how much different spins do contribute to transport properties. The three main ways to determine the spin polarization are photoemission, tunnel junctions and point contacts. The tunnel junctions and point contacts can be between two ferromagnets (magnetic tunnel junctions and point contacts) or between a ferromagnet and a superconductor (Tedrow-Meservey junctions and Andreev reflection point contacts). See figure 1.2.

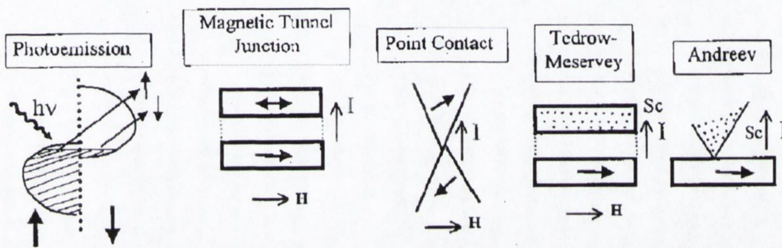

Figure 1.2. Polarization measurement experiments: photoemission, magnetic tunnel junction, point contacts, Tedrow-Meservey and Andreev reflection.

1.1.3 Spin currents and spin transfer

The most standard way to obtain spin polarised currents is to inject electrons from a ferromagnet into another material, generally a semiconductor, in a two terminal geometry [17]. However, due to conductivity mismatch, most of the polarization of the current is lost at the ferromagnet-semiconductor interface, and what is left is inevitably accompanied by a charge current [18].

Producing and measuring pure *spin currents* without an associated charge current is

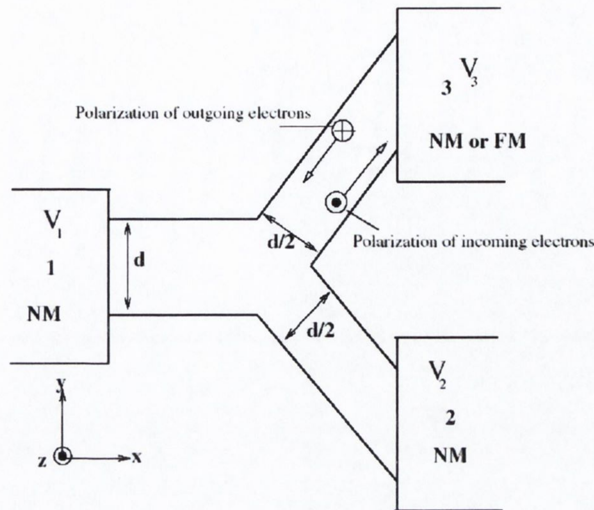

Figure 1.3. An schematic of a three terminal device to generate spin currents as suggested by Pareek [19]. At the two-dimensional $Y-$shaped conductor of the figure, the scattered electrons will be polarized along the z axis. However, the polarization for the two branches of the Y junction will be opposite. Hence, a three terminal structure would create spin currents from an unpolarized current in the presence of spin-orbit interaction. Pure spin currents without an accompanying charge current happen when one of the terminals, say terminal 3, acts as a voltage probe, the voltage V_3 is adjusted such that the total charge current flowing in terminal 3 is zero; i.e., $I_3^q = 0$. However, the spin current is not necessarily nill because the polarization of the outgoing electrons can be different from that of the incoming electrons.

one of the major and longer standing goals of spin electronics. Theoretical methods to produce spin currents have been proposed, for example, by using the spin-orbit interaction in the scattering by impurity atoms or defects (Fig. 1.3) [19]. Spin-orbit interaction causes a spin-asymmetry in scattering processes, i.e., electrons with one particular spin direction have a larger probability to be scattered to the right compared to the others electrons [20],[21]. The presence of an impurity atom or defects gives rise to spin-orbit interaction which has a polarizing effect on particle scattering that can be used to produce pure spin currents [21]. However, since it is predictable that the polarization thus obtained will be quite small, and dissociated from any charge flow, it is not clear if it would be possible to detect it, and it may be necesary to resort to the fabrication of a nanostructured device where the

spin-current could induced the movement of a domain wall trapped in a nanoconstriction patterned in a ferromagnetic third electrode (see Fig. 1.4). This would induce a change in the micro-magnetization of the sample which may be detected by, for example, magnetic force microscopy.

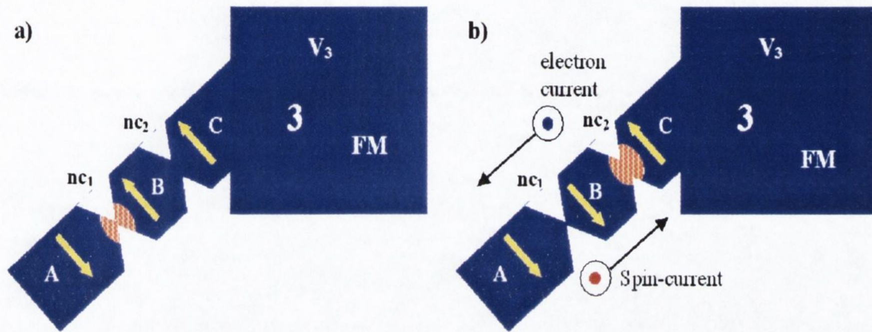

Figure 1.4. A method to detect the spin current generated by the experiment described in the figure 1-3. a) The narrow nanoconstriction nc_1 traps a domain wall [40]. b) The spin current pushes the domain wall to the wider second nanoconstriction, changing the magnetization of the region **B**.

Another way to produce spin currents that may not present as many experimental issues as the previous one, is to make use of the charge transfer that occurs due to the difference between the chemical potentials of any two materials that are in contact. If one the two materials has a polarization $P \neq 0$, the charge transfer has associated a spin transfer [22], [23]. The ability to induce spin polarization by simple contact between a ferromagnet and, say, a molecule, at room temperature opens a range of new possibilities for molecular and spin-electronics. For instance one can imagine a new generation of magneto-transport devices, where the active transport channel is electrically decoupled from the magnetic element. In this way the electrical signal will depend on the magnetic state of the contacts, although those are not involved directly into the transport process. This paves the way for the solution of the long-standing problem of spin injection from a magnetic metal, and can offer an alternative

to semiconductors spintronics via a polarised interface in any junction of a spin-polarized with a non-polarised material.

1.2 Electric transport

When studying the transport properties of a structure, we must take into account that the nature of the transport will vary depending on the size of the device related to the various length scales involved. The first length scale to consider is obviously the size of the system, L. The second one is the average distance the electron travel before colliding and being scattered, which is defined as the mean free path λ_{mfp}. This scattering can be caused by dislocations in the crystal, impurities or sample boundaries, in which case it will be elastic scattering: no energy is exchanged. Inelastic scattering arises from other scattering mechanisms such as phonon scattering and electron-electron interactions. One can define an elastic mean free path, or coherence length, l_{e} as the length travelled between two elastic scattering events, and in the same way an inelastic mfp, l_{i}. In the case of a ferromagnet the mean free path will be different for majority and minority electrons, and therefore we will need to define $\lambda^{\uparrow}_{mfp}$ and $\lambda^{\downarrow}_{mfp}$We can also associate a length scale associated with the quantum behaviour of the electrons and their wave character: the Fermi wave length λ_F, which is related to the Fermi velocity $v_F = \frac{\hbar}{m\lambda_F}$,with $\hbar$ the reduced Planck constant (see figure 1.5). Another useful characteristic lenghts are: λ_{L}, the Lorentz cyclotron orbit (circular movement induced by a magnetic field perpendicular to the current) at 4.2 K and 1 T, δ_{w}, the domain wall width (bulk) and λ_{sdp}, the spin diffusion length, or how long does the spin propagate before being flipped due to scattering.

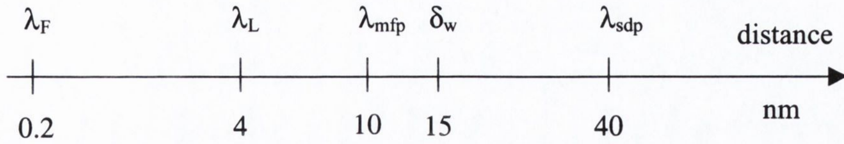

Figure 1.5. Different lenght scales for cobalt involved in electronic transport. λ_{L} is the Lorentz cyclotron orbit at 4.2 K and 1 T, δ_{w} is the domain wall width (bulk) and λ_{sdp} is the spin diffusion length. The λ_{mfp} here mentioned refers to the s electrons (with equal spin up and down population).

We can now classify the two distinct transport regimes in mesoscopic structures as follows. When $\lambda_F \ll L < l_{\mathrm{e}}, l_{\mathrm{i}}$, the electrons are said to behave ballistically, that is, they travel through the structure without being scattered. The other limit, $\lambda_F < l_{\mathrm{e}}, l_{\mathrm{i}} \ll L$, is the diffusive regime, where the electron undergo many scattering events while traversing the structure. When the electrons have to cross an energy barrier several eV high, they do so by quantum-tunnel effect, unless the voltage applied is as big as the barrier height, in which case the electrons are transmitted by field-emission.

In this section we will see a simple introduction to transport theory covering electronic transport through metals and energy barrier in meso and nanoscopic systems.

1.2.1 Diffusive and hopping transport

The Ohm's law $j = \sigma\varepsilon$ is a semiclassical method to calculate the conductivity of a material. In this approach, the electrical field (ε) is assumed to be sufficiently small that the response to the current, j, is linear, so that σ, a scalar, is the electrical conductivity. For this approach, we also assume that the momentum k is also a well defined scalar, and subsequently a good quantum number. For this assumption to be true, we require the wavelength of the electron to be small compared to the mean free path- the mean previously

defined, so the electron appears as a plane wave ($k_{\mathrm{F}}\lambda_{mfp} >> 1$, with k_{F} the Fermi momentum of the electron) before each scattering event.

The distribution function $f(k)$ of the electrons at equilibrium is the well-known Fermi-Dirac distribution:

$$f_0(k) = \frac{1}{\exp[(E(k) - E_F)/k_B T] + 1} \tag{3}$$

If we apply an electric field the conductivity can be found from an average of the electron velocity using this distribution function:

$$j_x = \sigma\varepsilon = \frac{e \int v_x f(v) dv}{\int f(v) dv} \tag{4}$$

where $v = \hbar k/m$ and noting that the integral involving f_0 is zero, since the Fermi-Dirac distribution describes the equilibrium state, when there is no net flow of electrons. The calculation of the conductivity is now done using the Boltzmann equation.

In its simplest form the Boltzmann equation is a simple expression of the steady state condition that the distribution function is not changing with time:

$$\frac{df}{dt} = \left.\frac{df}{dt}\right|_{field} + \left.\frac{df}{dt}\right|_{scattering} = 0 \tag{5}$$

The first term describes the fact that f is being driven away from equilibrium as the electrons are accelerated by the electric field and the second that the relaxation back to equilibrium due to scattering processes. Below we shall show how this simple expression can be used to calculate the conductivity in a free electron model, when we consider that the electrons do not interact with themselves and they behave like molecules of a noble gas. The derivative can then be expressed as:

$$\left.\frac{df}{dt}\right|_{field} = -\frac{df_0}{dE} \upsilon_x e \varepsilon. \tag{6}$$

If we assume that f will relax back to zero exponentially with a relaxation time, τ, we have that:

$$f = -\frac{df_0}{dE} \upsilon_x e \varepsilon \tau, \tag{7}$$

and substituting this into (4) we obtain:

$$\sigma = -\frac{e^2}{4\pi^3} \int \upsilon \tau \frac{df_0}{dE} d^3k. \tag{8}$$

The derivative of this is the Dirac delta function and so the integral over energy simply picks out the Fermi surface leaving us with a simple integral over the Fermi sphere, this results in [24]:

$$\sigma = \frac{e^2}{12\pi^3 \hbar} \langle \lambda \rangle S_F. \tag{9}$$

This form is useful to consider when the Fermi surface is not a simple sphere- as in Cu for example. $\langle \lambda \rangle$ is an average of the mean free path over the Fermi sphere and S_F is the area of the Fermi surface. It is straightforward to show that this equation is equivalent to the Drude formula for the conductivity

$$\sigma = \frac{\vec{j}}{\vec{\varepsilon}} = \frac{ne^2\tau}{m} \tag{10}$$

The τ here is explicitly the energy relaxation time, the time for f to relax back to zero or the Fermi sphere to relax back to the origin. If we use a more exact derivation we

find $\sigma = ne^2\tau_{tr}/m$ where τ_{tr} is the transport relaxation time which takes account of the effectiveness of large angle scattering over small angle scattering in destroying the electric current. Here electrons are seen as particles that can move freely in between occasional scattering events, where they loose all information about energy, direction and velocity after each event. The electrons are moving randomly, with mean velocity zero. The electric field accelerates the electrons, and the mean velocity is not zero any more, but is known as the drift velocity.

If we take (9) above and use free electron values for the area of the Fermi sphere we find

$$\sigma = \frac{1}{3\pi^2}\frac{e^2}{\hbar}\frac{1}{\lambda}(k_F\lambda)^2 \tag{11}$$

Note that $\frac{e^2}{\hbar}$ has units of Ω^{-1}; in fact, the quantum conductance G_0 is usually defined as $G_0 \equiv \frac{2e^2}{h} \simeq 12.9k\Omega$ (see section 1.2.2). For a typical strong scattering metal with $k_F\lambda \sim 1$, $\lambda = \dfrac{\hbar c}{pc}$ and $pc \approx \sqrt{2 \cdot E_K \cdot m_0c^2}$. If the electron has a kinetic energy $E_K = 1$ eV and rest mass energy 0.511 MeV, the associated wavelength is 1.23 nm, what gives σ about 2×10^4 $(\Omega\text{cm})^{-1}$, i.e. a resistivity of about 50 $\mu\Omega$cm.

So far we have assumed that the system was homogenous and so the distribution function has no spatial dependence. If we consider thin films or multilayers the the system is clearly inhomogeneous in one dimension so that for a thin film f goes to zero at the surfaces of the film.

The Fuchs-Sondheimer model [25] re-derives the Boltzmann equation and determines f, but includes the spatial dependence of f. If we refer back to the equation (6) we need to include the term involving $(d\mathbf{r}/dt) \cdot (\partial f/\partial \mathbf{r})$ and if we consider the electric field to be in

the x-direction and the z-axis to be perpendicular to the plane of the film, the Boltzmann equation in the same form as (7) becomes:

$$\frac{f}{\tau} = -\frac{df_0}{dE} v_x e \varepsilon + \frac{\hbar k}{m} \cdot \frac{\partial f}{\partial r} \tag{12}$$

which has the solution

$$f(z,k) = v_x e \varepsilon \frac{df_0}{dE} \left[1 + \exp\left(-\frac{mz}{\hbar \tau k_z} \right) \right] \tag{13}$$

All the previously used expressions assume that the electrons can travel through the medium as a continuum. If it is not so, the electrons need to tunnel between the different atomic sites. Hopping is a form of transport where the charge carriers are localized, and hop from one atomic site to another. The charge carriers will have to overcome an energy barrier to move from one site to the next. This activation energy leads to a temperature dependence of the conductivity of the form $\sigma \sim \exp(-b/T^{\alpha})$, where the factor α ranges from $\frac{1}{4}$ to $\frac{1}{2}$. The conductivity of the materials which present this hopping conductance is smaller than for metals, since the hopping is just a thermally-activated internal tunneling [26].

At low temperatures, however, the most frequent hopping process is not nearest-neighbor, the probability p to hop a distance R is [27]:

$$p(R) = \exp(-2\alpha R) \exp(-\Delta E / k_B T),$$

where $1/\alpha$ is decay length of localized wave. The probability is maximized not for nearest neighbours, but when $R = (8\pi N(E) \alpha k_B T)^{-1/4}$, where $N(E)$ is the density of states, giving rise to the process called variable range hopping.

1.2.2 Ballistic transport, quantum conductance and quantum interference

Sharvin in 1965 [28] found that for a point contact with a radius r smaller than the mean free path λ_{mfp}, the resistance R is given by:

$$\frac{1}{R} = \frac{2e^2}{h}\frac{k_F^2 A}{4\pi}, \tag{14}$$

with $A = \pi r^2$ the area of the point contact. The resultant values for the conductance of a nanocontact are discrete and multiples of the quantum of conductance $G_0 = \frac{2e^2}{h} \simeq (12.9k\Omega)^{-1}$ where e is the charge of an electron, and $\hbar$ the Planck constant . Obviously, this expression considers that there are no defects or impurities where the electron could scatter, which makes the conductance independent of the length of the contact, and gives values of resistance for a contact of radius $r = 10$ nm of only 1 Ω.

The conductance quantization is caused by the quantization of electron momentum in directions perpendicular to that of current flow. Consider two electron gas reservoirs connected by a narrow constriction with a diameter $2R$. We assume that the electrons move ballistically between the two reservoirs, and are only scattered by the boundaries of the constriction. This means that the electrons behave like a one-dimensional electron gas: in the z-direction the electron momentum is continuous, while in the x- and y-directions, due to the small size R of the constriction, the momentum is quantized. The energy of the electron can then be written:

$$E_n(k) = \left(n_x^2 + n_y^2\right)\frac{\pi^2\hbar^2}{4mR^2} + \frac{\hbar^2 k_z^2}{2m}, \tag{15}$$

with n_x and n_y the indices for the discrete allowed transverse modes, m the electron mass, and k_z the component of the wave vector in the z-direction. The first term on the right hand side of equation (15) is the quantized term, while the other term represents the continuous

contribution. Applying a small potential difference between the two reservoirs, $V_{bias} = (\mu_1 - \mu_2)/e$, leads to a difference in chemical potentials $(\mu_1 - \mu_2)$.The number of electrons N then contributing to the current is:

$$N = \frac{1}{2} g_n(E_F)(\mu_1 - \mu_2), \tag{16}$$

with $g_n(E_F)$ the density of states at the Fermi level for the allowed mode n. This leads to an expression for the charge current I_n due to mode n:

$$I_n = ev_{Fn}N = \frac{ev_{Fn}}{2} g_n(E_F)(\mu_1 - \mu_2), \tag{17}$$

with v_{Fn} the group velocity of mode n at the Fermi level. The density of states at the Fermi level for a 1D electron gas is given by:

$$g_n(E_F) = \left(2\pi \frac{dE_n(k)}{dk}\right)^{-1} = \frac{1}{hv_{Fn}}. \tag{18}$$

Finally, substituting equation (1.10) into (1.9) gives a conductance G_0 per mode of:

$$G_0 = \frac{I_n}{V_{bias}} = \frac{2e^2}{h}, \tag{19}$$

or for the total conductance G:

$$G = NG_0 = \frac{2e^2}{h} N, \tag{20}$$

with N the number of available modes below the Fermi level.

When changing the size of the constriction, we see from (14) and (15) that the number of allowed modes available for transport changes too, and this leads to a stepwise change in the observed conductance. When the size of the constriction is small enough (of the order of Angstroms), the energy level spacing becomes larger than the thermal energy, and conductance quantization can be observed at room temperature.

In the above derivation it is assumed that each electron emitted from the, say, left

reservoir, will reach the right reservoir. This implies a complete transmission for each electron wave in each mode. In general, this condition need not hold, and this leads to the Landauer formula, a generalization of equation (20):

$$G = \frac{e^2}{h}\left(\sum_{1}^{N_\uparrow} T_{i\uparrow} + \sum_{1}^{N_\downarrow} T_{i\downarrow}\right), \tag{21}$$

where the conductance is the sum over all available modes of the spin-dependent transmission probabilities T_i. For systems with spin degeneracy, and completely open or closed modes (T_i either 0 or 1), the Landauer formula reduces to equation (20).

This quantization of the conductance is only possible at a nano-scale, in an impurity-free region, and to be observed requires the fabrication of samples of that scale and purity, therefore this effect was not experimentally observed till 1988, when Van Wees et al.[29] measured the transport through a small constriction in a two dimensional electron gas (2DEG) when the width of this constriction is varied. This quantization has afterwards been systematically observed in metallic electrodeposited, point and breaking contacts. Widespread use is made of a STM, where the tip is driven into the sample, and the pulled back. This causes a nanowire to be formed, a behaviour similar to pulling some chewing gum apart. Both the electrical and mechanical properties of these nanowires can then be measured ([30]-[32]). For a review, see [33]

Mechanically-controlled break junctions, where the resistance of a wire is monitored while it is breaking, allow the measurement of quantum conductance steps, first demonstrated at the start of the 90s by Muller et al. [34] and have been used recently to successfully measure the magnetoresistance of atomic nickel contacts [35].

Quantum interference

The Boltzmann equation is correct in the limit that the mean free path is long com-

pared to the electron wavelength, i.e. $k_F\lambda \ll 1$. When the scattering is very strong, or the impurities are very close together as in disordered metals, or if the wavelength of the electrons is very long as in impurity band-conduction in semiconductors, then the spherical wave from the second scattering event can interfere with the incoming spherical wave. This interference leads to substantial corrections to the Boltzmann conductivity, eventually leading to localisation in the extreme case. One manifestation of these interference effects is a gradual reduction in the temperature coefficient of the resistivity so that for resistivities greater than around 150 $\mu\Omega$cm the resistivity actually decreases as the temperature rises. Such a decrease in the resistivity is often considered a feature of semiconductor behaviour, but in fact small negative temperature coefficients are typical in strong scattering disordered metals (Mooij correlation).

The quantum interference effects arise from the coherent interference of electron waves which have followed different scattering paths. Most of the paths interfere incoherently and make an additional contribution to the resistivity. But if we look at the special case of two waves following the same scattering path but in opposite directions they return to the starting point in phase and interfere constructively.

In the regime where $k_F\lambda \sim 1$ we often think of the electron motion as diffusive and executing a sort of random walk. The constructive interference enhances the amplitude of the wavefunction at the origin and so the effect of the interference is to increase the probability that the electron returns to the starting point. The effect is to increase the electrical resistivity or reduce the conductivity [24]:

$$\sigma = \sigma_B + \sigma_{QIE} = \frac{ne^2\tau}{m} - \frac{1}{2\pi^2}\frac{e^2}{\hbar}\left[\frac{1}{\sqrt{D\tau_0}} - \frac{1}{\sqrt{D\tau_i}}\right]. \qquad (22)$$

Here D is the diffusion constant ($D = (1/3)v_F\tau_0$) and τ_0 is the elastic relaxation time.

The negative temperature coefficient is the result of a reduction in the interference as the temperature rises. In the above equation the first term is the Boltzmann contribution to the conductivity which dominates the resistivity. However, when $k_F\lambda \sim 1$ the conductivity has a very small positive temperature coefficient. The second term is the decrease in conductivity due to interference, the full effect of which is experienced at $T = 0$. The third term describes the reduction in the interference effect as the temperature increases through the inelastic relaxation time, τ_i, from electron-phonon scattering or electron-electron scattering. This is because the constructive interference of the two waves must be in phase when they return to the starting point but if one has scattered from a phonon, energy is lost by one electron and the two waves are no longer coherent.

A negative magnetoresistance also results from the reduction in the interference in a magnetic field. The electrons of interest follow a closed path which will enclose a magnetic flux, this shifts the phase of the electron wavefunction, and the two electrons following opposite paths have their phase shifted in opposite directions. This of course destroys the coherence between the waves and so the constructive interference is reduced [24]:

$$\Delta\sigma = -\frac{1}{2\pi^2}\frac{e^2}{\hbar}\sqrt{\frac{eB}{\hbar}}. \tag{23}$$

Quantum interference is usually a small effect that becomes relevant only at very low temperatures and will be therefore of no consideration for the results presented in this work.

1.2.3 Magnetoresistance and domain wall scattering

In ferromagnetic materials the spin of groups of electrons or domains, due to exchange interactions, tends to point in a definite direction which aligns with an external magnetic field which exceeds the saturation field of the material. The exchange interactions are a direct consequence of Pauli's exclusion principle, which is due to the fermionic nature of the electrons itself. In an infinite bulk sample at zero Kelvin, the ground state would therefore be a homogeneously magnetized single domain. This is not possible for finite samples, because one single domain would lead to magnetic charges at the surface, and with it shape demagnetizing fields, which would increase the magnetostatic energy of the system.

This multiple domain structure, with alternating directions of magnetization [36] implies that, in between domains, the magnetization vector has to rotate from one direction to another. The resulting magnetic structure is called a domain wall (figure 1.6). Obviously, the magnetization in a domain wall is not uniform, leading to an increase in exchange, anisotropy and dipole energies. The process of domain formation is therefore a balance between the energy cost of forming the domain walls on the one hand, and the decrease in the magnetostatic energy on the other hand. This balance will determine the number and size of the domains. If the magnetostatic energy is very small, it is easy to form a single domain state, but if it happen to be much bigger than the other energies involved, each atom would have the magnetization pointing in a different direction and the ferromagnet would become a normal metal, but this is very unlikely to happen.

The width of a domain wall [37], or how quickly the moments rotate from one direction to the other, is determined by the exchange energy and the anisotropy. The former favors a parallel alignment of the moments, which tends to broaden the wall, with only a very gradual rotation of the magnetization vector. The later favors an abrupt change and hence

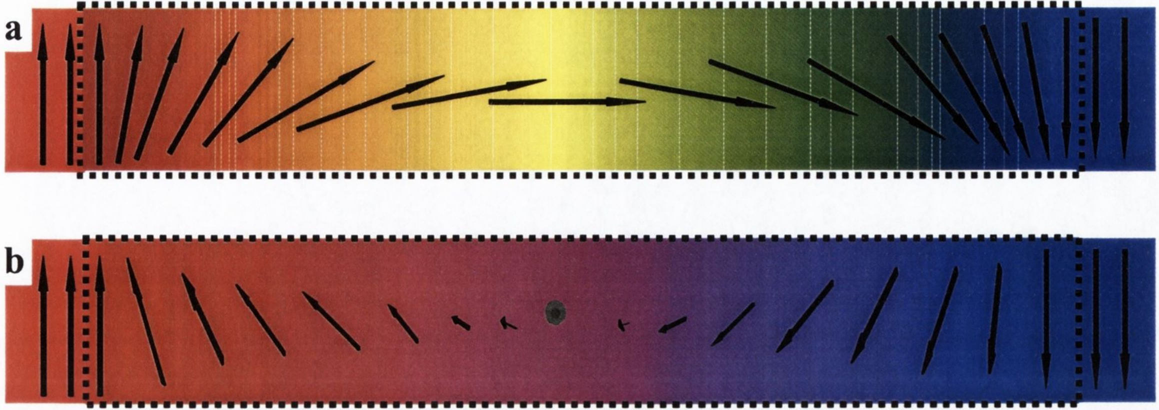

Figure 1.6. Magnetic domain walls. a) Rotation in plane of the magnetization (Neel wall) and b) rotation out of plane (Bloch wall). Neel walls are energetically favourable for thin films. The change from out of plane to in plane for permalloy occurs at about 30 nm.

a narrow wall. The total energy E of the wall, is given by:

$$E = E_{ex} + E_a = \int_{-\infty}^{\infty} \left[A \left(\frac{\partial \theta}{\partial z} \right)^2 + f_a(\theta) \right] dV, \tag{24}$$

with A the exchange stiffness, f_a the anisotropy energy density and θ the rotation of the magnetization between two adjacent moments in the rotation axis z. A stable wall configuration requires a minimization of the total energy with respect to the rotation of magnetization: $\frac{\partial E}{\partial \theta} = 0$. This leads us to the Euler equation for a domain wall:

$$\frac{\partial f_a}{\partial \theta} - 2A \frac{\partial^2 \theta}{\partial z^2} = 0. \tag{25}$$

For the uniaxial anisotropy case, with $f_a = K_u \sin^2 \theta$, where K_u is the uniaxial anisotropy constant, the wall profile can be calculated analytically:

$$\theta(z) = \arctan \left[\sinh \left(\frac{\pi z}{\delta_w} \right) \right] + \frac{\pi}{2}, \tag{26}$$

where $\delta_w = \pi (A/K_u)^{\frac{1}{2}}$ is the domain wall width. Typical values for δ_w in bulk are given in table 3.

Material	Ni	Fe	Co	Permalloy	Rare earth magnet
$\delta_w(nm)$	72	30	15	1000	5

(27a)

Table 3: Domain wall width δ_w for 3d ferromagnets, permalloy and a rare earth magnet.

On the other hand, the resistivity of a ferromagnetic metal can be expressed as:

$$\rho(T) = \rho_i + \rho_{ph}(T) + \rho_{e-e}(T) + \rho_m(B,T). \tag{28}$$

, where ρ_i is the intrinsic resistivity of the material, ρ_{ph} is due to electron-phonon interaction (which depends on the temperature), ρ_{e-e} is the electron-electron interaction (neglected in a free electron model) and ρ_m is the contribution due to magnetic fields or scattering with domain walls and spin disorder.

The magnetic contribution to the resistivity can be found from the general expression for the electric field ($\vec{\varepsilon}$) current in ferromagnetic materials in the presence of a magnetic field:

$$\vec{\varepsilon} = \rho_{\text{perp}}(B)\vec{j} + \left[\rho_{\text{para}}\left(\vec{B}\right) - \rho_{\text{perp}}\left(\vec{B}\right)\right]\left(\vec{m}\cdot\vec{j}\right)\vec{m} + \rho_{\text{H}}\left(\vec{B}\right)\vec{m}\times\vec{j} + \rho_{\text{DW}}\left(\vec{B}\right)\vec{j}, \tag{29}$$

where ρ_{perp} and ρ_{para} are respectively the components of the resistivity for a current perpendicular and parallel to the magnetic field. The first term of the equation is the Lorentz force, proportional to B^2 at low-T , what is called the cyclotron effect, and to B at high-T, and appears in all metals. The second term is the anisotropic magnetoresistance, which depends on the relative orientation of the magnetic moment $\vec{M}$ and the current density $\vec{j}$, and is due to spin-orbit coupling. The third term is the Hall effect ($\rho_H = \rho_o\vec{B} + \rho_{\text{EHE}}\vec{M}$ for the ordinary and extraordinary contributions respectively). The fourth term is due to spin diffusion, and provides effects such as giant magnetoresistance or the [5] domain wall scattering.

The domain wall magnetoresistance in a classical approximation [38] is due to the

changing local magnetic field experienced by a single particle with a spin, and the resultant mistracking of the spin versus this field, which gives raise to the expression:

$$\frac{\Delta R_w}{R} = \frac{2p}{(1-p)^2}\left(\frac{\hbar v_F}{J_{ex}}\right)\frac{1}{\delta_w^2}, \tag{30}$$

with J_{ex} the exchange energy, p the polarization of the material and δ_w the domain wall width.

In a quantum model, the resultant magnetoresistance for a current perpendicular (-> where the contribution of the domain wall to the resistivity is $\rho_\perp$) or parallel (-> $\rho_\parallel$) to the domain wall is [39]:

$$\begin{aligned}\frac{\delta\rho_\perp}{\rho_\perp} &= \left[\frac{\xi^2}{5}\frac{\left(\rho^\uparrow-\rho^\downarrow\right)^2}{\rho^\uparrow\rho^\downarrow}\left(3+\frac{10\sqrt{\rho^\uparrow\rho^\downarrow}}{\rho^\uparrow+\rho^\downarrow}\right)\right]\\ \frac{\delta\rho_\parallel}{\rho_\parallel} &= \frac{\xi^2}{5}\frac{\left(\rho^\uparrow-\rho^\downarrow\right)^2}{\rho^\uparrow\rho^\downarrow},\end{aligned} \tag{31}$$

, where $\xi \equiv \dfrac{\pi\hbar k_F}{4mJ\delta_w}$.

Using these models, the estimated increase in resistance in (Bloch) domain walls for 3d ferromagnets is:

	Fe	Co	Ni
$\frac{\delta\rho}{\rho}$	1.3 %	7.1 %	1.2 %

Table 4 : Contribution of the domain wall scattering to the resistance calculated from ((30)).

In the above calculations, the geometry of the sample is assumed to be of no importance, but the question is if this is still valid at the nano-scale or the actual bit size and devices for recording industry and spin electronics applications. Bruno addressed this issue and

calculated the structure and properties of a geometrically constrained domain wall in a constriction separating two wider regions [40]. He found analytical expressions for the domain wall width in three different models of constriction:

$$\begin{array}{ccc} \textbf{Model} & \textbf{Constriction} & \boldsymbol{\delta_w} \\ I & S = \left\{ \begin{array}{c} S_0 \text{ for } |x| \leq d \\ S_1 > S_0 \text{ for } |x| \geq d \end{array} \right. & \frac{8d}{\pi^2} \\ II & S = S_0 \left(1 + \frac{x^2}{d^2}\right) & \frac{8d}{\pi} \\ III & S = S_0 \cosh(x/d) & 2d \end{array} \tag{32}$$

One remarkable result of the calculation is that for this nano-scaled constrictions, the domain wall width is independent of material parameters such as the exchange stiffness and anisotropy constant, and depends only on the geometry of the constriction. Now the width δ_w will be now of the order of the size of the constriction d. These results are confirmed by Monte Carlo simulations of "isthmus" and "hourglass" geometries (similar to Model I and II, respectively) [43]. These simulations also show that the wall goes from a Néel-like configuration for narrow constrictions, via a cross-over region to Bloch-type for larger constrictions. Another result which arised from the Monte Carlo simulations, are the thermally-excited fluctuations between a Néel-type and a Bloch-type domain walls with different chirality depending on the shape and size of the point contacts [43], [44].

In the bulk, the domain wall width δ_w is much larger than the Fermi wave length λ_F, whereas for nanometric constrictions, the wall can become very narrow, in fact, as narrow as the constriction itself. This has important implications for the resistivity of the domain wall. The wall energy γ_w, which is $2\sqrt{AK}$ for a bulk wall, is now $\frac{\pi^2 AS_0}{2d}$ for the "isthmus" geometry-independent of the anisotropy constant K. And since the width of the domain wall is going to be roughly the size of the constriction, we may be able to increase the contribution of the domain wall resistance to the total resistance just by decreasing the size

of the constriction. This could be a way to increase the magnetoresistance of nano-scaled structures for sensor applications.

From the experimental point of view, the possible applications of this increased domain wall magnetoresistance effect has created a big interest. The matter is still not clearly resolved, and there is no agreement on the magnitude or even the sign of the effect. Matters are further complicated due to the difficulty of separating domain wall effects from ordinary, or Lorentz, and other anisotropic magnetoresistive effects, related for example to the presence of closure domains. Other experimental issues such as magnetostriction become also of fundamental importance due to the huge changes of resistance expected for nanocontacts when the electrodes suffer changes in size at the nanometric or even atomic scale.

The other important conclusion from the applications point of view is that, because the formation of a domain wall costs energy, walls tends to localize themselves in constrictions to minimize their surface area, and hence their total energy. Domain wall trap elements have been proposed for use in MRAM applications, due to their lower switching fields (~ 1 mT) and similar switching times (~ 1 ns), compared simple rectangular elements [45]. The driving of domain walls in permalloy micro and nano-structures with magnetic and electric fields has been studied in permalloy wires [46] and rings [47], magnetic multilayer devices [48], Co/Cu pillars [49] and spin valves [50].

1.2.4 Tunnelling and field emission

When an electronic current encounters an energy barrier which height is bigger that the applied difference of potential, the electrons can still cross the barrier thanks to their

quantum-wave behaviour. In the transport measurements of this work, this barrier will usually represent a narrow insulator region between two conducting electrodes. This barrier is essentially of a one-dimensional nature (perpendicular to the electron flow). If the tunneling barrier extends in the x direction, the momentum in the y and z directions can be taken to be constants of the motion.

For a square barrier ($\sim$ square well) the Schrödinger equation will have the simple form

$$\left(\frac{p^2}{2m}+V\right)\psi = E\psi, \tag{33}$$

where m is the electron mass, p the linear momentum, ψ the wave function, E the energy of the electron and V is constant in a given region. The general solution of (33) has the well-known form

$$\begin{aligned} \psi(x) &= ae^{ikx} + be^{-ikx}, & (34) \\ \frac{\hbar^2 k^2}{2m} &= E - V. & (35) \end{aligned}$$

When $E - V > 0$ the wave functions are plane waves. When $E - V < 0$ we will write $\kappa = ik$ and

$$\psi(x) = ae^{-\kappa x} + be^{\kappa x}. \tag{36}$$

If we assume real plane waves in regions I and III (figure 1.7 a and b) and tunneling in region II, and defining k_{j} (κ_{j}) with j=1,2,3 as the k (κ) vector at the j region, we can neglect $e^{-\kappa_2 w}$ in comparison to $e^{\kappa_2 w}$; in other words, we consider only a strongly attenuating barrier. Then we have

$$\begin{aligned} a_3 &= \frac{4k_1\kappa_2\varphi e^{-\kappa_2 w}}{(k_1^2+\kappa_2^2)^{\frac{1}{2}}\,(k_3^2+\kappa_2^2)^{\frac{1}{2}}}a_1, & (37) \\ \varphi &= ie^{-i\alpha}\exp\left(ik_1x_1 - ik_3x_2\right). & (38) \end{aligned}$$

The wave functions are now exponentially growing and decaying waves characteristic of barrier penetration problems. In a square strongly attenuating barrier, it can be found that the ration of the transmitted current j_t to the incident current j_i is [51]:

$$\frac{j_t}{j_i} = \frac{16 k_1 k_3 \kappa_2^2}{(k_1^2 + \kappa_2^2)(k_3^2 + \kappa_2^2)} e^{-2\kappa_2 w}. \tag{39}$$

The dominant factor of (39) is the barrier penetration factor $e^{-2\kappa_2 w}$. In typical problems of interest this factor may be $10^{-5} - 10^{-10}$, so that it tends to dominate the fraction. In more realistic problems this factor can seldom be calculated accurately, so that usually any experimental determination of the prefactor is doubtful or impossible [52].

The resistance and current, assuming that the electron conserves its energy when it tunnels through the barrier, can be approximated to:

$$R_T \approx \exp\left[\left(\frac{2t}{\hbar}\right)(\varphi m)^{\frac{1}{2}}\right], \tag{40}$$

$$I \approx V \exp\left[-\left(\frac{2t}{\hbar}\right)(\varphi m)^{\frac{1}{2}}\right]. \tag{41}$$

where t is the separation distance between the metallic electrodes (in angstroms)and φ the work function (in volts). Note that only 1 Å change in the separation distance, i.e., smaller than one atom layer, changes the resistance by an order of magnitude if the work function is about 4 eV.

A simple method to determine the potential barrier thickness and height from the $j-V$ characteristic was described by Simmons et al. [53]. The barrier is ideal, the image force is neglected (the effect is to round off the corners of the rectangular barrier and thus reduce the height and thickness). At low voltages, the expression for tunneling current across a

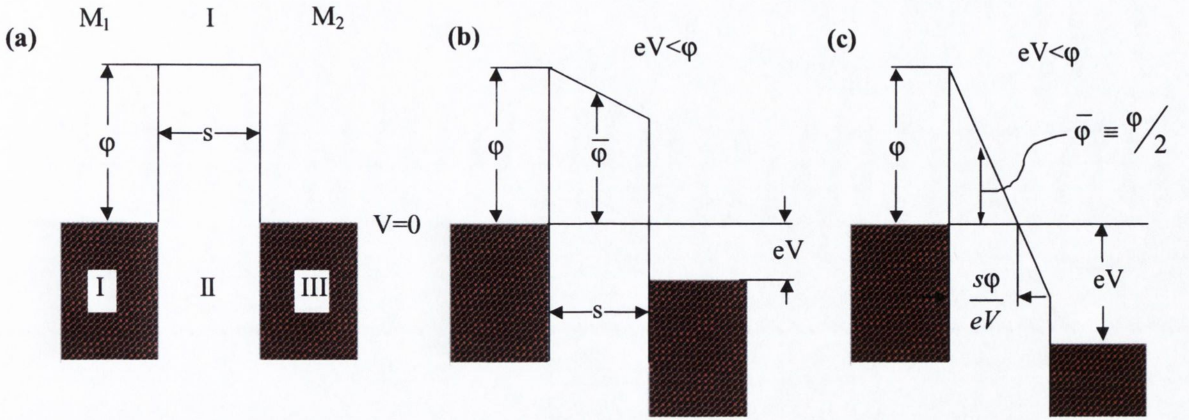

Figure 1.7. Schematic of the energy diagram for a square metal-insulator-metal barrier. a) Before a voltage is applied, b) when the applied voltage is small compared with the barrier height and c) when is bigger that the barrier height (field-emission).

metal-insulator-metal structure reduces to the following form:

$$j = j_0\left\{\left(\varphi - \frac{eV}{2}\right) \times \exp\left[-A\left(\varphi - \frac{eV}{2}\right)^{\frac{1}{2}}\right] - \left(\varphi + \frac{eV}{2}\right) \times \exp\left[-A\left(\varphi + \frac{eV}{2}\right)^{\frac{1}{2}}\right]\right\} \quad (42)$$

$$j = \beta\left(V + \gamma V^3\right) \quad (43)$$

where

$$\beta = \frac{3}{2s}\left(\frac{e}{\hbar}\right)^2 (2m\varphi)^{1/2} \exp\left[-\left(\frac{4\pi s}{\hbar}\right)(2m\varphi)^{1/2}\right] \quad (44)$$

$$\gamma = \frac{\pi m}{3\phi}\left(\frac{es}{\hbar}\right)^2, \quad (45)$$

where φ is the height and s the thickness of the equivalent rectangular barrier, J is the tunneling current density, and V is the device voltage. The expressions for s and φ are obtained from (45) and (45). Thus,

$$s = 4.94\gamma^{\frac{1}{4}} L^{\frac{1}{2}} \quad (46)$$

and

$$\varphi = \left(\frac{0.266}{\gamma^{\frac{1}{2}}}\right) L, \quad (47)$$

where

$$L = \log_{10}\left[\left(4.87 \times 10^{13}\right)/\beta\gamma^{\frac{1}{2}}\right], \tag{48}$$

and where s is in angstroms and ϕ is in electron volts.

If the height of the energy barrier is smaller that the applied difference of potential (in the case that the barrier represents an air or vacuum narrow gap between conducting electrodes, this happens when the electric field overcomes the electron work function), the transport is in the field-emission regime (see figures 1.7 and 1.8). The current I can then be expressed in function of the applied voltage V in terms of the Fowler-Nordheim equation [54]:

$$I = \left(\frac{aV^2}{w^2}\right)\exp\left(\frac{-b\varphi^{\frac{3}{2}}s}{V}\right), \tag{49}$$

where a and b are material constants, φ is the barrier height (or work function) and s is the gap width. A plot of $\ln\left(\frac{I}{V^2}\right)$ vs. V^{-1} in the field-emission regime has negative slope (Fig. 1.8).

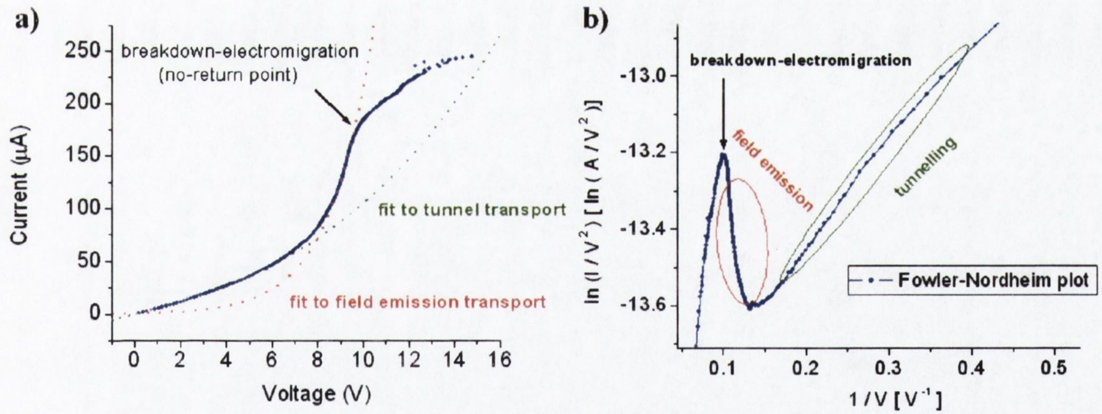

Figure 1.8. a) I-V characteristic of a magnetite nanocontact and fits to tunnel (Simmons) and field-emission regimes. At high voltages the sample is destroyed. b) Fowler-Nordheim plot of the same data. The negative slope is a sign of field-emission transport [52,54].

1.2.5 Heating and capacitive effects, breakdown and electromigration

Both tunnelling and field-emission can be considered as breakdown mechanisms. However, in this section, by breakdown we will refer to the threshold for the Towsend avalanche of gaseous ions, when the electronic current flows through air generating a spark. This sort of electronic transport can only happen at huge voltage drops (above 10^8 Vm^{-1} for air) and for distances of or above the micrometer scale.

In the case of nanostructures, it represents a current flowing directly on the air over the device. This mechanism is irreversible because it destroys or damages the device (figure 1.9) due to the high *air* temperatures generated, in contrast with the usual heating effect due to Joule's law, when the sample is heated by the passage of a current as $Q = RI^2t$, where Q is the heating, R the resistance, I the current and t the time the current is applied.

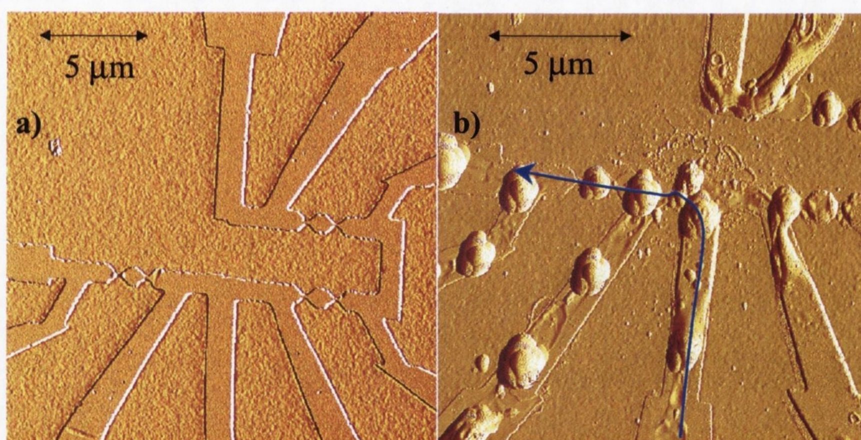

Figure 1.9. When the Towsend avalanche happens, not only is the device destroyed, but all the surroundings are also damaged or melted.

This effect can more easily happen when the electrodes are highly conductive and the nanostructure is fabricated with a low-conductivity, even if metallic, material. In that case, there is a capacitive effect, with a built voltage across both electrodes that discharges when

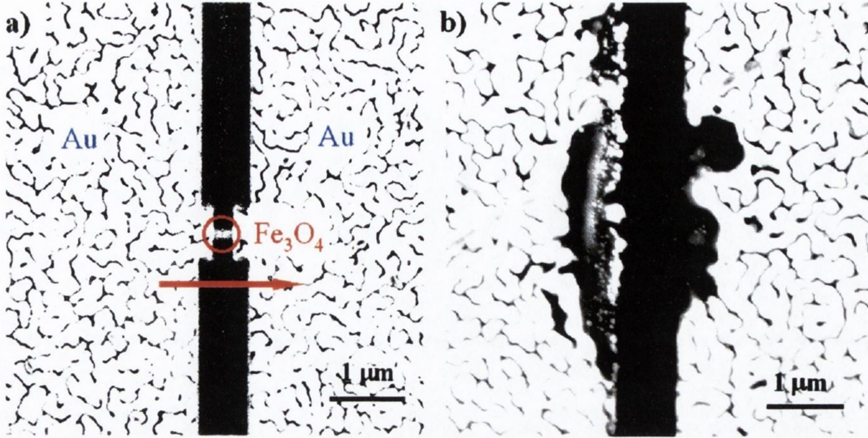

Figure 1.10. Figure: A nanobridge patterned on magnetite covered by gold (red circle) before a) and after b) a DC I-V measurement (up to 10 V). The milling process removes the gold over the nanostructure creating a low-conductivity region and a capacitor-like structure. The gold appears as a bright, meander structure in the image, where the magnetite is darker and granular. The arrow marks the current direction.

the drop of potential is high enough to cause a Towsend avalanche in the air gap over the low conductivity structure (Fig. 1.10).

Another effect that can damage our structures and change its transport properties is electromigration. When a charge carrier collides with the atoms that surround it, they impart a small momentum to them, sweeping the atoms in the direction of the carrier drift. The electromigration of ions requires a force due to the electric current that is:

$$F = qZ_A^*\varepsilon = qZ_A^* j\rho, \tag{50}$$

where q is the electronic charge, Z_A^* is the effective ion valence and ε is the electric field (force per unit charge) producing the electric current density. The mass transport of the electronic flow (electron wind) can cause then distortions in the lattice or even physically breaks the contacts for currents characteristically of order 10^{12} Am^{-2}. The fact that the force is proportional to the current density, makes the nanostructures more sensitive to this effect and will play an important role in chapters 3 and 4.

1.3 Noise measurements

Noise is usually considered as an wanted signal, a voltage or current fluctuation which impose practical limits on the performance of an electronic circuit or a measuring device. However, for more than fifty years, physicists have understood that noise is not always a nuisance: the electronic noise inherent in materials or devices conveys fundamental information on the system dynamics. Electrical noise studies are therefore of major interest both for estimating the intrinsic noise level and for a basic understanding of electronic mechanisms. Besides, the size reduction towards nanoscale devices tends to strongly enhance the apparent noise magnitude of the system [55].

Noise studies as a function of the lateral size and the design of the devices provide an insight into the limiting factors for any application. It has been shown that, with the fabrication of tiny samples, some active sources of noise may induce colossal electrical fluctuations with a lack of Gaussianity [56], which may lead to discrete fluctuations between two levels or random telegraph noise.

The electronic noise we will refer to in this work are the fluctuations in the voltage measured across a patterned structure when a current flows through it. These fluctuations have a random characteristic due to the stochastic nature of the process: the instantaneous values of the fluctuating entity cannot be predicted. Besides, most of the electronic noise we observe in materials and devices are stationary functions of time, the statistical analysis is independent of the time at which the signal is recorded. We will specify our stochastic process (electrical noise) as the power of the signal in the frequency domain, we can then

define the power spectral density (PSD) of the fluctuating process:

$$S_v(\omega) = \lim_{t \to \infty} 2 \frac{|V_t(i\omega)|^2}{t}. \tag{51}$$

Where $V_t(i\omega)$ is the Fourier transform of the fluctuating quantity $v(t)$, $\omega = 2\pi f$, f the frequency of the fluctuation and $i^2 = -1$. If the fluctuating entity is a voltage fluctuation, units of $S_v(f)$ are V^2/Hz. The integration of the PSD over all frequencies is equal to the variance $\sigma^2 = \overline{v^2} - \overline{v}^2$ of the signal.

Electrical noise in solids may originate from various sources such as defect motion, magnetic domain or spin fluctuations, charge carriers crossing an energy barrier, electronic traps, current redistribution within inhomogeneous materials. All these potential microscopic sources behave like "fluctuators"; once they are activated and physically coupled to the charge carriers constituting the current, they induce specific resistance or current fluctuations giving rise to the electrical noise we measure. Despite the random aspect of the fluctuating variable, a clear classification of the different kinds of noise has been carried out. It is mainly referring to the frequency dependence of the PSD.

1.3.1 White noise

White noise is the noise when the PSD is independent of the frequency. For example, a 1 nV fluctuation is as likely to happen 1 time in 1 second as it is to happen 3600 times in one hour. There are two kinds of white noise: the thermal (also called Johnson or Nyquist noise) and the shot noise.

1.3.1a Thermal noise

The first observations of thermal noise, are due to Johnson in 1927 [57], followed by the theoretical analysis based on thermodynamic calculations developed by Nyquist in 1928 [58]. Thermal noise appears in all resistors, resulting from a random thermally-activated motion of charge carriers in equilibrium with a thermal bath.

The power spectral density of the voltage fluctuations can be expressed by: $S_v(f) = 4k_BTR$ and the mean square noise voltage is equal to:

$$\overline{V^2} = 4k_BT\Delta fR \text{ and } \overline{I^2} = \frac{4k_BT\Delta f}{R} \tag{52}$$

Here, Δf is the frequency bandwidth at which the voltage is measured, R is the resistance value of the resistor and k_BT is the thermal energy. For example, the thermal voltage fluctuation measured at the terminals of a 1 kΩ resistor in a 1MHz frequency bandwidth are $V_{\text{rms}} = 4\mu V$. This means that 68 % of the voltage magnitude fluctuations fall within $\pm 4\mu V$. Matching the frequency bandwidth of the experiment with the frequency domain of the desired signal is an obvious and well-known way to improve the signal-to-noise ratio of the measurement.

Quantum corrections are expected at high frequencies (above the microwave regime) taking into account the lifetimes of the charge carriers. The $S_v(f)$ spectrum is then given by [55]:

$$S_v(f) = 4k_BTR\left\{\frac{hf}{k_BT}\left[\frac{1}{2} + \frac{1}{(\exp(hf/k_BT - 1))}\right]\right\}. \tag{53}$$

1.3.1b Shot noise

First measured by Schottky in 1918 [59], this frequency-independent noise is related to the passage of a current across an energy barrier. It is a direct consequence of the quantum

character of the charge carriers and it is due to the fluctuation of the current or voltage around a mean level for the randomly transmitted electrons. The PSD of the shot noise is also a flat spectrum expressed by: $S_I(f) = 2eI$. The current noise can be calculated as:

$$I_{\text{sh}} = \sqrt{2eI\Delta f}, \tag{54}$$

where I is the average current and Δf the frequency bandwidth. For high enough signal frequencies (above the microwave region), quantum corrections involving the lifetimes τ of the charge carrier emission affect the PSD above microwave frequencies and yield:

$$S_I(f) = 2eI\left[\frac{\sin(\omega\tau/2)}{\omega\tau/2}\right]^2. \tag{55}$$

Due to the barrier-related nature of this phenomenon, it is of fundamental importance in semiconductor devices and tunnel junctions. From the spin electronic point of view, shot noise has been found in ferromagnetic-insulator-ferromagnetic tunnel junctions, providing fluctuations up to a 35 % in tunnel magnetoresistance (TMR) signal at room temperature [60].

For tunnelling transport, since the thermal noise is dependent only of the resistance, the shot noise will dominate the frequency-independent part of the PSD once the applied current is over a threshold that can be found by using the Simmons equations (45), (45) and (52), (54) as:

$$2eI\Delta f > \frac{4k_BT\Delta f}{R} \rightarrow I > \frac{2k_BT}{eR} \rightarrow I > \frac{2K_BTw\beta\left(1+3\gamma V^2\right)}{e}, \tag{56}$$

when the applied voltage is much smaller than the barrier height, $eV \ll \varphi$, this can can be

approximated to:

$$I > \frac{2k_B T w \beta}{e}, \tag{57}$$

where w was defined as the cross-section of the tunnel junction and β the conductivity at low voltages.

For MHz and higher frequency applications like TMR read-heads, shot noise may set the optimum sensitivity of the sensor. The set-up point of the bias voltage should be a compromise between the absolute $V(H)$ voltage, the decreasing $\Delta V(H)/V(H = 0)$ MR value versus the applied electric field and the shot noise level defined by the current flowing through the device.

The thermal and shot noise are inherent to the material and device measured, and correspond to the lowest noise level one can measure. The noise level above the theoretical thermal noise is usually estimated in dB, originates from the electronic equipment, the impedance mismatch and an inefficient shielding and grounding of the circuit [61].

However, in most cases, once a current is applied through a material, voltage fluctuations appear at low frequency, which can be several orders of magnitude greater than the Johnson or the shot noise. These fluctuations are expected to constitute a limiting factor for low frequency applications, see figure 1.11. Their PSD spectrum follows a 1/f dependency, and is studied in the following section.

1.3.2 1/f noise

The commonly called "$1/f$ noise" refers to those fluctuations with a PSD which follow a $1/f^{\alpha}$ law, where the exponent α is equal or close to 1. This noise is also called "flicker" or

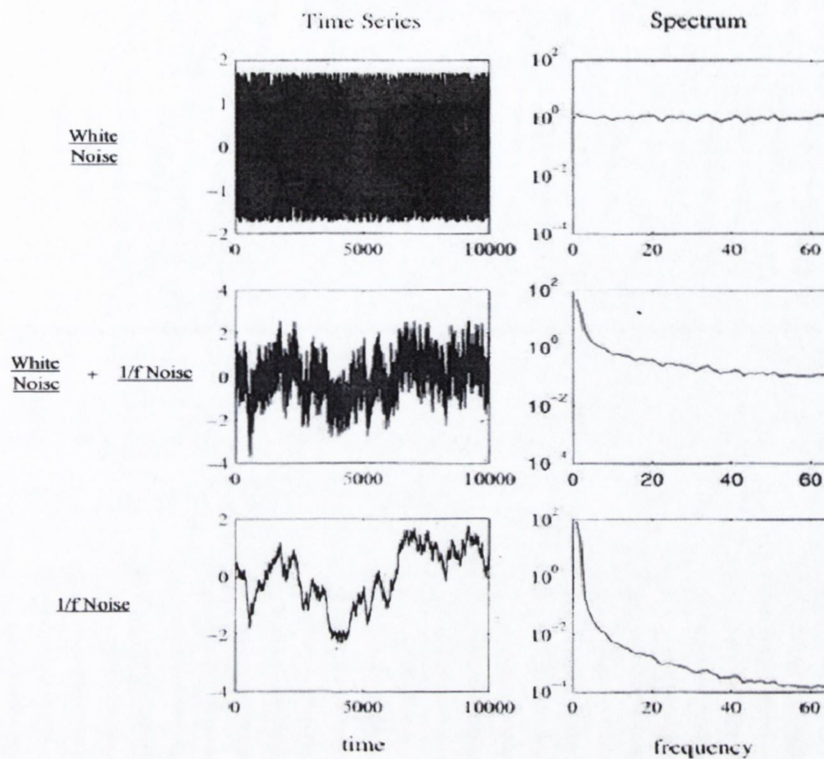

Figure 1.11. The white and $1/f$ noise in the real and the Fourier transform space. After [55].

"excess" noise because it appears on top (or in excess) of the white noise. Was first measured by Johnson as an additional current fluctuation in thermionic tubes added to the shot noise [62]. He found that this added noise had a spectral density that increased with decreasing frequency f.

The striking aspect of the $1/f$ noise which motivates a vast amount of research activity (one third of all publications on noise problems deal with $1/f$ noise) is its ubiquitous nature [55]. Over the last fifty years, it has been observed in a tremendous variety of systems, far beyond the borders of solid state physics: $1/f$ fluctuations have been reported in earthquakes studies [63], in the time dependence of the water level of the river Nile [64], in music [65], in biology [66]. Ionic current fluctuations through a neuro-membrane exhibit a $1/f$ spectrum

[67], and so does the human heartbeat frequency, which fluctuates with a PSD close to $1/f$ below 0.3 Hz [68].

$1/f$ electrical noise is of course also present in nanostructured and spin-electronic devices devices ([69]-[72]), in half-metallic ferromagnets [73] and CMR perovskites ([73]-[75]), independently of the dimensionality of the material.

The almost omnipresence of the $1/f$ noise lead to a demonstration of its intrinsic nature in a major experiment performed by Voss and Clarke in 1976 [76]: in zero current, fluctuations of the variance of the Johnson noise exhibit a $1/f$ power spectrum, which rules out any contribution of the driving current on the resistance fluctuations. The intrinsic $1/f$ noise can be discriminated from external contributions, usually due to the preamplifier used for the measurement, by studying the dependence $S_v(f) \propto V^2 \propto I^2$.

The $1/f$ noise has also practical applications, and can be used for the study of electromigration and degeneration of devices (Fig. 1.12). If 1/f noise is induced by fluctuations in the number of quasi-equilibrium vacancies in a sample is stationary, then the electromigration noise must be non-stationary, at current densities of j $\tilde{}10^{-11} - 10^{-12}$ A/m^2 the current dependence of noise PSD differs from quadratic, and $S \propto j^n$ with n = 3,4...7, also the α exponent in $1/f^\alpha$ increases (α is typically ~2 in electromigration processes). In submicron metal conductors with a bamboo structure, the activation energy determined from the temperature dependence of the $1/f^2$ noise PSD proved to be equal to the activation energy of diffusion across a crystal lattice [77]. This makes of noise a very sensitive tool to predict the mean failure current and time of devices (Fig. 1.12).

We have seen that the white noise varies with the resistance or the current applied to the sample, and hence inversely with the cross section of the sample, but the $1/f$ noise is,

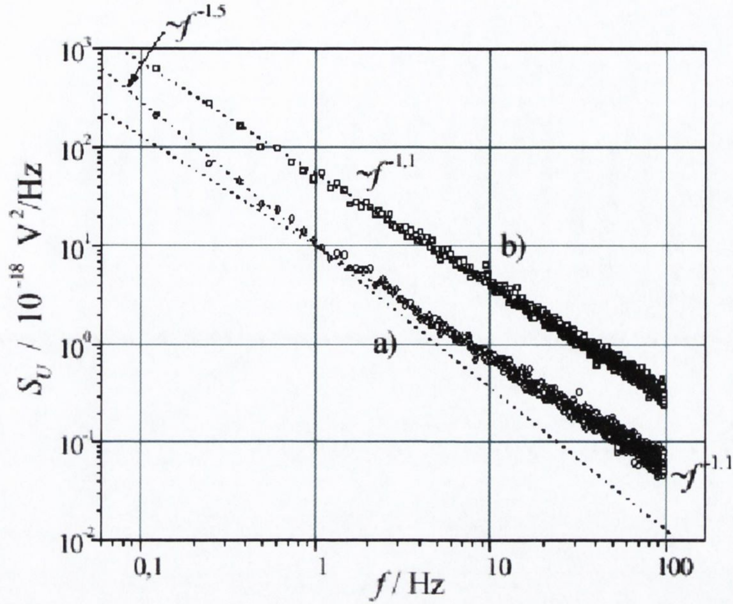

Figure 1.12. a) Noise spectrum after ca. 60 min current damaging (180 mA). The steeper component is previous relaxing during 60 min zero current. b) Relaxed noise spectrum after 100 min current damaging and > 60 min zero current. Observe the increase of the noise powe, whereas the resistance had not varied [77].

in a rough approach, inversely proportional to the volume of the sample studied ([78], [79]). This is because, while the size of the sample is reduced, the size of the noise sources remains unchanged, therefore they induce stronger fluctuations on the overall electronic transport. Obviously, this is true only as long as the size of the device is much bigger that the noise sources, and this argument is not applicable for atomic and nano-scaled devices, but gives an idea of the increased relevance of $1/f$ noise as we reduce the size of our devices.

Hooge [80] quantified the $1/f$ resistance fluctuations in1969 as:

$$S_v(f) = \frac{\gamma_H V^2}{N_c f}. \tag{58}$$

Here, V is the applied voltage, N_c the number of charge carriers in the noisy volume

and γ_H is a dimensionless constant for $\alpha = 1$, which is called Hooge's constant and refers to the noise level once the PSD is normalised by the volume and the applied voltage. Hooge's expression implies that the noise level is independent of the temperature. However, since the eighties, strong experimental evidence has been found that the Hooge's "constant" actually ranges from 10^{-6} to 10^{7} and is temperature dependent [55]. Besides, the normalisation by the number of charge carriers is strongly questionable because it would imply that each mobile carrier individually carries the noise. The lowest γ_H values have been obtained for bismuth and semiconductors with very clean surfaces. 10^{-3} to 10^{-2} are the "standard" Hooge's constants for well crystallised metallic films and semiconductors. The noise level is usually between 4 and 6 orders of magnitude higher in magnetic materials, oxides and nanocomposites.

In the framework of noise experiments on a micron scale and below and with the patterning of nano-structured materials, we expect new promising area of studies. In the case of a magnetic structure it will be possible to locate an unique domain wall, the measurement of resistance fluctuations through the wall should be strongly influenced by its scattering processes. It may probe intrinsic properties like the time-scale of spin dynamics within the magnetic inhomogeneity. Furthermore, the achievement of magnetic materials with sizes comparable to the mean free path of the charge carriers or the spin coherence length induces change in the conductivity processes toward the ballistic regime. Noise measurements are therefore thought to be an accurate tool to investigate the new conductivity regime. The spatial correlation of the fluctuations within few tens of nanometer should also be revisited.

The most customary concept on which most of the theoretical approaches are based is the concept of superposition of random and independent events coupled to the resistivity ([81],

[82]). If one assumes the existence of a single two-level process (TLP), also called "fluctuator", with one relaxation time τ, it has been demonstrated that the PSD of the fluctuations is a Lorentzian spectrum. If one considers now a physical system with a distribution of relaxation time $D(\tau)$, associated with independent TLP, the corresponding PSD is defined by:

$$S_v(f) \propto \int \frac{\tau}{1+w^2\tau^2} D(\tau) d\tau. \tag{59}$$

Considering a distribution of relaxation times equal to $D(\tau) \propto 1/\tau$, between two relaxation times τ_1 and τ_2, the integration of the Lorentzian yields:

$$S_v(f) \propto 1/f \text{ for } \tau_2^{-1} \leq f \leq \tau_1^{-1}. \tag{60}$$

In case of thermally activated processes following an Arrhenius law [82], $\tau = \tau_0 \exp(E/kT)$, where τ_0 is the attempt frequency, usually related to the phonon frequency in solids and E is the activation energy in a symmetric TLP, the energy distribution required to provide $1/f$ noise between $\left[\tau_2^{-1}; \tau_1^{-1}\right]$ is then:

$$D(E) = \text{constant for } E_1 = kT \ln\left(\frac{\tau_1}{\tau_0}\right) \leq E \leq E_2 = kT \ln\left(\frac{\tau_2}{\tau_0}\right). \tag{61}$$

Following the du Pré concept [82], Dutta, Dimon and Horn (DDH) proposed in 1979 a model based on a superposition of thermally activated random and independent processes with a broad distribution of transition energies [83], under the assumption that the number of fluctuators and/or their coupling strength to the conduction processes are independent of temperature. The richness of their approach is to extract from the temperature dependence of the PDS slope, $\alpha(T)$, the shape of the transition energy distribution $D(E)$ responsible for

the resistance fluctuations (Fig. 1.13), which provides in some cases a clear signature of the microscopic origins of the fluctuators. Following this model $\alpha(T)$ can be expressed as:

$$\alpha(T) = -\frac{\partial \ln S_v(f,T)}{\partial \ln f} = 1 - \frac{1}{\ln(w\tau_0)}\left(\frac{\partial \ln S_v(f,T)}{\partial \ln T} - 1\right), \tag{62}$$

and estimate of the energy distribution responsible for the fluctuations observed in the experimental frequency and temperature window:

$$D(E) \propto 2\pi f S_v(f,T)/kT. \tag{63}$$

Let us notice that a flat $D(E)$ distribution gives rise to a pure $1/f$ spectrum and a linear temperature dependence of the noise level. However, departure from the linearity with $\alpha(T)$ values different from 1 implies a non-zero derivative of the energy distribution, $\partial D(E)/\partial E \neq 0$. Assuming $\alpha(T) > 1$ (respectively $\alpha(T) < 1$) implies an excess in the density of the low (high) energy fluctuators and a negative (positive) derivative $\partial D(E)/\partial E$ over the energy window.

The DDH model has been essentially applied to noise in metals ([83], [84]). It is though that the rather high energies associated with the noise sources correspond to the energy necessary to create and induce atomic defect hops between equivalent sites in energy ([85], [86]). The coupling to the resistivity occurs via the different efficient cross-sections scattering between accessible sites.

$1/f$ electrical noise in magnetic materials:

As it should be expected, since magnetic dynamics interact with itinerant electrons (as, for example, in the electron scattering by spin waves in 3d ferromagnets [87]), magnetic ordering and magnetic dynamics affect the resistance fluctuations that form the electrical noise. This not only increases the order of magnitude of the measured PSD on magnetic

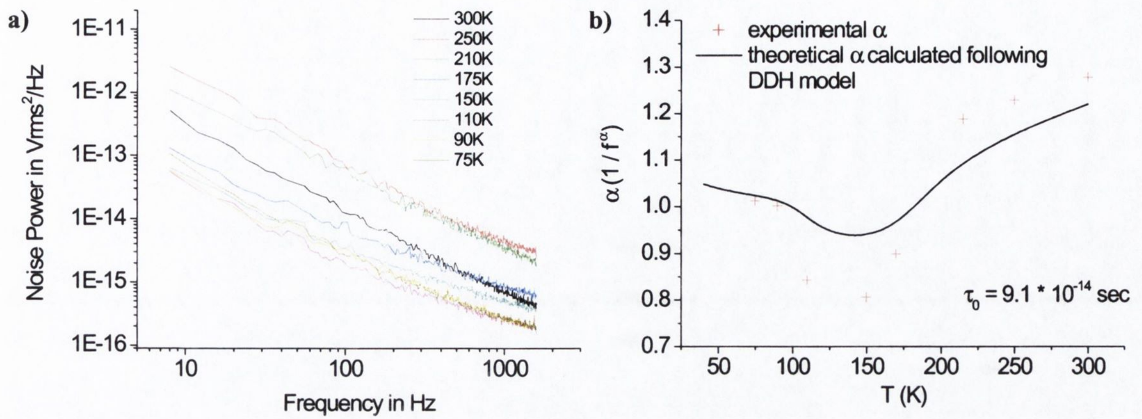

Figure 1.13. a) Temperature dependence of the $1/f^{\alpha}$ noise in an $La_{0.7}Sr_{0.3}MnO_7$ film 12 nm thick. b) Fit of the α parameter to the DDH model, which gives a reasonable qualitative and quantitative agreement. The minimum around 150 K is related with the density of states of $La_{0.7}Sr_{0.3}MnO_7$.

materials (half-metallic oxides [73] and CMR perovskite ([73], [88]-[90]), but also gives us an experimental tool to analyse the dynamics of the magnetic properties. Since $1/f$ noise can be studied in a range of frequencies from 10^{-3} to 10^{3} Hz , which is of the order of magnitude of magnetic domain relaxation, it provides information of magnetization relaxation and stability with time in the local area between the voltage probes, which can be patterned to form a well-defined microscopic, or even nanoscopic region. By studying the voltage fluctuations dependence with magnetic fields we can get an insight an insight into the spin or domain fluctuations, spin waves and other spin disorders, and, in some cases, the switching relaxation time of magnetic elements By using the DDH model, the magnetic volume or the fluctuating entities can also be inferred [91].

Giordano et al. [92] reported the measurements of low-frequency electrical noise of Ni epitaxial films at temperatures from 300 to 625 K. They found that the noise behaviour and associated noise spectra were distinctly different from those of other metals in this

temperature range, which they attributed to magnetic fluctuations. A maximum of resistance fluctuations near T_c has been observed in various ferromagnets and clearly demonstrates the strong influence of domain dynamics on the low frequency electrical noise. The two maxima for noise magnitude versus temperature found in the study; one around T_c (~625 K) and the other one well below, around 450 K were argued to imply microscopic changes in the fluctuating processes, but a direct proof of this argument would require the noise measurement of a well-defined microscopic or nanoscopic area, which magnetization and dynamics could be determined by other methods.

1.3.3 Non-Gaussian and random telegraph noise

White and $1/f$ noise conform to what is called the Gaussian noise. This noise can be modelled by the superposition of independent sources contributing individually and weakly to the variance of the fluctuating quantity. But if the number of independent contributors is very small, or if one (or a few) of them contributed strongly enough to be distinguished from the many others, then we can measure individually the fluctuations of this reduced number of noise sources.

One way to detect non-Gaussian effects on resistance fluctuations is to create a very small volume (below few μm^3) where there will be present only we a very small number of fluctuators which may be distinguished individually. In that case we can use the noise spectrum (formed by discrete fluctuations) to reveal the few "fluctuators" present in that region. We can then study the variations of the fluctuations with the temperature to estimate the activation energies of the fluctuation processes [93]. An example of this non-Gaussian

(NG) noise was found in nano-composite Fe-SiO_2 films [94] It was interpreted in terms of current redistribution in the conducting path due to quantum size effects.

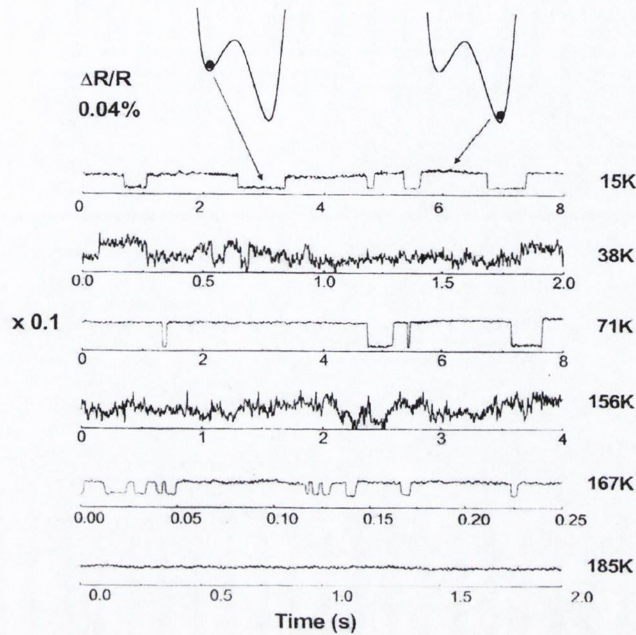

Figure 1.14. Figure: RTN in a LSMO sample and its temperature dependence. After [55].

An extreme case of NG noise when we have only one active fluctuator is random telegraph noise (RTN), an example of which we can see in the figure 1.14 (review [95]).The fluctuation process switches between two states which could be of electrical or magnetic origin coupled differently to the conductance, i.e., each state has a different contribution to the resistance. The time intervals between switching are random, but the two values accessible by the resistance are time independent. In most cases, the RTN is described by a thermally activated two level process. If one assumes an asymmetrical two-well system with energy barrier $E \pm \Delta E$ separating the two states the average time $\tau_i(T, H)$ spent in the i$^{\text{th}}$

state is expressed by:

$$\tau_i(T, H) = \tau_{i,0} \exp\left(\frac{E_i}{kT}\right). \tag{64}$$

From ((53)) and ((64)) we can see that:

$$S_v(f) = \frac{S_v^0(0)}{\cosh\left(\frac{\Delta E}{kT}\right) \times \left[\cosh^2\left(\frac{\Delta E}{kT}\right) + w^2\tau^2\right]}, \tag{65}$$

where $\tau^{-1} = \tau_1^{-1} + \tau_2^{-1}$ is the total rate of transition and $S_v^0(0)$ is the zero-frequency spectral density at $\Delta E = 0$. The PSD follows a Lorentzian spectrum with a corner frequency equal to τ^{-1}. We notice that the PSD of the noise decreases for an asymmetrical ($\Delta E \neq 0$) double-well as the low energy state is more stable. The same Lorentzian spectrum is obtained at low temperature when the switching process is governed by a tunnelling mechanism.

We point out that a statistical analysis of the occupancy lifetimes of the two states as a function of temperature or an applied electric or magnetic field provides unique insight into the energies of the system and its dynamics. Fundamental microscopic variables like the energy differences between two states, the volume of the fluctuating quantity and its intrinsic nature (defects motion, magnetic domains...) can be inferred. from the experimental view, the delicate task is to stabilise a well-resolved RTN over a long time for statistical averages.

Noise measurements in metallic nanobridges with a volume less than 8000 nm^3, and close to the ballistic regime, have shown random telegraph switching at low temperature ([96], [97]). Its origin was attributed to the displacement of individual defects by electromigration. RTN may also be the dominant low frequency noise in magnetic and non-magnetic tunnel junctions with an active area of less than few μm^2. This RTN in tunnel junctions is equivalent to a huge, discrete, shot noise (with fluctuations up to 50 %), where electrons are trapped

and de-trapped in defects located in the insulating layer ([97], [98]). These fluctuations can fully hide the TMR signal, as in case of electrodeposited [Ni/NiO/Co)] nanowires with cross sections less than 0.01 μm^2 [98]. The trapping probability is magnetic field dependent: under a given field, when the local magnetic state of the insulating magnetic oxide differs from the electrode magnetization, the trapping site acts like a spin blockage.

In tiny magnetic structures and in magnetic conductor devices like GMR metallic multilayers, RTN has also been reported as a predominant source of noise in the low frequency range. It is attributed to magnetic domain fluctuations ([99], [100]).

A statistical analysis of the RTN gives rise to an estimate of the magnetic domain volumes, their energy scale and the eventual domain-domain interaction. In a discontinuous GMR Permalloy-Silver multilayer with a lateral size reduced to few μm, Kirschenbaum et al. [101] presented first data of RTN with resistance switches around 1.2% due to thermally activated fluctuations of magnetic domains. From the analysis of the field dependence of the lifetimes of the "up" and "down" resistance states, they inferred a magnetic volume of the switching entity equal to 10^6 μ_B, concluding that the discrete resistance jumps involve correlated switching of a multi-grain complex. The activation energies of the "up" and "down" states, deduced from the temperature dependence of the RTN are respectively of the order of 80 meV and 400 meV. The large energy difference refers to a strongly asymmetrical two energy wells model. Local magnetic interactions may tend to favour one state to the detriment of the other.

Random telegraph noise can also be used to probe the magnetisation reversal of extremely small magnetic clusters. From the study of RTN, Coppinger et al. [102] investigated the single domain switching of the nanometric ErAs clusters in a matrix of GaAs. An angular

study of the influence of the applied magnetic field on the resistance switching rates demonstrates the sixfold magnetic anisotropy of the ErAs nanometric clusters, and evidences for macroscopic tunneling reversal of the EuAs cluster magnetisation at very low temperature.

Bibliography

[1] J.M.D. Coey in "Spin electronics" M. Ziese and M.J. Thornton eds., Springer (2001)

[2] G.A. Prinz, Science **282**, 1660 (1998)

[3] J. Gregg, W. Allen, N. Viart et al., J. Magn. Magn. Mat. **175**, 1 (1997)

[4] D. P. DiVicenzo, Science **270**, 255 (1995)

[5] M.N. Baibich, J.M. Broto, A. Fert, Phys. Rev. Lett. **61**, 2472 (1988)

[6] J.M.D. Coey, J.J. Versluijs, M. Venkatesan, J. of Phys. D: Applied Physics **35**, 2457 (2002)

[7] J.M.D. Coey and M. Venkatesan, J. Appl. Phys. **91**, 8345 (2002)

[8] S.P. Lewis, P.B. Allen and T. Sasaki, Phys. Rev. B **55** 10253 (1997); M.A. Korotin, V.I. Anisimov, D.I. Khomski and G.A. Sawatzky, Phys. Rev. Lett. **80**, 4305 (1998)

[9] K.I. Kobayashi, T. Kimura, H. Sawada et al., Nature **395**, 677 (1998)

[10] I.I. Mazin, Appl. Phys. Lett. **77**, 3000 (2000)

[11] R.A. de Groot, F.M. Mueller, P.G. van Engen and K.H.J. Buschow, Phys. Rev. Lett. **50**, 2024 (1983)

[12] R. Weht and W.E. Pickett, Phys. Rev. B **60**, 13006 (1999)

[13] M. Penicaud, B. Silberchiot, C.B. Sommers et al., J. Magn. Magn. Mater. **103**, 212 (1992)

[14] B. Nadgorny, I.I. Mazin, M. Osofsky et al., Phys. Rev. B **63**,4433 (2001)

[15] D.J. Singh Phys. Rev. B **55**, 313 (1997)

[16] Mazin I I, Phys. Rev. Lett. **83** 1427 (1999)

[17] S.A. Wolf et al., Science **294**, 1488 (2001), and references therein

[18] G.Schmidt et al., Phys. Rev. B **64**, 121202 (R) (2001)

[19] T.P.Pareek Phys. Rev. Lett. **92**, 076601 (2004)

[20] T. P. Pareek and P. Bruno, Phys. Rev. B **63**, 165424 (2001); P. Bruno, Phys. Rev. Lett. **79**, 4593 (1997).

[21] L. D. Landau and E. M. Lifshitz, Quantum Mechanics Vol. 3 (Pergamon, Oxford, 1980), pp. 583–588.

[22] M.S. Ferreira and S. Sanvito, Phys. Rev. B **69**, 035407 (2004)

[23] O. Céspedes, M.S. Ferreira, S. Sanvito et al., J. Phys. C: Condensed Matter **16**, L155 (2004)

[24] B.J. Hickey in "Spin Electronics", M. Ziese and M.J. Thornton eds., Springer (2001)

[25] E.H. Sondheimer, Adv. Phys. **1**, 1 (1952)

[26] N.F. Mott, Metal insulator transitions (2^{nd}edition) (Taylor and Francis, London, 1985)

[27] N.F. Mott, Philosophical Magazine **34**, 643 (1976)

[28] Y. V. Sharvin, Sov. Phys. JETP **21** (1965)

[29] B.J. van Wees, H. van Houten, C.W.J. Beenakker et al., Phys. Rev. Lett. **60**, 848 (1988)

[30] J.I.Pascual, J. Mendez, J. Gomez-Herrero et al., Phys.Rev. Lett. **71**, 1852 (1993); J.I. Pascual, J. Mendez, J. Gomez-Herrero et al., Science **267**, 1793 (1995)

[31] L. Olesen, E. Lægsgaard, I. Stensgaard et al., Phys.Rev. Lett. **72**, 2251 (1994)

[32] N. Agraït, G. Rubio, and S. Vieira, Phys.Rev.Lett. **74**, 3995 (1995)

[33] Nicolas Agrait, Alfredo Levy Yeyati, Jan M. van Ruitenbeek, cond-mat/0208239

[34] C.J. Muller, J.M. van Ruitenbeek, and L.J. de Jongh, Phys. Rev. Lett. **69**, 140 (1992)

[35] Viret M, Berger S, Gabureac M, et al.,Phys. Rev. B **66**, 220401 (2002)

[36] P. Weiss, J. de Phys. Rad. **6**, 661 (1907)

[37] F. Bloch, Z. Phys. 74, 295 (1932); L. Landau and E. Lifshitz, Phys. Z. Sowjetunion **8**, 153 (1935)

[38] M. Viret et al., Phys. Rev. B 53, 8464 (1996), J.F. Gregg et al., Phys. Rev. Lett. **77**, 1580 (1996)

[39] P.M. Levy and S. Zhang, Phys. Rev. Lett. **79**, 5110 (1997)

[40] P. Bruno, Phys. Rev. Lett. **83**, 2425 (1999)

[41] K. Hong and N. Giordano, J. Phys. C: Cond. Matter. **10**, L401 (1998); B. Çetin and N. Giordano, Mat. Science Eng. B **84**, 133 (2001)

[42] U. Ruediger, J. Yu, S. Zhang, A.D. Kent, and S.S.P. Parkin, Phys. Rev. Lett. **80** 5639 (1998); A.D. Kent, U.Ruediger, J. Yu, L. Thomas and S.S.P. Parkin, J. Appl. Phys **85** 5243 (1999)

[43] Y. Labaye, L. Berger and J.M.D. Coey, J. App. Phys. **91**, 5341 (2002)

[44] O. Céspedes, G. Jan, M. Viret et al., J. Appl. Phys. **93**, 8433 (2003).

[45] R.D. McMichael, J. Eicke, M.J. Donahue and D.G. Porter, J. Appl. Phys. **87**, 7058 (2000)

[46] C.C. Faulkner et al., IEEET Magn. **39** 2860 (2003)

[47] M. Klaui et al., App. Phys. Lett. **83**, 105 (2003)

[48] E.B. Myers, D.C. Ralph, J.A. Katine et al., Science **285**, 5429 (1999)

[49] J. Grollier, V. Cros, A. Hamzic et al., App. Phys. Let. **78**, 3663 (2001)

[50] J. Grollier, P. Boulenc, V. Cros et al., App. Phys. Let. **83**, 509 (2003)

[51] E.O. Kane in Tunneling Phenomena in Solids, E. Burstein and S. Lundqvist eds., Plenum, (1973)

[52] I. Giaever in Tunneling Phenomena in Solids, E. Burstein and S. Lundqvist eds., Plenum, (1973)

[53] J.G. Simmons and G.J. Unterkofler, J. Appl. Phys. **34** 1828 (1963)

[54] R H Fowler and L Nordheim, Proc. Roy Soc A **119**, 173 (1928)

[55] B. Raquet in "Spin Electronics", M. Ziese and M.J. Thornton eds., Springer (2001)

[56] L.S. Kirschenbaum, C.T. Rogers, S.E. Russek, and S.C. Sanders, IEEE Trans. Magn. **31**, 3943 (1995)

[57] J.B. Johnson, Nature 119, 50 (1927); Phys. Rev. **29**, 367 (1927)

[58] H. Nyquist, Phys. Rev. **32**, 110 (1928)

[59] W. Schottky, Ann. Phys. (Leipzig) **57**, 541 (1918)

[60] E.R. Nowak, M.B. Weissman and S.P.P. Parkin, Appl. Phys. Lett. **74**, 600 (1999)

[61] S. Demolder, M. Vandendriessche, and A. van Calster, J. Phys. E **13**,1323 (1980)

[62] J.B. Johnson, Phys. Rev. **26**, 71 (1925)

[63] S. Machlup, Proc. 6th Int. Conf. on Noise in Physical Systems, Gaithersburg, MD, USA, 157 (1981)

[64] M. Gardner, Scientific American **238**, 16 (1978)

[65] R.F. Voss and J. Clarke, J. Acoust. Soc. America **63**, 258 (1978)

[66] T. Musha, Proc. 6th Int. Conf. on Noise in Physical Systems, Gaithersburg, MD, USA, 143 (1981)

[67] D.E. Burgess, T.A. Zimmerman, M.T. Wise, et al., Am. J. Physiol. Regulatory

Integrative Com. Physiol. **277**, R894 (1999)

[68] T.R. Wigton, R.E. Sabbagha, R.K. Tamura, L. Cohen, et al., Obstet. Gynecol. **82**, 219 (1993)

[69] E.R. Nowak, M.B. Weissman, and S.P.P. Parkin, Appl. Phys. Lett. **74**, 600 (1999)

[70] H.T. Hardner, M.J. Hurben, and N. Tabat, IEEE Trans. Magn. **35**, 2592 (1999)

[71] M.A.M. Gijs, J.B. Giesbers, P. Belien et al., J. Magn. Magn. Mat. **34**, 1450 (1998)

[72] B. Doudin, G. Redmond, S.E. Gilbert and J.-Ph. Ansermet, Phys. Rev. Lett. **79**, 933 (1997)

[73] B. Raquet, J.M.D. Coey, S. Wirth and S. von Molnár, Phys. Rev. B. **59**, 12435 (1999)

[74] M. Rajeswari, A. Goyal, A.K. Raychaudhuri, M.C. Robson et al., Appl. Phys. Lett. **69**, 851 (1996)

[75] G.B. Alers, A.P. Ramirez and S. Jin, Appl. Phys. Lett. **68**, 3644 (1996)

[76] R.F. Voss and J. Clarke, Phys. Rev. B. **13**, 556 (1976)

[77] U. Behner et al. IEEE Transactions on Components, Packaging, and Manufacturing [p. 243]

[78] M.J. Buckingham in "Noise in Electronic Devices and Systems", J. Wiley &Sons (ed.), New York (1983)

[79] P Dutta and P.M. Horn, Rev. Mod. Phys. **53**, 497 (1981)

[80] F.N. Hooge and A. Hoppenbrowers, Physica (Amsterdam) **45**, 386 (1969); **42**, 331 (1969); F.N. Hooge, Physica **83**B, 14 (1976)

[81] J. Bernamont, A. de Phys. (Leipzig) **7**, 71 (1937)

[82] F.K. du Pré, Phys. Rev. **78**, 615 (1950)

[83] P. Dutta, P. Dimon and P.M. Horn, Phys. Rev. Lett. **43**, 646 (1979)

[84] J.H. Scofield, J.V. Mantese and W.W. Webb, Phys. Rev. B **34**, 723 (1986)

[85] J.H. Scofield, J.V. Mantese and W.W. Webb, Phys Rev. B **32**, 736 (1985)

[86] J. Pelz and J. Clarke, Phys. Rev. Lett. **55**, 738 (1985)

[87] Raquet B, Viret M, Sondergard E et al., Phys. Rev. B **66**, 024433 (2002)

[88] B. Raquet, A. Anane, S. Wirth et al., Phys. Rev. Lett. **84**, 4485 (2000)

[89] R.D. Merithew, M.B. Weissman, F.M. Hess et al., Phys. Rev. Lett. **84**, 3442 (2000)

[90] M. Rajeswari, R. Shreekala, A. Goyala et al., Appl. Phys. Lett. **73**, 2670 (1998)

[91] N.E. Israeloff, M.B. Weissman, G.A. Garfunkel et al., Phys. Rev. Lett. **60**, 152 (1988)

[92] N. Giordano et al., Phys. Rev. B. **53**, 14937 (1996)

[93] P.J. Restle, R.J. Hamilton, M. B. Weissman and M.S. Love, Phys. Rev. B **31**, 2254 (1985)

[94] Raquet B, Goiran M, Negre et al., Physical Review B **62**, 17144 (2000)

[95] M.J. Kirton and M.J. Uren, Adv. Phys. **38**, 367 (1989)

[96] K.S. Ralls and R.A. Buhrman, Phys. Rev. Lett. **60**, 2434 (1988)

[97] K.S. Ralls, D.C. Ralph and R.A. Buhrman, Phys. Rev. B **47**, 10509 (1993)

[98] B. Doudin, G. Redmond, S.E. Gilbert and J.-Ph. Ansermet, Phys. Rev. Lett. **79**, 933 (1997)

[99] F. Coppinger, J. Genoe, D.K. Maude et al., Phys. Rev. Lett. **75**, 3513 (1995)

[100] M. Xiao, K.B. Klaasen, J.C.L. van Peppen and M.H. Kryder, J. Appl. Phys. **85**, 5855 (1999)

[101] L.S. Kirschenbaum, C.T. Rogers, S.E. Russek and S.C. Sanders, IEEE Trans. Magn.

31, 3943 (1995)

[102] F. Coppinger, J. Genoe, D.K. Maude et al., Phys. Rev. Lett. 75, 3513 (1995), Phys. Rev. B **57**, 7182 (1998)

Chapter 2

Experimental method

2.1 Sample preparation and characterization

2.1.1 Thin film deposition

Practically all applications (with the exception of micro-electro-mechanics MEMs) for spin electronic devices require their fabrication from a thin film geometry. The films must have good electrical and magnetic properties, as well as a smooth topography allowing for the patterning of nanodevices fabricated from materials such as metals, metallic oxides and magnetic semiconductors. The deposition method must be able to remove the atoms from a target (see table 1) to deposit them on a substrate, producing a film with reproducible properties. The methods employed for the fabrication of thin films in this work include sputtering, thermal evaporation and pulsed laser deposition.

Bond	**Strength** (kJ/mol)	$\mathbf{E_b}$ (eV)
Ionic	590 – 1050	6 – 11
Covalent	125 – 850	1.3 – 9
Metallic	65 – 850	0.65 – 9
Van der Waals	4 – 45	0.043 – 0.43
Hydrogen bond	20 – 50	0.2 – 0.52
C–C	350	3.6
C=C	615	6.34
C≡C	840	8.7

Table1: Strength and energy of the different chemical bindings.

Sputtering is a vacuum process performed by applying a high voltage across a low-

pressure gas (usually argon) to create a plasma, which consists of electrons and gas ions in a high-energy state. These ions are accelerated towards a target, made of the desired material for the film, by a dc or rf voltage bias. Energized plasma ions strike the target and, under good vacuum, the struck target atoms will be ejected with enough energy to travel to form a bond with the substrate and the subsequent formation of a film of the extracted material on the substrate. To deposit on metallic substrates a DC bias is usually employed, whereas when the substrate is non-conductive, e.g., a polymer, a radio-frequency (RF) sputtering is generally used. The resulting crystallographic phase of the film depends on the substrate type, its temperature and the surrounding atmosphere. In the case of oxide films, e.g., magnetite, a partial pressure of oxygen is added to the argon.

Balanced magnetrons have a tightly confined magnetic field so the magnetic "lines of force" remain close to the target surface and the plasma is strongly confined to this area. This allows the field to be more easily optimized for high target utilization, reducing the deposition costs and, since electrons and ions are less likely to strike the substrate, the substrate stays cooler.

Thermal evaporation For this method, the desired coating metal is evaporated in a vacuum environment, and the atomic cloud formed coats all the surfaces in the line of sight between the substrate and the metal source. This method can produce shiny, smooth films up to 0.5 μm. The coating, however, is fragile and peels off easily, what makes it not good for high resolution lithography applications (see figure 2.1). However, is a very useful method for the metallisation of not very conductive thin films in the areas where we want to make electrical contacts.

PLD: Conceptually, pulsed laser ablation is an extremely simple technique, it is similar

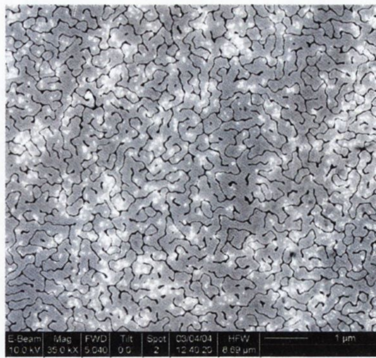

Figure 2.1. Evaporated gold film 60 nm thick on top of a Fe_3O_4 sputtered film. Thermal evaporation produces good-conductivity films, but the topography does not have the same quality as sputtered or PLD-deposited films.

to sputtering, but with a laser being used to create the ionic plasma. The setup consists of a target holder and a substrate holder housed in a vacuum chamber. A high-power laser is used as an external energy source to vaporize materials and to deposit thin films. A set of optical components is used to focus and raster the laser beam over the target surface. The advantages of pulsed laser ablation are flexibility, fast response, energetic evaporants, and congruent evaporation. The disadvantages are the limited uniformity, the presence of particulates and the target surface modification at it is being employed. This method is commonly used for the deposition of magnetic oxides such as manganites (e.g., $La_{0.3}Sr_{0.7}MnO_3$), double perovskites (e.g., Sr_2FeMoO_6) and magnetic semiconductors (see figure 2.2).

2.1.2 Atomic and magnetic force microscopy

The atomic force microscope (AFM),was invented in 1986 by Binnig, Quate and Gerber [2]. The AFM utilises a sharp probe moving over the surface of a sample in a raster scan to

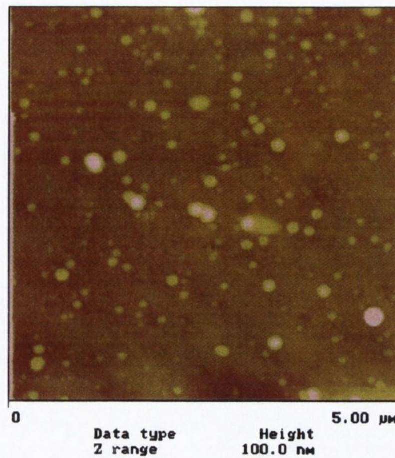

Figure 2.2. Atomic force microscope of a Co doped ZnO thin film deposited by PLD. The image shows the characteristic 'bubling' that appears in many PLD films. The film was deposited by C. Fitzgerald.

reproduce the topography of the sample surface thanks to a tip on the end of a cantilever which bends in response to the force between the tip and the sample.

The first AFM used a scanning tunnelling microscope at the end of the cantilever to detect the bending of the lever, but now most AFMs, including the Nanoscope Multimode III (Veeco) used in this work, employ an optical lever technique. In this optical update a laser is reflected at the edge of the cantilever and into a photodetector. As the cantilever flexes, the light from the laser is reflected onto different regions of the photodetector.

Contact mode is the easiest method of operation of the AFM. As the name suggests, the tip and sample remain in close contact as the scanning proceeds. By "close contact" we mean in the repulsive regime of the inter-molecular force curve, i.e., they are touching. The AFM measures the forces (at the atomic level) between the sharp probing tip and the sample surface by measuring the changes in the bending of the cantilever through the variation of the reflected laser spot position z in the photodetector. Images are taken by scanning the sample and measuring the deflection of the cantilever as a function of lateral position. As

the scanner gently traces the tip across the sample (in fact, is the sample who moves under the tip in our AFM), the contact force causes the cantilever to bend, and the electronics react maintaining a constant z using a positioning device is what is called the z-feedback loop.

The movement of the tip or sample is performed by an extremely precise positioning device made from piezo-electric ceramics in the form of a tube scanner [3]. The scanner is capable of sub-angstrom resolution in x-, y- and z-directions (z-perpendicular to sample), but the environmental conditions, such as vibrations, temperature and humidity fluctuations, lateral forces, sample roughness and adhesion of the tip to the gas-water layer on top of the sample, limit the resolution to approximately 2-5 nm laterally and to 0.1 nm for the z-direction for samples without sudden changes of topography (steps, as could be the case of focussed ion beam milled samples, see section 2.2.4) and 4-20 nm in lateral plus 1 nm in height for the more topographically challenged samples.

One of the drawbacks of remaining in contact with the sample is that there exist large lateral forces on the sample as the tip is "dragged" over the specimen, reducing the lateral resolution.

Tapping mode is the operation method used to solve this problem. Tapping mode is a patented technique by Veeco Instruments [4] that maps the topography by lightly tapping the surface with an oscillating probe tip. The cantilever's oscillation amplitude changes with sample surface topography, and the topography image is obtained by monitoring these changes and closing the z feedback loop to minimize them. When operated in air or other gases, the cantilever is oscillated at its resonant frequency (50 to 300 kilohertz usually) and positioned above the surface at a height h_T (amplitude setpoint) so that it only taps the

surface for a very small fraction of its oscillation period. While the tip is at the bottom of the oscillation this is still contact with the sample in the sense defined earlier, but the very short time over which this contact occurs means that lateral forces are dramatically reduced as the tip scans over the surface. When imaging poorly immobilised (e.g., nanotubes or nanobeads spread on a substrate) or soft samples (like organic cells), tapping mode may be a far better choice than contact mode for imaging.

In general, tapping mode is also much more effective than non-contact AFM for imaging larger scan sizes that may include large variations in sample topography. Tapping mode can be performed in gases, liquids, and some vacuum environments.

A major advantage of the tapping mode is related to limitations that usually arise due to the thin layer of liquid that forms on sample surfaces in an ambient imaging environment, i.e., in air or some other gas. The amplitude of the cantilever oscillation in tapping mode is typically on the order of a few 10's of nanometers, which ensures that the tip does not get stuck in this liquid layer.

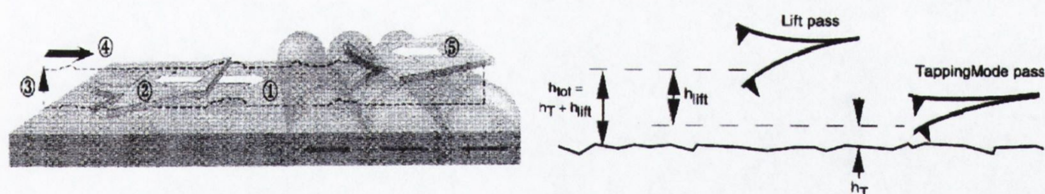

Figure 2.3. Schematic of the tapping and lift modes. Left: **1** & **2** the cantilever traces the surface topography on first trace and retrace, **3** the cantilever ascends to the lift scan height, **4** and **5** the lifted cantilever profiles topography while responding to magnetic influences on second trace and retrace. From the Veeco Multimode Nanoscope III manual.

Alternative methods of obtaining image contrast are also possible with tapping mode (Fig. 2.3). In constant force mode, the feedback loop adjusts so that the amplitude of the cantilever oscillation remains (nearly) constant. An image can be formed from this

amplitude signal, as there will be small variations in the oscillation amplitude, frequency or phase between the oscillations of the cantilever driving piezo and the detected oscillations in the photodetector (due to the control electronics not responding instantaneously to changes on the specimen surface).

This method offers its maximum possibilities in the non-contact mode for distances tip-to-sample greater than 1 nm, which is known as the lift mode. Van der Waals, electrostatic, magnetic or capillary forces produce changes in images of topography, whereas in the contact mode, ionic repulsion forces take the leading role [5].

Magnetic Force Microscopy (MFM) is an imaging mode derived from the lift mode operation that maps magnetic force gradient above the sample surface. This is performed through a patented two-pass technique, LiftMode [6]. This technique separately measures topography and another selected property (magnetic force, electric force, etc.) using the topographical information obtained first in tapping mode to track the probe tip at a constant height (Lift Height) above the sample surface during a second lift pass. This method minimises the topographically induced changes in the oscillation of the cantilever. When the tip is coated with a magnetic material (and the scanned sample is magnetic) there is a magnetic interaction tip-sample that can be mathematically modelled as a dipole-dipole interaction [7]-[10]. This interaction provides changes in the phase of the oscillation that are proportional to the second derivative of the magnetic field component perpendicular to the sample (figure 2.4).

The magnetic dipole-dipole force gradient in the z- direction (or second field derivative) varies with tip to sample distance z as z^5, decreases quickly as the tip to sample height is increased. However, as the lift height is increased, so is the interactive sample surface,

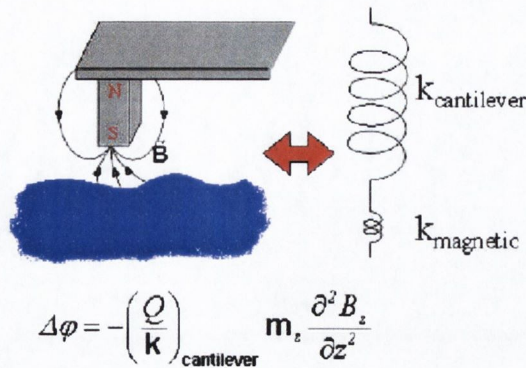

Figure 2.4. Modelling of the response of a MFM cantilever to a magnetic field after [6].

effect which would increase the signal proportionally to the increase of interacting magnetic material. The interactive surface will increase with z^2, and so will the signal if z is small compared with the domain size. This moderates the decrease of the signal as we increase the lift height, but also substantially reduces the resolution, which will be similar to the lift height. We must also take into account that the variation of the signal, $\Delta\varphi$, Δf or ΔAmp., is a weighted (changes in the signal will mainly occur at the bottom of the oscillation) integration over the tapping amplitude, which is of the order of the amplitude setpoint, and comparable with or even greater than the lift height. As the tapping amplitude is kept mostly constant along the measurement, the proportional change is smaller than the changes of the lift height.

It could then be concluded that the smaller lift heights will produce the better magnetic images, but this doesn't take into account topographically-induced artefacts. As the tip approaches the surface, van der Waals interactions, adherence and mechanical effects, such as tip repositioning, drift and temperature dilatation, induce artefacts which superimpose on the magnetic signal. These effects create the necessity for a compromise between the signal magnitude and the artefacts generated in the lift height. In practise, lift heights below 5

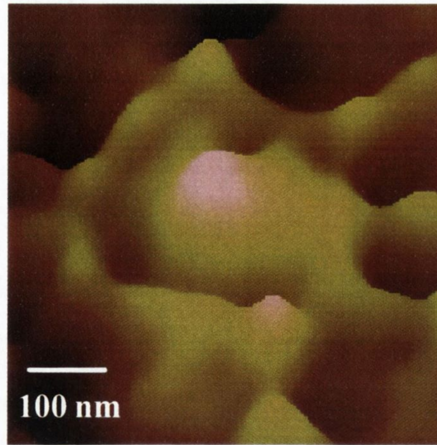

Figure 2.5. MFM of a Co doped-SnO_2 grain. The image shows the magnetic gradient around the grain due to the magnetic field variations around the topography of the grain and its interaction with the fields generated by the neiborhood grains. Film deposited by PLD by C. Fitzgerald.

nm for thin films and 20 nm for patterned or rough samples are not feasible. The typical resolution will then be of order of 10 nm (see figure 2.5).

2.1.3 Scanning electron microscope imaging

Optical microscopes have a physical limitation in the visible photon wavelength, around 350 nm for blue light. If we want to obtain images with higher resolution, we are forced to use methods were the incident particle has an smaller wavelength. One of the most obvious, and certainly the most used, candidates are the electrons.

In an electron microscope (figure 2.6), an electron beam is generated in a filament which can be made of various types of materials, tungsten and carbon being the most used. A voltage is applied to this filament, causing it to heat up and function as a cathode. The anode, which is positive with respect to the filament, forms a powerful attractive force for electrons, that are accelerated towards it. The electron beam, which typically has an energy

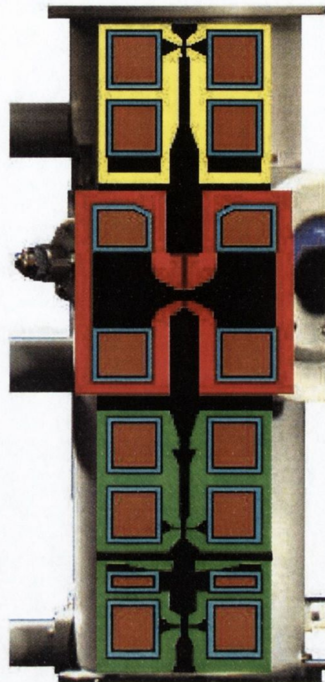

Figure 2.6. Schematic of an electron microscope. The two lenses at the top (yellow) are the condenser lenses. At low magnifications we normally spread the beam to illuminate a large area, while at high magnifications we strongly condense the beam.The lens outlined in red are the objective lens. This is the one used for focussing the image. It is also the lens that contributes most to the magnification of the image, usually a factor 50.The four lenses at the bottom (green) form the magnification system. A single knob on the microscope changes the magnification in steps (software control). Drawing from FEI website.

ranging from a few keV to 50 keV, is focused by two successive condenser lenses into a beam with a very fine spot size ($\sim$ 5nm). The beam then passes through the objective lens, where pairs of scanning coils deflect the beam either linearly or in a raster fashion over a rectangular area of the sample surface. As the primary electrons strike the surface they are inelastically scattered by atoms in the sample. Through these scattering events, the primary beam effectively spreads and fills a teardrop-shaped volume extending about 1 μm into the surface. Interactions in this region lead to the subsequent emission of electrons and x-rays, which are then detected to produce an image.

In a scanning electron microscope (SEM), the varying voltage is also applied to the coils

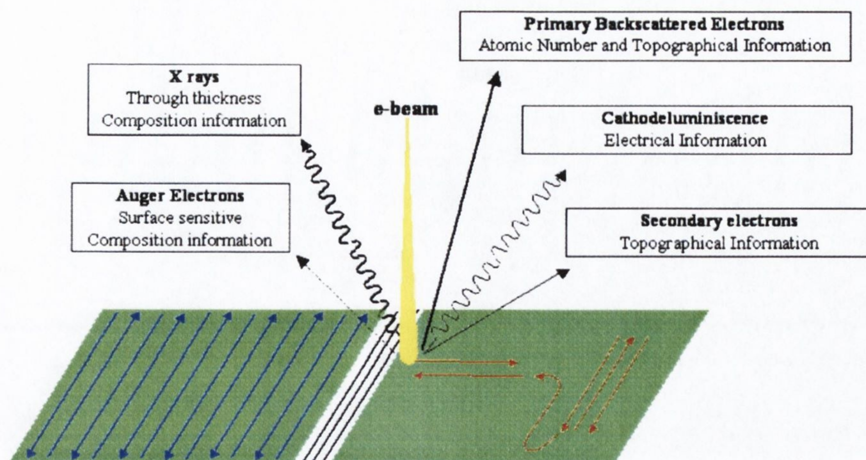

Figure 2.7. Raster (left, blue) and vector (right, red) scanning electron microscopy and the particle products.

around the neck of the cathode-ray tube (CRT) which produces a pattern of light deflected back and forth on its surface. The pattern of deflection of the electron beam is the same as the pattern of deflection of the spot of light on the CRT. The electron beam hits the sample, producing secondary electrons from the sample. These electrons are collected by a secondary detector or a backscatter detector, converted to a voltage and amplified. The amplified voltage is applied to the grid of the and causes the intensity of the spot of light to change. The image consists of thousands of spots of varying intensity on the face of a CRT that correspond to the topography of the sample. Two kinds of scan: vector (scanning mode in which beam is scanning selected areas only; after scanning of selected area is completed beam is turned off and moved to another area to be scanned) and raster (scanning mode in which beam is moving back and forth over the entire substrate; beam is turned on over designated area and then turned off until it will arrive at the next designated area).

The products of the incident beam are the following (figure 2.7) [11]:

.- Backscattered primary electrons (essentially elastically scattered incident electrons) can also be detected. Due to their much higher energy (approximately the same as the primary beam), these electrons may be scattered from fairly deep within the sample, resulting in less topological contrast than for the case of secondary electrons. However, the probability of backscattering is a weak function of atomic number, thus some contrast between areas with different chemical compositions can be observed.

.- Secondary electrons, are the most common imaging mode at low energy (<50 eV). Due to their low energy, these electrons must originate within a few tenths of a nanometer from the surface. The electrons are detected by a scintillator-photomultiplier device and the resulting signal used to modulate the intensity of a CRT that is rastered in conjunction with the raster-scanned primary beam. Because the secondary electrons come from the near surface region, the brightness of the signal depends on the surface area that is exposed to the primary beam. This surface area is relatively small for a flat surface, but increases for steep surfaces. Thus steep surface and edges tend to be brighter than flat surfaces resulting in images with good three-dimensional contrast (see figure 2.8). Using this technique, resolutions of the order of 5 nm are possible.

.- The Auger electrons, the final electrons from the Auger emission process. The primary excitation beam removes the first electron from a core level of sample atom to produce a vacancy. A second electron falls from a higher level into the vacancy and releases energy. This energy is carried off with the Auger electron which is ejected from a higher energy level. Since Auger electrons have an energy in the range of some 100 eV to a few keV, they are strongly absorbed by the specimen. Consequently, only Auger electron from the surface can be measured, making Auger spectroscopy a surface method.

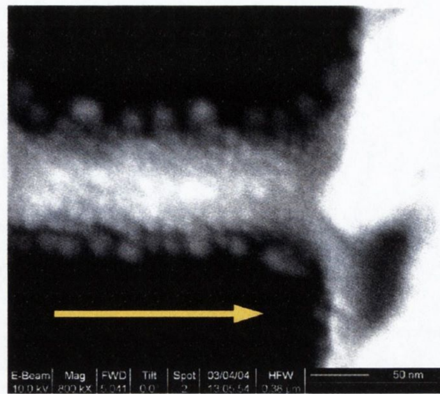

Figure 2.8. 800 k magnification SEM with secondary electrons detector. The sample is a magnetite nanobridge contacted by gold (right). The grains which form the bridge are 5-20 nm in diameter. The results corresponding to this sample are presented on section 4.3.2 and discussed in section 6.2.2.

.- Photons emitted when a sample electron is moved to a lower energy level (light luminescence). It is scanned by the electron beam and carries information about the material boundaries and defect structure.

.- X-rays. Carry thickness and composition information of the sample below the surface (down to ~1μm).

The magnification control is obtained by changes in the lens current, which in turn changes the focal length f of the lens. The resolution of the specimen is decreased with an increased working distance, because the spot size is increased. Conversely, the depth of field is increased with an increased working distance, because the divergence angle is smaller.

For the operation of the microscope it is obviously required that the samples are conducting or covered in a conducting layer, and it is also necessary a good grounding of the sample. High resolution SEMs as the one used in this work (SEM column from a FEI Dual Beam Strata 235) allow a resolution of a few nanometers with a magnification near $\times 1$M, pictured in the figure 2.8.

2.1.4 SQUID

The quantum interference effect was described in the section 1.2.2, and such is the behavior of the direct-tunneling current in the presence of an external magnetic field. A Josephson junction is made up of two superconductors, separated by an insulating layer so thin that electrons can pass through. When a Josephson junction is subjected to a magnetic field the maximum critical current in the junction depends on the magnetic flux through the junction. The tunneling current is predicted to be periodic in the number of flux quanta through the junction. The current depends periodically on the magnetic flux. For typical junctions the field periodicity is about T. In the superconducting circuit with two Josephson junctions in parallel one can observe interference effects similar to light waves in Young's double slit experiment. The total current depends on the flux inside the ring which can have a much greater area than a single junction. Called a SQUID- superconducting quantum interference device. It is useful for detecting very weak magnetic fields of the order of nT (vs. Earth's of 45 μT). A superconducting quantum interference device (SQUID) is a mechanism used to measure extremely weak signals, such as subtle changes in the human body's electromagnetic energy field, and SQUIDs are commonly used to image brain activity due to the brain waves fields generated by current-carrying neurons. Because they measure changes in a magnetic field with such sensitivity, they do not have to come in contact with a system that they are testing.

SQUIDs are usually made of either a lead alloy (with 10% gold or indium) and/or niobium, often consisting of the tunnel barrier sandwiched between a base electrode of nio-

bium and the top electrode of lead alloy. A radio frequency (RF) SQUID is made up of one Josephson junction, which is mounted on a superconducting ring. An oscillating current is applied to an external circuit, whose voltage changes as an effect of the interaction between it and the ring. The magnetic flux is then measured. A direct current (DC) SQUID, which is much more sensitive, consists of two Josephson junctions employed in parallel so that electrons tunneling through the junctions demonstrate quantum interference, dependent upon the strength of the magnetic field within a loop. DC SQUIDs demonstrate resistance in response to even tiny variations in a magnetic field, which is the capacity that enables detection of such minute changes.

2.1.5 Transport measurements

For the spin-electronic application of nanostructured devices, it is obviously indispensable to characterize the electronic transport properties of such devices, which allow to extract information of the material (as will be the case of the Andreev measurements described on section 2.1.5 c), study the differentiated transport properties of the device and its performance limitations.

2.1.5a I-V characteristic and magnetoresistance

Standard 4-point I-V measurements are carried out in this work. The I-V characteristic is obtained via a Keithley 2410 source-meter, with a current and voltage steps of 50 pA and 10 μV and maximum compliances of 2 A or 2.1 kV (power limit of 20 mWatts). The resistance of the nano-devices ranges from 1 kΩ to several MΩ and it is always at least two orders of magnitude higher than the contact resistance and at least one order of magnitude higher

than the resistance of the electrodes-thin film tracks connection to the device.

The magnetoresistance measurements are carried out in three different set-ups. The first one consists of a transport probe connected to the Keithley 2410 and introduced in a Multimag MM-2000-26.5 from Magnetic Solutions, with variable field up to 2.0 Tesla, 360° field rotation and a bore size of 26.5mm, which allows measurements of R(B) and R(θ) with field steps $\geq$20 mT. The second and third set-ups are respectively transport probes connected again to a Keithley 2410 and introduced in the bores of superconducting magnets which produce magnetic fields up to 5 T with field steps as low as 0.01 mT in ambient and vacuum environment respectively.

2.1.5b Noise measurements

Most of the noise measurements carried out for this work were obtained in a four point DC configuration. In fact, the noise measurement system is very simple: we apply a voltage on the sample and we read the current, this will give us the resistance and thus the resistance fluctuations, which can be more easily read by using a preamplifier.

This method has two drawbacks:

1. We have to use a very low noise power supply, batteries being the only source able to give a sufficiently low noise level. The problem with batteries is that the noise level changes with the charge remaining in them, so the experimental running time is limited thus limiting the low frequency measurements. Let us remember that the time necessary to obtain the PSD is inversely proportional to the frequency of the noise, in such a way that if for a 100 Hz measurement 1 second is generally enough, we need 100 seconds for a 1 Hz measurement and around 30 hours to obtain the PSD for a 1 mHz measurement.

2. The fluctuating part of the resistance is very low compared with the fixed one. and

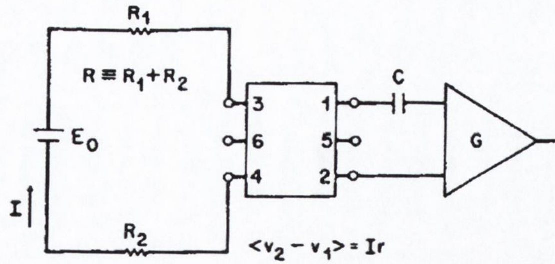

Figure 2.9. Schematic of the 4 point DC noise measurement set-up.

it may be hard to find a small fluctuating signal in big DC background.

The first problem will not affect us. Thanks to the high impedance of the samples, the current in the circuit is very small, and the variations in the voltage of the battery are negligible even in a timescale of days. To solve the second problem we can use a blocking capacitor to get rid of the constant voltage and be able to read only the fluctuations of the signal (see figure 2.9). But the capacitor in series with the impedance of the sample behaves as a high-pass filter, and we are limited to frequencies above the characteristic frequency $f = \frac{1}{\tau} = (R \cdot C)^{-1}$.

To investigate the low frequency noise we need to apply AC signals, preferably of a frequency where the preamplifier performance is optimum. If even with this method the signal is too weak, we can use lock-in amplifiers in cross-correlation [9] for the measurement of the resistance fluctuations.

2.1.5c Andreev reflection

In the Andreev reflection experiment [10] a superconducting (ferromagnetic) point contact is put in contact with the ferromagnetic (superconducting) sample and the conductance of the interface measured. Due to the Andreev reflection, the supercurrent conversion is limited by the minority spin population near the Fermi surface, and the conductance can reveal

the spin polarization at the Fermi level of the metal (figure 2.10) [12]. The point contact at the interface is usually made by mechanical point contact or by STM, where a sharpened tip is slowly approached to the sample until the conductance is equivalent to that of a very narrow nanocontact.

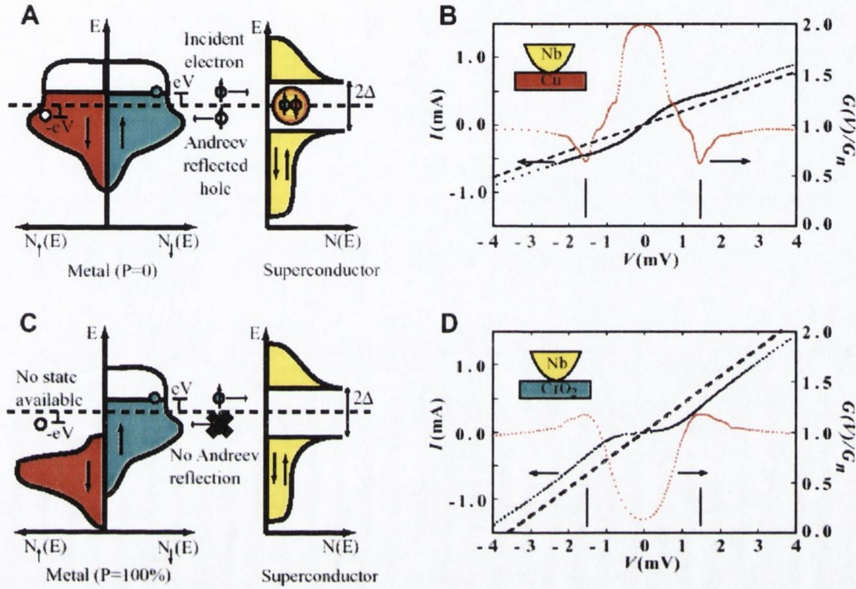

Figure 2.10. Andreev reflection after [12]. (A) Schematic of the process for $P = 50\%$ when the Andreev reflection is unhindered by a spin minority population at E_F. The solid circles denote electrons and open circles denote holes. (B) Experimental measurement of the I-V and differential conductance dI/dV at a Nb point contact on Cu at 1.6 K . The vertical lines denote the bulk gap of Nb: $\Delta(T = 0)$ =1.5 meV. The dashed line is the normal state I-V for a conductance of G n=0.194 ohm^{-1}. (C) Schematic of process for P -> 100% when there is no supercurrent conversion at the interface. (D) Experimental I-V and dI/dV at $T = 1.6$K via the Nb point contact on CrO_2. The dashed line is the normal state I-V for a conductance of $G = 0.417 ohm^{-1}$.

2.2 Nanofabrication

As we pointed out in the first chapter, reliable and reproducible fabrication of magnetic nanostructures is required for the technological implementation of spin electronics. For this we need fabrication methods that allow us to pattern nanodevices made of different magnetic materials and geometries (figure 2.11). Three different methods haven been employed to fabricate the nanostructures measured in this work: electrodeposition, e-beam lithography and focussed ion beam (FIB) milling. All these methods have different resolution, capabilities and drawbacks that are resumed in the Appendix to this chapter.

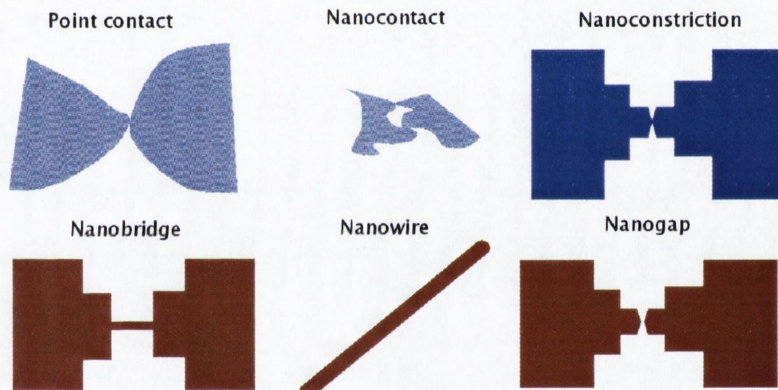

Figure 2.11. Types of nanostructures. Those on blue are usually reported to be ballistic, while those on red are usually considered diffusive.

2.2.1 U-V lithography, wet and dry etching

Lithography is the process used to transfer a pattern to a layer of polymer deposited on top of the thin film we want to pattern. In UV-lithography this transfer is made by exposing to UV light a Cr-glass mask (which acts as a shield to the radiation) put in contact

with a photoresistive material whose properties vary when exposed to UV radiation (figure 2.12). If the photoresist becomes soluble in certain solvents (as dilute acetone) after being exposed, it is called positive photoresist (the remaining photoresist reproduces the pattern of the mask), if the photoresist exposed becomes insoluble it is called negative (the remaining photoresist is the opposite pattern). After the exposure to UV light is made in those areas not protected by the mask, we remove the exposed photoresist (if it is positive) or the not exposed (negative). The resolution of the pattern depends on the wavelength of radiation used to expose the resist: photolithography (or optical lithography) uses UV radiation. Our mask aligner is a Karl Suss MJB 3, which utilises a lamp with a UV lengthwave λ of 250 nm (theoretical resolution limit). This method as we describe it cannot then produce real nano-scale devices, but it is a good initial step for the patterning of contact masks and μm tracks that can be reduced in lateral size in a later process (focussed ion beam, described in section 2.2.4).

The resolution of the UV-lithography is reduced by vibrations and non-uniformities in the photoresist film, and the practical limit is 0.5 to 1 μm. The type of photoresist and the processing used will also condition this resolution. In general, the faster the spinning, the thinner will be the photoresist, giving initially better resolution because the radiation will spread less around the pattern. However, as we thin the photoresist, this polymer layer being always slightly non-uniform in height, it becomes harder to get a good developing because the ratio thickness-nonuniformities is reduced and some areas are developed much before than others. This effect where the photoresist in overdeveloped in some areas will decrease the resolution, and eventually will destroy the pattern. A compromise must thus be achieved between the speed, acceleration and time of the spinning to obtain layers which

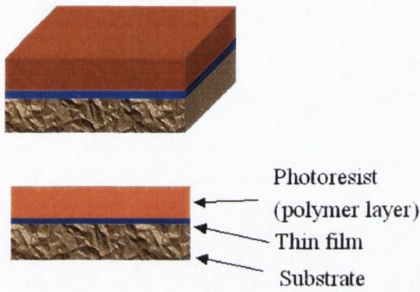

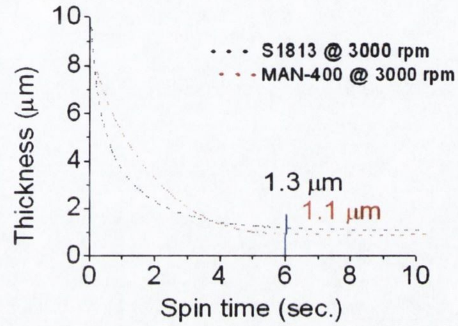

Cr mask (~ μm) on glass
(1.25 mm or 1.5 cm)

Contact mode (theoretical res.
limit→ UV length wave .4 mm)

Developing

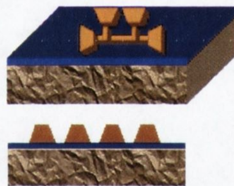

Dry etching

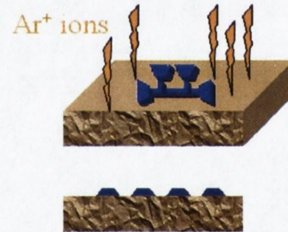

Figure 2.12. UV lithography schematic. Top left: Photoresist deposition. Top right: Photoresist thickness vs. spinning time at a speed of 3000 rpm. Bottom: exposure, developing and etching processes.

are thin and very uniform. The standard process used in this work is described in the table 2. For this work we used a spin coater EMS model 4000 with spin speed from 1 to 9000 rpm and 9 programmable steps, and a hot plate EMS model 1000-1 with temperatures from 50° C to 150° C, accuracy of $\pm$1% across the working surface and a possible substrate size up to 150 mm.'

Action	Speed (rpm)	Acceleration (rpm/s)	Time (s)
Dispense Primer	500	1000	2
Spin Primer	3000/1800	1000	15/15
Dispense Photoresist	0	0	0
Spin Photoresist	4500	3000	40

Table 2: Standard spinning process for the positive photoresist Shipley 1813 used in this work after [13].

If the contact between the mask and the photoresist is not good enough, the mask will create a shadow on the photoresist, this shadow will have the same features than the mask but with increased size, resulting in a decrease of the resolution. This effect can also be used to our advantage to create new patterns (figure 2.13).

Once the photoresist is developed, we can remove the area of the film that is not protected by the photoresist, the process of etching or milling. This can be done by the use of appropriate acids (wet etching), by accelerated Ar^+ ions which strike the sample and remove the surface atoms (Ar milling, see figure 2.14 for a schematic), which is the method commonly used in this work, or by a mixed process in which a gas is injected and ionised with a high RF power supply, striking the sample and removing the material which reacts with the selected gas.

Wet etching is the fastest and easiest process and we used it frequently during this work, but it cannot achieve resolutions below a few μm due to the underlaying (below the photoresist) removal of material. For a higher resolution, the Ar^+ milling provides ideal atomic resolution in any material, the speed and non-selectivity (anything in front of the

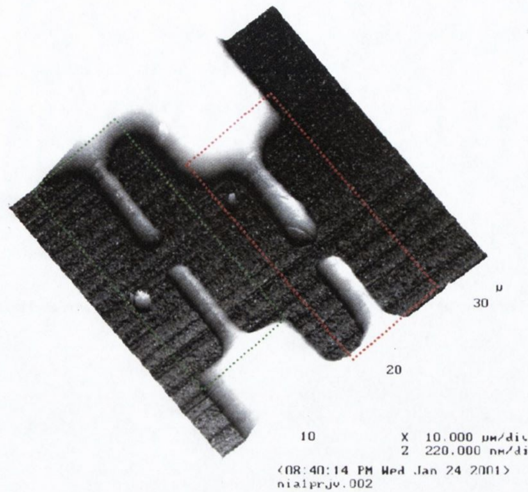

Figure 2.13. Litographed micro-track with a mirror-like artefact achieved on a negative photoresist from a single gap mask. Due to a microscale separation between sample and mask during the UV exposure process the light is reflected on the shiny metallic chip, exposing twice the photoresist and tranferring twice the pattern. The green line marks the original pattern and the red one the ghost-reflected pattern.

beam will be removed, although the speed of milling may vary) of milling being the only drawbacks (see table 3).

Material	Milling ratio (*)
Gold	10
Silver	6
SiO_2	5
Copper	3
Nickel/Cobalt/Iron	2
LSMO/SFMO	1.5
Magnetite/Nb/Ti	1
Glass	< 1

*** nm/minute** @ 500 W RF power optimised

Table 3: Milling ratios for different materials in the Ar^+ process used in this work.

Our system is operated with a cryopump, under initial vacuum of $\sim 2 \times 10^{-7}$ torr, a working pressure of 1.8×10^{-5}, gas flow of 0.2 sccm, magnet current of 2 A and a RF power of 500 W (0 W reflected). The use of higher gas flow (≥ 0.25 sccm) produces a pink plasma

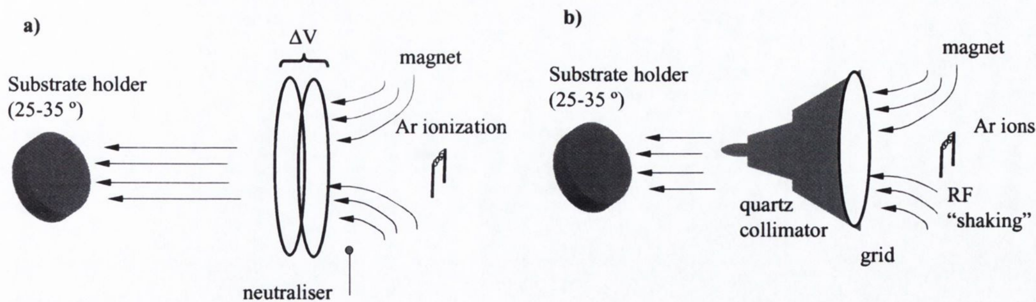

Figure 2.14. Dry Ar^+ milling schematic for DC accelerated a) and RF shaked and collimated b) beams. The sample is positioned at an angle for an optimum etching, but needs to be rotated to obtain good uniformity.

(instead of blue-purple) with almost no milling power, lower gas flow or magnet current ($\leq$ 0.19 sccm or $\leq$ 1.7 A) produce an unstable plasma which tends to disappear with time, and higher magnet currents ($\geq$ 2.2 A) give rise to more reflected power.

The last process, reactive ion etching (figure 2.15), has the advantage over Ar^+ milling of being a selective milling process: depending on the reactive gas employed we will mill some materials instead of others, but the main drawback is that most magnetic materials (including 3d ferromagnets) do not have a suitable reactive gas and we have to use Ar once more.

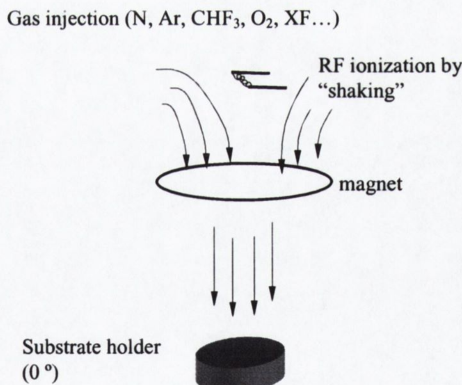

Figure 2.15. Reactive ion etching schematic

Finally, we must mention the lift-off technique, used in UV and e-beam lithography. In this technique, the film is deposited after the lithography instead of before, and therefore doesn't require an etching or milling process. A thin film is deposited on top of a photoresist film previously exposed and developed. usually with a thickness ratio of no less than 1:5 respect to the photoresist employed to avoid to form a continuous film. After the thin film deposition, the sample is immersed in a strong solvent (usually warm acetone) to dissolve the photoresist and the film on top of it. This way, the film will remain only at the areas which have previously been developed, i.e., the regions where we removed the photoresist.

To enhance the resolution of optical lithography, extremely short wavelength UV (λ below 200 nm), mirror projection printing (steppers) and phase shift masks are employed in the semiconductor industry. Optical photolithography processes can then be capable of resolution below 100 nm. However, for higher resolution, other techniques as electrodeposition, e-beam lithography and ion-beam milling are required.

2.2.2 Electrodeposition of nanostructures

In the fabrication of nanostructures, a cheap, simple way to create atomic-scale nanocontacts and nano-scale nanowires is electrochemistry. The fabrication of electrodeposited atomic-size nanocontacts was first reported by Morpurgo in 1999 [14]. To electrodeposit an atomic contact two metallic electrodes with a separation of $\sim$ 100 nm are first fabricated by e-beam lithography. This gap is subsequently filled by electrodeposition from an aqueous solution containing the ions of the desired material by using one of the contact pads as the working electrode of an electrochemical cell. By monitoring the resistance between the two pads with a lock-in amplifier it was possible to stop the electrodeposition at the very moment the resistance matches a desired value of a few kΩ, similar to the quantum of conductance, what indicates an atomic size contact (see figure 2.16). The electrodeposition can be done by applying a constant voltage between the solution from which we want to take ions (counter electrode) and the sample where we want to deposit them (working electrode) or potentiostatic mode, or by applying a constant current between the electrodes, the galvanostatic mode.

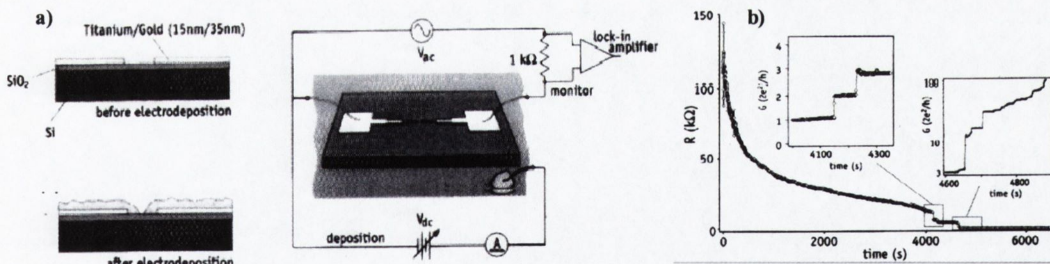

Figure 2.16. Fabrication of nanocontacts departing from a 100 nm gap by electrodeposition as described in [14]. a) Schematic of the sample before and after the electrodeposition, and the diagram of the circuit employed. b) Quantum steps on the monitored resistance for the nanocontact.

We have introduced three modifications to the method described by Morpurgo to allow for the use of UV lithography (figure 2.17) in what we call *ele*ctrochemical *na*nodeposition (ELENA):

1.- After the lithography and etching to define the track structure, the photoresist layer is not removed. This allows us to etch and deposit in only two dimensions.

2.- Then we deposit a second layer of photoresist leaving by lithography a gap over the zone of the track where we want to define nanocontact. In that gap only the top of the track is protected, but not the sides where the electrochemical processing takes place.

3.- The track is electrochemically etched until the desired nanocontact resistance is reached or until a gap is formed, which may be subsequently refilled by electrodeposition. We have no need of e-beam lithography to etch the small gap (on the order of 100nm. or much smaller if we want).

With the concentrations specified above we use an etching current of 1 to 20 mA and a deposition current of 10 to 100 mA. This gives us etching-deposition times of the order of 1000 sec. for a track 50 μm wide, the residual photoresist impeding the process. We must also take into account that the voltage required for Ni deposition is above the voltage to start hydrogen evolution, and that part of the current will be due to H^+ and not Ni^+ ions, and that most of the deposition will occur on cables used to contact the sample, since these cables offer a surface much bigger than the unprotected track. The counter electrode used was a solution of Ni sulphate from 0.01 to 0.05 M and 0.1 M of Boric acid [15].

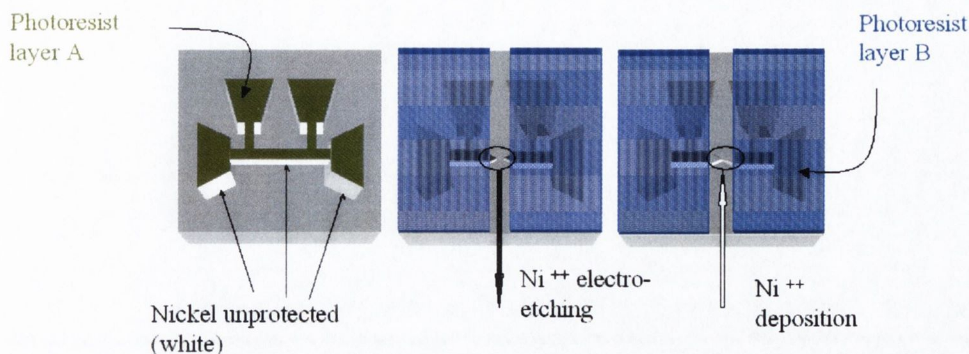

Figure 2.17. Schematic of the ELENA process. The photoresist A (positive) after the UV lithography is not removed, protecting the top of the sample. A second layer of photoresist B (negative) is spinned to define the region where we want to form a nanocontact. The material from the walls of that region is removed till we form a very narrow gap, which we subsequentlly refill.

The way we connect the electrochemical electrodes to the sample can also simplify or modify the process as a function of the initial gap distance and the desired deposition geometry (see Fig. 2.18). We can, for example, deposit at one or both sides of the gap or connect one of the lithographed pads to the counter electrode, providing higher electrical gradients which will create higher aspect ratio, elongated contacts.

This latest example, where one of the pads is connected to the working electrode, was successfully used to fabricate Ni nanocontacts in a T geometry by García et al. in 1999 [16], and has since then provided numerous results in transport through nickel nanocontacts (see section 3.1). For this geometry, the electrodeposition process is self-limited. When the contact is formed, the current flows through the nanocontact rather than from the aqueous solution to the working electrode. Of course, for this method to work, it is necessary that the rate of removal of material from the track connected to the counter electrode be lower than that deposited on the working electrode. If the method is used in the potentiostatic mode and we introduce a limit to the current flow, the process will automatically stop when the

resistance of the contact is approximately equal to the voltage applied divided by the current limit set. This way we can also control the approximate final resistance of the nanocontacts without having to monitor it, but the contacts formed are always in the nm range rather than in atomic scale.

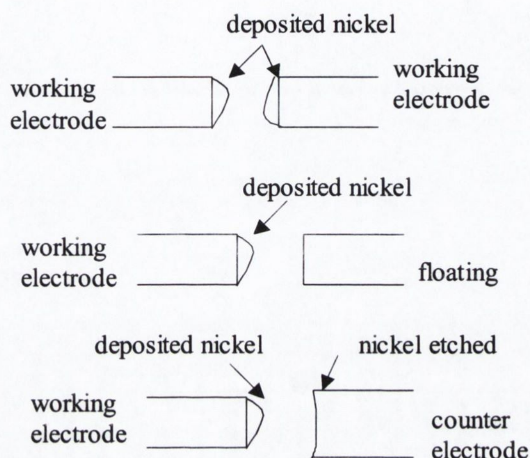

Figure 2.18. Different ways to contact the working and counter electrodes to the sample to deposit a nanocontact. In the first method the metal is deposited both sides of the gap, and is specially useful for the bigger gaps. The second method, where the metal is deposited only on one side of the gap, is required when we want to preserve the geometry of one of the electrodes or to reduce the fabrication speed. The last method allows for self-limited electrodeposition (see text).

The electrodeposition process can also be used to fill a porous membrane (Fig. 2.19). These membranes are usually polycarbonate or anodised alumina films metallized on one side, from 1 to 100 μm thick, and with porous sizes which vary from 5 to 500 nm. The grain size of the electrodeposited material must obviously be smaller than the pore size, and this creates numerous problems to deposit nanowires with a diameter below some 20 nm.

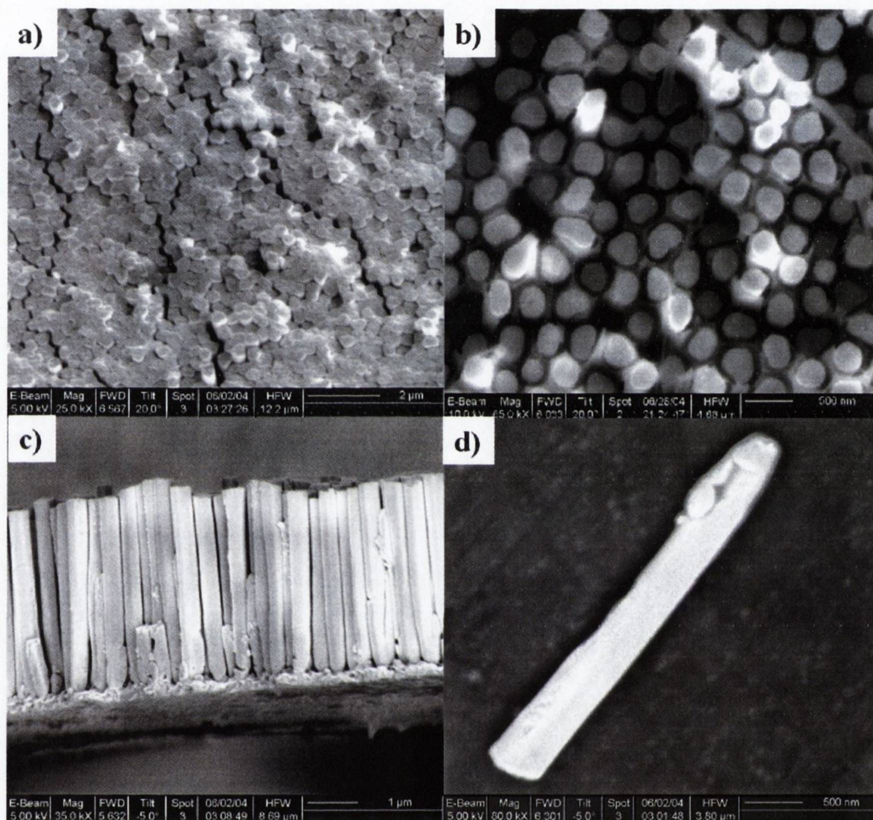

Figure 2.19. SEMs of nanowires deposited in alumina membranes previously disolved. a) & b) Top view of electrodeposited cobalt nanowires in membranes with same pore size and different pore spacing. c) Lateral view of CoPt nanowires. The gold contact used for the electrodeposition can be seen at the bottom of the wires. d) Isolated single bistmuth nanowire. Electrodeposition made by F. Rhen and N. Chaure.

2.2.3 e-beam lithography

The electron beam generated by an electron microscope can be used in a lithography technique which employs electrons rather than UV light to expose the resist. No mask is used, as the pattern is transferred directly into the resist. Since the wavelength λ of the electrons is much smaller than that of UV light, the technique is used for the patterning of nanostructures down to 20 nm resolution, and also to manufacture high resolution masks for photolithography and X-ray lithography.

The actual exposed area is bigger than the spot size due to the proximity effect, i.e., the scattering of electrons in irradiated resist. But the ultimate resolution of the technique will be given by the size of the polymer-resist employed and the lift-off process rather than the exposed area.

The resist commonly used is poly-methylmethacrylate (PMMA). PMMA (which possess a sensitivity of 100 μCcm^{-2} [17]) can provide a resolution down to 20 nm. It is based on special grades of polymethyl methacrylate designed to provide high contrast, high resolution for e-beam, deep UV (220-250nm) and X-ray lithographic processes. In the exposure process the molecule is broken in fragments, each retaining one of the bonding electrons in a process called homolysis (figure 2.20).

To make the lift-off easier and/or to allow for the deposition of films thicker than a few tens of nanometers, another copolymer, MMA, is commonly used as a resist in combination with PMMA, forming a bi-layer lift-off resist process, see figure 2.21.

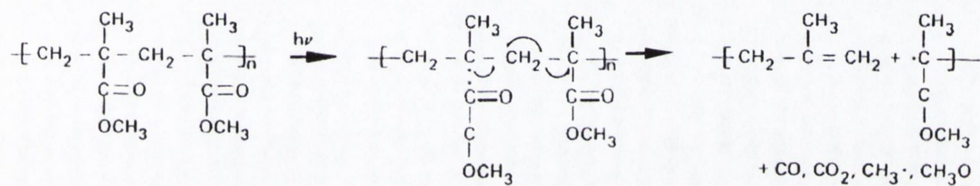

Figure 2.20. Mechanism of radiation-induced chain scission in PMMA after [17]. Homolysis of the main-chain carbonyl carbon bond is indicated as the initial step. Acylcarbon-oxygen, σ-bond homolysis also occurs, but rapid decarbonylation ultimately leads to the same indicated products.

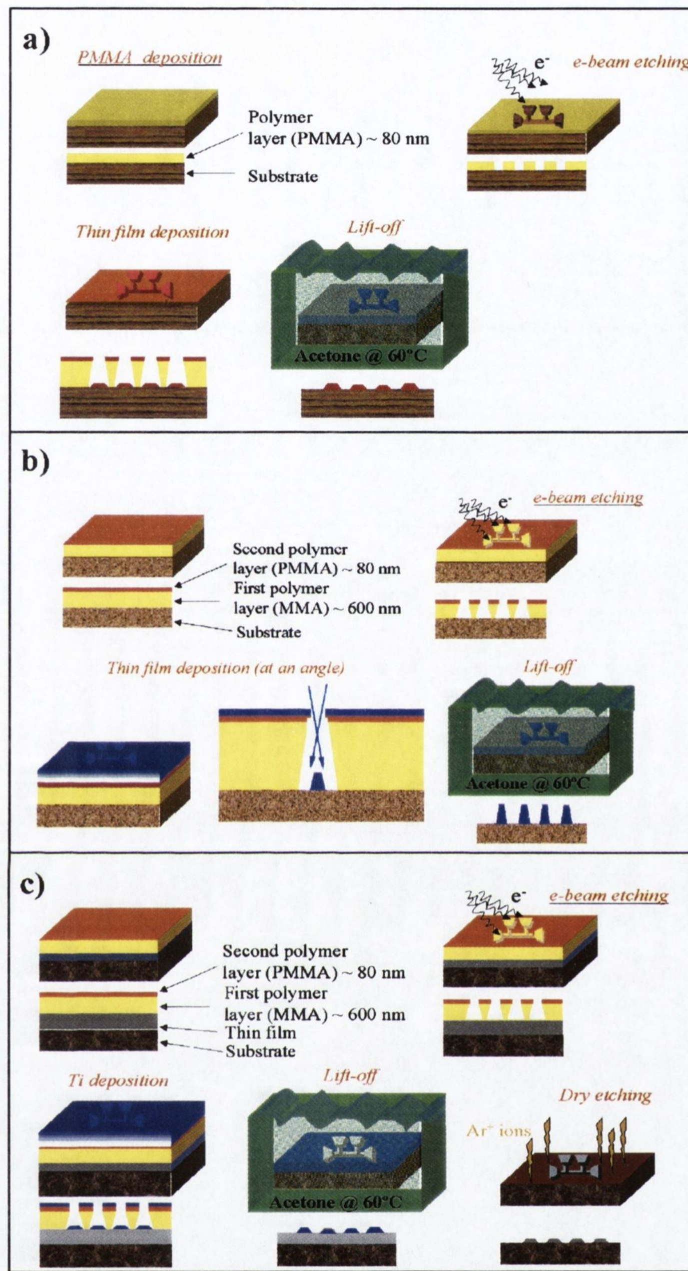

Figure 2.21. Schematic of three different e-beam lithography processes. a) 'Direct' lithography, the structure is patterned in a PMMA resist and a thin film is deposited, after a lift-off, the film only remains in the exposed places. Only useful for very thin films ($\leq$ 20 nm). b) 'Shadow' lithography, an added MMA layer facilitates the liftoff and, if the deposition is made at an angle, can improve the resolution (hole-size) obtained in the PMMA layer. c) 'Mask' lithography, a Ti protective layer is deposited to avoid the etching of the places exposed by the e-beam. This allows the patterning of a previously deposited film.

2.2.4 Focussed ion beam milling

In a similar fashion to the way a tungsten filament is used to generate a beam of electrons in an electron microscope, a Ga tip filament (due to its low melting temperature compared with other metals and the low toxicity compared with Hg) can be used to produce a beam of ions by applying a high suppressor and extractor voltages ($\sim$ 1 and 10 kV respectively). This ions can be collimated to form a spot no much bigger than that generated in an electron microscope. In the system used for this work, a dual beam Strata 235 from FEI, an ion spot size of 7 nm is theoretically possible.

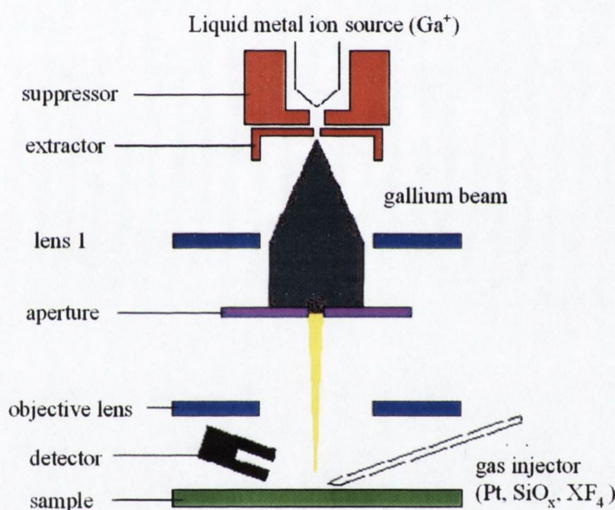

Figure 2.22. Shematic of the operation of a FIB for ion imaging, ion milling and gas-assisted milling and metal/insulator deposition from a gas organic precursor.

Due to the higher mass (-> energy) of the ions compared with the electrons, this beam can be used not only to image samples that may be difficult to see under an electron beam (due to low conductivity, for example), but also to remove material from those regions where the ion beam spot hits the sample (ion beam milling), or to deposit materials injected from

an organic gas precursor in the irradiated area.

An ion-beam lithography equivalent to the electron beam lithography is possible, and in fact this lithography technique in which the resist is exposed to the accelerated ions, can provide a better transfer resolution than e-beam lithography, due to the limited scattering of ions in the resist, which reduces the proximity effect. However, for the results obtained in this work, we will use the ion-beam as a direct patterning tool that allows the removal of material around a nanostructure, we can use the ion milling process to remove material from a previously lithographed metallic μm track and define a nanostructure as seen in figure 2.23. For this patterning, the resolution will be limited by effects such as redeposition, underlayer milling, proximity effects and spot size (which is in fact a gaussian distribution of ions with a width at half height of several nm).

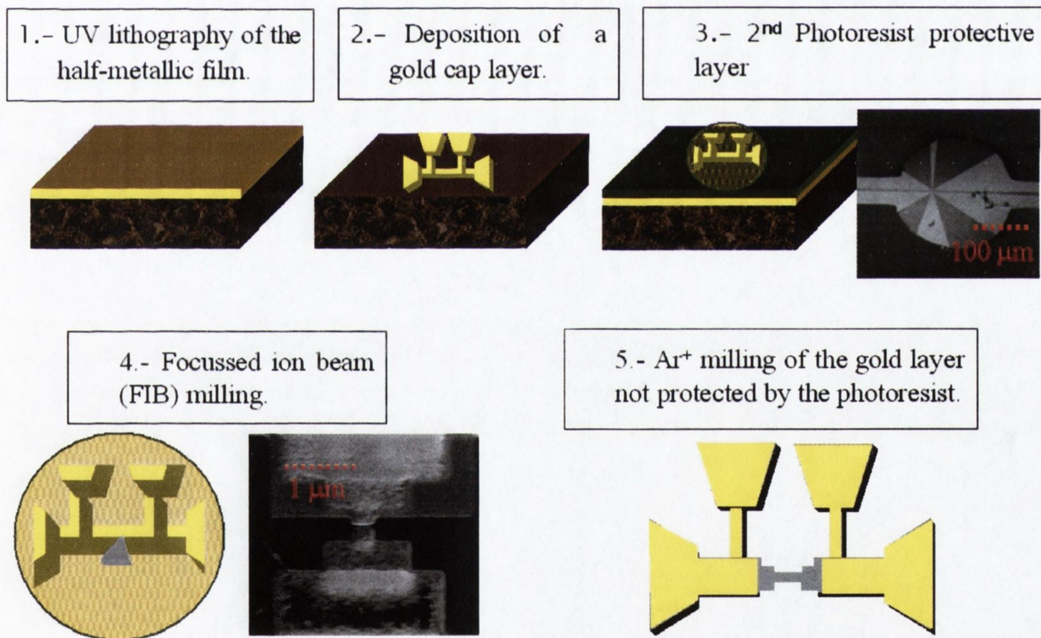

Figure 2.23. Steps to fabricate a nanostructure by direct FIB milling with metallised pads.

To increase the conductivity of the sample and/or reduce the resistance contribution

of the electrodes, the nanostructures can be contacted with Pt deposited with the ion beam from the gas precursor(figure 2.24a). Twenty nm nanostructures can be achieved by using FIB milling, which has the advantages over e-beam lithography of allowing an almost-simultaneous imaging of the patterned structures, eliminating the necessity of lift-off (which can eventually reduce the resolution) and can pattern films up to a few μm thick. UV lithography is still required though, since the ion-beam cannot mill the large volumes (20 μm^3 being the practical limit) required to pattern contact pads.

The main experimental drawback of this method is the Ga implantation that results of the ion milling and, mostly, from employing ion imaging (figure 2.24b). To reduce this Ga^+ implantation and the material redeposition, it is recommendable to employ ion currents as low as possible, to take images only with the electron beam, reduce the milled areas (by lithographing small regions of order of 10 μm^2 first), use gas enhanced etching if we require the use of high currents and, finally, if the material is very sensitive to Ga doping, to use the ion beam to implant an insulator mask (SiO_x) and remove the non-protected region by Ar milling (figures 2.24 c) and d).

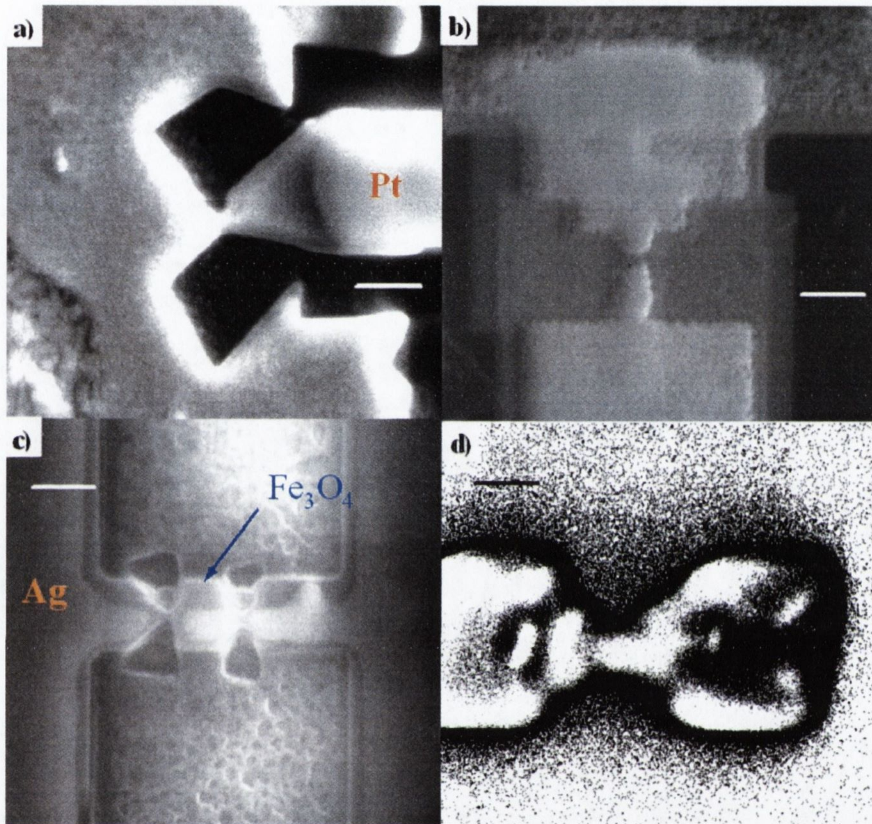

Figure 2.24. SEMs of FIB-patterned structures. a) Magnetite nanoconstriction with deposited Pt contact (to the right of the constriction). b) Ion-imaged nanostructure, Ga^+ damage (dose of $\sim 10^{15}$ ions$\cdot$cm^{-2}). c) Milled magnetite double nanoconstriction metallised with silver and using only e-beam imaging. d) SiO_x FIB-deposited mask for a nanoconstriction. Scale bars are 500 nm for the top pictures and 200 nm for the bottom ones. The current flow is from left to right (right to left) in all the pictures.

2.2.5 Patterning of in-plane Andreev reflection samples

We explained in the paragraph 2.1.5c how the Andreev reflection effect can be used for the measuring of polarization of materials via a superconductor-normal metal point contact. However, this method was previously used in mechanical point contacts, generally between a thin film and a STM tip. We have expanded this method for the direct measurement of the local polarization in magnetic nanostructures patterned from thin films. The method consists of 8 steps (see figure 2.25): a) a Nb film about 50 nm thick is deposited and the transition temperature measured, b) half of the film is covered with photoresist, the other half is developed by UV lithography, c) half of the Nb film is etched by Ar^+ milling and the total milled depth is measured by AFM, d) a Cu or Ni film of equal thickness to the total milled depth is sputtered, e) the Cu or Ni on top of the photoresist is lift-off with acetone at 60°, f) contact pads and a 20 μm track are lithographed, g) Ar^+ milling of the uncovered film and h) patterning by focussed ion beam (FIB) of a nanoconstriction at the Nb-Cu or Nb-Ni interface.

In this eight-steps method, described in the figure, the nanocontact is patterned through FIB milling at the boundary between from two previously deposited thin films, one of which is a type I superconductor (Nb in this work) and the other is the metal which local polarization we want to find. By measuring the conductance with voltage as described in 2.1.5c, we can deduce the polarization of the metal in the nanostructure. These nanocontacts have a higher resistance than the usual one for Andreev point contacts (10 to 100 kΩ compared with 100 Ω) and the transport is probably not ballistic but diffusive. The diffusion of the electrons will lead to spin scattering and spin-flip in the neighborhood of the nanoconstric-

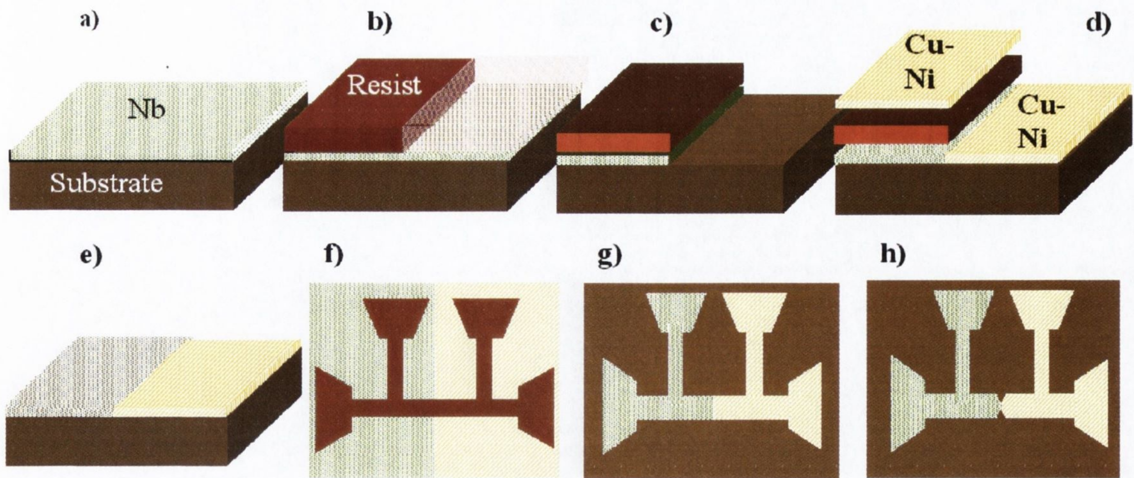

Figure 2.25. Schematic of the eigth steps fabrication process described in the text.

tion, reducing the effective spin polarization. This can be taken into account by the inclusion of an effective barrier (Z parameter) at the interface of the superconductor-metal material in the model.

Appendix: Comparative table:

In the table 4 we have a brief comparison of the basic characteristics for the different fabrication methods described in the section 2.2.

Method \ Feature	Resolution	Stability	Materials versatility	Device versatility (shapes)†	Other characteristics
Electro-deposition	Atomic (pcs) 4 nm (nws)*	Degrades in minutes	Metallic elements and alloys	No	· Cheap & easy · Chemical pollution
E-beam lithography	15-20 nm	N/A	Any (mask)	Yes (3D)	· No contamination · Best size ratio
FIB patterning	5 nm	N/A	Any	Yes (3D+)	· Allows etching and deposition · Ga^+ contamination
Point-breaking contacts	Atomic	Minutes-seconds	Any	No	· Easier way to atomic resolution · No use in industry
AFM patterning / *lithography*	20 nm	N/A	Some metals/*Any*	Yes (2D)	· Highly specific · Still developing

Table 4: Comparison of the different nano-fabrication methods.

* pcs≡point contacts; nws≡Nanowires

† Device versatility:

No –> Device geometry can not be predetermined.

2D –> Allows patterning of films with thickness of order 10 nm.

3D –> Allows patterning of films with thickness of order 100 nm.

3D+ –> Allows patterning of films with thickness of order 1 μm.

Bibliography

[1] E. Steinbeiss in "Spin electronics" M. Ziese and M.J. Thornton eds., Springer (2001)

[2] G. Binnig, C.F. Quate, C. Gerber, Phys. Rev. Lett. 56, 930 (1986)

[3] http://spm.phy.bris.ac.uk/techniques/AFM/ (July 2004)

[4] Nanoscope Multimode SPM manual, Veeco instruments.

[5] http://www.sst.ph.ic.ac.uk/photonics/intro/AFM.html (July 2004)

[6] www.Veeco.com

[7] R. Yongsunthon et al., J. Appl. Phys. 92 1256 (2002)

[8] J. Lohau, S. Kirsch, A. Carl, G. Dumpich and E.F. Wassermann, J. Appl. Phys. 86, 3410 (1999)

[9] John. H. Scofield, Rev. Sci. Instrum. 58, 985 (1987)

[10] A.F. Andreev, Sov. Phys. JETP 19, 1228 (1964)

[11] http://mse.iastate.edu/microscopy/beaminteractions.html

[12] R.J. Soulen, J.M. Myers, M.S. Osofsky, B. Nadgorny et al., Science 282, 85 (1998); S.K. Upadhyay, A. Palanisami. R. N. Louie and R.A. Buhrman., Phys. Rev. Lett. 81, 3247 (1998)

[13] http://www.nnf.ncsu.edu/cleanroommanuals/RC8Spinner2.pdf (July 2004)

[14] A.F. Morpurgo, C.M. Marcus and D.B. Robinson, Appl. Phys. Lett. 74, 2084 (1999)

[15] A. Fert, and L. Piraux., J. Magn. Magn. Mat. 200, 338 (1999)

[16] N. García, M. Muñoz and Y.W. Zhao, Phys. Rev. Lett. 82,2923 (1999)

[17] http://dot.che.gatech.edu/henderson/introduction_to_electron_beam_lithography.htm (July 2004)

Chapter 3

Transport measurements in nickel nanostructures

It has been shown experimentally that the conductance of electrodeposited nickel nanocontacts depends strongly on the local magnetization configuration of the regions adjacent to the contact [1], and much has been done to try to reproduce and understand this result. Further experiments carried out in electrodeposited nanocontacts [2],[3] and magnetite point contacts [4] gave rise to MR ratios in excess of 500 %, and magnetoresistance of order 100,000 % at room temperature for ballistic Ni nanocontacts with conductance values near the quantum of conductance $(12.9\ k\Omega)^{-1}$ has been reported [5], while MR ratios of order 1000 % have been measured several times ([2],[3],[10]). Similar results have been obtained also LSMO point contacts [3], and (Ga,Mn)As wires with nanoconstrictions [11]. In both electrodeposited and point contacts, the magnetoresistance scales with the size of the nanocontact [3],[10].However, attempts to reproduce these results in clean and controlled conditions, as in nickel break junctions [6], nanowires [7],[8] and electrodeposited nanocontacts of atomic size [8] with conductance values from 1 to 10 G_0, have given MR ratios no bigger than 40 % with a typical value of $\sim$1 %.

Using theoretical arguments of previous work, this ballistic magnetoresistance has been interpreted in terms a domain wall scattering in the vicinity of the nanocontact [12],[13]. However, theoretical calculations [14] and measurements of single domain wall contribution to the magnetoresistance [15] show that a domain wall cannot be responsible for this huge

values of the MR; even assuming the presence of spin-polarized oxygen in the contact region, which could lead to electronic transport through spin-polarized p oxygen states, MR ratios no higher that 700 % are obtained in the calculation [16]. The presence of a dead layer in the nanocontact, transparent to the electrons and equivalent to a zero width domain wall, formed during the electrodeposition by materials present in the solution and/or NiO_x, was suggested by García [17], although no direct proof has been provided.

Magnetostriction is an important experimental issue, since a change in length of a few ppm of the total size of the device (which is of order mm.) could represent a drastic change of the width and resistance of the nanocontact. Arguments have been given to dismiss it as the origin for the ballistic magnetoresistance in nanocontacts [4],[18],[19], but the details of the micromagnetic configuration will be relevant, and it has been suggested that the behaviour of the electrodeposited nanocontacts is dominated by magnetostriction or magnetic dipole forces.

In patterned nanostructures, where the nanocontacts are stable and magnetostriction should be negligible due to the bonding of the film to the substrate, no significant MR has been measured for nickel [9],[20], permalloy [21] or cobalt nanocontacts [22]. Magnetostriction remains the main objection to the domain wall or dead layer theories, although there are recent attempts to eliminate the magnetostrictive effects from electrodeposited nickel contacts [23].

In order to understand the transport properties of nickel nanocontacts, and to eliminate either magnetostriction or non-adiabatic transport as the origin for the huge MR ratios, we have used FIB, e-beam lithography and electrochemical methods to fabricate nickel nanocontacts. This allows us to control and duplicate ferromagnetic nanostructures easily in new

materials and to compare the transport properties of samples prepared in different ways, in a search for a common pattern of behaviour. The use of the FIB for magnetic nanotechnology investigations allows the fabrication of nanostructures on a scale down to 10 nm by ion milling, but it is on that scale that gallium implantation, due to the Ga^+ ions used in the milling, and structural damage may impair the magnetic properties of the ferromagnetic materials and affect their properties. In this chapter we present measurements of magnetic structures about 20 nm in size patterned by FIB and we compare them with data obtained on samples prepared by other methods.

3.1 I-V characteristic and magnetoresistance

3.1.1 Fabrication and I-V characteristic:

The results refer to samples patterned from a wafer with a 60 nm Ni film sputtered over a 200 nm layer of amorphous SiO_2 on a Si substrate. Samples from Ni films 60 nm thick covered with a cap layer and growth by molecular beam epitaxy on MgO (epitaxial) and glass were also fabricated for control purposes.

Samples patterned by e-beam and FIB had a well-defined structure with a double nanoconstriction (Fig. 1); the purpose of this pattern is to study the possibility of trapping a domain wall in the narrower constriction and pushing it by means of the spin-pressure generated by a spin-polarised current into the wider constriction [4]. Current-induced magnetisation instability and switching was theoretically predicted in the 90's [24],[25] and experimental evidence of this behaviour has been reported [26],[27].

On the other hand, the samples prepared by a combination of standard UV lithography and electrochemical nanodeposition (ELENA), following the method first described by Morpurgo et al. [28] and later modified for the use of UV lithography [29], are nanocontacts with a given resistance. In this method we cannot control the geometry of the contact, but the electrodeposition process can be stopped at a given resistance, which corresponds to the resistance of a small ballistic nanocontact (a few kΩ).

The samples show long-term stability (weeks for the electrodeposited ELENA samples and months for the others) and similar transport characteristics. The I-V characteristic is measured on four consecutive cycles and with different starting points, giving always the

same result. For all the samples fabricated on top of a SiO_2 layer the I-V was found to be non-linear and asymmetric, independent of the method used for their fabrication, and with a resistance range from 1 to 24 kΩ. The peak of the dV/dI characteristic is at voltage from 50 to 80 meV (see figure 3.1).

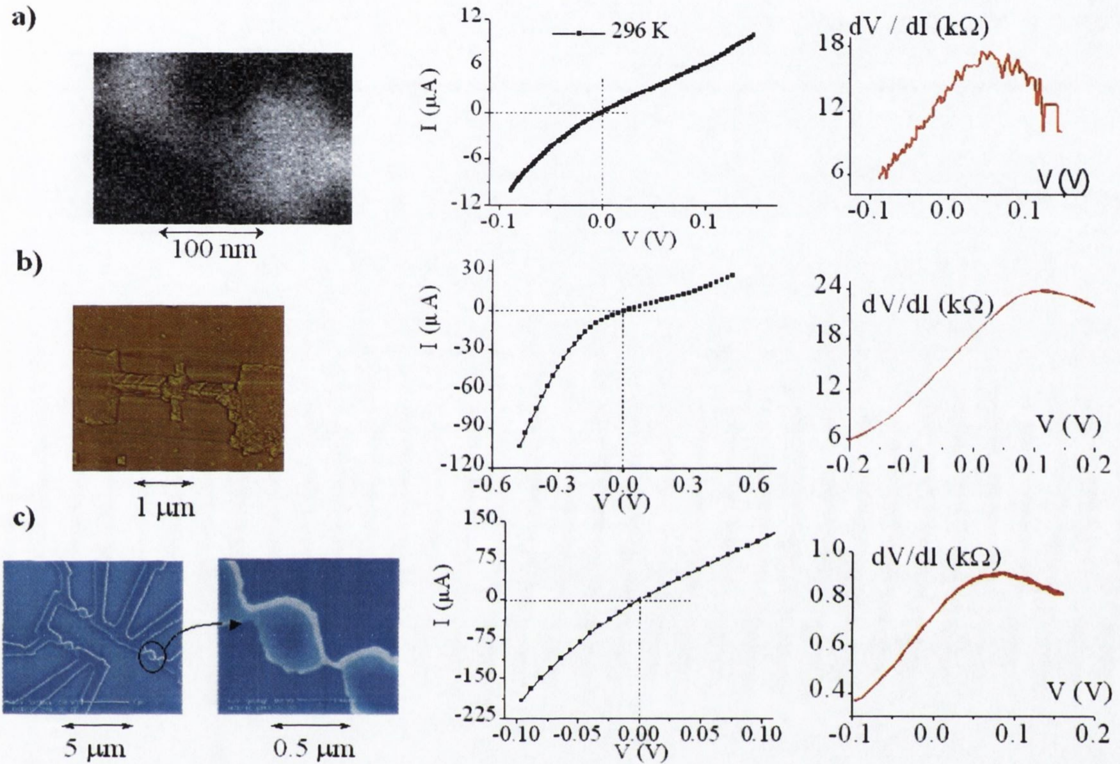

Figure 3.1. The I-V of nickel nanostructures on a SiO_x substrate is non-linear and asymmetric, with a resistance peak around 0.8 eV for all the samples independently of the method of fabrication: a) Electrodeposition, b) FIB and c) e-beam lithography.

The $\frac{dV}{dI}$ peak remains at the same voltage when we change the temperature even if the resistance itself varies by more than one order of magnitude and the non-linearity and asymmetry of the $\frac{dV}{dI}$ are also changed (Fig.3.2). Since this peak seems to be an intrinsic property of these samples, we´ll follow the convention of considering it to be in the positive side of the I-V.

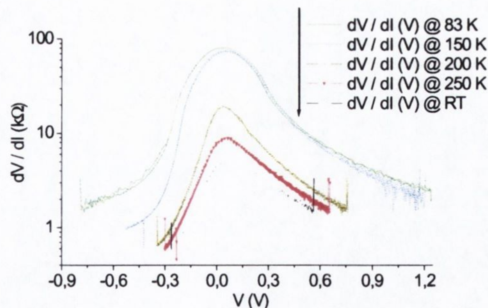

Figure 3.2. Figure 2: Variation of the conductance of a FIB-milled double nanoconstriction with the temperature. The resistance peak remains roughly at the same position for all the temperatures, but the non-linearity (ratio of resistances at low and high voltages) and asymmetry (ratio of resistances for negative and positive voltages) is altered.

One epitaxial Ni film grown on MgO and one single crystal film deposited on glass were used for the fabrication of control samples. The nanoconstrictions (simple or double) patterned on these films show a I-V characteristic that is linear when the resistance of the device is small ($\lesssim$ 15 kΩ) and non-linear when the resistance is of order of 20 kΩ or higher (see figure 3.3). All the samples have a symmetric I-V characteristic, the samples with a non-linear I-V have the maximum of resistance at 0 V, and the conductance vs. voltage can be fitted by a $a + b\mathrm{V}^2$ dependence. On the other hand, Pt nanoconstrictions deposited by FIB on $\mathrm{SiO_x}$ substrates do show non-linearity, asymmetry and an out-of-zero $\frac{\mathrm{dV}}{\mathrm{dI}}$ peak. Therefore, the asymmetry and non-linearity for low resistance samples, must be somehow associated with the substrate. The possibilities will be discussed in the section 6.1. The data in the following sections will refer to samples fabricated on $\mathrm{SiO_x/Si}$ substrates.

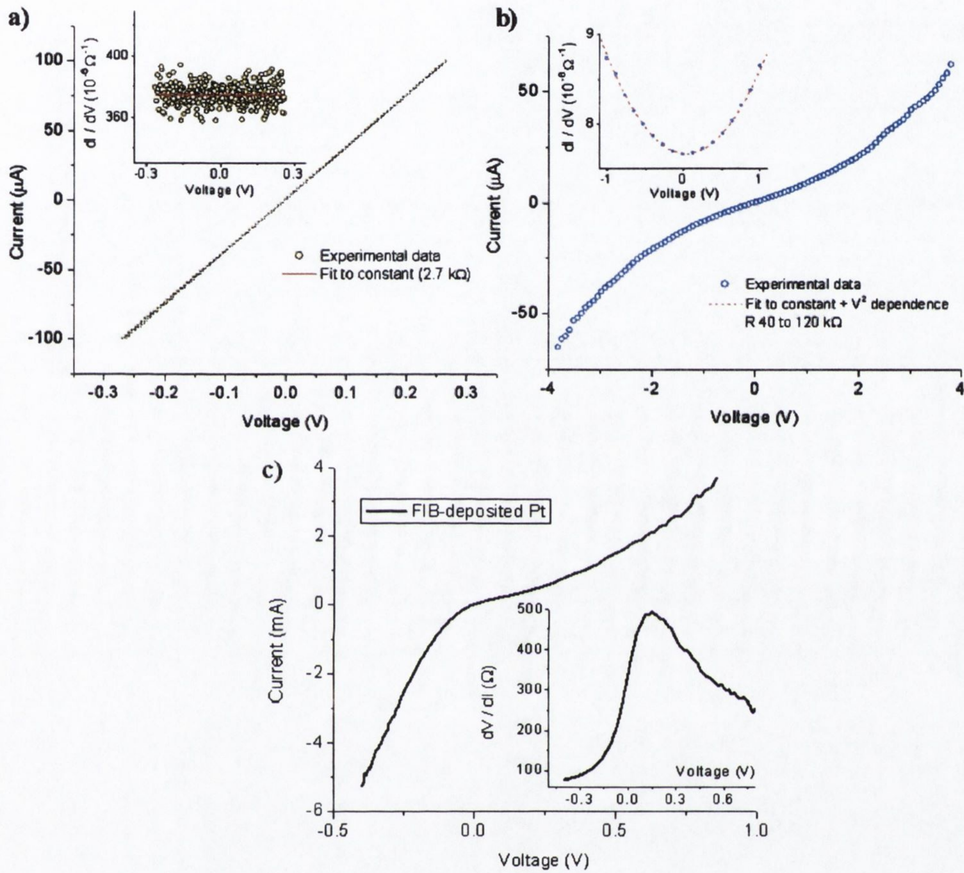

Figure 3.3. I-V characteristic of the control samples. Nanoconstrictions made on MgO substrates with transport characteristics a) linear and low resistance (<12.9 kΩ) b) non-linear (symmetric) and high resistance (>12.9 kΩ). c) Transport characteristic of a FIB-deposited, Ga rich Pt nanoconstriction on SiO_x substrate.

3.1.2 Magnetic field effect and relaxation:

The samples fabricated on a SiO_2 substrate show MR ratios that ranged from 1% to 50000 % (we will define the magnetoresistance as $\frac{\rho_H - \rho_0}{\rho_0} \times 100$, what is sometimes called the "optimistic" value). The huge MR ratios obtained are always negative (the resistance is reduced), independently of the direction of the applied field.

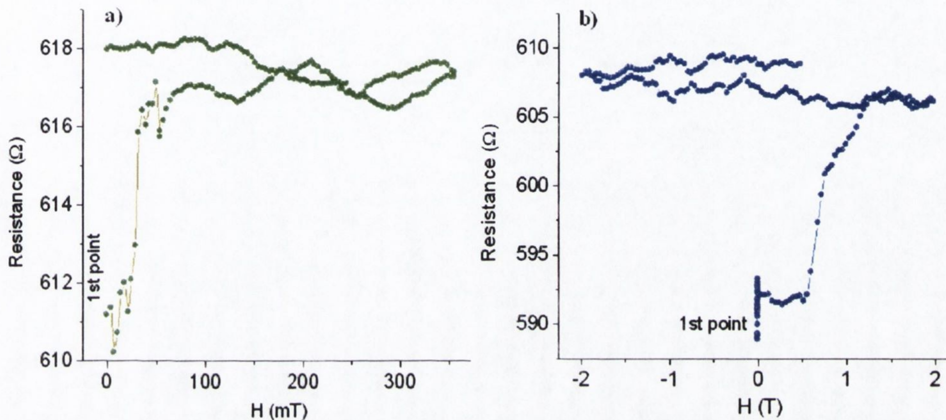

Figure 3.4. Magnetoresistance measurements on electrodeposited samples: a) field parallel to track and MR of approximately 1 % with a switching field of 30 mT and a saturation field of 80 mT. b) Field perpendicular to sample MR of 2.5 % with a switching field of 500 mT and a saturation field of about 1-1.5 T. The increase of resistance after 2 T is due to sample heating.

However, most of the samples present a positive magnetoresistance with values of order 1%. The resistance does not increase uniformly with the field, but remains roughly constant and then varies quite suddenly at a certain "switch" field, till we reach another saturation field from which the sample does not vary its resistance, even when the field is taken back to zero or is applied in the opposite direction. Both the "switching" and the saturation fields depend on the sample and the direction of the applied field, and can vary by one order of magnitude depending if the field is parallel or perpendicular to the track (see figure 3.4).

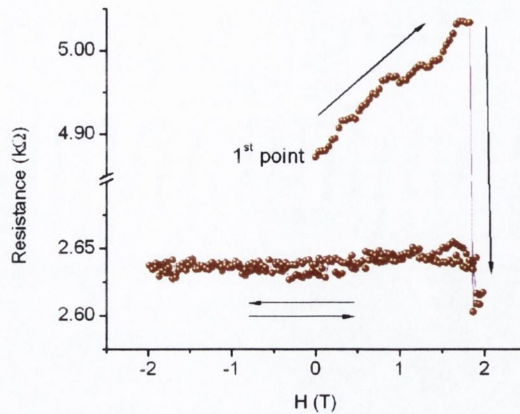

Figure 3.5. ELENA sample which shows magnetic switch. After an initial increase of resistance with field (perpedicular to sample) as in previous samples, the sample suffers a change of state where the resistance is reduced to half of its previous value.

The increase of resistance can sometimes give way to a sudden decrease of resistance. Initially, the resistance increases with the field by 1 or 2 %, but when we reach a certain magnetic field the resistance drops by a 30 to 50 %. The switching field is of order of 2 T for configurations perpendicular to the sample, and once more the sample does not recover to the initial (high) resistance state when we take the field back to zero or when we apply it in the opposite direction, this effect is shown in the figures 3.5 and 3.6.

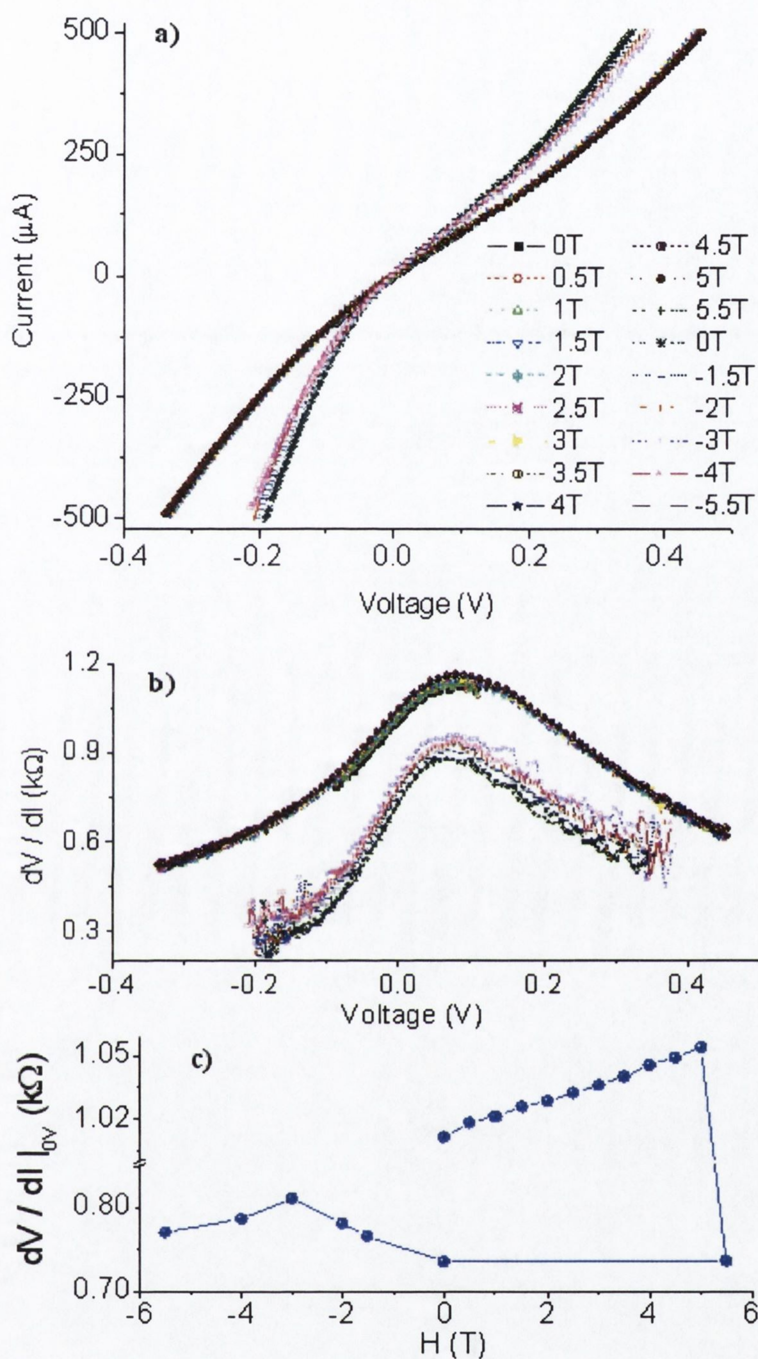

Figure 3.6. Transport characteristic of an e-beam lithographed nickel sample. a) Magnetic field effect ('switch') in the I-V and b) corresponding dV/dI (V) characteristic. c) Resistance at zero voltage vs. magnetic field. The resistance increases with the field by approx. 1 % T^{-1}untill a switch value (5 T) is reached, then the resistance drops by a 40 % and remains at that value for any field.

The drop of resistance can reach values of several thousand % at fields of order 10 mT and at room temperature. This we have observed for both ELENA and FIB samples. When a magnetic field is applied, the I-V becomes much more linear and symmetric (fig. 3.7 a and c), and the effect causes a hugh change of resistance at low voltages, going from conductance values below G_0 at 0 V (defining $G_0 = e^2/2h = 12900\ \Omega^{-1}$) to conductance values $\geq 10\ G_0$ at 0 V when a field of order 10 mT is applied.

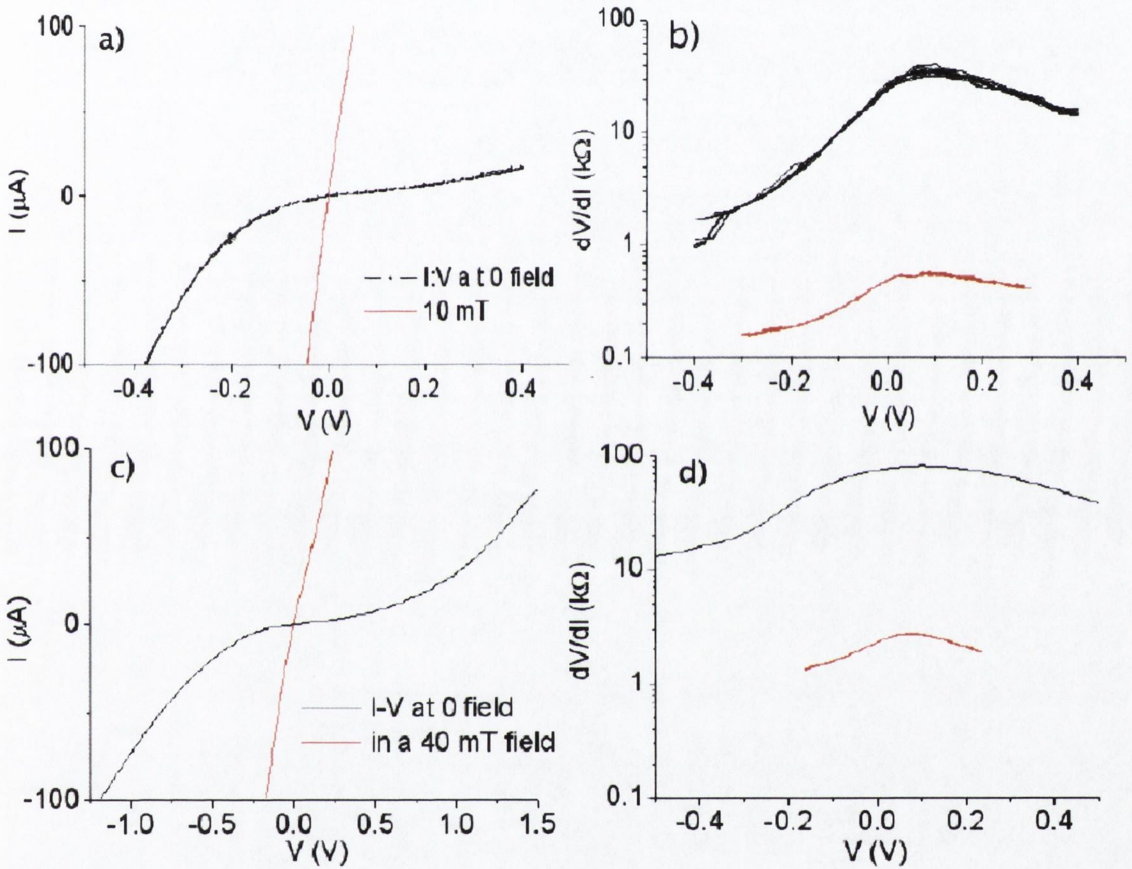

Figure 3.7. a) I-V characteristic of a FIB patterned double constriction with and without a field and b) $\frac{dV}{dI}$ ($\sim$resistance) derived from a). c) I-V characteristic of a ELENA nanocontact and d) derived $\frac{dV}{dI}$.

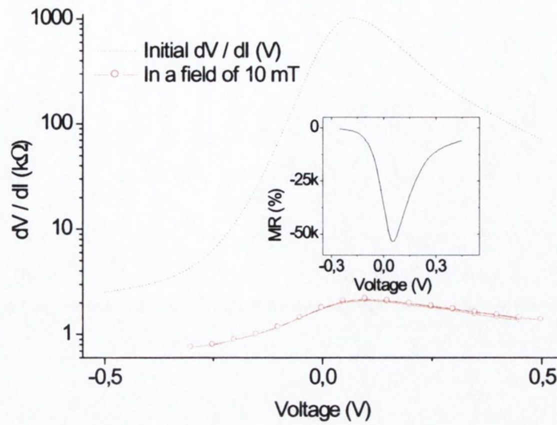

Figure 3.8. Figure 4: Highest variation of conductance obtained for a FIB milled simple. Inset: 'optimistic' MR ratio $= \dfrac{\rho_{\rm H} - \rho_0}{\rho_0} \times 100$.

The maximum MR measured for a FIB sample is 5 x 10^4 % and 5 x 10^3 % for the ELENA samples (Fig. 3.7 b and d). The maximum magnetoresistance ratio was obtained after heating in open air at 250° a FIB patterned sample for several minutes. The MR is highly voltage dependent, tending to increase the linearity and symmetry of the I-V curve, as we can see in the figure 3.8. It is due to this change in the linearity of the I-V which imply a huge decrease of the resistance at low voltages. The maximum of the magnetoresistance coincides the with the peak of the resistance (~80 mV applied).

This effect is not immediately reversible. On reducing the applied field to zero, the resistance does not revert to its original, high value. The relaxation times can be very long, going up to a couple of months when a strong magnetic field of 1 T is applied in the perpendicular direction (Fig. 3.9), and sometimes the sample does not recover the original resistance after applying a field unless it is heated. Once the sample recovers a value of resistance similar to the initial, a magnetic field of equal magnitude can be applied again to

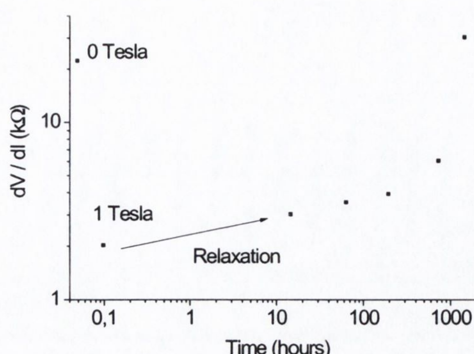

Figure 3.9. Recovery of the resistance after a magnetic field being applied: the original resistance of the sample was 22 kΩ, after apply a magnetic field of 1 Tesla it went down to 2 kΩ and then relaxated to 30 kΩ after 1500 hours (approx. 2 months). The deduced activation energy for a characteristic time τ_0 of 10^{-12} sec. is ~0.6 V The process can not be speeded up by applying a magnetic field in any direction.

obtain a MR effect of similar magnitude(Fig. 3.10).

The long recovery times are probably due to the rearrangement of the magnetic moments at both sides of the nanoconstriction (or nanoconstrictions, if we refere to the double nanoconstrictions patterned by FIB and e-beam lithography), process that will be given by the exchange and thermal energies. If we do not heat our samples, sometimes they never go back to a resistance as high as the initial one, but remain in the low resistance state. This is akin to magnetic hysteresis. Magnetic microsimulations[1] on Ni double nanoconstrictions show that the demagnetised state is always one with a vortex in the centre, and when a field perpendicular to the current line is applied, the reversal proceeds with a vortex state, but when the field is parallel to the current, the vortices do not reappear after the 1st saturation (see the figure 3.11 for the magnetization in the relaxed state or the Appendix to this chapter for more details).

None of the nanostructures (10 single and double nanoconstrictions) fabricated from the control films on MgO and glass with a cap layer showed a magnetoresistance above 2 %.

[1] Courtesy of M. Viret, Physique de l'Etat Condensé, CEA, Gif-Sur-Yvette, France

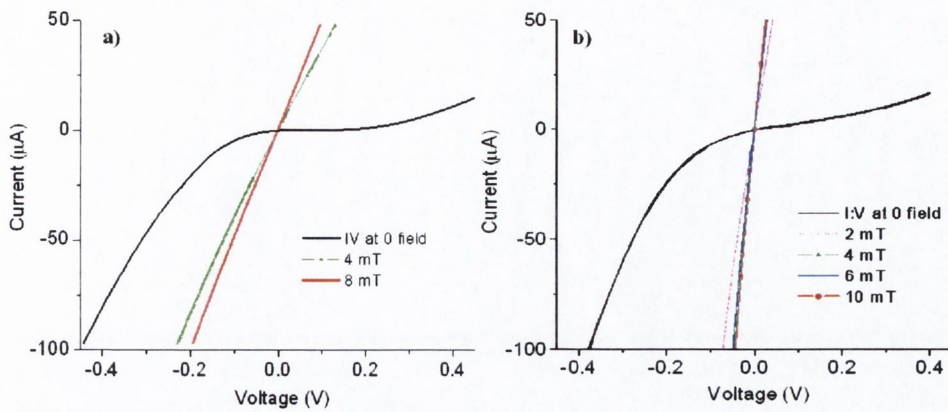

Figure 3.10. a) Magnetic field effect on the I-V characteristic of a FIB patterned sample. After the magnetic field is applied the transport is mostly linear and symmetric, with a big reduction of the resistance at low voltages. b) The I-V after the relaxation is once more highly non-linear and asymmetric and a magnetic field of a few mT is again enough to saturate the sample into a linear, symmetric and low resistance state.

Plausible explanations are discussed in section 6.1.

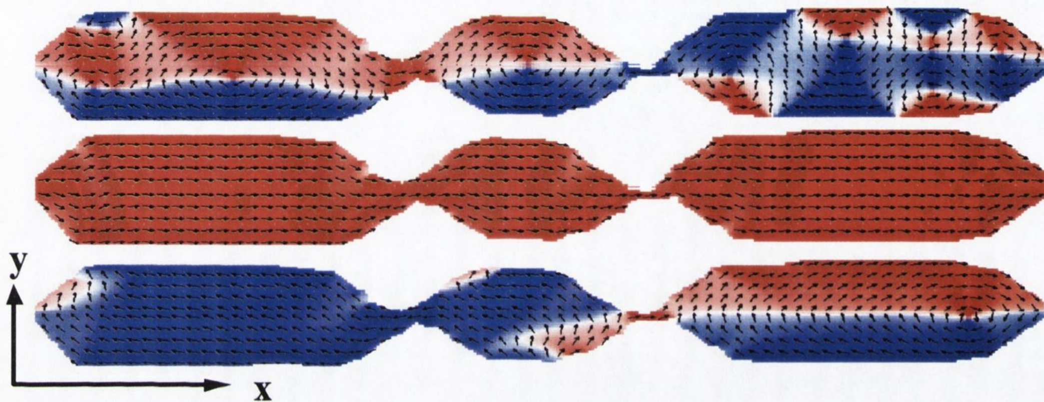

Figure 3.11. Micromagnetic simulations (see text) based on the SEM of a lithographed double constriction (figure 3.1 c). The coulour code is: blue for the +**x** direction, red for −**x** and white for the perpendicular in-plane direction. The initial random state (up) is vortex-like and the sample saturates to a **x**− magnetization in a field of just 8 mT, the middle picture is the remnant state. For fields in the y direction the sample does not saturate even at fields of 100 mT (the magnetization at the nanoconstriction remains in the x direction). Down image is the remnant state after a 100 mT field is applied in the y direction. See Appendix for more details.

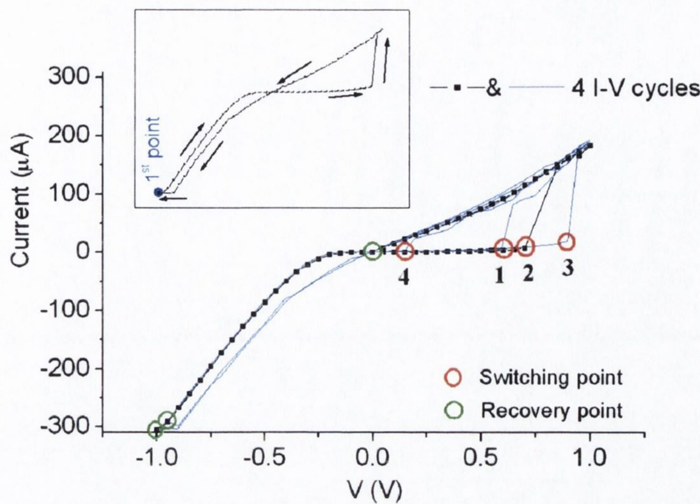

Figure 3.12. Electrical switch and hysteresis on a FIB patterned sample. The curve was taken varying V and measuring I. The numbers refer to the order of switching in the four cycles.

3.1.3 Electrical switching:

Apart of the magnetic effect, electrical switching and hysteresis are observed in some of the FIB patterned double nanoconstrictions on SiO_x/Si substrates (figure 3.12). This electrical switching happens when the current exceeds a threshold of 5 to 10 μA, after which the residual I-V is more linear and symmetric reducing the resistance up to a factor 100, in a similar fashion to the changes of the I-V characteristic after a magnetic field being applied.

This effect was seen only on the double nanoconstrictions patterned by FIB. However, electrical switching and hysteresis for ELENA and e-beam lithographed samples was also measured, but instead of having changes of resistance of two orders of magnitude at currents of about 5-10 μA, these other samples present reversible, smaller changes of resistance of about a factor 2, and at higher currents from 100 μA up to 10 mA (Fig. 3.13).

The electrical switching observed in the FIB double nanoconstrictions is magnetic field

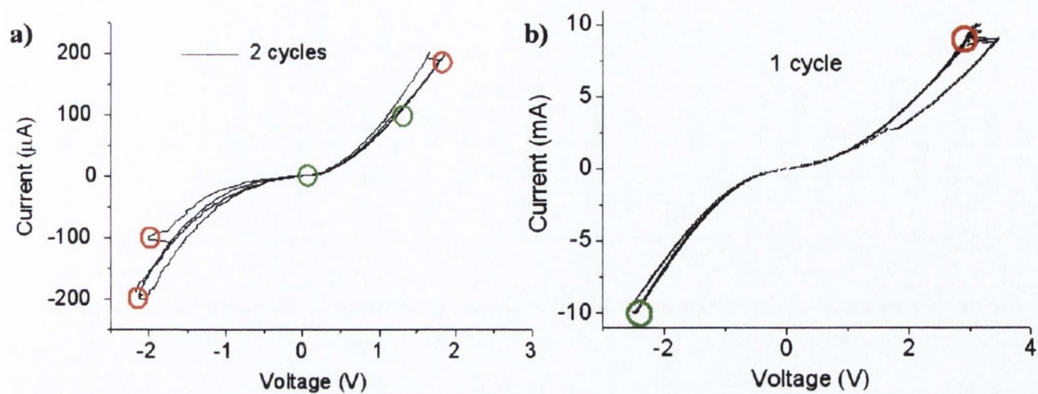

Figure 3.13. Instabilities on the I-V characteristic of a ELENA sample. The curves were taken varying I and measuring V. The red circles mark the switching points and the green circles the recovery points.

dependent. An applied magnetic field non only reduces resistance, asymmetry and non-linearity, but also eliminates the electrical switching and hysteresis, which is present once more when the sample relaxes (after hours or days) to a similar state to the original one. See the figure 3.14.

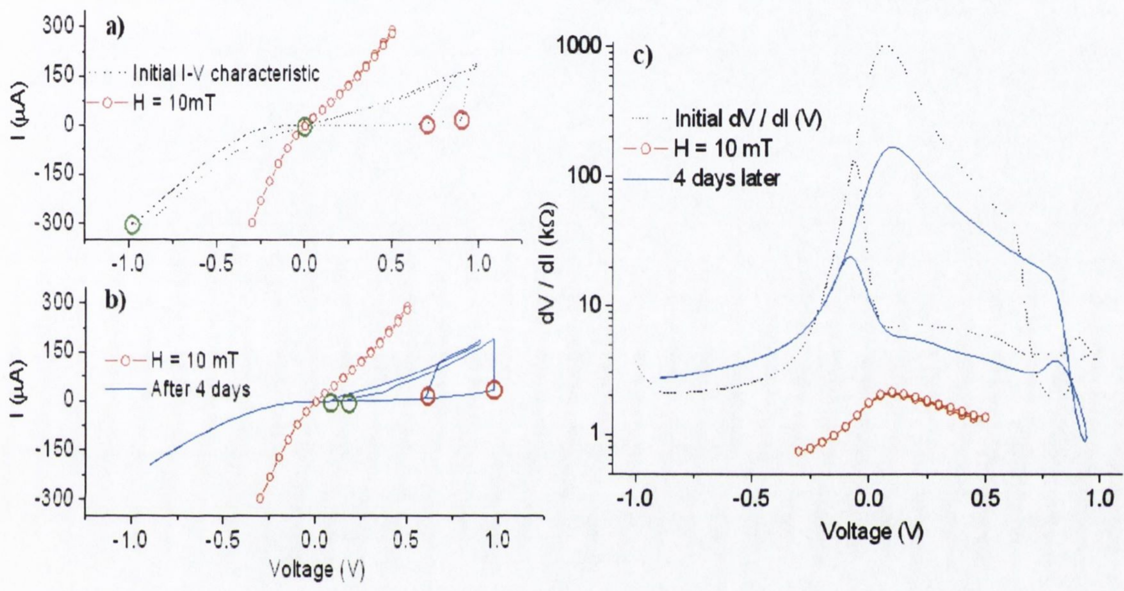

Figure 3.14. Figure 8: a) I-V and electrical switching before and during a magnetic field of 10 mT being applied, b) during a magnetic field being applied and after the recovery time. c) dV / dI corresponding to the I-Vs displayed on a) and b) with recovery points at 0 V. The red circles mark the switching points and the green circles the recovery points.

3.2 Noise measurements of nickel nanostructures

3.2.1 Noise characteristic

As we pointed out in the first chapter, noise measurements do not only impose a practical limitation to the performance of the devices, but also give information about the non-adiabatic processes, and the electronic and magnetic dynamics of the system.. Heating effects, electromigration, etc. can be more easily detected or even predicted by noise measurements. In the case of nano-scaled devices, electromigration, heating and stability are looming obstacles for their application and noise measurements are an invaluable tool to study the best performance conditions, as well as the dynamic micro-behaviour, of the structures.

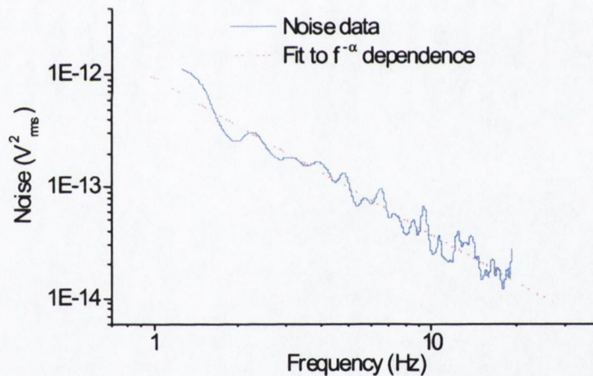

Figure 3.15. Typical PSD for one of the nickel nanostructures fabricated in this work. The spectrum shows the $1/f^{\alpha}$ characteristic with $\alpha = 1.4$. The noise level γ_H at $f = 1$ Hz is 10^{-12}.

At high current densities (above 10^{10}-10^{11} A/m^2) the transfer of momentum from the conduction electrons to the atoms, especially defects and impurities, trends to displace the atoms through the material, mainly along grain boundaries, an effect known as electron-

wind electromigration. This effect becomes critical when working when working with devices comparable in size to the atoms being moved, and the consequences for the lifetime of the device [3] and the possible applications of the effect [4] have been studied for the past 15 years. But relatively little has been done to investigate electromigration in nanostructured magnetic materials, and the possible relation between noise and magnetic order.

The noise spectra of nickel nanostructues shows a characteristic PSD with a $\frac{1}{f^\alpha}$ dependence, being α from 0.8 to 1.4. The normalised (to applied voltage) noise levels vary from 10^{-12} $\mathrm{V}^2_{\mathrm{rms}}$ to 10^{-8} $\mathrm{V}^2_{\mathrm{rms}}$ at 1 Hz. When FIB patterned samples are fit to Hooge's experimental model $\frac{S_V(f)}{V^{\,2+\theta}} = \frac{\gamma_{\mathrm{H}}}{n_c V f^{\,\alpha}}$ (see section 1.3.2), with standard values for the Hooge's constant γ_{H} from 10^{-2} to 10^{-3} [30], and considering carrier concentrations of about 10^{28} m^{-3}, the low noise characteristics levels give fluctuator volumes of order $10^{-23} - 10^{-24}$ m^3, but for samples with the higher noise levels the fluctuator volume obtained would be of order $10^{-27} - 10^{-28}$ m^3, that is, around 1 nm^3.

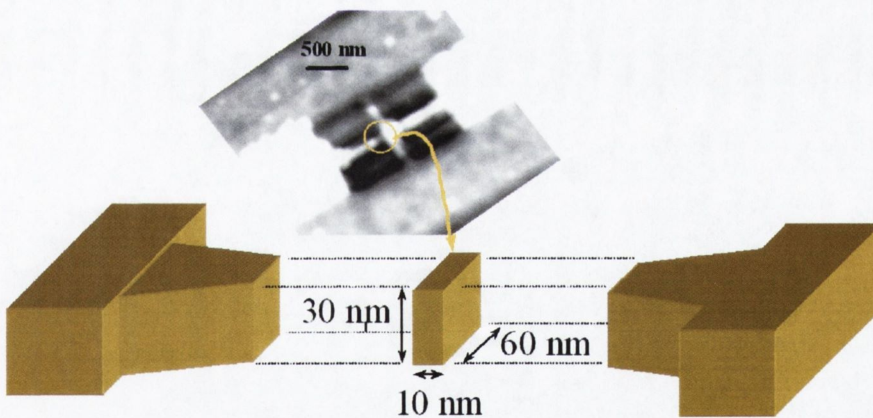

Figure 3.16. Deduced fluctuator volume from the previous noise spectrum (bottom), and AFM of the sample which generates it (top). The fluctuator volume is in agreement with the size of the narrowest constriction of the FIB milled sample.

3.2.2 Asymmetric behaviour and electromigration:

We pointed out in the last section that the I:V characteristic of our device is non-linear and asymmetric, and this asymmetry is also present in the noise spectra of some devices, especially at relatively high currents ($\gtrsim$ 250 μA). If we look at the fluctuations for small applied voltages of $\sim$ 10 mV ($\leq$ 10 μA applied current), near the limit of detection for our equipment, the noise signal is the same for both senses, but at bias voltages of $\sim$ 100 mV or above we observe that the $\frac{1}{f^{\alpha}}$ gaussian noise spectra is different for both positive and negative senses of the current (Fig. 3.17).

The difference is not only quantitative (noise level γ_H), but also qualitative (noise exponent α), and therefore cannot be re-normalised or explained in terms of a different resistance for both current directions. When we observe the real-time fluctuations (that is, the direct noise signal as appears in an oscilloscope instead of the Fourier transform we get in the noise spectra displayed by a spectrum analyser), we can see that there is an "extra" noise added to the 50 Hz and $\frac{1}{f}$ noise represented by the presence for the positive current of isolated bursts of high voltage fluctuations during periods of up to 1 sec. These shivers of the system are absent for the negative sense of the current.

Simmilar bursts on the noise fluctuations have been observed in metallic nanobridges and attributed to electromigration [31]. In fact, when a very high current pulse of $\sim$ 10 mA is applied to the system during one second, it is possible to observe a reversible change of the transport characteristic, with lower resistance and higher linearity and symmetry, in an effect similar to that described in the previous section when a magnetic field is applied. The electrically induced change of behaviour reverses in the time scale of 100 hours, but this time

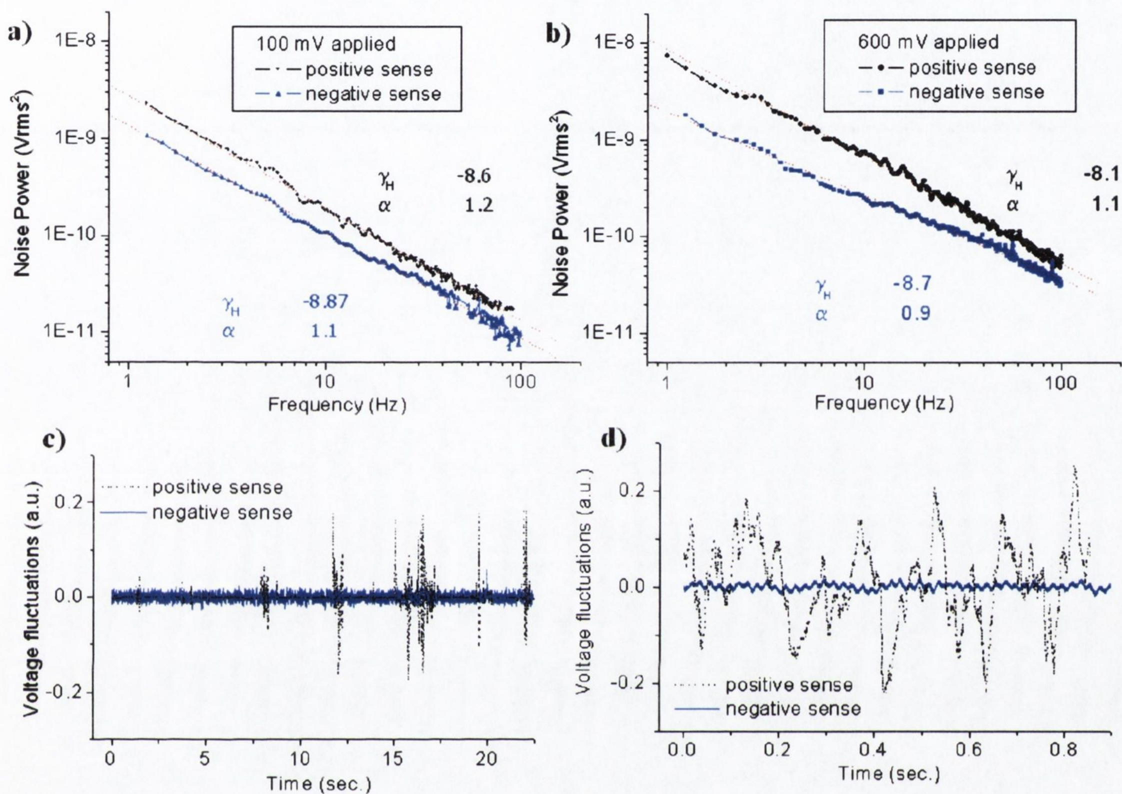

Figure 3.17. a) PSD for an e-beam sample at 100 mV ($\simeq 90\ \mu$A $\sim 4\times10^{11}$ Am^{-2}) applied. The noise level and exponent are different for positive and negative voltages. b) PSD at 600 mV ($\simeq 700\ \mu$A $\sim 3\times10^{12}$ Am^{-2}) applied. The differences for positive and negative current are increased, as it is the noise level for both senses. The noise spectra a) and b) are normalised to 1 V applied. c) Real time fluctuations, where we can see the shivers of the system for the positive sense that do not appear for the negative. d) Zoom over one of these bursts. The high 50 Hz noise present in the negative sense is due to bad wiring (long cable to carry the signal).

can be reduced by applying a high current of similar value to the first one ($\sim$ 10 mA) in the opposite sense.

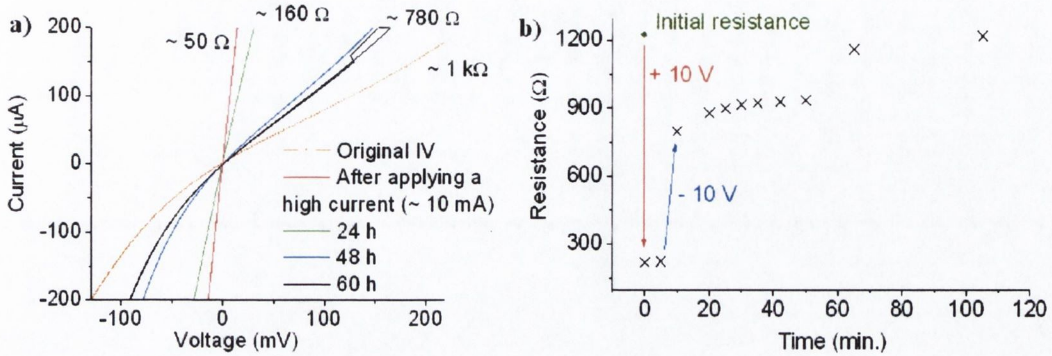

Figure 3.18. a) Effect of a high current of 10 mA on the I-V characteristic of a e-beam lithographed sample. The resistance drops from 1 kΩ to 50 Ω, and the I-V becomes more linear and symmetric. b) A high current (~voltage) applied in the opposite sense of the first one can increase the resistance and reduce the relaxation time from hours to minutes.

However, the asymmetry of the I:V curve, with a different resistance depending on the sense of the current must be somehow related to the geometry of the constriction itself. We see that after applying a high current, the resistance of the device is reduced by a factor 20, and the I:V characteristic then becomes linear and symmetric, before slowly reversing to its original state (Fig. 2). This experiment can be reproduced, but now applying a current in the negative sense after first having reduced the resistance with a current in the positive sense, we can see that the relaxation time is reduced to a few minutes. The effect is therefore dependent of the sense of the current and can both reduce or increase the resistance, whereas a thermal effect would be independent of the sense of the current. These measurements were performed on samples fabricated on SiO_x/Si substrates.

3.2.3 Magnetic field effect on the noise spectra

In the presence of a magnetic field (Fig. 3.19), the slope of the 1/f noise measured at high applied currents (> 100 μA) is increased ($\Delta\alpha$), although the noise magnitude for high frequencies (> 10 kHz) is the same as when there was no magnetic field applied. The variation of the α coefficient with field depends on the direction of the applied field, and variations of α up to a 10 % in fields of order mT for the parallel configuration, or 20 % for fields of the order of 1 T in the perpendicular configuration.

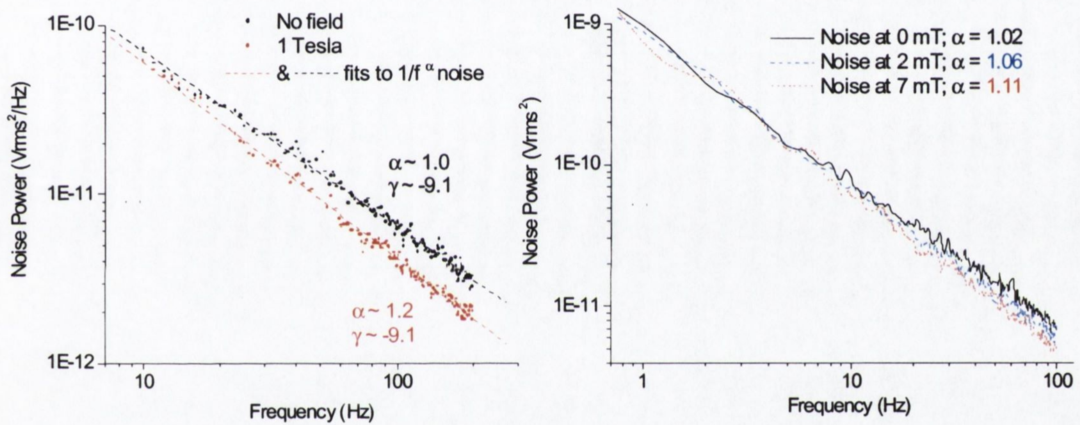

Figure 3.19. Magnetic field effect on the α exponent of the $1/f^{\alpha}$ noise. If the field is applied perpendicular to the track (a) a field of up to 1T is required to obtain changes of the order of 10 %. b) In a field applied parallel to the sample, a few mT are enough to change a 10 % the α exponent. The noise level is not affected by the magnetic field.

3.2.4 Random telegraph noise (RTN)

It was mentioned at the start of the section that the sampled fluctuator volume deduced from the noise spectra with higher γ_H coefficient was about 1 nm^3. This is not possible, as

we can see in the AFM and SEM images at the beginning of the chapter. One of the reasons this may happen is that the volume of the fluctuators is comparable in size with the sampled volume and Hooge's formula is not valid any more.

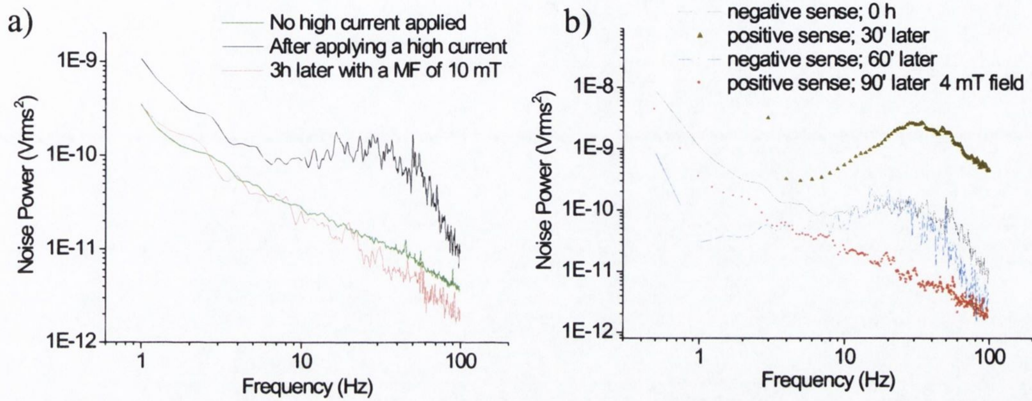

Figure 3.20. a) After applying a high current, non-Gaussian noise (bump at 20-30 Hzs) appears on the noise spectrum that was previously just $1/f$ noise. The anomaly dissapears in the presence of a 10 mT field. b) The non-Gaussian noise can be generated again by applying once more a high current; it appears for both senses of current, it is stable on time (~hours) and dissapears on fields as small as 4 mT.

On the other hand, we have pointed Gaussian, $\frac{1}{f}$ noise as the common noise feature for nickel nanocontacts and nanoconstrictions, however, noise measurents carried out in a 4 probe DC configuration of nickel constrictions approx. 20 nm wide fabricated by e-beam litography show non-Gaussian fluctuations in their noise spectra after a high current ($\sim$ 10 mA) being applied. It must be pointed out that the voltage applied to obtain the noise signal is quite small (60 mV –> 60 μA for this sample), and that subsequently the shivers previously described in the section 3.2.2 do not appear. The initial noise characteristic before the high current being applied, shows the typical noise spectrum of these samples, a $\frac{1}{f^{\alpha}}$ characteristic with $\alpha \sim 1$ and a noise level of $\gamma_{\mathrm{H}} \simeq 10^{-9}$, but after a current of 10 mA is applied, non-Gaussian noise (bumps) appears mingled with the $\frac{1}{f}$ noise, increasing the noise

level at frequencies from 10 to 100 Hz (see the figure 3.20).

Due to the bad quality of this noise signal, a long time of averaging is required to take the measurement. If we apply a magnetic field of a few mT, we can bring the noise characteristic back to the usual $\frac{1}{f}$ spectrum. However, as every measurement needs of the order of 30 minutes to collect the averages, the measurement in the magnetic field was taken 90 minutes after the first trace. This could be due to a reduction of the two level fluctuation in time, but the deviation for the negative sense of the current from 1/f noise had actually increased after 60 minutes (Fig. 5 a), and we would expect the RTN to persist during the 30 minutes that takes to collect the spectrum in a magnetic field, unless it has a magnetic origin.

Looking at the real time fluctuations, we observe that a new type of noise, nor $\frac{1}{f}$, nor shivering, shows up in the 0.1 sec. range after the high current being applied.

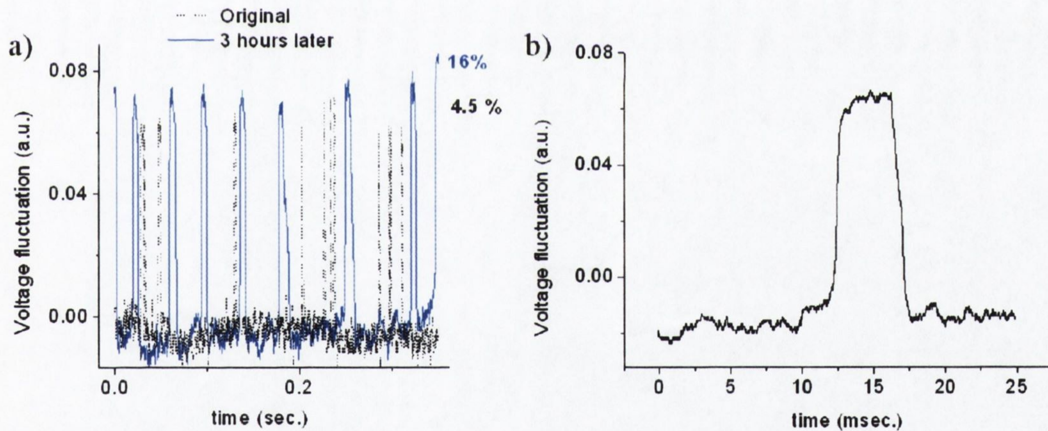

Figure 3.21. a) After applying a high current, the real time fluctuations show a two-level random telegraph noise in the time-scale of ~30-50 msec. (4.5 % of the time in the high resistance state). After a few hours, the sample remains a longer time in the high resistance state (16 %). b) Time zoom which shows that the permanence in the high resistance state is 5-10 msec. (16 % of the time). The fluctuations are approximately 0.1 % of the applied signal.

This noise, superimposed to the 'common' fluctuations, represents a fluctuation of the

system between two discrete levels, the so called random telegraph noise (RTN) described in section 1.3.3, with a difference of resistance between the two levels of approximately 0.1 %

The time spent in the high resistance state increases as we increase the temperature, and the discrete fluctuation eventually disappear with an increase of the temperature of more than about 15° C.

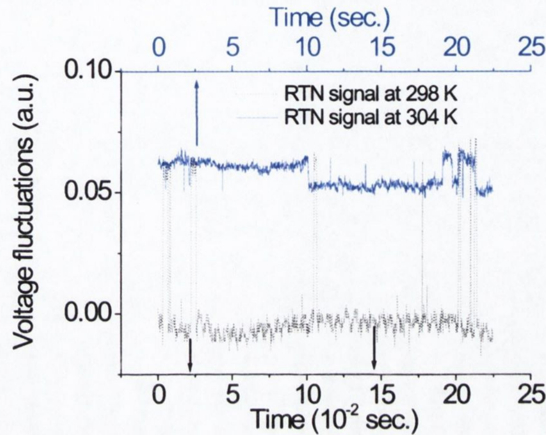

Figure 3.22. By increasing the temperature the RT fluctuations become smaller ($\sim 10^{-2}$ %) and persist for a longer time (seconds). At 304 K the sample spends now around 50 % of the time in each state. For temperatures above 310 K the RTN dissapears.

3.3 Spin polarization of nickel nanoconstrictions measured by planar Andreev reflection

The huge magnetoresistance (MR), up to 10^5 %, found in electrodeposited nickel nanocontacts [32], [33] and similar to the results presented in this work for both electrodeposited and patterned nanostructures, have puzzled the scientific community for the past five years. The frequent explanation of magnetoresistance due to a domain wall trapped in the nanocontact is only possible if the polarization of the nickel at room temperature is much higher than the commonly accepted low temperature value of 42-46 % [34], [35].

Theories have been proposed in terms of the presence of an electrical dead layer in the nanoconstriction. NiO_x and/or materials from the solution bath used during the electrodeposition (or implanted Ga in the case of FIB patterned structures) would form this dead layer [17], where the s-band electrons would be trapped and in nickel only the d electrons would be left to contribute to the conductance. Values of MR up to 700 % have been theoretically predicted due to the conductance through spin-polarized oxygen p states in a NiO_x-Ni nanocontact [16]. To explain even higher MR ratios, a narrowing of the d-band at the nanocontact has been suggested.

However, there is no direct proof of an increased spin polarization at the nanocontact, and magnetostriction and magnetic dipole forces must be considered before the ballistic MR explanation, at least for electrodeposited nanocontacts, where the sample is not bound to a substrate.

It was introduced in the second chapter (section 2.1.5c) the Andreev reflection technique [36], which can be applied to measure the spin polarization at the Fermi level of

ferromagnetic materials [34], [35]. In this method, a superconducting (ferromagnetic) point contact is put in contact with the ferromagnetic (superconducting) sample and the conductance of the interface measured. Due to the Andreev reflection, the supercurrent conversion is limited by the minority spin population near the Fermi surface, and the conductance can reveal the spin polarization of the metal. The point contact at the interface is usually made by mechanical point contacts or by STM, where a sharpened tip is slowly approached to the sample until the conductance is equivalent to that of a very narrow nanocontact. To test the possible explanation for the MR found in our nanostructures, we need to adapt this technique to the thin film geometry, what we did via the seven-step fabrication process for edge junctions described in the section 2.2.5 (Patterning of in-plane Andreev reflection samples).

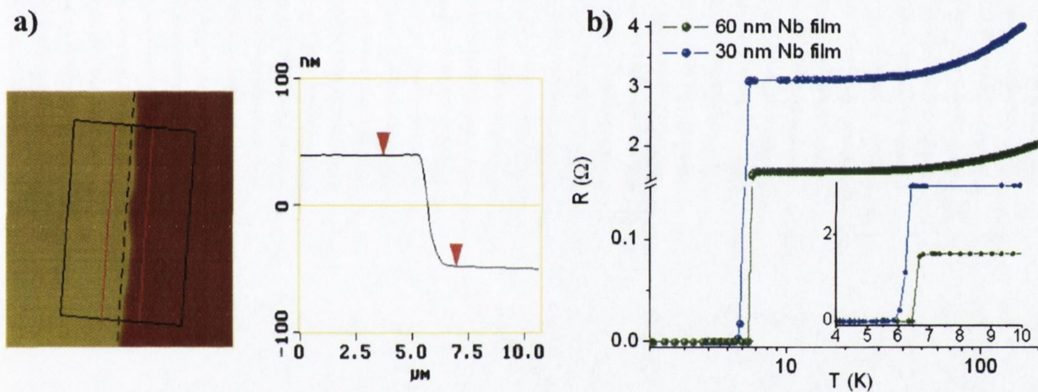

Figure 3.23. a) The milling speed of SiO2 is 5 times faster than that of Nb, this makes very difficult to stop the milling at the proper time and a AFM is required to know the exact NM film thickness to be deposited. b) The two sets of films used, 60 and 30 nm thick, show a transition temperature of 5.8 and 6.4 K respectively. The resistivity at 10 K for both films is $4 \times 10^{-8} \Omega cm^{-1}$. is the dependence of the transition temperature with the thickcness of the Nb film. This effect was discussed for both single-crystal and polycrystalline Nb thin films by Jiang et al. [37] and explained in the framework of a strain-induced model.

To fabricate an edge juntion following this method, the first step is to measure the transition temperature of the deposited Nb film, which will probably be different from the bulk value and will depend on the quality of the film, its thickness and the strain induced

by the substrate [37]. Another step due to experimental considerations is that the Nb film is milled at a much slower pace than the SiO_2 substrate (see figure 3.23) and a precise thickness measurement is required to find the exact amount of metal to be deposited to have both thin films at the same height and a good interface.

The third and most important problem that appears when fabricating these junctions is the quality of the interface.

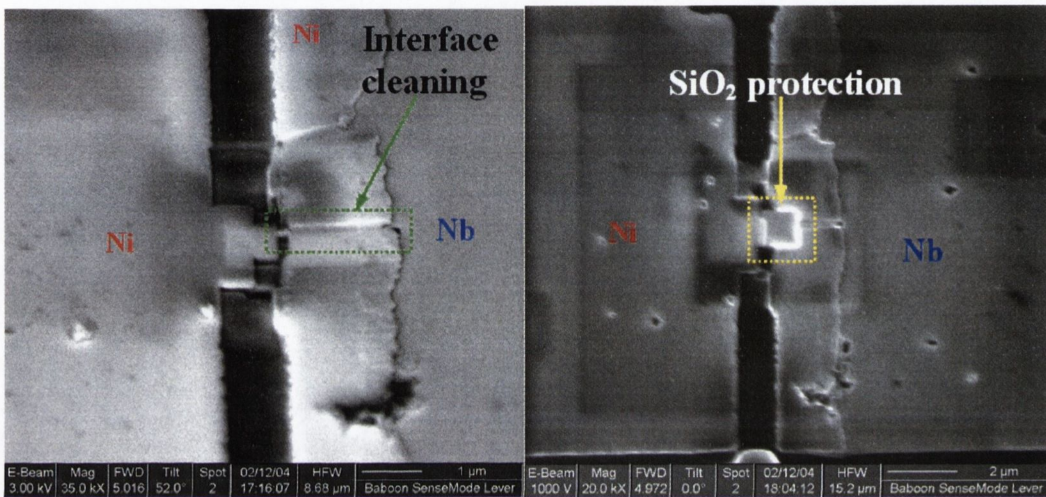

Figure 3.24. The lift-off during the preparation of the Nb-NM edge junctions leaves sometimes bad interfaces with NM on top of the Nb. This top layer can be etched with the ion beam (a), and the walls of the constriction (the top is covered by Au) can be protected from oxidation by depositing SiO_2.

The lift-off process leaves sometimes interfaces with a normal metal (NM) layer on top of the Nb thin film, and to create a nanoconstriction at the boundary between both films we need to remove the metal on top of the niobium (see figure 3.24 left). Furthermore, once the sample is taken out of the vacuum-enviroment of the dual beam, it starts to oxidise. The top of the Nb film is covered by a Au cap layer, but the walls of the nanostructure are vulnerable to damage. To prevent it, a layer of insulator SiO_2 can be deposited on top of the nanostructure (see figure 3.24 right), but if the resistance of the constriction is above some

10 kΩ, it was observed that the SiO_2 layer provides a parallel transport path, so we tend to protect the sample with photoresist inmediatly after the patterning rather that to deposit in-situ an insulator layer.

Figure 3.25. The white arrow marks the boundary between Nb and SiO_2. The picture shows a reduction of the thickness of the Nb film at the constriction due to a bad focussing of the ions.

The FIB allows us to pattern a nanoconstriction at the boundary of the Nb-Cu or Nb-Ni interface (figure 3.25), although there is the possibility of Ga^+ implantation and Ga-rich redeposited material. To reduce this possibility, only electron beam images were taken, and the milling was done at the lowest possible current of 1 pA. The difference in conductivities and electronic levels between the Nb and the NM, together with the, usually, bad quality at the interface of the NM film, make easy to distinguish between both materials while patterning.

The bad quality of the interface leads sometimes to another problem: temperature-dependent strain of the films. This strain, which could be of order of 10^{-6}, is in some occasions big enough to open a gap between both films at low temperature. This process is

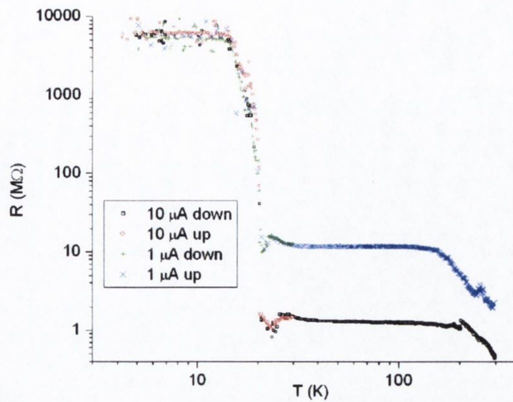

Figure 3.26. The bad quality of the bonding of the film at the interface may be the reason for the increase of resistance with temperature and the final jump to an insulator regime.

reversible, and the nanocontact can be formed once more by increasing the temperature, but if the gap is opened at a temperature above the superconducting transition, the sample will obviously be useless for Andreev reflection measurements (an example is presented in the figure 3.26).All these experimental difficulties, together with the numerous patterning steps, have as consequence a very low sucess rate for Andreev reflection in the edge junctions. Only around 5 % of the initally lithographed samples present a good contact with a clean interface (Fig. 3.27).

The nanocontacts that do have a good interface, still present a higher resistance than the usual one for Andreev point contacts (10 to 100 kΩ compared with 100 Ω), and the transport is probably not ballistic but diffusive. The diffusion of the electrons will lead to spin scattering and spin-flip in the neighborhood of the nanoconstriction, reducing the effective spin polarization. This can be taken into account by the inclusion of an effective barrier (Z parameter in the model) at the interface of the superconductor-metal material, and the samples fabricated following this method do show sometimes clear evidence of Andreev reflection, with different conductance above and below the superconducting gap (Fig. 3.28).

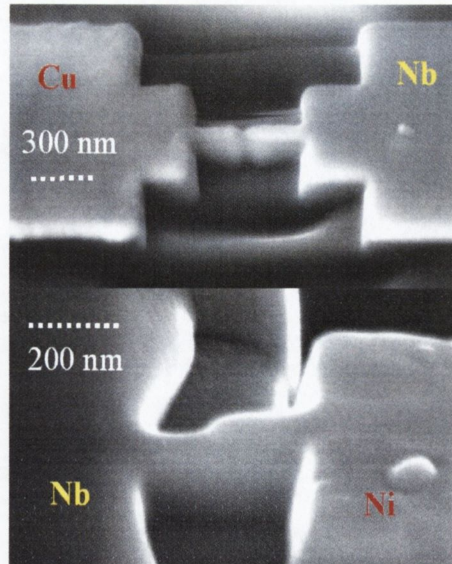

Figure 3.27. SEMs at 52 degree of the thin film plane of a Cu-Nb and a Nb-Ni nanoconstriction.

The normalized conductance versus voltage can be fitted to find the local spin polarization of the material., the fits are carried out using a modified version of the BTK (Blonder-Tinkham-Klapwijk) theory [10], which was developed to analyse G vs. V for normal/superconducting contacts. The BTK theory, gives a simple explanation to describe the I-V curves of normal-supreconducting microconstrictions by describing the crossover from metallic to tunnel junction behavior. The detailed calculations were performed within a generfalized semiconductor model, with the use of the Bogoliubov equations [38] to treat the transmission and reflection of particles at the N-S interface. By including a barrier of arbitrary strength at the interface, it is possible to compute a family of I-V curves ranging from the tunnel junction to the metallic limit. Excess current, generated by Andreev reflection, vary smoothly from $\frac{4\Delta}{3eR_N}$ in the metallic case to zero for the tunnel junction. Charge-imbalance generation, previously calculated only for tunnel barriers, can be recalculated for an arbitrary barrier strength, and detailed insight into the conversion of normal

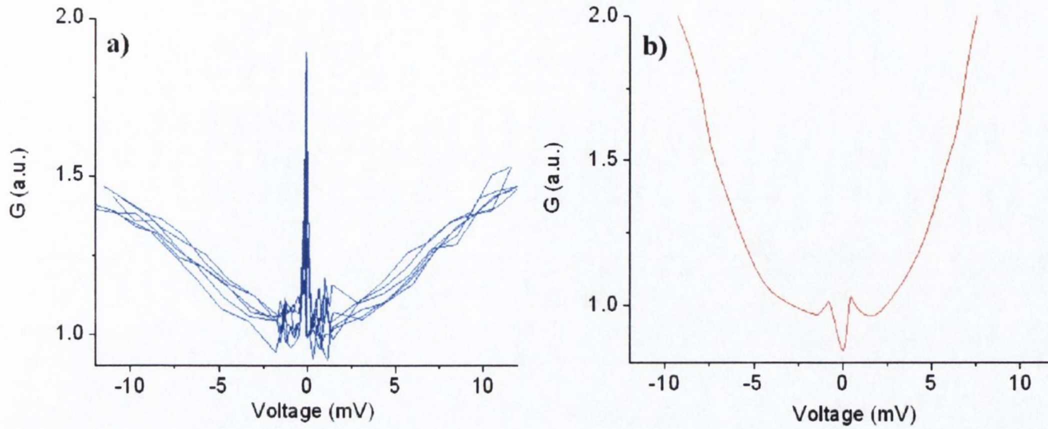

Figure 3.28. Raw data of a 4-point DC measurement of the conductivity G vs. the voltage for a Cu-Nb a) and a Ni-Nb nanoconstriction. a) Shows the increase (doubling) of conductance expected for a NM when the voltage is smaller than the superconducting gap. b) In a ferromagnet, the conductance inside the gap decreases due to the polarization of the electrons (see previous chapter).

current to supercurrent at the interface is obtained. The calculated differential conductance offers a particularly direct experimental test of the predictions of the model. The scattering of electrons, represented in the BTK model by the parameter Z (barrier height), erases the magnetic memory of the electrons. The high Z values can be deduced from the G(V) graph in the high peaks at the superconducting gap voltages (see figure 3.29). For badly connected (oxidised) interfaces, the scattering (tunneling) can be so intense that once the electrons finally cross the boundary, they are not polarised.

The current is given by:

$$I \propto \int [\mathrm{F}(\mathrm{E}-\mathrm{V},\mathrm{T}) - \mathrm{F}(\mathrm{E},\mathrm{T})] \times [1 + \mathrm{A} - \mathrm{B}]\, \mathrm{dE}, \tag{1}$$

Where F is the Fermi function, A is the Andreev reflection probability and B the probability of normal reflection.

The BTK model was modified [2] to include spin polarization. This is achieved by

decomposing the total current into polarized and non-polarized parts:

$$\mathrm{I} = (1 - \mathrm{P})\,\mathrm{I}_{\mathrm{unp}} + \mathrm{P} \cdot \mathrm{I}_{\mathrm{pol}}, \tag{2}$$

The model has been further modified by Strijkers [39] to account for the proximity effect first predicted by Cooper [40], and caused by diffusion of Cooper pairs from a superconductor into a metal, creating a weakly superconducting layer at the interface with a different transition temperature. This layer has a lower superconducting gap than that of the superconductor and thus two superconducting gaps are required for data fittings, one for the bulk superconductor and one for the proximity layer. Possible evidence for this effect will be shown in the figure 3.30 b).

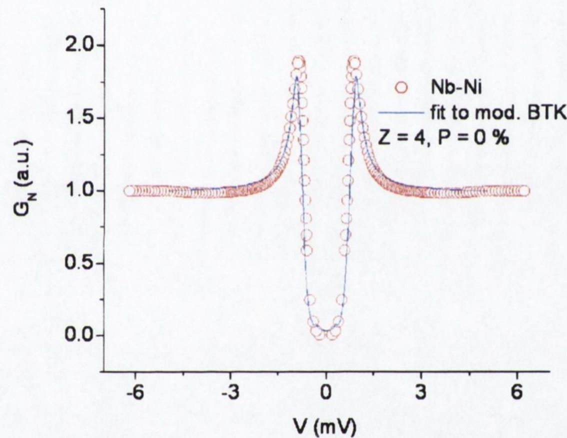

Figure 3.29. For high Z values, the scattering is so numerous that the resultant polarization is null. In the figure, a 500 kΩ Ni-Nb edge junction. Computation done by E. Clifford.

The fitting of the data shows that, for nickel nanocontacts, the samples are sometimes so resistive, i.e., there is so much scattering (-> spin-flip), that the resultant measured polarization is close to 0 %. An example is shown in Fig. 3.29, where the Z parameter is very high (> 2), maybe due to the presence of an oxide layer between the nickel and the

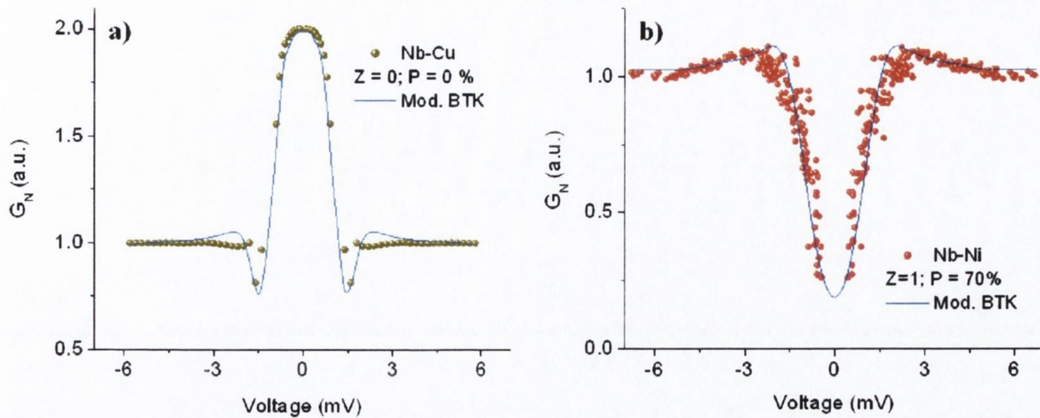

Figure 3.30. In cleaner interfaces with Z values ≤ 1, it is possible to deduce the polarization of the nanostructured NM. a) Cu-Nb nanocontact gives a polarization of 0 % (Z = 0, ballistic transport) and b) a Ni-Nb nanocontact gives a polarization for a Ni nanoconstriction of 70 %. The shoulder at $G_N \approx 0.3$, V$\approx$ 0.7meV maybe due to the proximity effect (see text). Computation done by E. Clifford.

niobium. In the case of an oxide layer, to extract the polarization we would need to apply a magnetic field and observe the displacement of the peaks, but the critical field for niobium is only 200 mT, so this method is impractical.

Other samples however show smaller values of Z, evidenced by the absence of peaks at the superconducting gap, which allow a measurement of the polarization. In Fig. 3.30 a) we can see an Nb-Cu constriction that shows the doubling of the conductance below the superconducting gap, in agreement with what is expected for a normal metal. The fitting gives Z = 0 and a polarization P = 0% as expected for Cu.

For a nickel nanoconstriction we observe that the conductance is greatly reduced for voltages below the superconducting gap. The fit to the model gives values of Z = 1 and P = 70 % (Fig. 3.30 b), which is much higher that the accepted value of 46 % and reinforces the hypothesis of a highly polarized Ni-NiO_x nanoconstriction, due to s electrons trapping and d-band narrowing. This may help to explain the origin of the huge MR values in electrodeposited and FIB milled nickel nanocontacts (see section 6.1).

Apendix: Micromagnetic simulations

Micromagnetic simulations carried with OOMMF by M. Viret based on the SEM of a double nanoconstriction patterned by e-beam with fields applied parallel and perpendicular to the track:

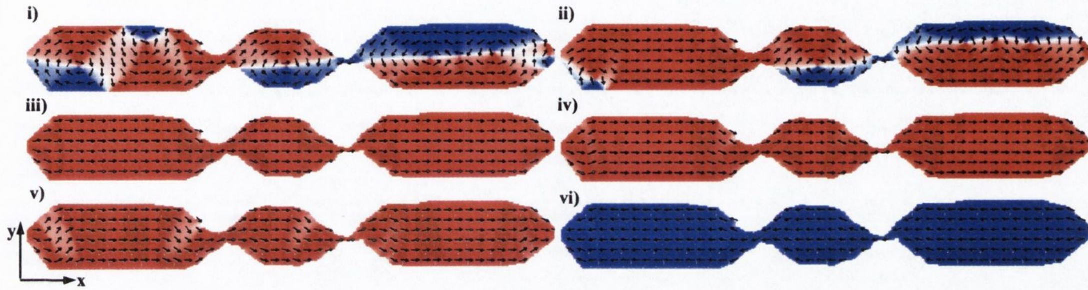

Figure 3.31. For a field applied in the **x** direction: i) initial random state (dif. from previous, but always vortex-like), ii) at +4 mT, iii) +8 mT (saturated), iv) remnant state, v) -4 mT and vi) -8 mT, the sample turns to the opposite direction without forming the vortex state again.

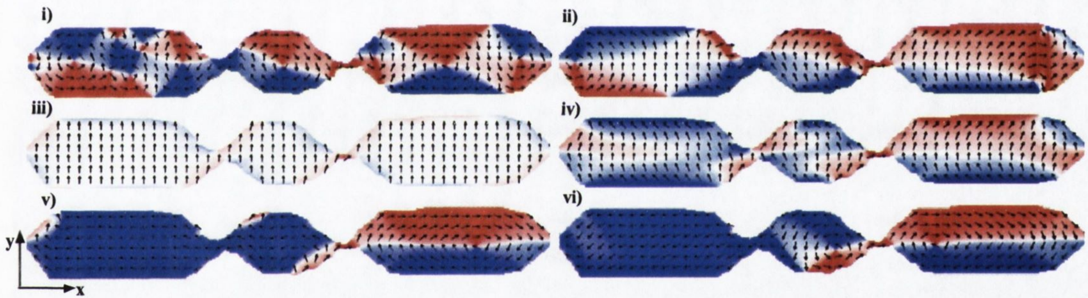

Figure 3.32. For a field applied in the **y** direction: i) Initial random state, ii) at a field of +12 mT, iii) at 100 mT (sample mostly saturated except the narrowest constriction, which magnetization remains in the **x** direction), iv) at +12 mT in the way back to 0, v) remnant state, vi) at -12 mT, the sample's magnetization turns to the $-\mathbf{y}$ sense forming the vortex state.

Bibliography

[1] N. García, M. Muñoz and Y.W. Zhao, Phys. Rev. Lett. 82 (14) 2923 (1999)

[2] H. Wang, H. Cheng and N. Garcia, cond-mat/0207516v1 (2002)

[3] H.D. Chopra and S.Z. Hua, Phys. Rev. B 66 (2) 020403 (2002)

[4] J.J. Versluijs, M.A. Bari and J.M.D. Coey, Phys. Rev. Lett. 87 (2) 026601 (2001)

[5] M. Viret, S. Berger, M. Gabureac et al., Phys. Rev. B 66 (22) 220401 (2002)

[6] D. Kelly, J.E. Wegrowe, T.K. Truong, Phys. Rev. B 68 134425 (2003)

[7] B. Cetin and N. Giordano, Materials Science and Eng. B 84 (1-2) 133 (2001)

[8] C.S. Yang, J. Thiltges, B. Doudin and M. Johnson, J. Phys.-Cond. Mat. 14 (50) L765 (2002)

[9] S.Z. Hua and H.D. Chopra, Phys. Rev. B 67 (6) 060401 (2003)

[10] S.H. Chung, M. Muñoz and N. García, Phys. Rev. Let. 89 (28) 287203 (2002)

[11] C. Rüster, T. Borzenko, C. Gould et al., Phys Rev. Let. 91 (21) 216602 (2003)

[12] P. Bruno, Physical Review letters 83 (12) 2425 (1999)

[13] Y. Labaye, L. Berger and J.M.D. Coey, J. App. Phys. 91 (8) 5341 (2002)

[14] G. Tatara and N. García, IEEET Mag. 36 (5) 2839 (2000)

[15] R. Danneau, P. Warin, J.P. Attane et al., Phys. Rev. Lett. 88 (15) 157201 (2002)

[16] N. Papanikolau, J.Phys.: Cond. Mat. 15 5049 (2003)

[17] N. García, cond-mat/0207323 (2002)

[18] N. García H. Wang, H. Cheng et al., IEET Magn. 39 (5) 2776 (2003).

[19] O. Céspedes, E. Clifford and J.M.D. Coey, to be published in J. App. Phys.

[20] R.A. Buhrman in http://www.nnf.cornell.edu/2003cnfra/2003cnfraPhys.pdf, 244-5

[21] M. Klaui, C.A.F. Vaz, J. Rothman et al., Phys. Rev. Lett. 90 097202 (2003)

[22] M. I. Montero, R. K. Dumas, G. Liu et al., Phys. Rev. B 70, 184418 (2004)

[23] M.R. Sullivan, D.A. Boehm, D.A. Ateya et al., submitted to Phys. Rev. B.

[24] L. Berger, Phys. Rev. B 54 (1996) 9353

[25] J.C. Slonczewski, J.Mag.Mag.Mat. 195 (2) L261 (1999)

[26] C.C. Faulkner, D.A. Allwood, M.D. Cooke, et al., IEEET Magn. 39 2860 (2003)

[27] M. Klaui, C.A.F. Vaz, J.A.C. Bland et al., App. Phys. Lett. 83 105 (2003)

[28] A.F. Morpurgo, C.M. Marcus and D.B. Robinson, App. Phys. Let. 74 (14) 2084 (1999)

[29] O. Céspedes, M.A. Bari, G. Jan et al., J. Mag. Mag. Mat. 242 (Part I) 492 (2002)

[30] G. P. Zhigal'skii, Physics-Uspekhi, 40 (6) 599-622 (1997)

[31] K.S Ralls and R. A. Buhrman, Phys. Rev. B 44, 5800 (1991)

[32] N. García, M. Muñoz and Y.W. Zhao, Phys. Rev. Lett. 82 (14) 2923 (1999)

[33] G.E. Blonder, M. Tinkham and T.M. Klapwijk, Phys Rev. B 25, 4515 (1982)

[34] R.J. Soulen, J.M. Byers, M.S. Osofsky, Science, 282, 85 (1998)

[35] S.K. Upadhyay, A. Palanisami. R. N. Louie and R.A. Buhrman., Phys. Rev. Lett. 81, 3247 (1998)

[36] A.F. Andreev, Sov. Phys. JETP 19, 1228 (1964)

[37] Q.D. Jiang, Y.L. Xie, W.B. Zhang, H. Gu et al., J. Phys.: Cond. Matt. 2, 3567 (1990)

[38] See, for example, http://www.fuw.edu.pl/~dobaczew/hfbtho16w/node5.html

[39] G.J. Strijkers et al., Phys. Rev. B 63, 104501 (2001)

[40] L.N. Cooper. Phys. Rev. Lett. 6, 689 (1961)

Chapter 4

Transport measurements in Fe_3O_4 and $La_{0.7}Sr_{0.3}MnO_3$ nanostructures

We defined in the first chapter the polarization P as the difference in the electron population of a conducting ferromagnet at the Fermi level depending if the electrons are spin up or down. In a half-metal, the spin of all the conduction electrons is either up or down, which gives a spin-polarization for a half metal of 100 %. Fe_3O_4 (magnetite) and $La_{0.7}Sr_{0.3}MnO_3$ (LSMO) are ferromagnets with high spin polarization at room temperature and predicted to be half-metallic at 0 K. This makes of magnetite and LSMO two of the best candidates as sources and analysers of spin-polarized currents for spin-electronic devices. It would also be in these and other half-metals where effects such as ballistic, domain wall and tunnelling magnetoresistance are maximized. This has been proven by measurements in magnetic tunnel junctions fabricated with half-metallic electrodes [1], but almost all the work done in transport in magnetic nanostructures has been carried out in 3d metals, mainly nickel (see previous chapter), and alloys as permalloy [2]. The exception is the work performed in point contacts of ferromagnetic oxides such as Fe_3O_4, LSMO and CrO_2 ([3]-[5]), and the Heusler alloy $Co_2Cr_{0.6}Fe_{0.4}Al$ [6].

These measurements gave promising results and some insight into the underlying mechanisms of electron transport in nanoscaled half-metals. However, since these mechanical nanocontacts degrade in a few minutes, they have no technological applications, and it still

remains unclear if the huge magnetoresistive ratios found sometimes are due to spin-polarized transport trough a domain wall or to a mechanical magnetostrictive effect.

In this chapter transport measurements carried out on Fe_3O_4 and LSMO nanostructures patterned by FIB on thin films 50-150 nm thick are presented. On the one hand, the study of the transport through these structures can give us a better knowledge of the mechanism followed by a highly spin-polarised current to cross very narrow domain walls and the subsequent origin of the huge MR measured in point and electrodeposited nanocontacts. On the other hand, these patterned nanostructures are stable on time and bounded to a substrate, thus eliminating magnetostrictive effects and making feasible their use in technological applications. We could then envisage the possible application of BMR nanocontacts and other nanostructures fabricated from half-metallic thin films, such as the "peanut" [3] device, magnetic sensors, memory elements or magnetic transistors.

We will also see that the transport through nanoconstrictions, nanobridges and nanogaps fabricated by focused ion beam milling in LSMO and magnetite thin films exhibits a behaviour that can be metallic or semiconductor-like with temperature, with ohmic, tunnelling or field-emission behaviour depending of the structure and the applied voltage. Electromigration will play an essential role in the transport properties of our nanostructures, with changes in the transport characteristic and the samples physical structure after high currents are applied (see figure 4.1). We will use these effects to achieve different sample geometries and transport regimes (e.g., from tunnelling to field-emission).

Finally, we will study the effect of a magnetic field in the different transport regimes and structures, with electrical hysteresis and large magnetoresistance values up to 8000 % for magnetite and 100 % for LSMO. Unless it is specified otherwise, all the measurements

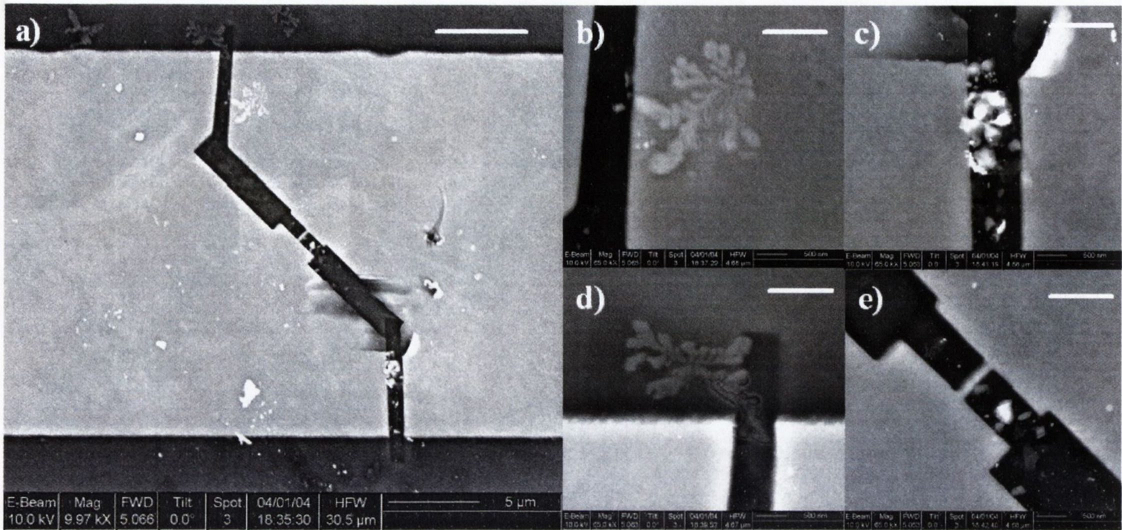

Figure 4.1. Effect of a high current on a magnetite nanobridge. a) Nanobridge and surrounding track (scale bar = 5 μm). b-e) Zooms over different regions of the sample (scale bar = 1 μm). Observe the fractal-like structures in b-d) and the displaced debris in e).

of this chapter were carried out at room temperature.

4.1 Sample fabrication

The Fe_3O_4 films were grown by dc-magnetron sputtering on MgO, Al_2O_3 and $MgAl_2O_4$ substrates by S. Watts in TCD and A. Bollero at the University of Leipzig[1]. For the films grown in TCD we used a pure Fe target in 3x10^{-3} mbar Ar and 4x10^{-5} mbar O_2 atmosphere at a substrate temperature of 673 K on MgO(001) and sapphire substrates in a Leybold Z550-S system with a base pressure of 10^{-7} mbar. The LSMO films were grown by PLD by K. Doerr and colleagues in Dresden[2].

The patterning of the structures was done by direct FIB milling. A FIB can pattern

[1] Department of Superconductivity and Magnetism, under the supervision of M. Ziese.
[2] Leibniz Institute for Solid State and
Materials Research (IFW), Magnetism and Superconductivity Laboratory, Dresden.

nanostructures on these films with a lateral size of around 20 nm, departing from a previously lithographed track a few μm wide. The reason we use direct FIB milling for the patterning is the simplicity and accuracy of the method, which allows the imaging of the nanostructures, and avoids the waste of films by optimising the milling conditions by doing test millings in small areas first. The best lateral resolution we can achieve in the structure will depend of the materials employed and the milling currents (see figure 4.2).

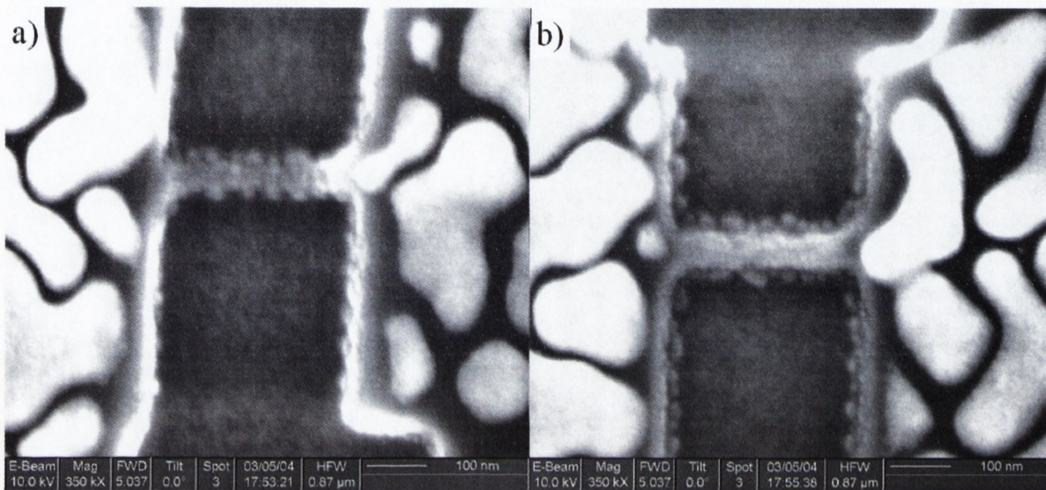

Figure 4.2. Nanobridges patterned on a magnetite film 90 nm thick covered with evaporated gold 60 nm thick. a) Milling at 10 pA during 15 sec. of an area of 6000 nm^2 (equivalent to the milling of a 150 nm thick Si film) and b) Milling at 10 pA during 12 sec. of the same area (equivalent to the milling of a 120 nm thick Si film).

The geometries of the patterned nanostructures used in this work are nanoconstrictions (single and multiple), nanobridges and nanogaps (Fig. SEMs).

Nanoconstrictions and nanobridges were patterned to study the behaviour of the electrons when suffering a sudden change of their spin-environment. As it was stated in the 3rd chapter, a domain wall is expected to form at a ferromagnetic nanoconstriction, dividing the magnetization direction both sides of the constriction. The size of this domain wall is expected to be on the scale of the nanoconstriction, which would imply a change of the mag-

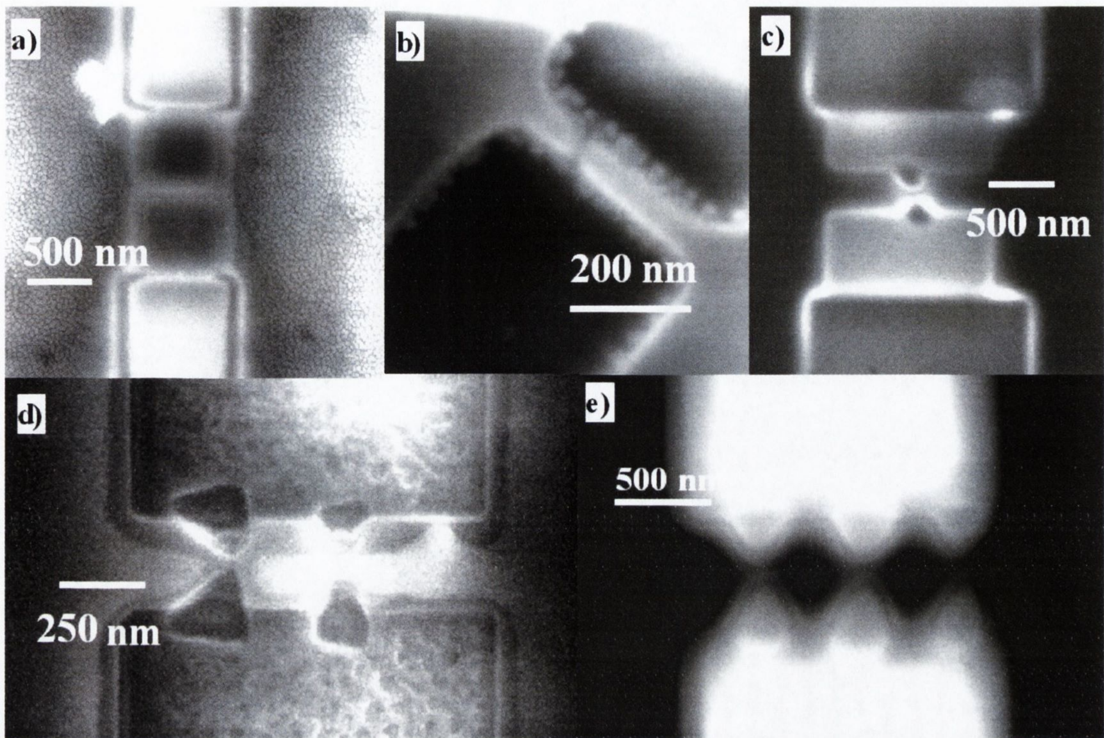

Figure 4.3. SEMs of a LSMO nanobridge a), magnetite nanogap b), LSMO single nanoconstriction c), magnetite double nanoconstriction (with a silver cap layer remaining on top of the areas that are not too narrow) d), LSMO triple nanoconstriction e).

netization across some tens of nm. The expected high polarization in the nanostructures patterned in these materials, and the brusque change in the direction of the magnetization of a thin film could give rise to high magnetoresistive effects. The nanobridges were patterned to compare the transport properties with those of the nanoconstrictions. More particularly, nanobridges were patterned across areas which show high magnetic contrast in the MFM images (see section 4.3), similar to what is seen at magnetite anti-phase boundaries (APBs) where, due to a lattice mismatch, there is a brusque change in the direction of the magnetization of a magnetite thin film. The FIB allows the patterning of a nanobridge across one of these APBs by alternative imaging and positioning of the patterned nanostructure.

It may also be possible to study the spin-dependent tunnelling of the electrons between two half-metallic or ferromagnetic electrodes and across an insulator by patterning a nanogap between two ferromagnetic conducting electrodes. This is equivalent to a magnetic tunnel junction, which is made by depositing a very thin insulator layer between two ferromagnetic or half-metallic films, but in the case of FIB-milling we do it by opening a very narrow gap ($<$ 10 nm) with the Ga^+ beam (which may cause Ga-doping related issues that will be discussed later) or by applying a high electrical current to a narrow nanoconstriction and "blowing" it. Magnetic tunnel junctions have proved to provide high magnetoresistance ratios, especially those made with half-metallic electrodes [1].

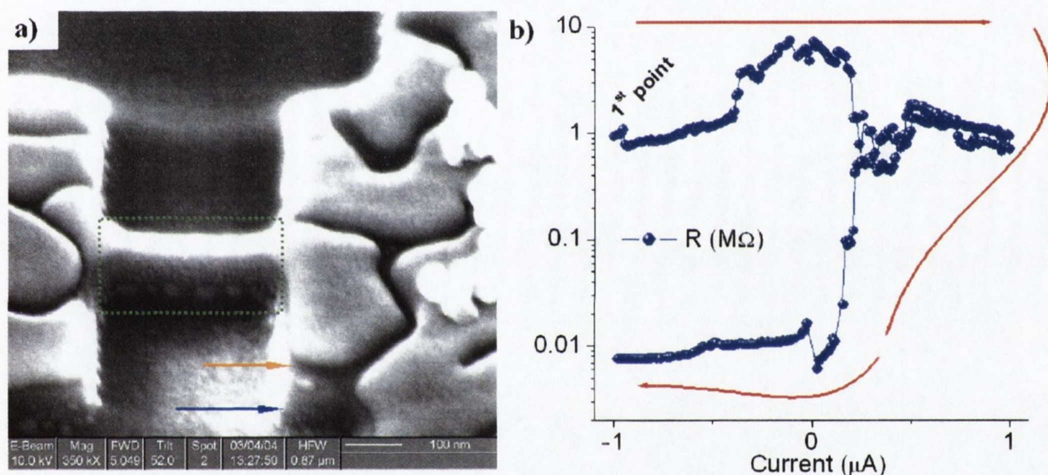

Figure 4.4. Electromigration on a magnetite nanobridge covered with gold. The granular structure of the resulting milled nanostructure favors the instability of the resistance of the sample. a) SEM of the sample, the orange and blue arrows mark the gold-magnetite and magnetite-spinel boundaries respectively. b) R vs. I characteristic. A positive current displaces one (or more) of the grains closing the contact.

It was mentioned at the beginning of the chapter that the transport properties can be affected, or even controlled, by the application of high currents. This is especially true in magnetite nanostructures, where the FIB milling leaves a grainy pattern (Fig. 4.4 a) very suitable for electromigrative effects. These grains which form the nanobridge (see the area

delimited by the green rectangle, figure 4.4), 5 to 20 nm in diameter, can be easily displaced by currents as low as 1 μA, changing drastically the transport properties of the nanostructure (see figure 4.4 b), in a process that allows us the control of the resistance and geometry of the device even after the patterning.

4.2 Electric transport

4.2.1 Electric transport in LSMO and magnetite nanoconstrictions

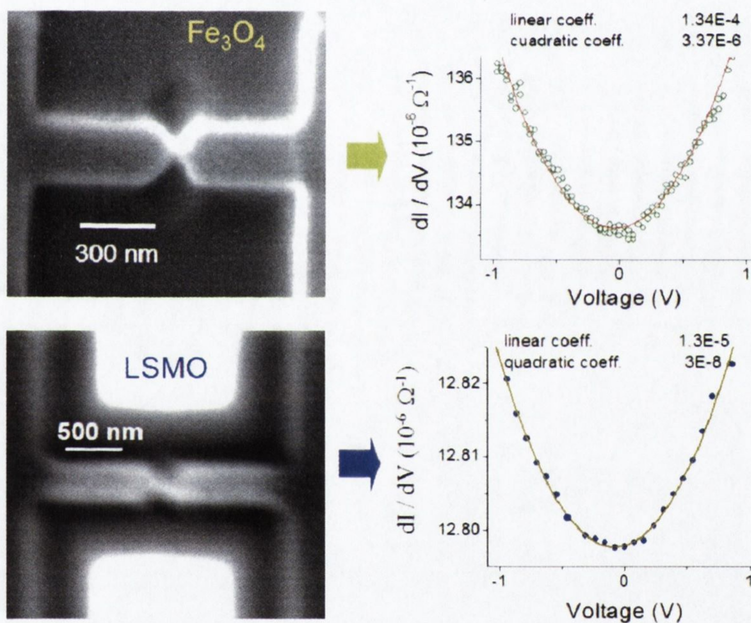

Figure 4.5. Top: SEM of a magnetite nc and its G vs. V characteristic. Bottom: SEM of a LSMO nc and its G vs. V characteristic. Note: the conductance units are chosen such that the inverse would give the resistance of the sample in MΩ (around 10 kΩ for the magnetite nc and 100 kΩ for the LSMO nc).

The I-V characteristic of a current crossing a rectangular tunnel barrier can be expressed in the Simmons formulation as I= β(V+γV^3), where β is the conductance of the

sample and γ the cubic parameter. γ and β can be related to the height and width of a hypothetical square barrier as:

$$L = \log\left(\frac{4.87\times10^{13}}{d\times\beta\gamma^{1/2}}\right) \Bigg\| \begin{array}{l} s\ (\text{barrier width in Å}) = 4.94\cdot\gamma^{1/4}L^{1/2} \\ \phi\ (\text{barrier height in eV}) = 0.266\cdot L/\gamma^{1/2} \end{array} \tag{1}$$

where d is the cross section of the barrier in square meters.

The values for β and γ in nanoconstrictions and nanobridges are: $\beta \sim 10^{-5} - 10^{-4}\ \Omega^{-1}$ for LSMO and magnetite, and γ varies from 10^{-3} to 10^{-2} V^{-2} in magnetite nanoconstrictions and from 0 to 10 V^{-2} for LSMO nanoconstrictions ($\gamma = 0$ for LSMO nanoconstrictions with conductance $G \geq 5\ G_0$). No qualitative difference was found between in the I-V characteristic of single, multiple nanoconstrictions and nanobridges (except those patterned across induced APBs, that will be discussed in the section 4.2.2).

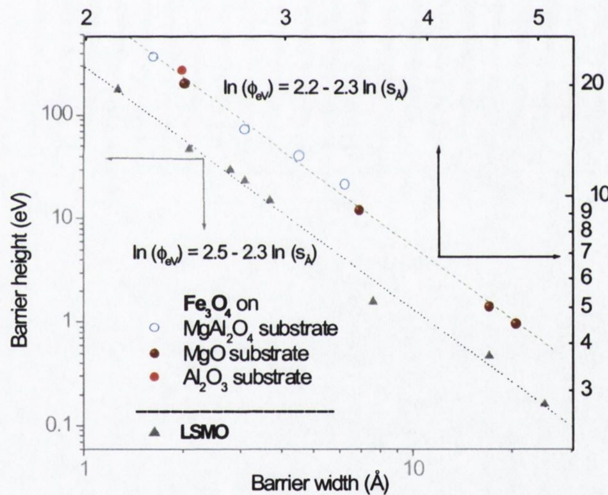

Figure 4.6. Dependence of the deduced barrier height and width from the Simmons fitting for LSMO and magnetite nanoconstrictions with conductance $G \leq G_0$.

The I-V characteristic can then be fitted to the Simmons equations, and the transport expressed in terms of a hypothetical rectangular barrier (1), although this does not imply that we have transport across a rectangular barrier.

We find that the barrier height and width calculated from these equations are related as

$$\ln(\text{height [eV]}) = 2.2 - q \cdot \ln\left(\text{width } \left[\mathring{A}\right]\right) \text{ for magnetite and,} \quad (2)$$

$$\ln(\text{height [eV]}) = 2.5 - q \cdot \ln\left(\text{width } \left[\mathring{A}\right]\right) \text{ for LSMO.} \quad (3)$$

independent of the substrate employed, with $q = 2.3$ for both materials. This description of the I-V characteristic, with a current proportional to $V+\gamma V^3$, is valid for low voltages (< 5V); at higher voltages breakdown mechanisms such as field-emission, heating effects, Towsend avalanche and electromigration are predominant.

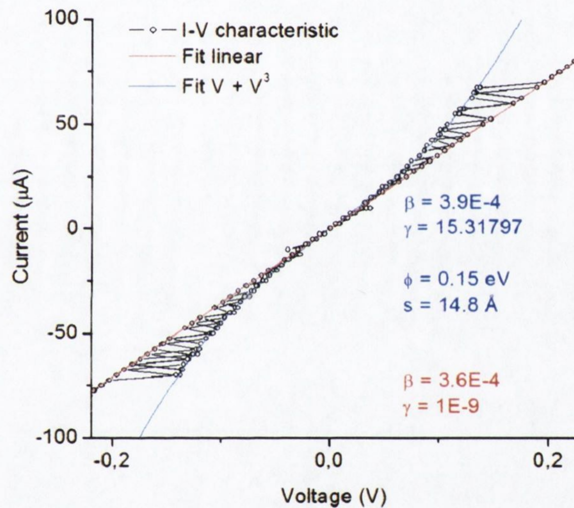

Figure 4.7. The transport across a LSMO nc shows discrete fluctuations between ohmic and tunnelling behaviour. The measurement was carried out by varying the current and measuring the voltage.

For a LSMO nanoconstriction with low resistance we found that the I-V at low voltages fluctuates between a purely Ohmic ($\gamma = 0$) and a tunnelling ($\gamma = 15$) characteristic (Fig. 4.7). Similar fluctuations had already been observed in the conductance of LSMO point contacts, and were attributed to transitions between ballistic and diffusive transport [3]. After the

initial measurements the sample remained in the Ohmic state, with $\gamma = 0$, in which it shows a 1.5 % of MR in a field of 0.4 T at RT (see section 4.3.1).

We found that LSMO nanoconstrictions can have both a metallic-like behavior, where the resistance drops with the temperature down to a certain saturation temperature of 50-100 K, or a semiconductor-like behavior in which the resistance increases when reducing the temperature if the sample has been imaged with the ion beam. The equivalent activation energy for the semiconducting behaviour is ~100 meV down to 200 K and then continues increasing at a different pace that is not exponential with T^{-1}. The activation energy of 100 meV is typical for transport in LSMO films above the Curie temperature, so from the R(T) curve we can deduce the Curie temperature of the nanoconstriction itself, which can vary from the film temperature due to the Ga doping.

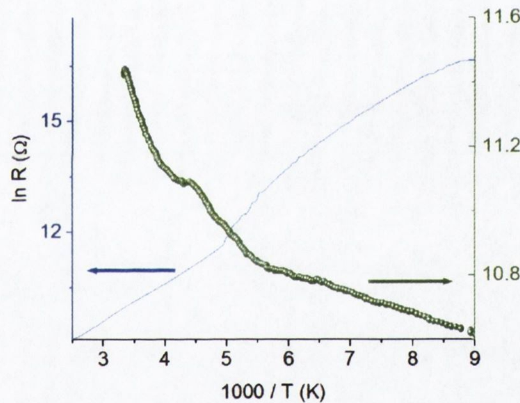

Figure 4.8. R vs. T for two LSMO ncs. In blue (line), an ion-irradiated (by ion-imaging) LSMO nc with a semiconducting-like behaviour. In green (dots), a LSMO nc with metal-like behaviour.

In the next sections we will study the transport characteristics of nanobridges and the field emission regime. We will consider as nanogaps not only the samples with a milled gap between the conducting electrodes, but also those nanocontacts which transport behavior and resistance points to the presence of an insulator layer at the nanoconstriction, i.e., samples

with a resistance above $\sim$ 1M Ω, although most of the milled gaps present resistances in excess of 100 MΩ.

4.2.2 Electric transport in magnetite nanobridges

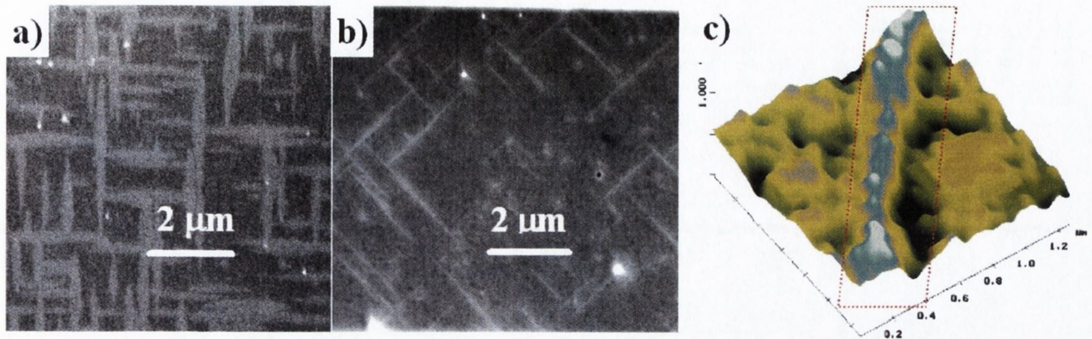

Figure 4.9. SEMs of magnetite thin films 90 nm thick a) after films degrading for > 1 year and b) depositing from a target of magnetite and Fe_2O_3. c) MFM of the vecinity around one of the white lines that appear in a). The image shows a high magnetic contrast across the line (delimited by the red rectangle).

It is possible to enhance the appearance of antiphase boundaries (APBs, boundary with antiferromagnetic coupling between magnetite grains due to a lattice mismatch) in magnetite thin films by the degradation of Fe_3O_4 films 90 nm thick (leaving them 1 year in ambient conditions) or the sputtering from Fe_3O_4+Fe_2O_3 targets[3]. These "enhanced" APBs appear as regions of low conductivity at the SEM, and show big changes of the gradient of the magnetic field as it is mapped across one of them (see figure 4.9).

The transport properties of a nanobridge patterned across one of these enhanced APBs should resemble those of the nanoconstrictions, since in both cases the electrons have to suffer a sudden change in their spin-environment. We find that the resistance of the nanobridges is higher than that of nanoconstrictions (for equal cross sections), but the I-V characteristic has a very similar qualitative behaviour for both geometries, so not to have too high impedances we pattern these nanobridges with 50-100 nm in width, rather than 20-50 nm as was the

[3] Films deposited by A. Bollero and M. Ziese at the University of Leipzig on $MgAl_2O_4$ substrates by sputtering from Fe_3O_4 and Fe_3O_4+Fe_2O_3 targets.

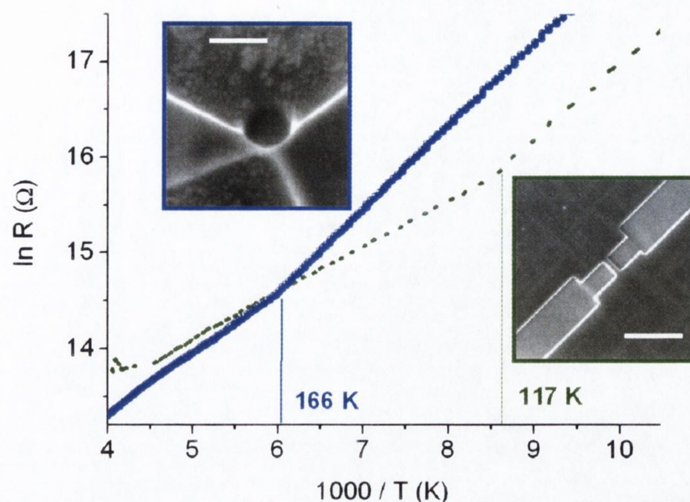

Figure 4.10. R vs. T for a magnetite nanoconstriction (green, dashed) and a nanobridge across a APB (blue, scatter). The nanoconstriction shows an inflexion point of increasing energy gap below 117 K, whereas the nanobridge shows the inflexion point at 166 K. Below ~ 90 K the resistance is too high to be readed by our instruments.

The R(T) characteristic of the nanobridges and nanoconstrictions shows an exponential increase of resistance as we decrease temperature. The increase presents two different slopes: for nanoconstrictions the change of slope occurs at 166 K and for nanobridges across APBs at 117 K. Below those inflexion points the resistance increases faster with decreasing temperature, and below 117 K that increase of resistance with temperature is similar for both geometries.

We mentioned at the end of the section 4.1 that the grainy structure of the FIB-milled nanostructures makes them prone to electromigrative processes. In the case of magnetite nanobridges, we can use electromigration to our advantage and control the movement of grains to create insulating barriers with a deduced width (from eqs. (1)) as narrow as we want (see figure 4.11).

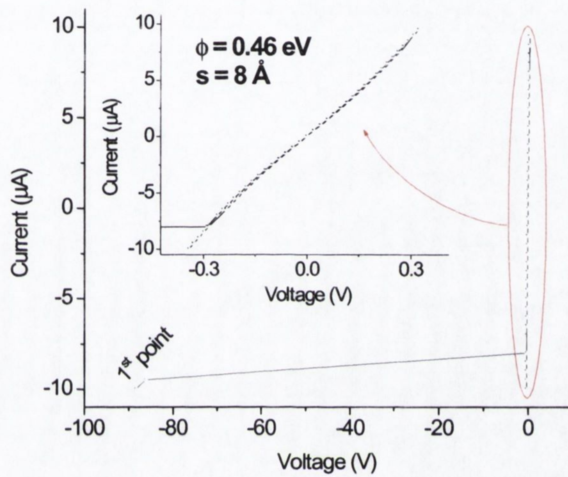

Figure 4.11. I-V characteristic of a magnetite nanoconstriction when a high voltage is applied. Inset: the resulting I-V after applying 100 V can be fitted with the Simmons equations to find a barrier 0.46 eV high and with just 8 Å ($\approx$ lattice parameter of Fe_3O_4) width. The sample in this state shows a 1.7 % MR.

4.2.3 Electric transport in the field emission regime

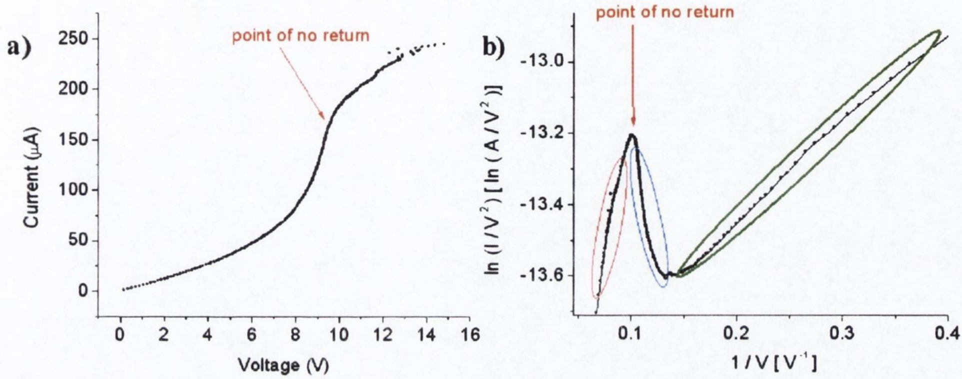

Figure 4.12. a) I-V characteristic of a magnetite nanoconstriction. At around 7 V there is a change in the slope of the curve and above 10.5 V (or 175 μA) the transport characteristic is irreversibly modified. b) Fowler-Nordheim plot of the same data. The green, blue and red circles outline the tunnelling, field-emisison and breakdown respectively.

For magnetite samples with a resistance above 250 kΩ, a different I:V characteristic is found at high voltages ($>$ 5-10 V). Above those voltages, the tunnelling characteristic of equation (1), gives way to a steeper increase of current with voltage. In these devices, where the potential drop above the threshold across the nanozone gives electric fields of order 10^9 V m^{-1} or 1 Vnm^{-1}, the tunnel barrier is distorted to a triangular shape leading to field-emission [7], as explained in the section 1.2.4. The emitted electrons are accelerated across the nanogap, but they do not create a discharge (avalanche breakdown) there because the mean free path of the electrons in air is much longer than the width of the gap. The field-emission region is described by the Fowler-Nordheim equation [7]:

$$I = \left(\frac{aV^2}{w^2}\right) \exp\left(\frac{-b\varphi^{\frac{3}{2}} s}{V}\right), \tag{4}$$

where a and b are material constants, φ is the barrier height (or work function) and s is the gap width. A plot of $\ln\left(\frac{I}{V^2}\right)$ vs. V^{-1} in the field-emission regime has negative slope.

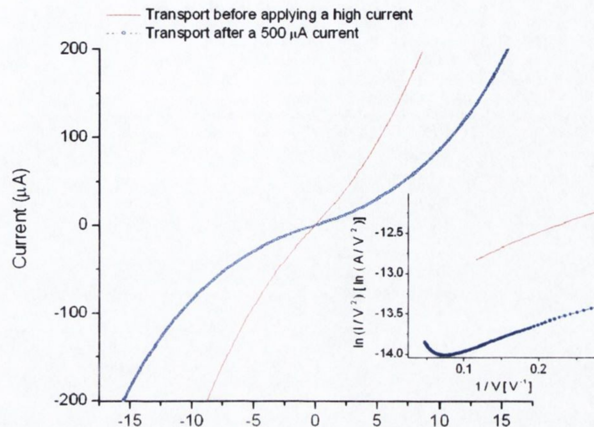

Figure 4.13. Transport characteristic of a magnetite nanoconstriction before and after a 500 μA current is applied. After the high current is applied the Fowler-Nordheim plot (bottom right) shows evidence for field-emission transport (negative slope).

The field-emission regime can be induced by applying a high current ($\geq$ 500 μA) into a low-resistance device. The current may displace material out of the constriction, changing the nanoconstriction into a nanogap, or modify the geometry in the vicinity of the nanostructure. In this way, by applying a high current across a nanoconstriction, we can observe changes in the resistance of the sample and an upturn in the Fowler-Nordheim plot that was not there before (Fig. 4.13). The electromigrative process can also be used to form very narrow gaps from what initially was a conducting nanoconstriction.

The effect of a high current is not only evident in the resistance or the transport characteristic of the sample, but also in the SEM images. After a high current is applied, the sample can be deformed in the vicinity of the nanoconstriction (figure 4.14).

Since the field-emission regime implies the deformation of an insulator energy barrier due to the high voltages applied, we should be able to study this transport regime by the

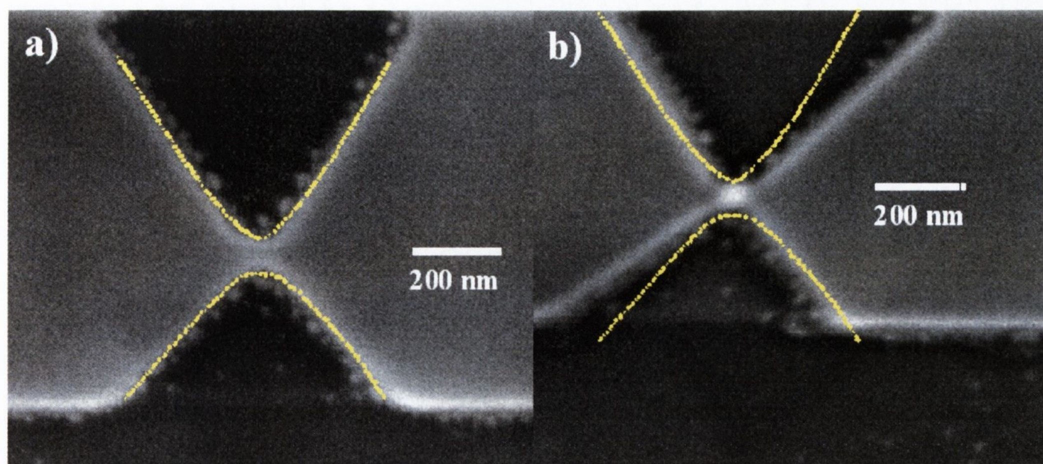

Figure 4.14. SEMs of a magnetite nanoconstriction before (left) and after (right) a 500 μA current being applied. The yellow lines are to indicate the original shape of the constriction.

patterning of FIB-milled nanogaps with a very narrow separation between the electrodes. Samples with a gap of 5-30 nm (see figure 4.15), show a very high resistance above 100 MΩ. These samples do not show any change in the presence of a magnetic field, the transport is dominated by capacitive and heating effects (Fig. 4.16) and no evidence of field-emission transport was found.

However, these samples are a good example of the effect of Ga^+ doping in the transport across our nanostructures. Assuming a gap of 10 nm, with a cross section 50 nm wide by 10 nm thick, and with a typical resistance of about 250 MΩ, would give a resistivity of 5 Ωm^{-1}, to be compared with the values of no more than 10 mΩm^{-1} that we obtain for our films. This means that hypothetical parallel conduction paths formed by Ga doped-substrate will not contribute significatively to the transport.

Since the transport properties of this patterned nanogaps vary with each measurement, it is not possible to extract any useful information from these samples, and we will not discuss this structures any more.

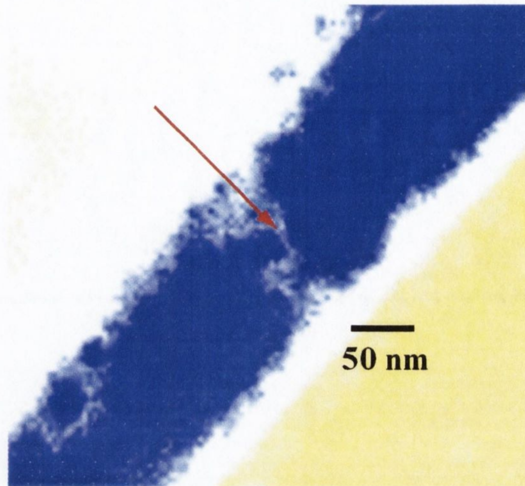

Figure 4.15. SEM of a FIB-milled gap (pointed by the red arrow) between two Fe_3O_4 electrodes (blue).

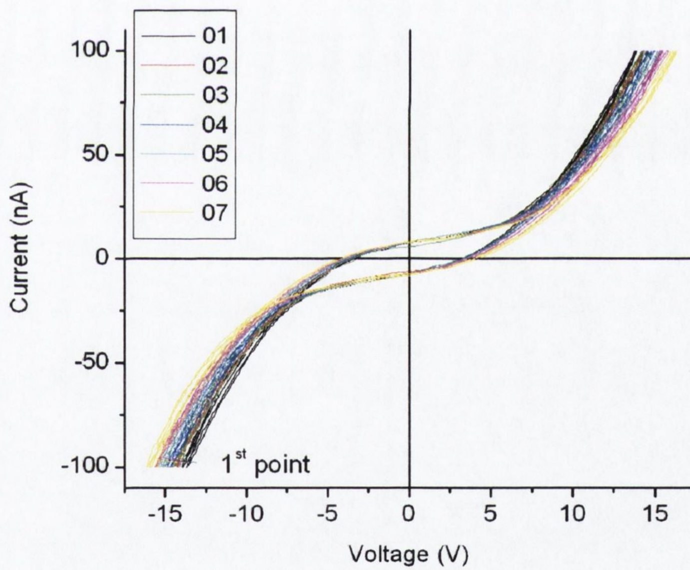

Figure 4.16. Transport characteristic of a FIB-milled nanogap. The resistance if of order 100 MΩ, and there is a capacitive effect evidenced by the hysteresis and non-zero current at zero voltage. Heating effects are also present, as we can see by the increased resistance in each successive measurement.

4.3 Magnetic field effect

In this sections we will see the effects of a magnetic field on the transport across LSMO and magnetite nanostructures, mainly in the resistance ($\sim \beta$) and the cubic (γ) coefficient of the I-V characteristic. The so called "optimistic" and "realistic" magnetoresistance (MR) ratios are defined as:

$$\begin{aligned} \mathrm{MR}_{\mathrm{optimistic}} &= \frac{\rho_{\mathrm{H}} - \rho_0}{\rho_{\mathrm{H}}} \times 100 \\ \mathrm{MR}_{\mathrm{realistic}} &= \frac{\rho_{\mathrm{H}} - \rho_0}{\rho_0} \times 100, \end{aligned}$$

with ρ_0 and ρ_{H} the resistance values before and after a magnetic field being applied.

4.3.1 Magnetic field effect in LSMO and magnetite nanoconstrictions

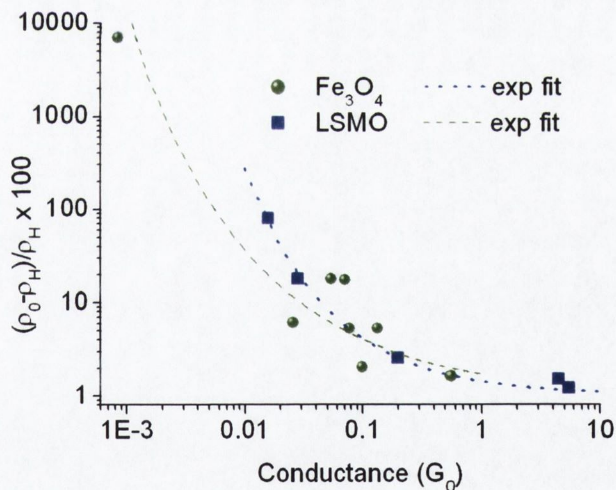

Figure 4.17. Scaling of the "realistic" MR ratios with the conductance (before the field is applied) in units of $G_0 \equiv 12.9\mathrm{k}\Omega$ obtained for LSMO and magnetite nanoconstrictions at a field of 0.4 T at 0 V and room temperature. The dashed line is a fit of the data.

When a magnetic field is applied, most of the samples ($\sim$ 75-80 %) don't present any or a small ($\lesssim$ 3 %) MR. However, a significant number of nanoconstrictions and nanobridges ($\sim$ 15-20 %) show an M R $\geq$ 3% at room temperature and fields of 0.4 T. Only two samples ($\sim$ 5%) show the high MR ratios observed in electrodeposited Ni nanocontacts and half-metallic point contacts of 100 % and more (magnetite with 8000 % and LSMO with 100 %). The magnetoresistance scales with the conductance (MR $\propto$ V^2 see figure 4.17), and tends to zero for values of conductance below 1 G_0. Similar scaling was found in half-metallic point contacts [3],[5]. The relaxation times for the samples to return to their initial resistance vary from hours (for the smaller changes of about 1-5 %) to days (for changes above 10 %). The relaxation times are not changed when heating the sample and once relaxed, the sample may or may not show a magnetic field effect again.

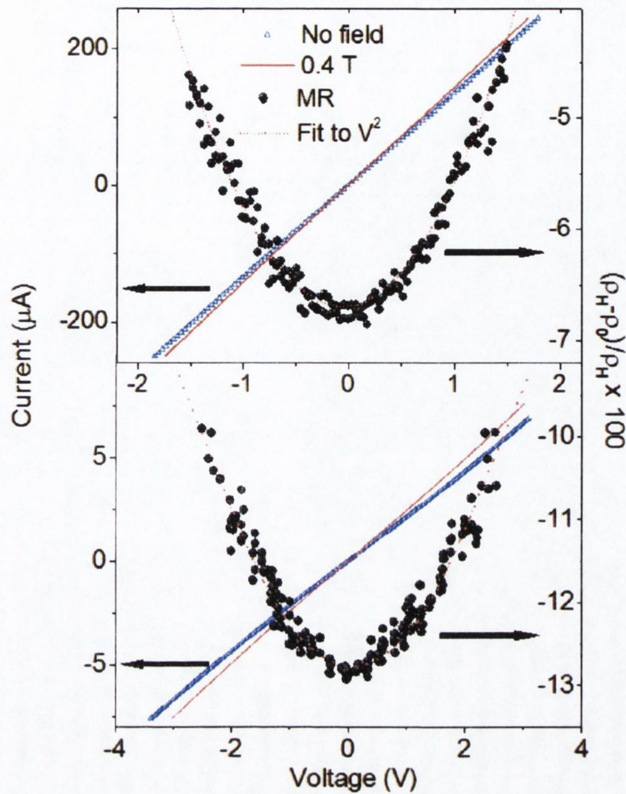

Figure 4.18. Typical I-V and MR characteristic (for samples which do show an effect) of a magnetite (top) and a LSMO (bottom) nanoconstriction. Note the dependence of the MR with V^2.

We can see in the figure 4.18 that the samples which present considerable variations of the resistance do change not only their conductance β, but their cubic dependence on the voltage too. The magnetic field usually (but not always) tends to reduce the value of γ, increasing the linearity of the I-V characteristic, which gives higher MR values for lower voltages. Some of the samples are not saturated at a field of 0.4 T, and we can apply higher fields to study the dependence of the linear (β) and the cubic (γ) coefficients, and the asymmetry of the I-V characteristic with the applied magnetic field.

The variation of the coefficients for the LSMO sample depicted in the figure 4.19

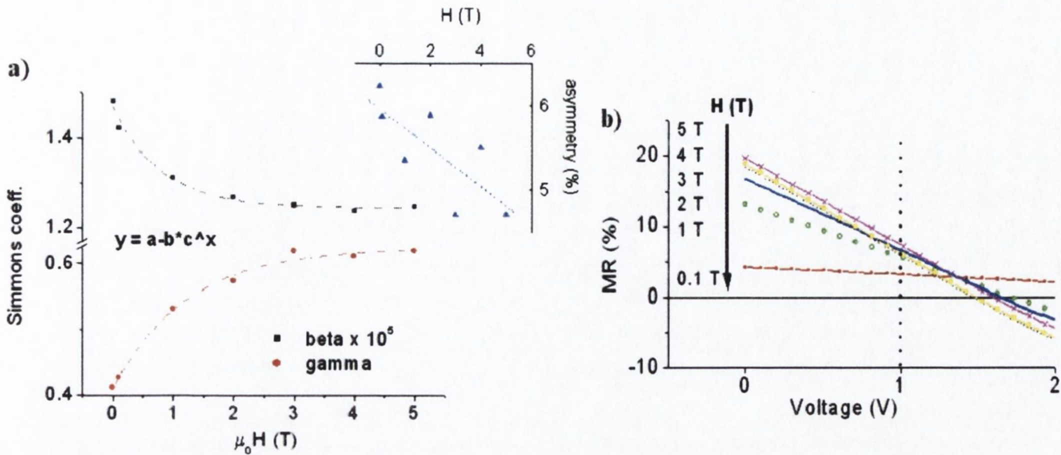

Figure 4.19. a) Variations of the Simmons coefficients β and γ (from $I = \beta\left(V+\gamma V^3\right)$) in a LSMO nanoconstriction. The dotted lines are asymptotic fits. The inset refers to the asymmetry in the resistance for voltages of ± 0.2 V. b) Dependence of the MR values with the applied voltage and the magnetic field, the data for 4 and 5 T overlaps. The MR is predicted to change of sign at $\sim$ 1.5 V, but the data points are taken only up to 1 V (dotted line) to avoid heating effects and electromigration. The sample conductance G vs V at voltages above 0.5 V has not parabolic dependence (sample saturates).

(initial resistance at 0 V of 70 kΩ), gives changes of the conductance (β) that are partially compensated in the slope of the I-V ($\equiv$ the resistance of the sample) by the changes of the γ coefficient, and the resultant MR is highly dependent of the applied voltage (Fig. 4.19 b), and it would change it sign at 1.5 V, but the resistance saturates before that point and our measurements go only up to 1 V to avoid to damage the sample. An increase of the γ coefficient imply by the equations in (1) an increase of the barrier width roughly proportional to $\gamma^{1/2}$ and a decrease of the barrier height proportional to $\gamma^{1/4}$, i.e., the barrier at 5 T would have become a 20 % wider and a 10 % lower. The asymmetry of the I-V characteristic (i.e., the percentual difference between the resistance at a voltage of $+x$V and the resistance at a voltage of $-x$V) is reduced in the presence of a magnetic field (figure 4.19 a), inset).

The changes of resistance displayed in the figures 4.19 and 4.20, even if quite considerable, still fall short of the huge values measured in half-metallic point contacts. However, we

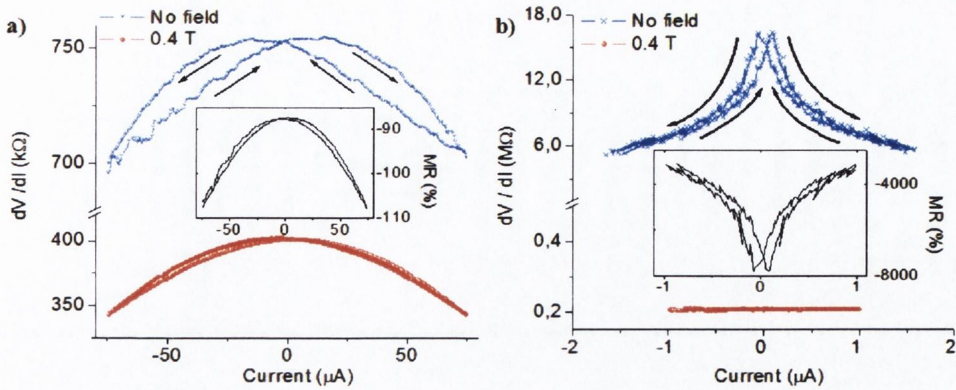

Figure 4.20. a) $\frac{dV}{dI}$ vs. current of a LSMO nanoconstriction before and after a 0.4 T field is applied. b) G vs. current for a magnetite nanoconstriction. Both nanoconstrictions show electrical hysteresis previous the magnetic field being applied, and huge magnetoresistance values. The insets in both graphs show the "optimistic" MR ratios.

have measured similarly high MR values in LSMO and magnetite FIB-milled nanoconstrictions. The interest of these measurements does not rely only on the changes of resistance, though. The samples with the highest MR ratios for LSMO and magnetite, show electrical hysteresis previous the magnetic field being applied. This electrical hysteresis that disappears in the presence of a magnetic field (Fig. 4.20). The non-linearity is also drastically affected by the magnetic field. In the figure 4.20 a) we can observe how the magnetic field has not only multiplied by a factor two the conductivity, but has also greatly increased the γ parameter (as happened with the LSMO sample of figure 4.19) and almost completely eliminated the electrical hysteresis previously present. The changes observed for the magnetite nanoconstriction (Fig. 4.20 b) are even more radical, with a variation of the conductivity of a factor 100 and the disappearance of the curvature of the I-V ($\gamma = 0$) and of the electrical hysteresis.

However, changes of resistance with the magnetic field above 20 % are rare, and as we said at the start of the section, most of the MR values obtained lay in the range of 1 to 10

%. The role that a domain wall may play both in the magnetoresistance and the electrical hysteresis present in these samples will be discussed in the section 6.2.

4.3.2 Magnetic field effect in magnetite nanobridges

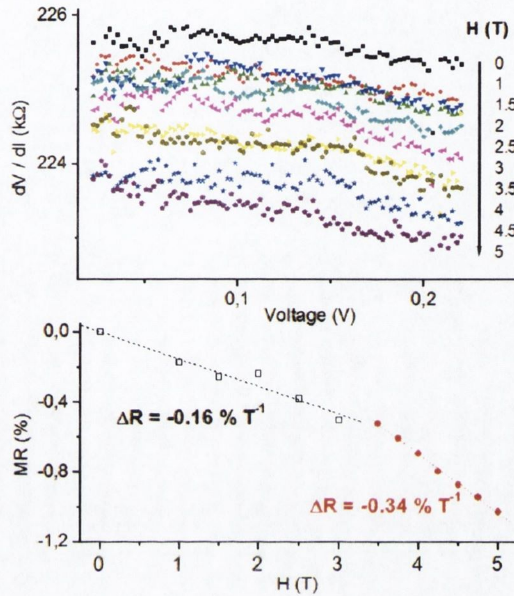

Figure 4.21. MR for a magnetite nanobridge across a APB. Top: variation of the resistance with the voltage and the magnetic field. Bottom MR vs. magnetic field.

In the case of nanobridges across APBs, the variations of the β and γ parameters are still present, but are always of the order of 1%. The magnetic field increases the conductivity (β parameter), with slopes that vary from 0.1 to 0.3 $\%T^{-1}$ depending on the direction and magnitude of the applied magnetic field (see figures 4.21 and 4.22).

The increase of the conductivity is twice as high for configurations where the magnetic field is parallel to the nanobridge (-> perpendicular to the APB) than when the field is perpendicular to the nanobridge (-> parallel to the APB), see the figures 4.22 a & b. We

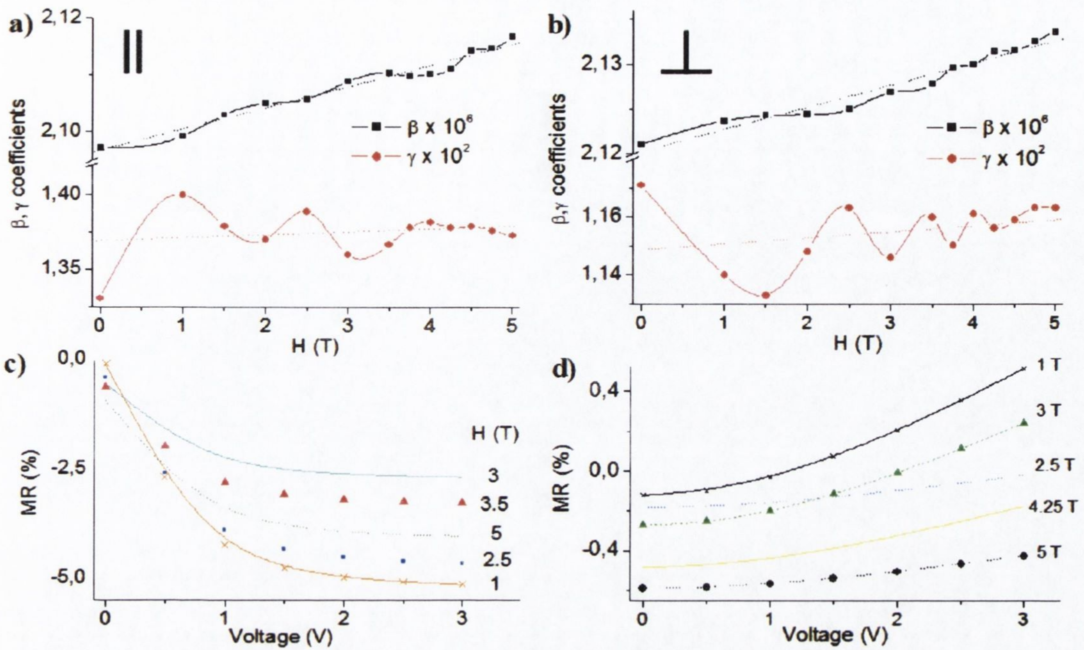

Figure 4.22. Variations of the Simmons coefficients β and γ with the magnetic field for a magnetite nanobridge across a APB for parallel a) and perpendicular to bridge (in-film plane) b) configurations. The continuous lines are a guide to the eye and the dotted lines are linear fits. c) and d) are the resultant MR vs. Voltage and different magnetic fields for the parallel and perpendicular configurations respectively.

can also observe that the γ parameter, even if remains roughly constant, oscillates (damped oscillation) with the magnetic field (figures 4.22 a & b). This reflects a small, negative MR at low voltages (Fig. 4.22 c & d), but the variations of the γ coefficient dominate at high voltages and the size, or even the sign (Fig 4.22 d) of the MR depend on the position of the γ parameter in the oscillation (at a maximum or a minimum) with the magnetic field. However, the oscillations damp at high field, whereas the β coefficient increases continuously (without saturating), so the increase of conductivity dominates at high magnetic fields, giving a negative MR at high field even at high voltages up to 3 V (above those voltages, field-emission and electromigration take over), where the cubic coefficient is more relevant

(Fig. 4.22 d).

If the saturated resistivity of the nanobridges would be similar to that of the nanoconstrictions, that would imply that the magnetic field should reduce the resistance of the nanobridge by a factor 10, what taking into account the slope of about 0.2 $\%T^{-1}$, would mean that we would need a field of 5000 T to eliminate the APB crossed by the nanobridge! The origin of the MR and the oscillations of the Simmons coefficient γ , which we will initially associate to the granular structure of the nanobridge, will be further discussed in the chapter 6.

4.3.3 Magnetic field effect in the field emission regime

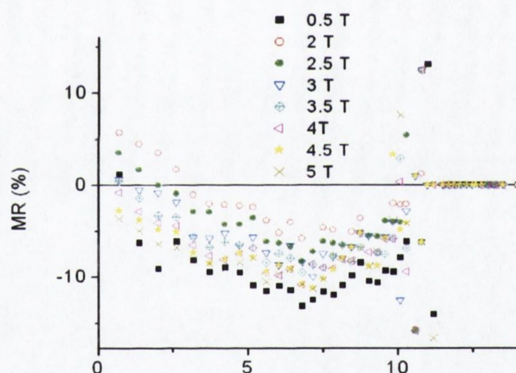

Figure 4.23. MR vs. Voltage at different magnetic fields. For voltages above 11 V the MR is zero at every field. The deduced barrier heigh from the Simmons equations for this sample is 10-15 V (depending on the asumed cross section).

Samples with a transport characteristic in the field emission regime present a I-V that is shifted by the magnetic field, magnetoresistance that is also highly dependent on the applied voltage, vanishing when the voltage reaches the field-emission regime after a region of scattered points near the threshold (Fig. 4.23). We will see in section 6.2 that this

threshold is field dependent. For voltages in the field-emission regime, the slope of the I-V curve does not change with the magnetic field, giving no MR, but there is a shift in the applied voltage (Fig. 4.24 a). This is equivalent to a change of the slope of the Fowler-Nordheim plot (Fig. 4.24 b). For the deduced barrier heights of about 1-10 eV, a change of

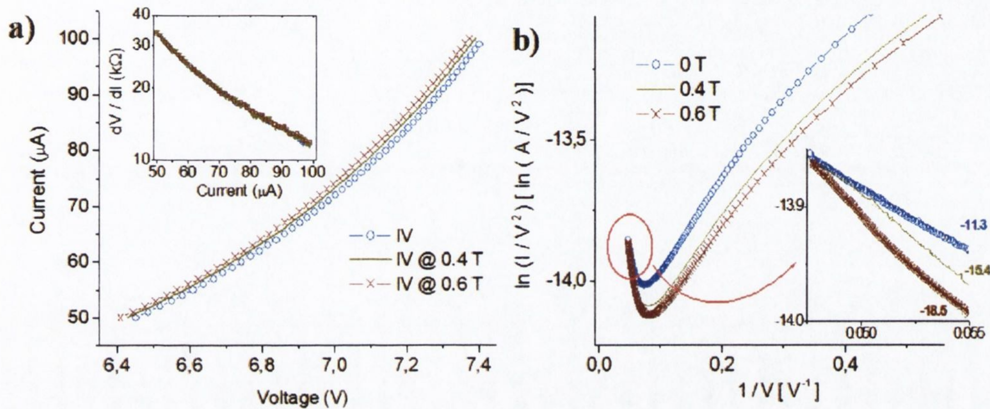

Figure 4.24. a) Magneti field effect on the I-V characteristic of a nanogap in the field-emission regime. Inset: R vs. Current (data points overlap). b) F-N plot for the same data displayed in a). The inset is a zoom at high voltages with the resultant slopes from the linear fit.

the slope in the Fowler-Nordheim plot of 1-10% per Tesla (figures 4.24 and 4.25) implies a change of the barrier height > 100 meVT^{-1}.

We must also remark that these devices, once in voltages that deform the barrier ($\equiv$ field emission), are unstable, and an excessive increase in the current ($\gtrsim 250$ μA usually), can easily destroy them or modify the transport conditions. Also, the gap is not uniform, and is likely that there will be more than one tunnelling point.

The magnetic field effect in the field-emission regime presents a quite different case from the nanoconstrictions or APBs. Here we have an insulator (or low-conductivity layer) between the two ferromagnetic electrodes. The magnetic field effects can then be explained in terms of the relative alignment of the magnetization of the electrodes and the Lorentz

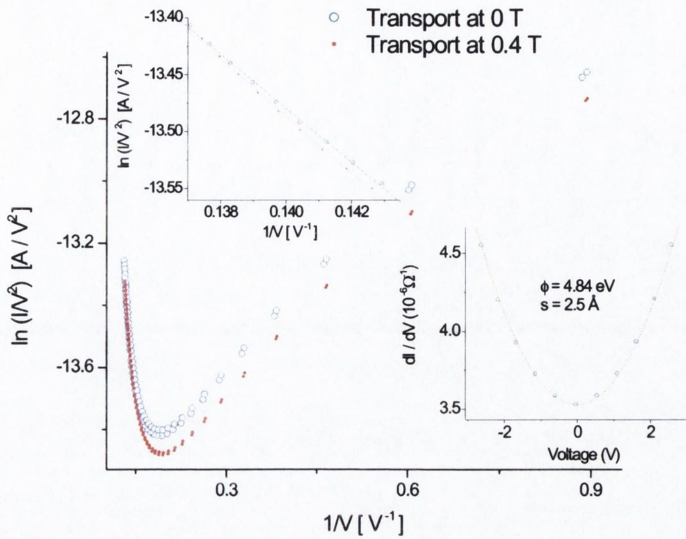

Figure 4.25. Fowler-Nordheim plot (see text) of the transport across a nanogap between two magnetite electrodes before and after a magnetic field of 0.4 T being applied. Top inset: Zoom at high voltages of the F-N plot. Right inset: Conductance vs. Voltage plot with and without a magnetic field (data points overlap). The line is a fit to a parabolic dependence.

the transport mechanism is also tunnelling, but the changes in the barrier width and height with voltage and, more importantly, with the magnetic field, changing the barrier height up to 100 meVT^{-1}, may predominate over other effects (as the cyclotron effect, which would produce a linear increase of the resistance with the field, or classical TMR effects dependent on the density of states of spin up and down electrons both sides of the junction).

To explain such changes in terms of the Zeeman splitting [8],[9] we would need to assume g factors of order 1000, and the most likely explanation is that the height of the barrier, associated with the misalignment of the magnetic moments both sides of the gap, is reduced with the magnetic field in a quantity equivalent or similar to the variations of the exchange energy between both domains (which can easily be in the range of 100 meVT^{-1}). The discussion will be fulfilled in section 6.2.

Bibliography

[1] J.M. De Teresa, A. Barthelemy, A. Fert, J.P. Contour et al., Science 286, 507 (1999)

[2] M. Klaui et al.,Phys. Rev. Lett. 90, 097202 (2003)

[3] J.J. Versluijs, M.A. Bari and J.M.D. Coey, Phys. Rev. Lett. 87, 026601 (2001)

[4] J.M.D. Coey, J.J. Versluijs and M. Venkatesan, J. Magn. Magn. Mat. 226, 688 (2001)

[5] S.H. Chung, M. Muñoz, N. García, W.F. Egelhoff et al., J. App. Phys. 93, 7939 (2003)

[6] E. Clifford, M. Venkatesan, R. Gunning and J.M.D. Coey, Sol. State Com. 131, 61 (2004)

[7] R H Fowler and L Nordheim, Proc. Roy Soc A **119**, 173 (1928)

[8] L. Esaki, P.J. Stiles and S. von Molnar, Phys. Rev. Lett. 19, 852 (1967)

[9] T. Siegrist, S. von Molnar and F. Holtzberg, Appl. Phys. Lett. 47, 1087 (1985)

Chapter 5

Contact induced magnetism in carbon nanotubes

It was discussed in the first chapter the possibility of creating a spin current dissociated from the charge, and we gave a brief explanation of the experiment proposed by Pareek [1] to achieve such a pure spin current. It was also suggested an experiment where this spin current could be detected by the use of ferromagnetic double nanoconstrictions that would trap a domain wall. In the previous two chapters the transport properties of such ferromagnetic nanostructures were shown. It is easy to see from those results that, even if the nanostructures present very interesting properties, it is difficult to fabricate a double nanoconstriction with the size, magnetic and transport qualities that allow for a reproducible switching.

Another way to create spin currents suggested in the first chapter was the use of molecules in contact with ferromagnetic materials, in particular, carbon nanotubes (CNTs) in contact with ferromagnetic thin films.

On the other hand, there are recurrent reports that graphite [2] and other forms of carbon [3]-[5] can exhibit a weak ferromagnetic moment, which persists well above room temperature. An explanation in terms of bond defects or impurities is usually proposed [4]-[6]. Studies of magnetic carbon report moments per unit mass ranging from $\sigma = 10^{-3}$ up to 20 $\mathrm{Am^2kg^{-1}}$,[5] values that are put in perspective by comparing with the 465 $\mathrm{Am^2kg^{-1}}$ that is equivalent to a graphite moment of 1 Bohr magneton per carbon atom. The graphite mag-

netization corresponding to 1 μ_B/C is M = 1020 kAm^{-1}. The weakness and variability of these moments, together with the question of whether samples are ever completely pure, clouds the significance of the measurements. The magnetization distribution may be inhomogeneous [4],[6], and can sometimes be related to specific defects [6]. Common magnetic impurities such as iron (σ = 220 Am^{2}kg^{-1}) and magnetite (σ = 80 Am^{2}kg^{-1}) may play a role [1].

A recent examination of samples of a graphite nodule from the Canyon Diablo meteorite [7] concluded that there was a residual magnetization corresponding to a moment m $\approx$ 0.05 μ_B/C, which was unexplained by the magnetic phases present in the nodule. It was suggested that the ferromagnetism was due to a magnetic proximity effect induced at the interfaces of graphite with nanoscale magnetite or kamacite ($Fe_{93}Ni_7$) inclusions. The experiment presented in this chapter was designed to look for experimental evidence of contact-induced magnetism, and gain some understanding of its origin and possible applications.

The idea we examine in this chapter is to place a multi-walled carbon nanotube (MWCNT) in contact with a ferromagnet and measure the spin transfer associated with the alignment of their chemical potentials. The problem of detecting the tiny spin transfer against the huge background magnetic moment of the ferromagnet was resolved by taking a smooth ferromagnetic thin film as a substrate and looking for a stray field around the nanotube. Uniformly magnetized thin films create no stray field, whatever their direction of magnetization. Therefore any observed stray field must arise from the tube. Cobalt and magnetite were chosen as magnetic substrates, Co because it forms a rather strong chemical bond involving Co $3d_z^2$ and graphite p_z electrons (see the Appendix), and Fe_3O_4 because it

[1] cgs conversion: magnetic moment per unit mass σ: 1 Am^{2}kg^{-1} = 1 emu·g^{-1}; magnetic moment per unit volume M: 1 kAm^{-1} = 1 emu·cm^{-3}(4π M); magnetic field H: 1 kAm^{-1} = 12.6 Oe.

is a half-metal with a high magnetic ordering temperature (860 K), where the spin transfer should be equal to the charge transfer. Si and Cu substrates are used for control purposes.

5.1 Atomic force imaging of MWCNTs: artefacts and other issues

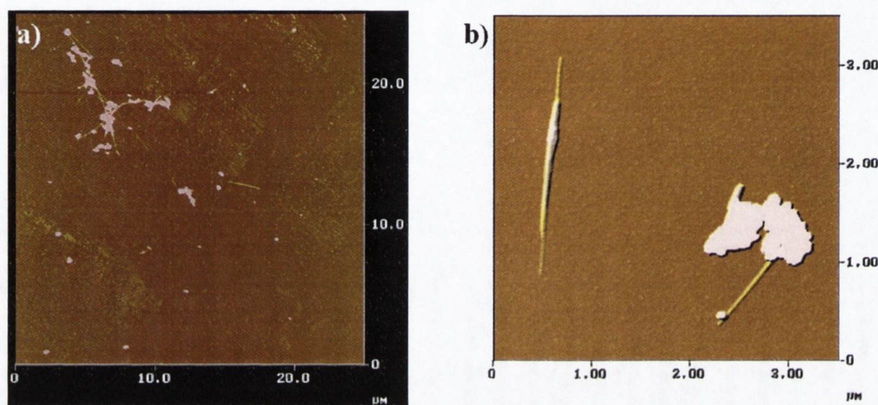

Figure 5.1. a) Typical AFM image of nanotubes spread on a thin film. b) Two MWCNTs, one of them attached to a carbon blob.

Since most of the results presented in this chapter are magnetic force microscope images (MFMs) of carbon nanotubes, there are several issues that must be taken into account when analysing the results. MFM may be the only tool able to detect and distinguish (from the substrate signal) the stray magnetic field coming from a nanotube due to the electron transfer from a ferromagnetic substrate, however, partly because of that sensitivity, MFM images are prompt to generate features which may be mistaken with real magnetic contrast. This is specially true when imaging loose, relatively rough objects (compared with a smooth thin film substrate) as carbon nanotube laid on thin films are (see figure 5.1), and we will need to discern artefacts from the real signal for a proper analysis. Artefacts will account

for about 30 % of all the images obtained during this work.

The tubes were placed on the different substrates, and topographic and magnetic images were recorded by atomic and magnetic force microscopy at room temperature using a 'Nanoscope III' instrument. The magnetic information was obtained in the lift mode with permalloy or Co-Cr coated tips (which have a permanent magnetic moment), using amplitude or phase detection. Unless it is specified otherwise, the pictures will come in groups of two: the topography (AFM) will be on the left and the magnetic signal (MFM) on the right.

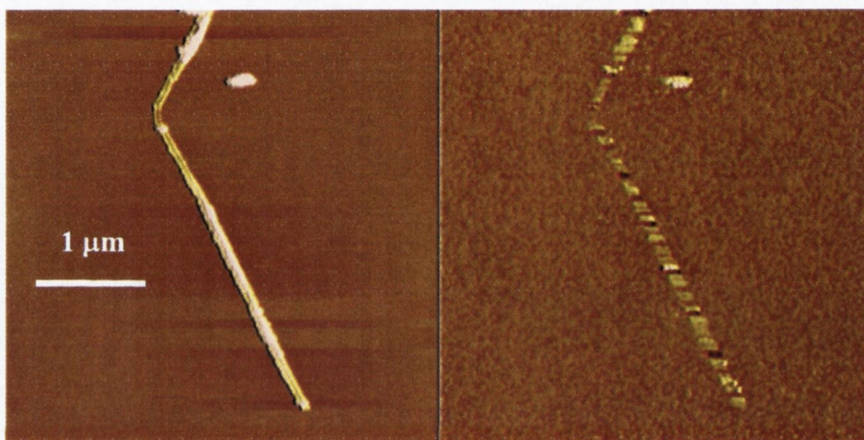

Figure 5.2. One of the most common artefacts is the "striped pattern". The scales are 100 nm (AFM, left) and 0.7° (MFM, right).

One of the most common artefacts is what will be called in this work the "striped pattern". In this artefact, an elongated feature (i.e., the nanotube) appears with narrow regions (~ ´domains´) of different magnetic gradients, always with the magnetic contrast perpendicular to the scan direction. If the tip is made of a material with a high magnetic moment, and our sample is easy to magnetize, the tip may be able to change the magnetic moment of the sample to point it parallel with that of the tip itself, generating a magnetic image with along-scan magnetic domain. However, for this effect (which would prove the

sample to be magnetic) to explain a multidomain pattern as the one seen in figure 5.2, it would be necessary that the tip would be able in some regions to change the magnetic moment of the tube and in some other regions not.

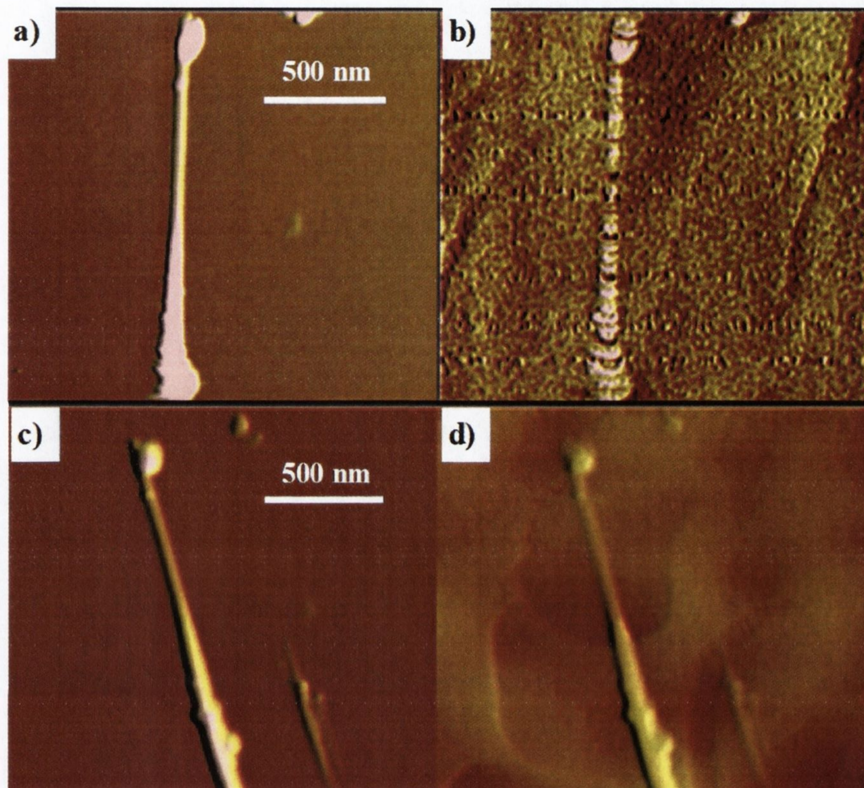

Figure 5.3. a) and b) show the AFM/MFM of a nanotube attached to a carbon blob (out of the picture, too rough to be imaged). The scan is made with a big amplitude-lift height ratio, and the tip is continuously hitting the tube, creating the striped pattern in the MFM and altering the position of the tube, both of which can be observed in its original state with heigher lift heights on c) and d). The MFM on d) shows the most common, almost omnipresent, artefact, a "ghost" or reproduction of the topography observed in the AFM. See the text for its origin and how to avoid it.

During the experiments, we have not found a way not to produce, or to eliminate, this artefact, which may be due to changes in the electrostatic interaction between tip and sample, or in the humidity/temperature conditions (and therefore changes in the tip adhesion). The problem may then be solved by increasing the lift height maintaining the tip amplitude

constant, but that implies a lost of sensitivity which we cannot afford when imaging the nanotubes. However, the artefact is easy to be recognized, since it is dependent of the scan direction, not reproducible, and presents numerous domains along the nanotube in the scan direction. We will therefore consider as a bad image, and not as a result, any image with nanotubes with magnetic contrast only in the direction perpendicular to the scan.

The "stripped pattern" can indeed be sometimes be the result of a big scan amplitude or a small lift height. When using a too big amplitude, the tip is hitting hardly the surface of the nanotube, leading not only to artefacts such as the striped pattern, but also to changes on the position of the nanotube. If the nanotube is anchored (because is linked to a big carbon blob, for example), it cannot be displaced, but can be deformed (see Fig. 5.3 a and c), and the magnetic image is meaningless. By reducing the scan amplitude, the nanotube topography can be scanned normally and the real magnetic image appears. However, another artefact, that will from now on be called the ´ghost image´, appears. This artefact is a reproduction of the topography of the sample (nanotube and substrate) on the magnetic image (see Fig. 5.3 c and d), and its due to the adhesion of the tip to the surface of the sample. This artefact does not present contrast, it only appears as a superposition of the topography on the magnetic contrast, and can be eliminated by substracting the topographic image from the magnetic image (what can be easily done with the nanoscope software), or by using high scan amplitudes combined with high lift heights.

It may be useful to remember that to take an AFM image, two scans are made. During the first scan the tip supposed to oscillate at a certain height (amplitude setpoint) and amplitude, hitting gently (henceforth tapping) the sample and recording its topographic features (surface), while during the second (lift) scan the tip should move at a constant

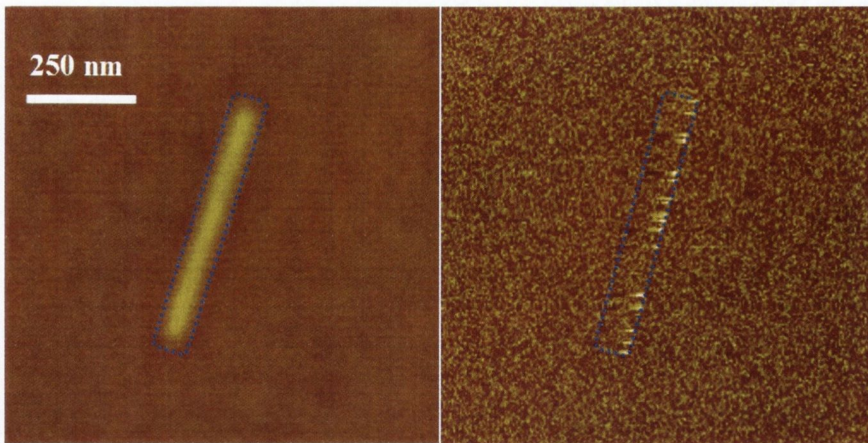

Figure 5.4. When the lift height is small compared with the scan amplitude, or too small to follow the topography of the saple without touching it (lift heights $\lesssim 10 \times R_{ms}$ of the sample), the tip may hit the surface on those places where the topography is rough, i.e., when it encounters a CNT, producing bright spikes. The MFM scan (right) is made from right to left.

height (lift height) above of the sample without ever touching it, and interacting only via magnetic forces.

When the scan amplitude is correct and the tip does not hit the tube too hard during the topography scan, not altering its position nor deforming it, but the lift height is small compared with the scan amplitude during the lift scan, a new artefact appears. In this artefact, the tip hits the higher features of the sample (i.e., the top of the nanotube), giving rise to bright spikes on the magnetic image (Fig. 5.4). This artefact is easily recognisable, and can be solved just by increasing the lift height or by reducing the scan amplitude during the lift scan.

Finally, the most misleading artefact, especially if we lack any magnetic information concerning the sample (for example, an initial idea of what the magnetic contrast of the substrate should be), is the generated by changes in the feedback loop (-> electronic gains in the different amplifiers of the atomic microscope). These changes can generate small signals

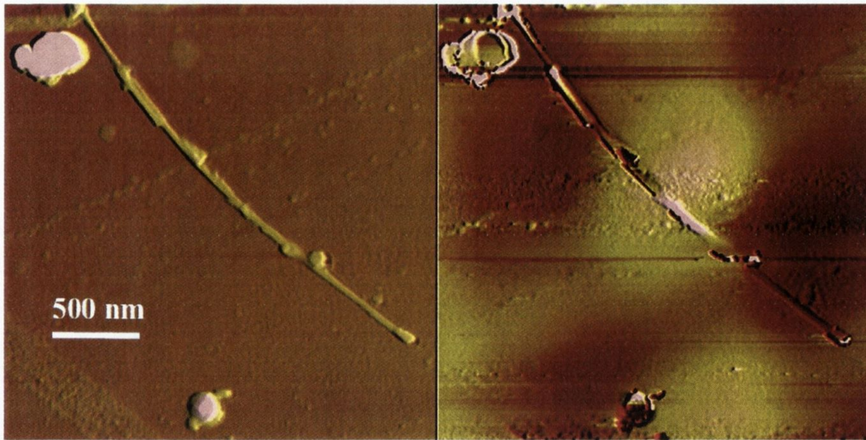

Figure 5.5. The MFM signal can be sometimes completely misleading. The image corresponds to a AFM/MFM image of a MWCNT on a copper substrate. Not only the nanotube, but the Cu substrate also shows magnetic contrast (see the text).

with no intrinsic origin whatsoever that may look quite like a magnetic image. A perfect example is the image of a nanotube on a copper substrate depicted on figure 5.5. This artefact appears mainly in the amplitude mode, it is not reproducible, its magnitude independent of any scan parameter, and it has been observed only on non-magnetic substrates, where the intrinsic signal is null.

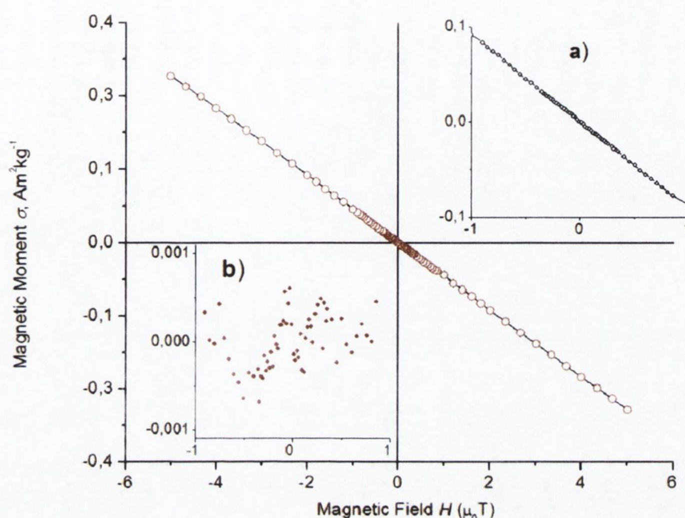

Figure 5.6. Susceptibility of the multiwalled carbon nanotubes measured at room temperature using a SQUID magnetometer. Inset b) shows the magnetic moment per unit mass once the diamagnetic contribution is substracted. Transition metal impurities measured by inductively-coupled plasma (ICP) are below the detection limit of 1 ppm. Any ferromagnetic moment of the tubes is less than 5 10-4 A m2 kg-1, corresponding to a magnetization M < 0.001 kA m-1.

The nanotubes are ropes composed of several multiwalled strands, obtained by arc-discharge [8]; they were chosen for ease of imaging and freedom from ferromagnetic impurities. The diamagnetic susceptibility is $\varkappa$ = -8 x 10^{-8} m^3kg^{-1} (Fig. 5.6). Any ferromagnetic moment of the tubes is less than 5x10^{-3} A m^2 kg^{-1}, corresponding to a magnetization $M <$ 0.009 kA m^{-1}.

Measurements of transition metal impurities in the nanotubes by the inductive coupled plasma method (ICP) give levels below the detection limit of 1 ppm. Other types of nanotubes are unsuitable because they are prepared using a catalyst of iron or cobalt, which contaminates the carbon.

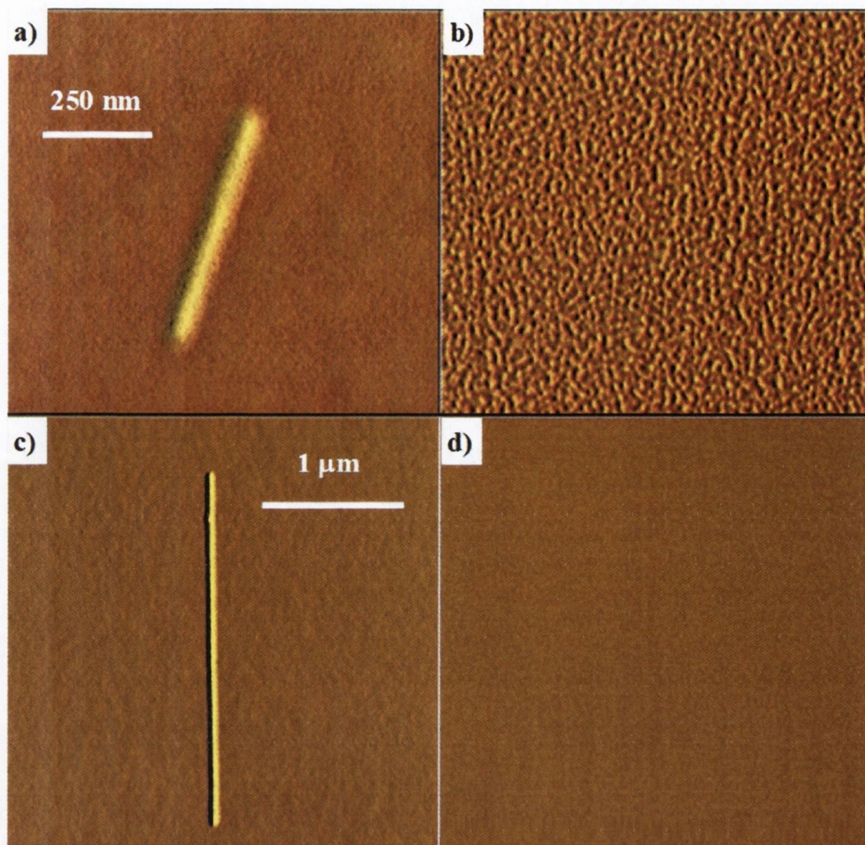

Figure 5.7. AFM of carbon nanotubes on copper a) and silicon c) and their corresponding MFMs on b) and d) respectively. The MFM images do not show magnetic contrast. The colour contrast of the pictures has been enhanced to allow for a better analysis.

A typical AFM image of tubes laid on non-magnetic silicon and a copper substrates is shown in Figs. 5.7 a) and c); the corresponding MFM images in Figs. 5.7 b) and d) are featureless; the tube is nonmagnetic and produces no stray field. Similar null results are obtained in all non-magnetic substrates, discarding artefacts.

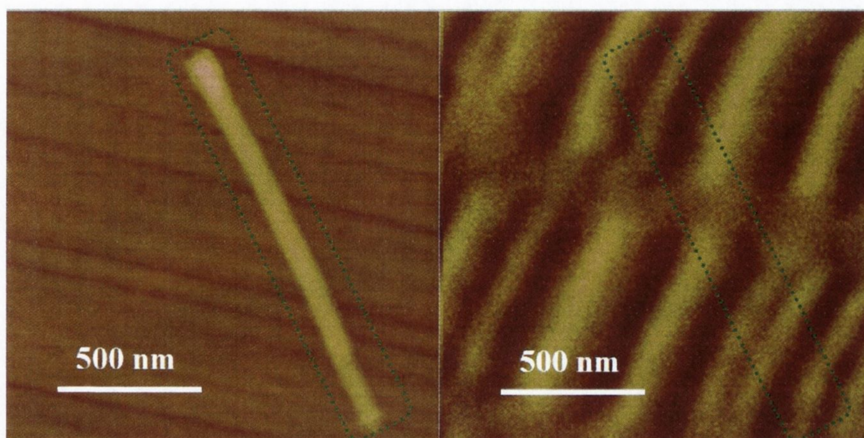

Figure 5.8. AFM/MFM of a carbon nanotube laid on a 20 Gb hard disk.

Furthermore, images of nanotubes laid on magnetic substrates covered with an insulator layer (i.e., hard disks) did not show any magnetic contrast either (see figure 5.8).

The images on cobalt or magnetite substrates are quite different. The topographic image on a sputtered cobalt film 60 nm thick with a mean surface roughness of 0.35 nm is similar to the previous ones but now there is magnetic contrast (Fig. 5.9).

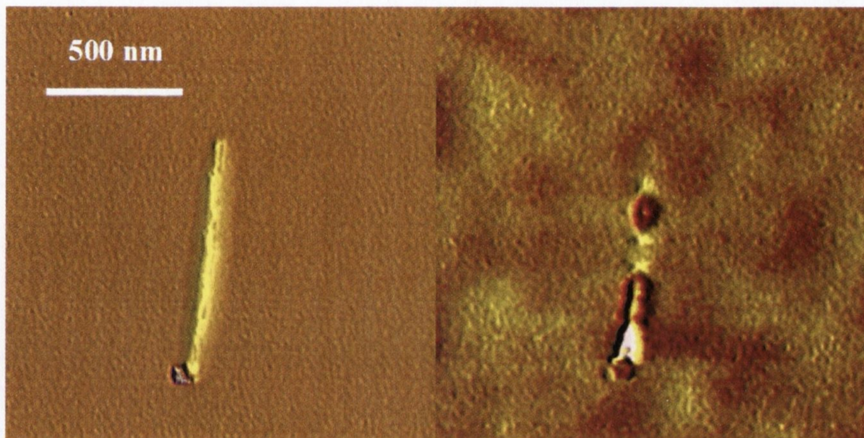

Figure 5.9. AFM (left) and MFM (right) of a carbon nanotube laid on a cobalt substrate. The MFM this time shows magnetic contrast, not only on the ferromagnetic substrate, but on the nanotube itselft too. The colour contrast of the pictures has been enhanced to allow for a better analysis. We must remark that the samples have been briefly exposed to air, and an oxide layer between the nanotube and the substrate of $\sim$1 nm may probably have formed, but it may be broken in the binding of the tube.

Approximately 15 % of all tubes placed on magnetic substrates exhibited contrast in their magnetic images. The stray field from the nanotube is usually unrelated to any stray field arising from the substrate, but it can be sometimes difficult to distinguish from the substrate signal (Fig. 5.10), and the gradient is usually bigger at the edge of the nanotube.

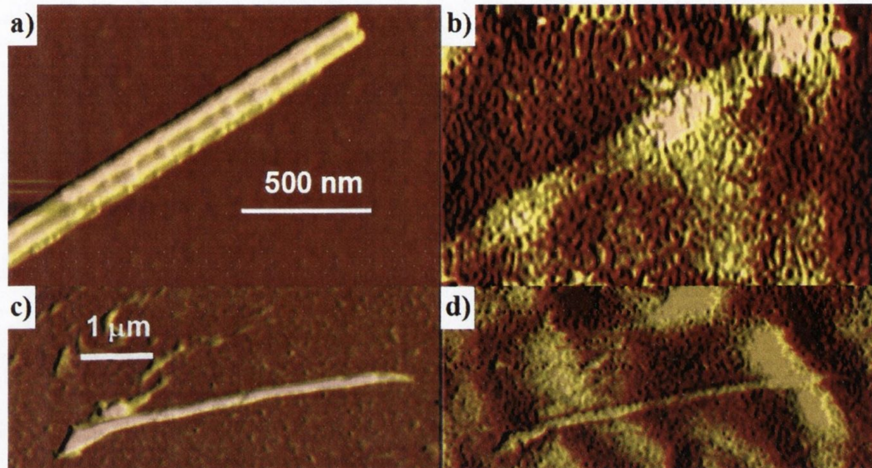

Figure 5.10. a) and c) AFM, b) and d) MFM of two MWCNTs on a cobalt film. The magnetic contrast seems to be higher at the tips of the nanotubes, although it is difficult to differenciate it from the substrate contrast, especially on d). The colour contrast of the pictures has been enhanced to allow for a better analysis.

Most of the times the MFMs of MWCNTs on magnetic substrates show the contrast along the tube axis, but in some occasions it is possible to observe magnetic contrast along the axis perpendicular to the tube (see figure 5.11).

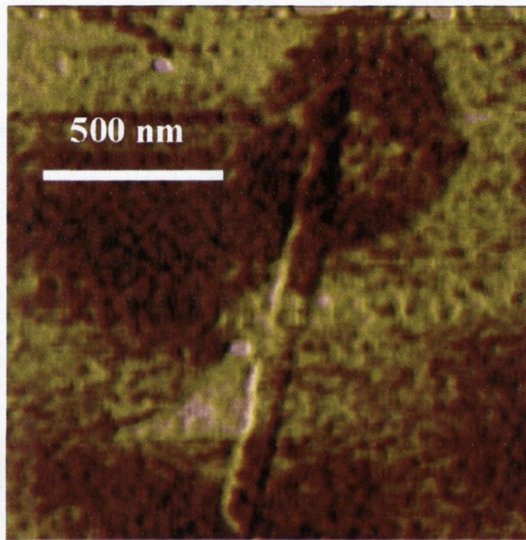

Figure 5.11. MFM of a tube laid on a magnetite substrate which shows magnetic contrast on the edges of the tube.

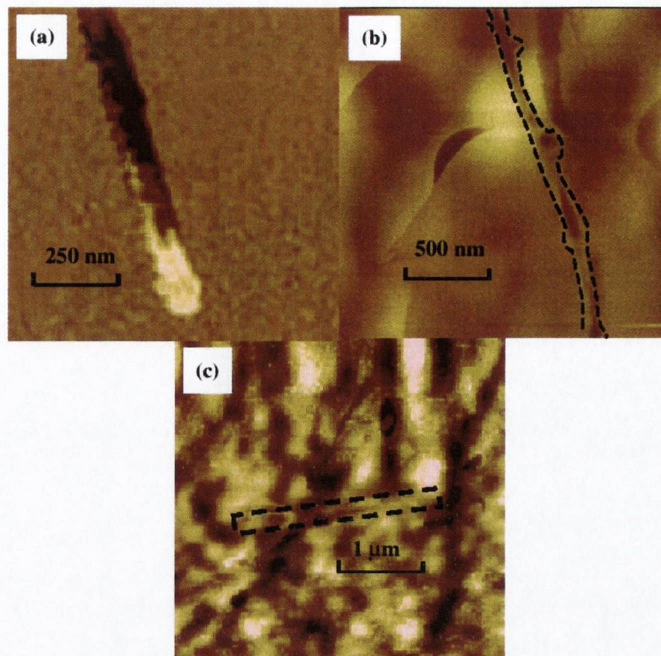

Figure 5.12. Magnetic force micrographs of multiwalled nanotubes on different cobalt substrates obtained with a Co-Cr coated tip in the phase mode at lift heights in the range 40 to 70 nm. a) The edge of a rope composed of two or three tubes on a uniformly magnetized Co substrate (the vertical scale is 0.5°), where the magnetic force micrographs shows magnetic contrast between and along the tubes. Panel b) shows another tube on a Co substrate which itself shows weak magnetic contrast, but that in the tube is different from that of the substrate (1° scale). Panel c) shows a substrate with strong magnetic contrast (3° scale) to which the tube is essentially transparent.

The stray field gradient from the tube can be compared with the magnetic signal from the substrate. In Fig. 5.12a magnetic contrast is shown for a sample lying on a flat cobalt substrate that has been magnetised and generates no discernible contrast. Fig 5.12b on the other hand, shows a nanotube on top of a non-uniformly magnetized Co film, which itself produces some magnetic contrast, but additional contrast due to the tube is visible. In Fig. 5.12c, there is a much stronger signal from the cobalt film, which has been deposited on a polycrystalline ruthenium seed layer, which helps to promote perpendicular anisotropy, and the tube makes no perceptible contribution to the strong magnetic contrast provided by the substrate.

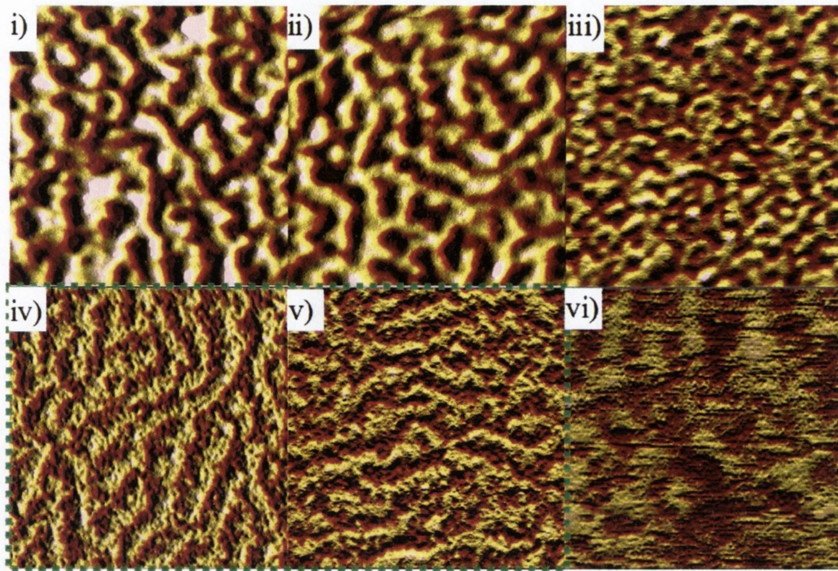

Figure 5.13. MFM images of magnetite thin films i) 400 nm, ii) 200 nm and iii) 60 nm thick measured with a hard-coated tip. iv) 400 nm and v) 200 nm thick, measured with a soft coated tip and vi) 20 nm measured with a hard-coated tip. All the images where taken at similar scan setpoints and amplitudes, with a lift height of 20 nm. The roughness of all the films is R_{ms} = 0.3-0.5 nm and the scan size is 10 × 10 μm in all the pictures.

For an optimum signal, we need a substrate that produces a visible, small and easily recognisable magnetic signal to avoid artefacts and be able to discern the nanotube signal. As it was mentioned at the start of the chapter, we chose magnetite due to its high spin-polarization. Studying the magnetic signal coming from different magnetite thin films, it is possible to observe that the magnetic signal of magnetite films 150-400 nm thick measured with a permalloy-coated tip, presents a quite characteristic "wavy" pattern, that is nevertheless small enough (order of 0.5° in the phase mode or 50 mV in the amplitude mode) to allow for the observation of stray fields coming from nanotubes (see figure 5.13 and, in particular iv and v). Shape anisotropy of the film ensures that its magnetization lies mainly in-plane, but the soft tip, more sensitive to surface variations, may react more easily to weak stray fields coming from surface irregularity, ripple domains or Bloch walls.

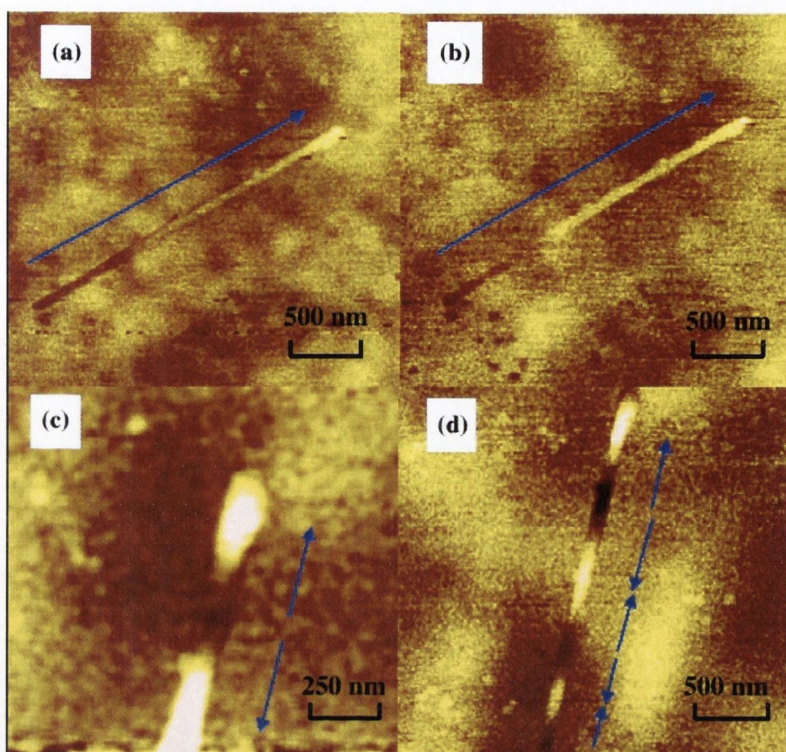

Figure 5.14. Magnetic force micrographs of a multiwalled nanotube lying on a magnetite substrate obtained in the amplitude mode with a low moment, permalloy-coated tip. a) Scan at 60 nm lift (the scale is 60 mV) b) Scan at 90 nm lift (scale 40 mV); the tube shows a single domain configuration magnetized along its length (blue arrow). In c) and d) scans of the same tube in a slightly different position are shown at 40 (c) and 120 (d) nm lift with a scan direction at 45° with respect to that used for a) and b); the scale is 40 mV for both pictures. The original dipole configuration has split into several into several domains.

The figure 5.14 shows some images of a carbon nanotube on a Fe_3O_4 film 180 nm thick taken at different scan heights with a permalloy-coated tip. The magnetic images in Fig. 5.14a and 5.14b show little contrast from the magnetite substrate, and clear bipolar contrast from the nanotube, as expected if it were a single domain magnetized along its length. These images suggest that the tube is aligned with the direction of magnetization of a single, in-plane domain in the substrate. The images in Fig. 5.14c and 5.14d are of the same tube in a slightly different position (probably displaced or twisted by the AFM tip) and scanned at

a different angle.

The data in Fig 5.14 indicate that the magnetic contrast depends weakly on lift height in the range from 40 to 120 nm. In practice, the signal phase $\Delta\varphi$ is roughly constant at close tip-sample separations [9]. For example, when magnetic fields are generated by a passing current through single a turn coil of radius r, it has been observed that $\Delta\varphi$ varies as (1-l/r) for distances $< r$, where l is the lift height [10]. At low lift, the magnetic field of up to 30 kA m^{-1} generated by the tip can interact with the tube or the substrate [11], or the tip can change the position of the nanotube.

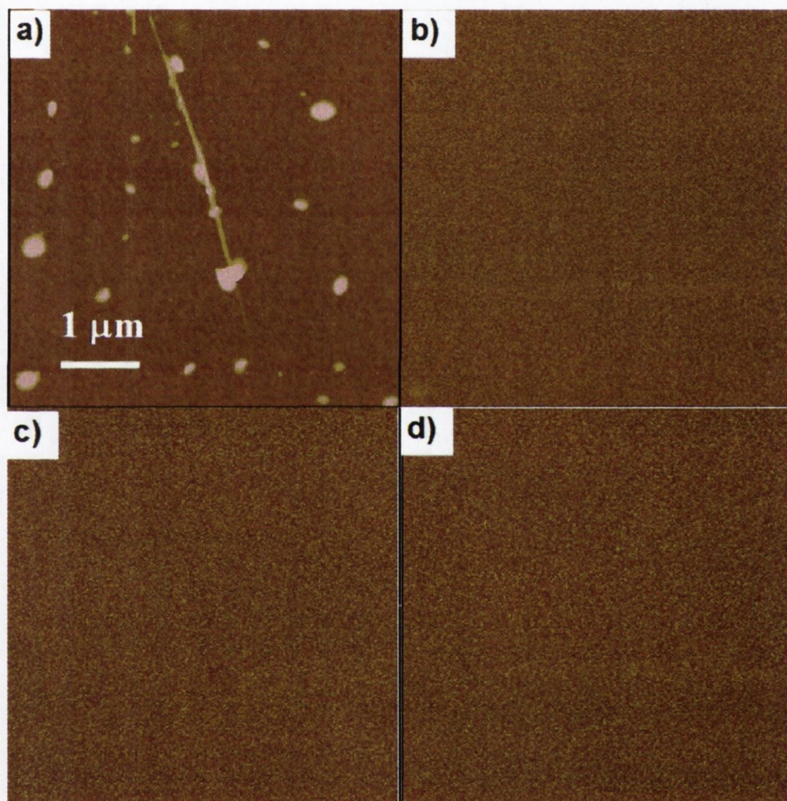

Figure 5.15. Atomic force microscopy picture of the topography of a nanotube laid on a silicon (80 nm scale). Magnetic force microscopy in phase mode of this tube before b), during c) and after d) a 15 mT field being applied by using a small permanent magnet (0.5° scale).

An attempt to detect the diamagnetic signal from nanotubes when a magnetic field is applied was made by applying small fields up to 15 mT to the sample while the MFM image was being taken. No magnetic contrast is detected, as it would be expected since the moment of the tubes would be just $2\times10^{-3}\text{Am}^2\text{kg}^{-1}$, and the field in the neighborhood of tube no more than 10^{-3} Am^{-1} ($\sim 1\mu$T). It is not possible to apply bigger fields, due to micro and macro displacements of the sample holder and the nanoscope itself when applying fields of order 100 mT.

Appendix: theoretical calculations

The charge transfer for a (5,5) carbon nanotube on a Au (111) surface was calculated as 0.1 electrons per contact carbon atom [13]. When the densities of states for spin up (↑) and spin down (↓) electrons at the Fermi level of the metal substrate are quite different, we expect a similar degree of spin transfer. This spin transfer was first calculated for C layers on Co superlattices [14], see figure 5.16. Note the considerable spin-splitting of the graphite π band at the Fermi level (red line) due to the proximity with the Co. Mülliken population analysis and a detailed study of the spin-density demonstrated that the relevant coupling between the C p_z orbitals and the Co is given by the $pd\sigma$ hopping integral with the Co d_{z^2} 2 orbitals.

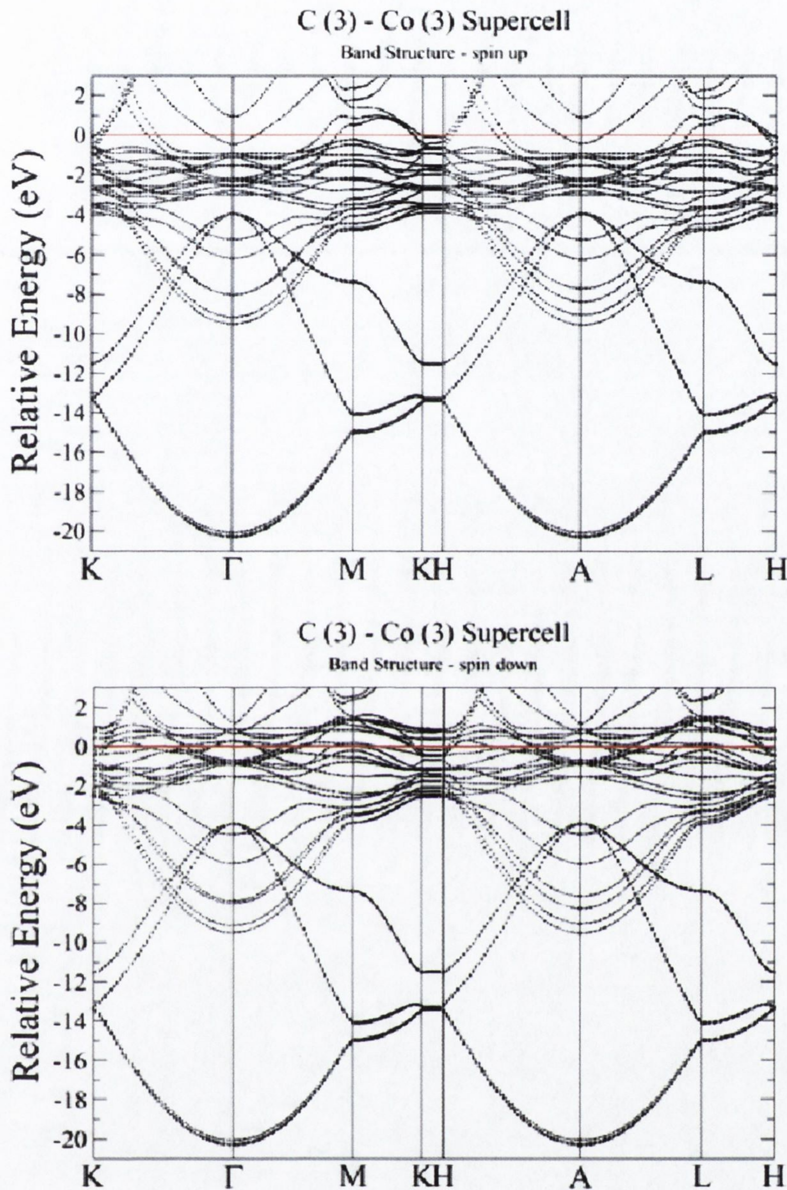

Figure 5.16. Band structure obtained for a Co/C superlattice, where we consider respectively three mono-layers of graphite and three monolayer of hcp Co. The calculations have been performed with the density functional theory code SIESTA using the local spin density approximation for the exchange correlation potential.

Ferreira and Sanvito [15] analysed this by assuming that the electronic structure of both the magnetic and non-magnetic material can be accurately described by a single-particle Hamiltonian, and that the non-magnet has a hollow cylindrical structure atomically commensurate with the magnetic surface on which it lies. The change in density of states upon the band formation is written in terms of the separate single-particle Green functions for the isolated nanotube and the magnetic surface. Their central results [15] are two expressions, one for the spin dependent charge transfer to the nanotube:

$$\Delta N_T^\sigma = \mathrm{Tr}\left\{\rho_M^\sigma(E_F)\left[V_T(E_F) - \langle V_T\rangle\right] + \rho_T(E_F)\left[V_M^\sigma(E_F) - \langle V_M^\sigma\rangle\right]\right\}, \quad (1)$$

and the other for the energy cost associated with the transfer:

$$\Delta E = \sum_\sigma \mathrm{Tr}\left|N_M^\sigma\langle V_T\rangle + N_T\langle V_M^\sigma\rangle\right|. \quad (2)$$

Here $\rho_i^\sigma(E_F)$ and N_i^σ are the spin-σ (σ=$\uparrow$,$\downarrow$) densities of states at the Fermi level and the total number of electrons, respectively; $i = T$ refers to the tube and $i = M$ to the substrate. are the energy-dependent contact potentials produced by the tube on the substrate ($i = T$) and by the substrate on the tube ($i = M$), and are averages over the relevant bandwidth. All these quantities, which can be accurately calculated, are matrices in the space of the relevant orbitals; the trace is taken over all the orbitals. in Eq. 2 must be negative for the spin and charge transfer to occur. The induced magnetization is the net spin imbalance of the electrons transferred to the nanotube. The contact potential is the single particle Green function and t is the coupling matrix between the substrate and the tube. Here t parameterises the interaction between the two materials. In practice it is the hopping integral between the orbitals responsible for the chemical bonding. Magnetism is induced not just because we have a magnetic substrate, but also because the spin polarized

orbitals contribute to the chemical bond. Charge transfer, induced magnetic moment and energy cost all depend quadratically on t, which therefore sets both the size of the magnetic moment and the relevant energy scale.

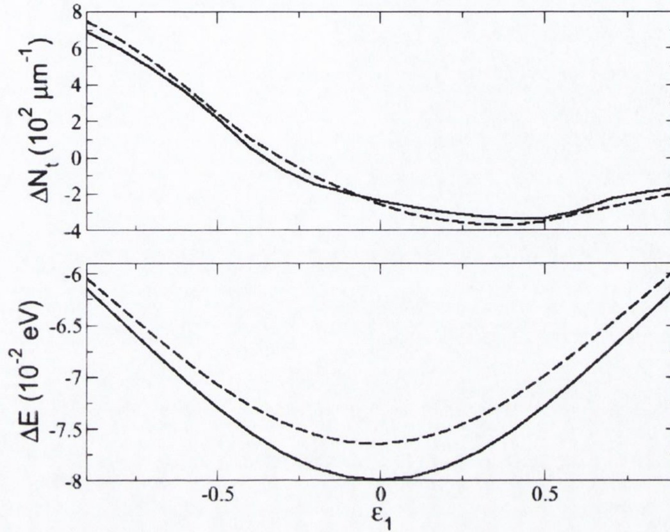

Figure 5.17. Charge transfer (ΔN_t) and the respective energy gain per unit cell (ΔE) for different band alignments. The parameter ε_1 corresponds to the center of the substrate band. Solid and dashed lines refer to (3,3) and (8,8) armchair nanotubes, respectively.

Specifically they considered an (8,8) armchair nanotube described by a single-band tight-binding model with hopping parameter $\gamma = 2.5$ eV where 6γ is the width of the graphite π-band [17], in contact with a magnetic transition metal with a 5 eV wide spin-polarized d band which is assumed to be orbitally degenerate. We take t to be the $p - d\sigma$ hopping parameter between Co and C based on density functional calculation for a Co/C superlattice, evaluating $t = V_{pd\sigma} = 0.45$ eV by using Harrison's scaling law [16] with a Co-C band length of 2.72 Å. This gives magnetic moments $m \approx 0.1\ \mu_B$ per contact carbon atom, and energy gains per unit cell $\Delta E \approx 0.1$ eV. Results which confirm that the induced magnetic moment in the carbon nanotube should be observable at room temperature.

Bibliography:

[1] T.P.Pareek Phys. Rev. Lett. **92**, 076601 (2004)

[2] P. Esquinazi, A. Setzer, R. Höhne, C. Semmelhack et al., Phys. Rev. B 66, 024429 (2002).

[3] T.L. Makarova, B. Sundqvist, R. Höhne, P. Esquinazi et al., Nature 413, 716 - 718 (2001).

[4] K. -H. Han, D. Spemann, R. Höhne, A. Setzer et al., Carbon 41 785 (2003).

[5] T.L. Makarova, Magnetism of carbon-based materials, in 'Studies of High Temparature Superconductors'(Ed A. Narlikar) 45 107 (2003)

[6] P. Esquinazi, D. Spemann, R. Höhne, A. Setzer et al., Phys. Rev. Lett. 91 227201 (2003)

[7] J.M.D. Coey, M. Venkatesan, C.B. Fitzgerald, A.P. Douvalis & I.S. Sanders, Nature 420, 156 (2002).

[8] Y. -K Kwon, S. Saito and & D. Tománek, Phys. Rev. B 58, R16001 (1998)

[9] R. Yongsunthon, E.D. Williams, J. McCoy, R. Pego et al., J. App. Phys 92, 1256 (2002)

[10] J. Lohau, S. Kirsch, A. Carl, G. Dumpich and E.F. Wassermann, J. App. Phys. 86, 3410 (1999)

[11] S. McVitie, R.P. Ferrier, J. Scott, G.S. White and A. Gallagher, J. App. Phys. 89, 3656 (2001)

[12] R.C. O'Handley, Modern Magnetic Materials, (Wiley, New York, 2000), pg. 681-3

[13] A. Rubio, D. Sanchez-Portal, E. Artacho, P. Ordejon and J.M. Soler, Phys. Rev. Lett. 82, 3520 (1999)

Bibliography:

[1] T.P.Pareek Phys. Rev. Lett. **92**, 076601 (2004)

[2] P. Esquinazi, A. Setzer, R. Höhne, C. Semmelhack et al., Phys. Rev. B 66, 024429 (2002).

[3] T.L. Makarova, B. Sundqvist, R. Höhne, P. Esquinazi et al., Nature 413, 716 - 718 (2001).

[4] K. -H. Han, D. Spemann, R. Höhne, A. Setzer et al., Carbon 41 785 (2003).

[5] T.L. Makarova, Magnetism of carbon-based materials, in 'Studies of High Temparature Superconductors'(Ed A. Narlikar) 45 107 (2003)

[6] P. Esquinazi, D. Spemann, R. Höhne, A. Setzer et al., Phys. Rev. Lett. 91 227201 (2003)

[7] J.M.D. Coey, M. Venkatesan, C.B. Fitzgerald, A.P. Douvalis & I.S. Sanders, Nature 420, 156 (2002).

[8] Y. -K Kwon, S. Saito and & D. Tománek, Phys. Rev. B 58, R16001 (1998)

[9] R. Yongsunthon, E.D. Williams, J. McCoy, R. Pego et al., J. App. Phys 92, 1256 (2002)

[10] J. Lohau, S. Kirsch, A. Carl, G. Dumpich and E.F. Wassermann, J. App. Phys. 86, 3410 (1999)

[11] S. McVitie, R.P. Ferrier, J. Scott, G.S. White and A. Gallagher, J. App. Phys. 89, 3656 (2001)

[12] R.C. O'Handley, Modern Magnetic Materials, (Wiley, New York, 2000), pg. 681-3

[13] A. Rubio, D. Sanchez-Portal, E. Artacho, P. Ordejon and J.M. Soler, Phys. Rev. Lett. 82, 3520 (1999)

[14] J. M. Soler, E. Artacho, J. D. Gale, A. Garcia, J. Junquera, P. Ordejon and D. Sanchez-Portal, J. Phys. Cond. Matter 14, 2745 (2002)

[15] M.S. Ferreira M.S. and S. Sanvito, Phys. Rev. B 69, 035407 (2004)

[16] W.A. Harrison, Electronic Structure and the Properties of Solids, (Dover, 1980)

[17] S.A. Wolf, D.D. Awschalom, R.A. Buhrman, J.M. Daughton et al., Science 294, 1488 (2001).

[18] C. Joachin, J.K. Gimzewski, & A. Aviram, Nature 408, 541 (2000)

[19] K. Tsukagoshi, B.W. Alphenaar and H. Ago, Nature 401, 572 (1999)

[20] A. Bachtold, P. Hadley, T. Nakanishi and C. Dekker, Science 294, 1317 (2001)

[21] Y. Huang, X. Duan, Y. Cui, L.J. Lauhon et al., Science 294, 1313 (2001)

[22] P.G. Collins, M.S. Arnold and P. Avouris, Science 292, 706 (2001)

[23] T. Rueckes, K. Kim, E. Joselevich, G.Y. Tseng et al, Science 289, 94 (2000)

Chapter 6

Discussion

6.1 Transport in nickel nanoconstrictions

The first striking characteristic of the transport across nickel nanoconstrictions is the non-linearity and asymmetry, independent of the method employed for its fabrication (electrochemistry, FIB or e-beam lithography), but present only in the samples fabricated on SiO_x-Si substrates (see the figure 6.1). The samples patterned on MgO and glass substrates show a symmetric transport, with non-linear coefficients only for constrictions with conductances below G_0 (12.9 kΩ).

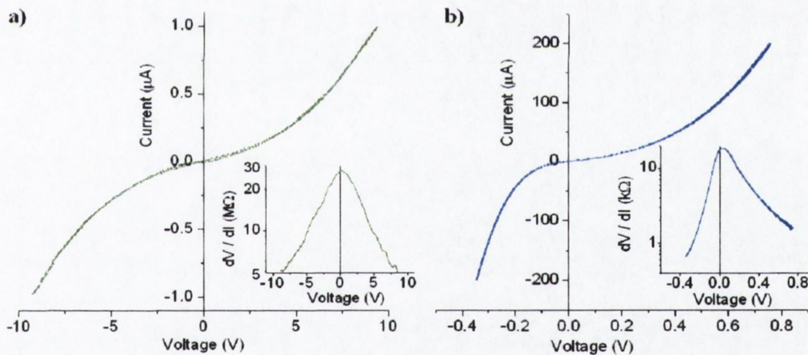

Figure 6.1. I-V and R (V) (insets) characteristics of double nickel nanoconstrictions patterned on MgO a) and SiO_2 b) substrates.

The second characteristic are the three clearly distinct behaviours found for the MR of samples patterned on SiO_x-Si substrates. The first kind of MR, seen in the figure 6.2a), and present in the samples with lower resistances ($\lesssim$ 1kΩ), is a small increase of about 1-2 % of

the resistance with the field, up to a saturation point that is dependent of the field-direction (~ 10-100 mT for parallel configurations, 0.1-2 T for perpendicular configurations). In the second MR effect, found in samples with resistances of 1 to 5 kΩ, the resistance initially increases by a few %, but is suddenly halved when the field reaches a certain value (~ 2 tesla for the figure 6.2 b, up to 5 T in other cases). The third effect (figure 6.2 c) is a huge drop of resistance at low fields (order of mT), together with a big reduction of the non-linearity and asymmetry (Fig. 6.2c).

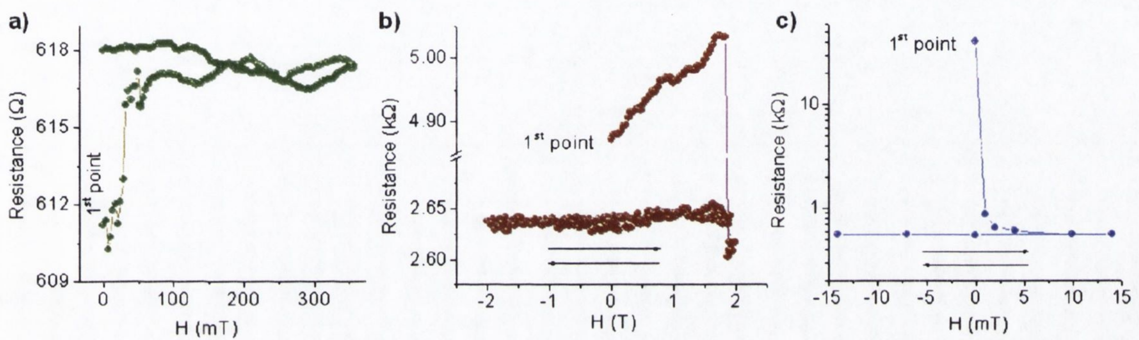

Figure 6.2. Field effects on Ni nanostructures: a) Small increase of order 1 %, b) Small increase followed by a sudden drop of about 50 %, c) Huge decrease of resistance up to 50000 % at small fields.

The first objection usually raised to the huge MR ratios present in electrodeposited nickel nanocontacts is magnetostriction. In our case, we could say that the I:V is not linear before the field is applied because we depart from a gap and the current is tunnelling (although the resistance of the e-beam sample is too small to have a gap). When the field is applied, a magnetostrictive effect closes the gap, greatly reducing the resistance. To explain why the I:V is not linear even after the field is applied (where we assume that we have formed or increased the size of a contact) we still need to resort to some other mechanism, like a domain wall, that does not allow an adiabatic or ohmic flow of electrons through the

contact.

However, a magnetostrictive effect would be highly dependant on the direction of the applied field, we could increase the size of the contact by applying the field in a certain direction, but we could as well decrease or not change its size at all if we apply it in a perpendicular direction, so we should measure both positive and negative MR at a certain field by varying the direction of the applied field. The big changes of resistance (> 10 %) always reduce it, but the small changes ($< 5\%$) always increase the resistance, independent of the direction of the applied field. And, as we said in the third chapter, the relaxation times of the sample to come back to its original state are in the order of days, while the relaxation times for magnetostriction are more in the order of fractions of second.

The second common explanation for the big MR ratios found in electrodeposited nickel contacts is to assume the presence of a domain wall trap in the nanocontact. In order to understand also the magnetoresistance effect and the asymmetry in the I-V curves of our nickel nanoconstrictions, we can first consider the following scenario: in the absence of a magnetic field, the leads have opposite magnetisation and a sharp domain wall is formed at the constriction. This domain wall creates a very strong scattering potential. When the magnetic field is applied, the magnetic moments of the leads align and the wall is eliminated. The resistance is reduced and this gives rise to the MR effect.

Furthermore, the fabrication process is likely to produce uneven contacts. Therefore, the coupling of the constriction with the leads is asymmetric. This, added to charging effects due to the reduced dimension of the nanoconstriction, leads to a diode-like I-V curve (Fig. 6.3).

This situation has bee modelled by Rocha et al. [1]. Their model assumes the nanocon-

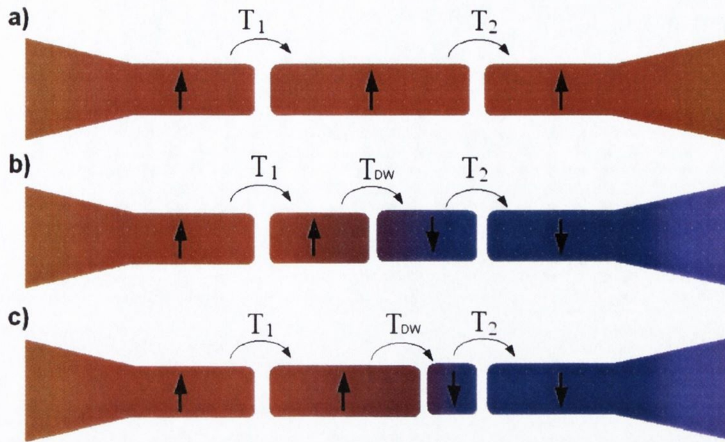

Figure 6.3. Top: Parallel configuration, $T_1 \simeq T_2$ small, geometrically-induced asymmetry. Middle: Domain wall pinned in the centre of the chain. TDW represents its impedance. Large MR in addition to the geometrical asymmetry. Bottom: The domain wall is not in the centre of the chain. The different size of the islands can lead to very different charging effect depending on the sense of the current $\rightarrow$ large MR and asymmetry

striction as a 2 by 2 nickel atomic chain connected to two semi-infinite Ni electrodes, with the electronic structure calculated by a two band tight-binding model and the transport calculated within the framework of the non-equilibrium Green's function formalism in the Keldysh approach [5].

Under these conditions, the built-in asymmetry in the leads is such that the coupling to the right lead is half as great as to the left one. When a forward bias is applied and the right lead is more weakly coupled than the left one, the leads have different spin configurations, electrons will be trapped inside the constriction in a Coulomb blockade type of regime. The opposite happens when a negative bias is applied

In the case of anti-parallel configurations, the asymmetry in the I-V curves is very large, qualitatively matching that of the experiments. Once we apply a magnetic field and hence align the magnetic moments, the asymmetry is reduced. Moreover, it was also found that the I-V curve is completely symmetric when the asymmetry of the coupling is lifted,

what can give rise to a huge magnetoresistance in a nanocontact.

However, these calculations start from the assumption that the nanocontact is only a few atoms wide. Even if it is likely that the nanoconstriction is covered by NiO_x, reducing the actual conducting path (and from the SEM and AFM images we can see that they are initially 20-50 nm wide), it is very difficult to believe that several samples oxidised to the point of leaving just a few Ni atoms in the nanoconstriction. Nor does it explain why there is no asymmetry or magnetoresistance in the samples fabricated on MgO or glass substrates. We also need to assume that the nanostructures are fully ballistic, when the Z parameter calculations for Ni-Nb (or Ni-NiO_x-Nb) junctions from the Andreev measurements are always well above 0 (ballistic contacts would give smaller values [2]). On the contrary, they are usually so high ($Z > 2$) that do not allow for a measurement of the polarization of the material (tunnelling behaviour).

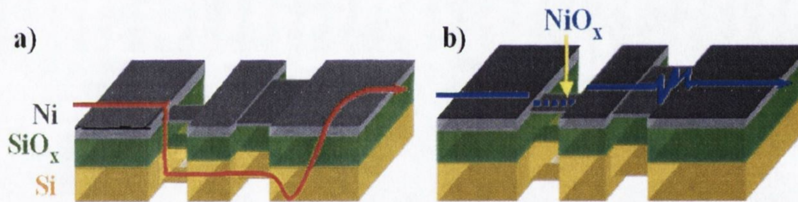

Figure 6.4. Transport asymmetries could be due to parallel conduction channels via SiO_x a) and/or NiO_x b). The latest would imply the tunnelling of electrons only for the few nm where the NiO_x does not allow for metallic transport.

An alternative, and more plausible explanation is based on the presence of an antiferromagnetic, insulating layer of NiO_x at the nanoconstriction (schematic in figure 6.4). When the sample is fabricated on SiO_x substrates, the bottom of the structure can be oxidised by natural oxidation and might also be from the migration of oxygen atoms from the silicon lattice to the nickel, forming a ring of NiO_x around the Ni structure which may or may not

fully close the conducting path, although the heat of formation of SiO_2 is much larger than for crystalline NiO. If the sample is not fully oxidised even at its narrowest parts, there is a remnant conductive Ni path that the electrons can use, maybe in parallel with the other oxide paths (depending on the conductivity of the Ni at the constriction an the thickness of the layers). When the nanoconstriction is fully oxidised (samples with higher resistance), the electrons must then tunnel through the SiO_x and/or the NiO_x layers to cross it, giving rise to non-linear and asymmetric effects, due to multiple tunnelling and/or interface asymmetries. This is very unlikely to happen when using MgO as substrate, in this case, either there is an open nickel channel and the resistance is well below G_0, or the conduction path is closed and the resistance is above G_0 with a typical tunnelling behaviour.

The out-of-zero peak of the resistance, which also appears only for samples patterned on SiO_x substrates, either nickel or FIB-deposited Pt nanoconstrictions (consistently at 60-90 meV for Ni nanostructures on SiOx, at higher voltages for Pt), may then be due to differences between the Fermi level of the two materials that allow for the conduction (NiO_x-SiO_x /// Pt(GaO_x)-SiO_x), deforming the tunnel barrier and generating the artefact [3]. We must remark that Pt structures deposited by FIB have high gallium doping levels (even > 10 %) and low conductivities (one to three orders of magnitude above bulk Pt).

For samples with a conductance $G \lesssim G_0$, as we reduce the temperature, both the resistance and the non-linearity increase, while the peak of the resistance is shifted (Fig. 6.5), effect that can even change the sign of the asymmetry. We attribute this behaviour as due to the thermally activated transport in: a semiconductor (SiO_x) and/or hoping in insulating antiferromagnetic material (NiO_x).

Further evidence of the presence of a NiO_x layer on SiO_x substrates, and its effects on

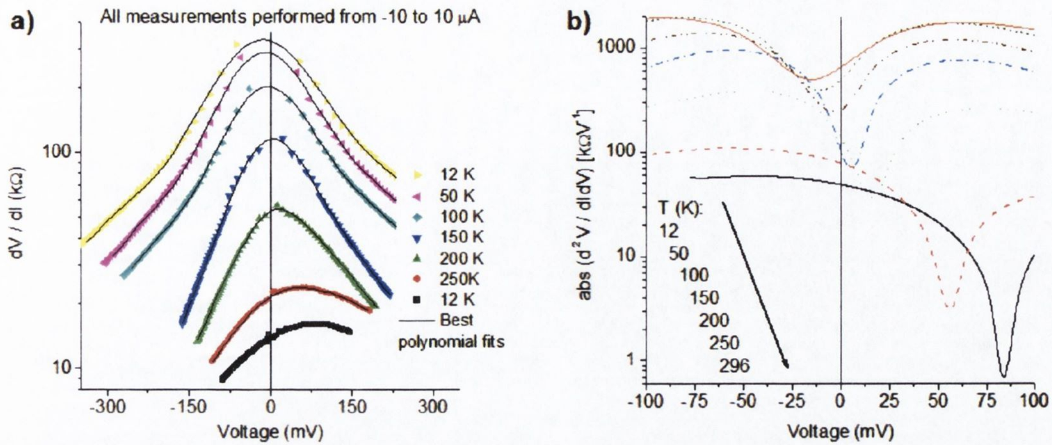

Figure 6.5. Transport dependence with temperature. a) dV / dI (-> resistance) vs. voltage at different temperatures. As we reduce the temperature the resistance and non-linearity increase. b) The graph of d^2V / dIdV vs. voltage gives us the position of the peak of resistance (an inflexion point in on the left is a minimum on the right graph). Changes in temperature shift its position, changing the asymmetry of the I-V characteristic.

when Z is below 1, the deduced polarization is almost twice than that of bulk nickel (see figure 6.6a), but not $\sim$ 100 %, as it would be required to explain the huge magnetoresistance values in terms of narrow domain walls for even 180^0 changes of magnetization over a 1-atom distance. This is probably due to the absorption of s electrons by the oxygen atoms of the surrounding NiO_x ring and to the local narrowing of the d band in the nanostructure [4]. But can this NiO_x layer explain the different magnetoresistive effects, that can go up to 50000%?

The biggest magnetoresistive ratios were found for samples that had been heated, which also presented the lower conductivity values, well below the quantum of conductance G_0 (that we have taken to be equal to $\frac{2e}{h}$ = 12.9 kΩ), see Fig. 6.6b). For samples with conductivities between 1 and 15 G_0, the mixed increase of resistance plus switching effects were measured.

The smaller values of a few % were found for the samples with higher conductivity, well above the quantum of conductance. This means that there are many Ni conduction channels

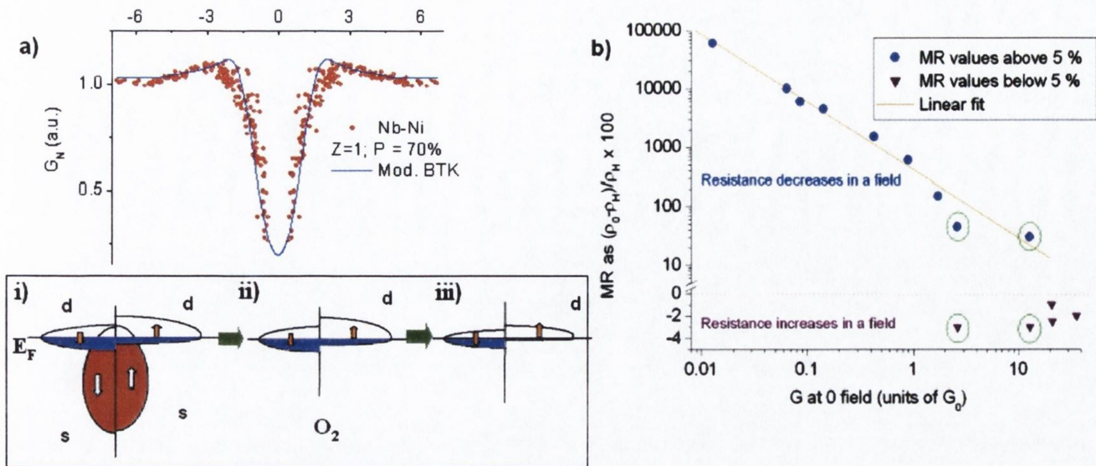

Figure 6.6. Magnetic properties of Ni nanoconstrictions. a) Polarization at a Ni/NiO_x/Nb edge junction measured by Andreev reflection. Inset: schematic of the changes of the band structure Ni/NiO_x nanoconstriction (i) due to the absorption of *s* electrons by oxygen (ii) and the narrowing of the *d* band (iii). b) Scaling of the magnetoresistance with the initial resistance of the device. Samples in a circle present both an increase and a drop of resistance depending on the field (those points are not included in the fitting).

open at the nanoconstriction, and the NiO_x layer is not greatly affecting the transport. The magnetoresistance can then be explained in terms of the presence of a domain wall trapped at the nanoconstriction (not all the samples show MR, therefore only some of them do have a domain wall trapped), and the subsequent anisotropic magnetoresistance (AMR) associated with its elimination [5].

The huge MR values can be associated with the presence of a NiO_x layer. NiO is a 'Mott-Hubbard ' insulator, an antiferromagnetic (coordination number $z = 6$) material due to the superexchange interaction between the Ni atoms via the oxygen. NiO remains insulating above the Néel temperature (524 K), and its transport properties are determined by the level of vacancies-donors due to the big bandgap U, of order of 6 eV. This usually gives rise to a thermally activated, hole hoping transport (for the transport properties of intrinsic NiO and their association with either *sp* or *d* conduction see [6], for magnetic exchange in

NiO [?] and for the effect of non-stoichiometry in the conductivity and capacitance of the material [8]). NiO presents superparamagnetic behaviour for particles with a diameter below 100 nm [9].

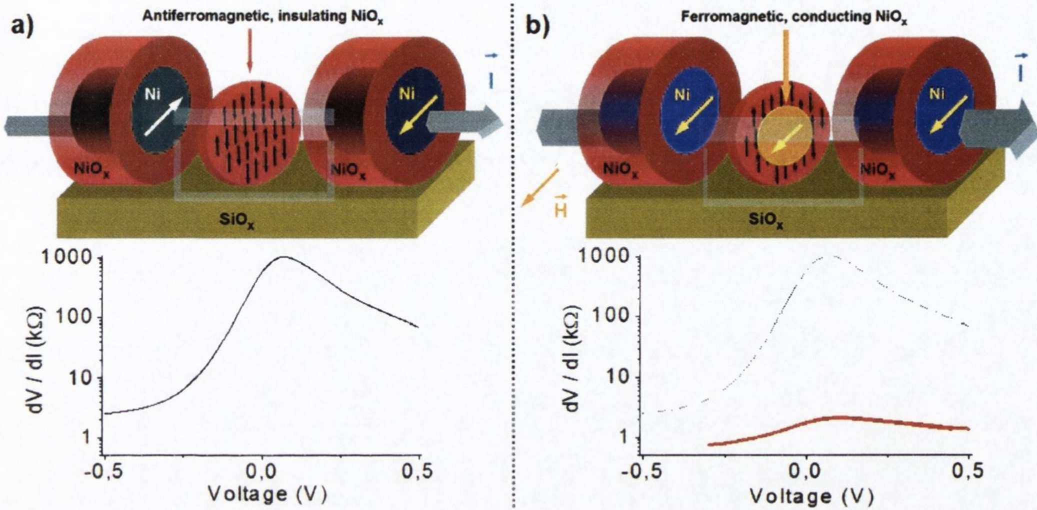

Figure 6.7. a) Schematic representing the initial state of a Ni/NiO_x nanoconstriction and its measured $\frac{dV}{dI}$ (V) characteristic. b) Schematic which shows the transition of the NiO_x layer to ferromagnetic-conducting when a magnetic field is applied. $\frac{dV}{dI}$ (V) characteristic when the field is applied (in red, continuous line).

Originally, the NiO_x layer at the nanoconstriction is antiferromagnetic and insulating, and the magnetic moments at both sides of the constriction point in different directions. When a small magnetic field is applied, both moments will point to the same direction, and the exchange energy between the Ni electrodes and the NiO_x layer (where the antiferromagnetic state would not be as stable as in the crystalline case [?]) may be able to force part of the antiferromagnetically aligned moments of the the NiO_x to become ferromagnetic and, at least partially, conducting, opening conduction channels that were previously closed, and changing the status of the constriction from insulating (100 kΩ to 1 MΩ) to diffusive ($\simeq$ 1kΩ), as we can see in the figure 6.7. This would explain why the magnetoresistance

changing the status of the constriction from insulating (100 kΩ to 1 MΩ) to diffusive ($\simeq$ 1kΩ), as we can see in the figure 6.7. The same effect is obtained independently of the direction of the applied field (making unlikely magnetostriction or magnetostatic artefacts). This would explain why the magnetoresistance scales with the conductivity; the more insulating (thicker, antiferromagnetic...) is the NiO_x layer, the bigger is the drop of resistance when a field is applied and the NiO_x layer becomes conducting.

The variation of the resistance with the temperature complies also with this explanation. In samples with a conductivity below G_0 (before a field is applied, or for those samples which show no magnetic field effect) the resistance increases exponentially when reducing the temperature (Fig. 6.8). This R(T) characteristic can be fitted to transport across two channels; a semiconducting channel with a band gap of 0.13 eV and very low intrinsic conductivity (e.g., SiO_2 with an impurity band), and a second channel with a hopping transport characteristic ($\ln R \propto \sqrt{\frac{1}{T}}$), activation energy of 0.2 meV and a moderate conductivity at low temperatures (e.g., amorphous, non-stoichiometric NiO_x, which presents low activation energies at low temperatures see page 173 of ref. [10]). However, the R(T) characteristic also resembles the R(T) characteristic of Li-doped NiO (given the initial slope, $Li_xNi_{1-x}O$ with x ≈ 0.02). The transport across SiO_x is then evidenced by the peak in the resistance rather than by the R(T) behaviour.

Since intrinsic conductivity in NiO must be through the *d* and/or the hybridised *sp* bands, this temperature dependence could be explained as due to transport via weakly localized electrons in the *d* band. The *d* bands in NiO do not overlap (nor above or below the Néel temperature), but maybe in the case of amorphous, non-stoichiometric NiO_x, the gap between the *d* bands is small enough to allow for an overlap at a finite temperature, which

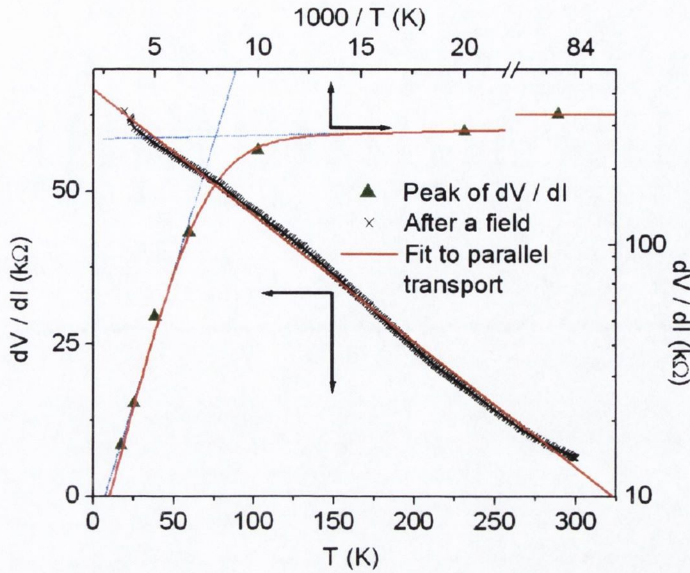

Figure 6.8. Variation of the resistance with the temperature for a sample which shows no magnetic field effect (up triangles) and a sample after a field is applied and the resistance decreased by about 500 % (crosses). The first one (triangles) can be fitted to parallel transport with two channels, one with a dependence of $\ln \frac{dV}{dI} \propto \frac{1}{T}$ (activation energy 0.13 eV and $R|_{T\longrightarrow\infty} = 1.2\ \Omega$) and the other with $\ln \frac{dV}{dI} \propto \sqrt{\frac{1}{T}}$ (activation energy 0.2 meV and $R|_{T\longrightarrow\infty} = 300\ \Omega$). The second one (crosses) increases linearly with the temperature.

polarons. Either case would give rise to a magnetically-induced metal-insulator transition, or MIT (this does not happen for crystalline NiO, as is evidenced by the fact that NiO remains insulator above the Néel temperature). For the transport characteristics of Li-doped NiO and MIT on transition metal compounds see the reviews [10] and [11]. However, a detailed calculation using a LSDA+U model [12] would be required to verify that such a change for the electrons in the *d* band would be possible when the moments are aligned.

The samples with intermediate resistances near G_0 present the most complicated behaviour, with mixed positive and negative MR. Since the sample has a conductance above G_0 is logical to assume that the NiO_x layer is not fully covering the constriction but, since the resistance is quite high ($> 1\ k\Omega$), and the I-V characteristic is non-linear and slightly

asymmetric, the NiO_x offers alternative transport paths. The initial increase of resistance can also be attributed to the annihilation of a domain wall present at the nanoconstriction (-> AMR). The fact that this increase does not saturate until very high fields (2 and 5 T), could be due to the presence of a significant NiO_x layer (which for samples with smaller resistance would be thinner, allowing for smaller saturation fields, that can be of order 50 mT, as seen previously) surrounding the nickel and pinning the domain wall. Once the domain wall is eliminated, and the nickel domains at both sides of the constriction are pointing in the same direction, the NiO_x layer becomes ferromagnetic and conducting, giving rise to a drop of resistance which value will depend on the ratio between the cross-sections of the NiO_x and Ni layers (see figure 6.9). Since this drop of resistance is of about 50 %, it means that if the constriction is, say, 30 nm in diameter, the oxide layer penetrates around 4 nm.

As we have explained, to allow for the big MR effects, the nickel conduction path must be either fully closed by NiO_x or surrounded by it. In the case of smaller effects, with increase of resistance of a few %, the NiO_x layer may also help to pin a domain wall at the constriction. This may explain why the samples fabricated on MgO do not show any significative MR value, since oxygen atoms are much more likely to migrate from a SiO_x than from a MgO substrate. We must also remember that many of the samples were heated to produce the high MR values.

The long relaxation times would be due to the return of the domains to their original magnetization state, a process that may be slowed down by the presence of NiO_x.

Noise measurements give further evidence of a NiO_x layer with a pinned domain wall, as well as the relevance of electromigration, and how sensitive are these devices to electrical currents. In the presence of a magnetic field (Fig. 6.10a) at high voltages, the slope of the

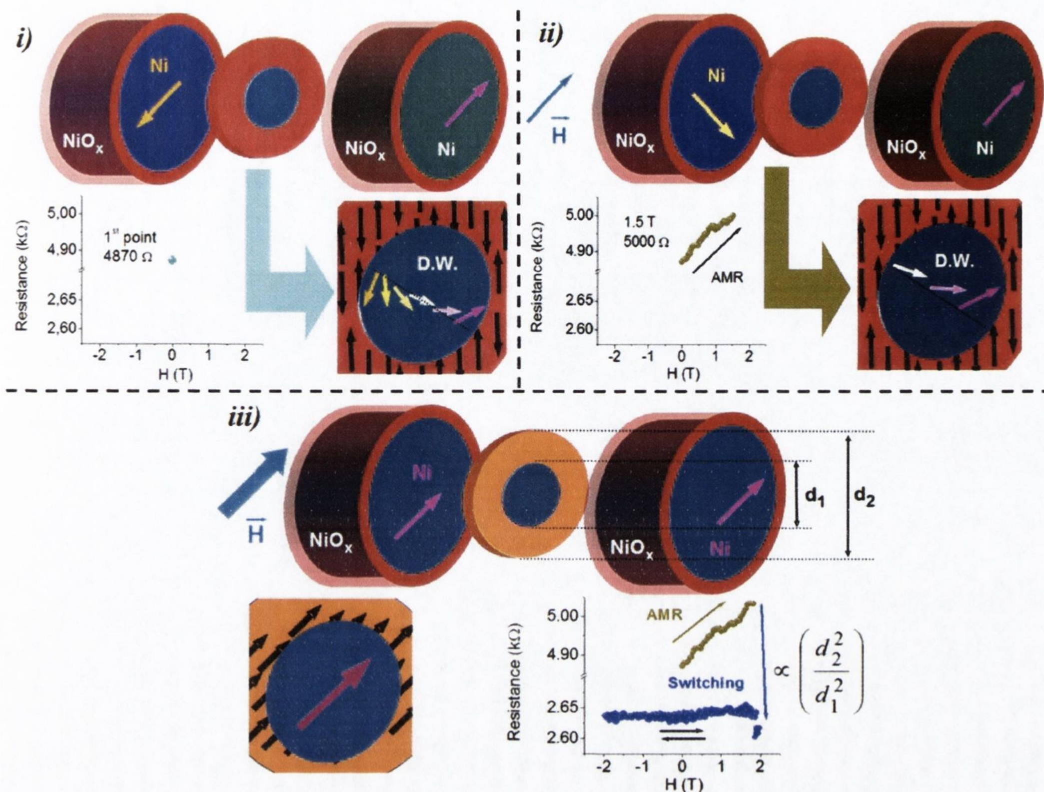

Figure 6.9. i) Initial state of a junction of $\sim$ 5kΩ resistance. The NiO_x layer does not fully close the conduction channel and a domain wall (DW) is formed at the nanconstriction. ii) A magnetic field changes the domains sizes, reducing the domain wall and increasing the resistance by a few %. iii) Once the domain wall is eliminated, the exchange energy is big enough to magnetize the NiO_x switching the conductance value in a percentage proportional to the ratio of the NiO_x/Ni surfaces at the nanoconstriction.

1/f noise is increased, although the noise magnitude for high frequencies (> 10 kHz) is the same as when there was no magnetic field applied. We interpret this effect by assimilating the domain wall to a grain boundary. When no magnetic field is applied, a domain wall delays the passage of material through the constriction, giving rise to an increase of the noise magnitude at certain frequencies, and these frequencies depend of the applied voltage, being higher for higher voltage. The high noise levels present in some samples, which we saw would give unrealistic sample volumes, are due to the shot noise generated by the tunnelling process.

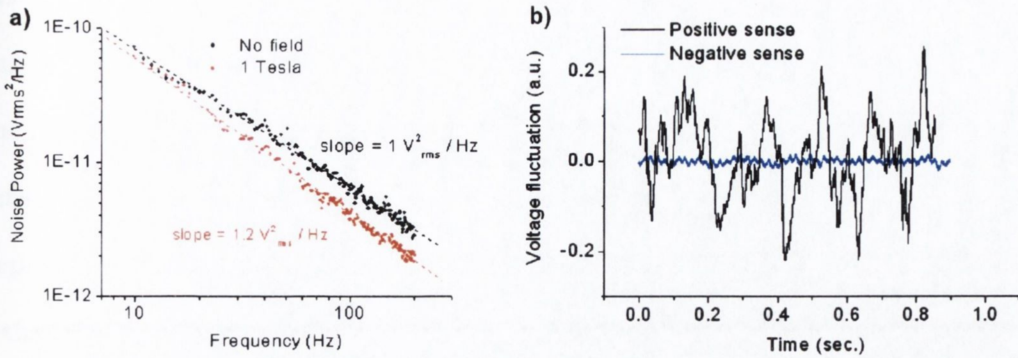

Figure 6.10. Noise characteristic of a nickel nanoconstriction and the magnetic field effect.

The shivers of the system, present when the current is applied in the positive sense (defining positive sense as the one where the max. of $\frac{dV}{dI}$ appears), see Fig. 6.10b), are absent for the negative sense of the current and may be also related to a difference in the geometry of the constriction that leads to a different pressure on the loose atoms and the domain wall [16].

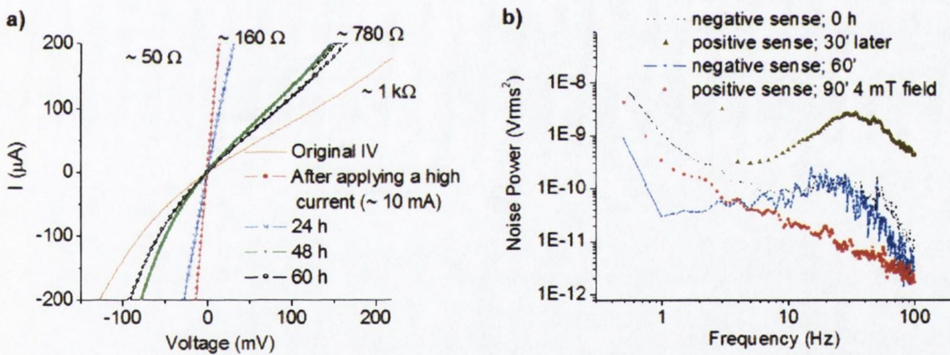

Figure 6.11. a) Change of resistance after a high current (~ mA) is applied (1 kΩ to 50 Ω) and the slow (~ days) recovery. b) Noise characteristic after a high current (~ 500 μA) is applied.

High currents of several mA can induced structural changes and drastically affect the transport characteristic. We saw that the resistance of the device could be reduced by a factor 20 by applying a high current of a few mA, and the I:V characteristic became then

linear and symmetric, before slowly reversing to its original state (Fig. 6.11a). We saw in the third chapter that the experiment could be reproduced, but now applying a current in the negative sense after first having reduced the resistance with a current in the positive sense. That way the relaxation time was reduced to a few minutes. The effect is therefore dependent of the sense of the current and can both reduce or increase the resistance, whereas a thermal effect would be independent of the sense of the current. It then seems evident that the high current is displacing material from the vicinity of the nanoconstriction, changing its geometry and transport properties (see figure 6.12). This material then drifts back to its original position or oxidises after some hours, unless it is pushed by a reverse current, which decreases the time necessary to revert to the original state.

It is then that the noise spectrum of our sample becomes completely different from the usual Gaussian noise, with a big increase in the noise power at low frequencies (6.11b). It was shown in section 3.2 that these "bumps" were associated to two-level random telegraph noise. However, this RTN only appears after a high current has been applied, and disappears after a magnetic field is applied. We also saw that, as time passes, the sample remains for longer periods of time in the high resistance state. A similar effect could be achieved by increasing the temperature, reducing then the amplitude of the fluctuation at the same time as increasing the time spent in the high resistance state. Further increases of temperature eliminated the noise (which if not will eventually disappear after a few hours).

The origin of the fluctuations can also be attributed to the dual nature (antiferro to ferromagnetic -> insulating to conducting) of this amorphous NiO_x nanoconstrictions. As we have seen, after applying a high current, nickel atoms are displaced into the constriction. This atoms may interact (via exchange energy) with the NiO_x in the neighborhood, inter-

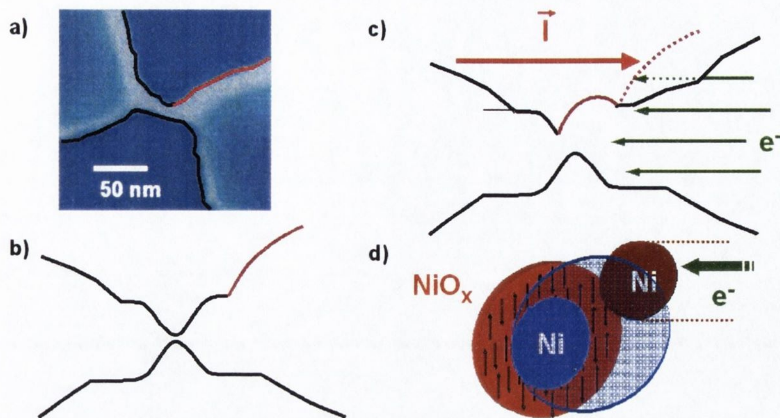

Figure 6.12. a) SEM of the nanoconstriction where the change of resistance is observed and b) schemtic which represents it. After a high current is applied the nickel in the vicinity of the nanoconstriction can be displaced increasing the conductivity -> c) lateral and d) perpendicular schematics.

action which might be sufficient to alter the magnetic behaviour of a few NiO_x cells from antiferromagnetic (high resistance level) to ferromagnetic (low resistance level). See the data and schematic of the figure 6.13. As time passes, an oxide layer forms around the moved Ni atoms, reducing the interaction and increasing the time the sample spends in the high resistance state. This process can be accelerated by heating up the sample, and eventually the fluctuations disappear leaving the sample in the high resistance state (figure 6.13b).

The fluctuations are about 0.1 % of the applied signal. The SEM image of this sample (seen in figure 6.12a) shows a constriction 20 nm wide. This sample presented the AMR+switching behaviour, with a drop of resistance of 35 %, from which we can deduce that the NiO_x layer is a ring of some 2 nm in width, what leaves some 15 nm in diameter of Ni -> $\sim 1.5 \times 10^3$ Ni atoms. After applying a high current, the resistance drops by a factor 20, therefore we have some 30000 Ni atoms in the constriction contributing to the conductance. The displaced atoms probably form a more or less spherical 'blob', some 5 nm in radius, attached to the constriction (schematic shown in Figs. 6.12c & d). Assuming that

the conductivity of ferromagnetic NiO_x is similar to that of Ni, to provide changes of resistance of 0.1 %, we would need just some 30 NiO_x cells (probably those in contact with the displaced nickel 'blob') fluctuating in its magnetic-conducting behaviour to give rise to this RTN.

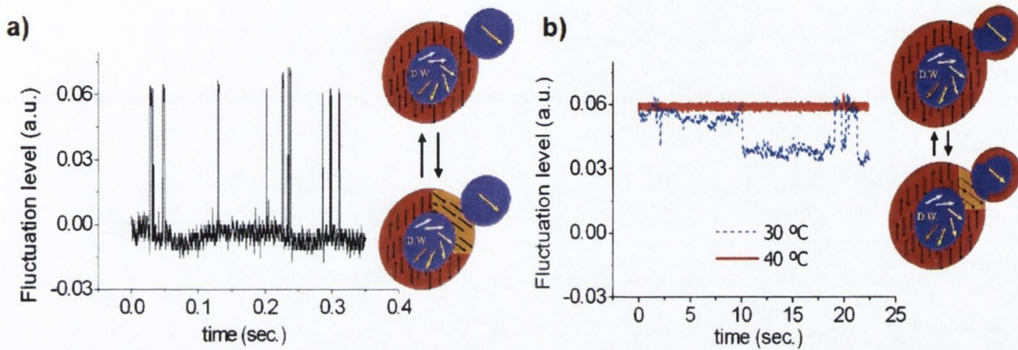

Figure 6.13. a) RTN at room temperature (~ 20°C) and schematic with a possible explanation of its origin (see text). b) As time passes, or when the temperature increases, the displaced Ni is oxidised and the RTN is reduced, with the resistance stabilising in its higher value.

The last effect to be discussed is the electrical switching and hysteresis observed at about 2-20 μA in some FIB-patterned double nanoconstrictions. This effect may also be explained by electromigration. But the phenomena should work in both directions; if it is possible for us to increase the size of (or create a new) our contact, we should be able of decrease or even destroy it. However, what we observe in our samples is the switching of our sample between two discrete states , this would mean, if we want to maintain the electromigration explanation, that we have a "loose" cluster of Ni and that we can move it at currents of a few μA (compared with the few mA which generated RTN in the previous sample) from one of the pads into the contact and back to the pad. We would need to have in the proximity of the contact one of these loose clusters in each of our samples. Rather than cluster displacement it may be more likely that the effect is due to lattice distortions

or to a magnetic origin (figure 6.14).

In the first case, the electron wind induces lattice distortions which may increase the size of the contact. This distortions remain until the current goes back to zero or a negative current is applied. In the magnetic explanation, the spin-polarized current of up electrons coming from the left (according to schematic in figure 6.14 b) tunnels through the NiO_x and/or the SiO_x (high resistance state), and induces changes in the magnetic moment at the left of the constriction (due to electron population <-> spin injection). Thanks to the fact that the inter-constrictions region is a vortex state (microsimulations), the amount of material which moment has to be changed is much smaller that it would be if all the area had a define moment pointing in a single direction. When the magnetic moment of the left is aligh with that of the right, the NiO_x changes to its ferromagnetic-conducting state, reducing the resistance by a factor 100. Similar electrical switching effects have been found in spin valves [13].

We must also take into account that the switching disappears in the presence of a magnetic field. A magnetic field could affect the dynamics of the cluster but we find unlikely that a field of 10 mT applied in any direction could avoid its movement from the pad into the contact. This together with the fact that this behaviour is only found in double nanoconstrictions (when a vortex state can be formed in the inter-constrictions region) points to the magnetic origin.

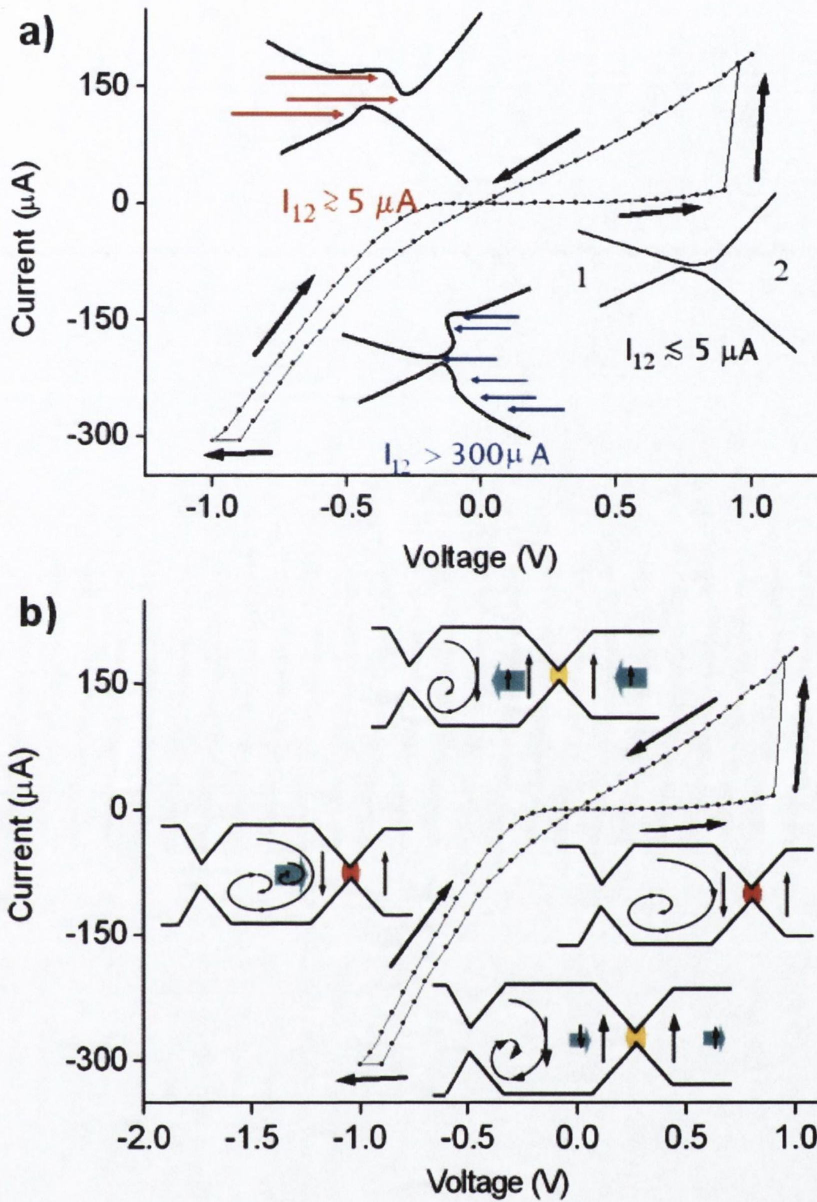

Figure 6.14. The electrical switching and hysteresis observed in some samples can be explained in terms of lattice distortions due to high currents and closed conduction paths a) or as due to changes in the magnetic moment of the inter-nanoconstrictions region induced by the spin-polarised current.

6.2 Transport in LSMO and magnetite nanostructures

6.2.1 LSMO and Fe_3O_4 nanoconstrictions

Various electron transport processes can be envisaged in the nanozone between the two sides – diffusive, ballistic, or hopping transport, tunneling or field emission. Furthermore, in magnetically-ordered solids, the magnetization may be continuous or discontinuous in the nanozone, which determines on whether or not the exchange interactions propagate across it. But even when they do propagate, exchange and magnetic structure may differ from that of the bulk, on account of the preponderance of surface atoms with reduced coordination.

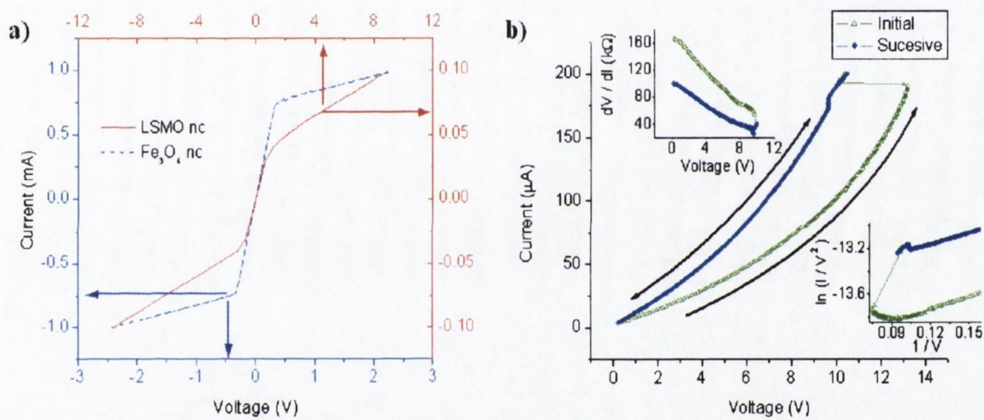

Figure 6.15. a) Heating effect observed in the changes of resistance of LSMO and Fe_3O_4 nanoconstrictions. b) High currents ($> 100\ \mu A$) can induce electromigration and permanent changes on the transport characteristic.

The transport across LSMO and magnetite nanoconstrictions is always non-linear and symmetric. Heating, field-emission and electromigration effects take over at relatively high currents (100-500 μA). The transport and structure of these samples can therefore be damaged much more easily that those of nickel nanostructures of similar size. This may be due

to the use of better insultators as substrates, or to the lower conductivity of the LSMO and magnetite nanostructures (one or two orders of magnitude below that of Ni nanostructures, what is in agreement with the difference in conductivity of the films). This is the first point we must take into account when working with these devices (see figure 6.15).

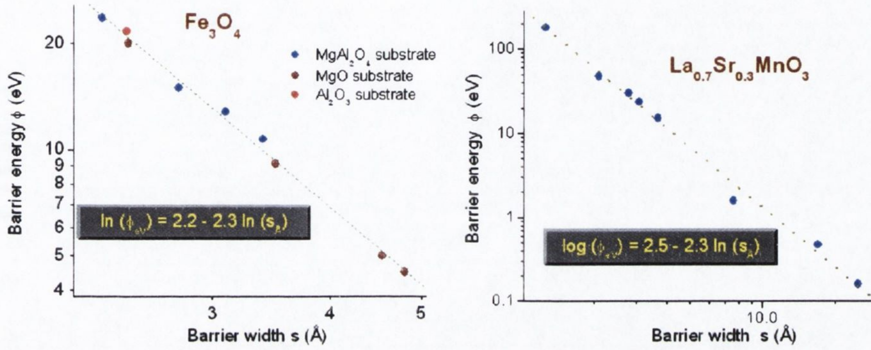

Figure 6.16. The barrier heigh and width deduced from the linear and cubic parameters of the I-V characteristic present a common dependence, pointing to a common energy barrier, but a similar depedence has been attributed to an artefact of the model [14].

Furthermore, the mixed behavior of the R(T) characteristic, with LSMO samples that show a semiconductor-like behaviour, may be due to the Ga doping on samples which have been imaged with the ion beam. For samples only imaged with the electron beam the gallium atomic percentage is reduced below 0.5 % (to be compared with about 6 % for Fe in the case of magnetite) and below the limit of detection of 0.1 % for samples protected with a silver cap layer 50 nm thick that is later removed by Ar milling (Fig. 6.17). These samples do not show any abnormality in their R(T) characetristic.

Once these artefacts are considered, our first remark is related to the non-linearity of the transport. The linear and cubic coefficients of the I-V characteristic (β and γ respectively, with β the conductance), or equivalently the barrier height and width deduced from the Simmons equations, have a logarithmic dependence that is independent of the substrate

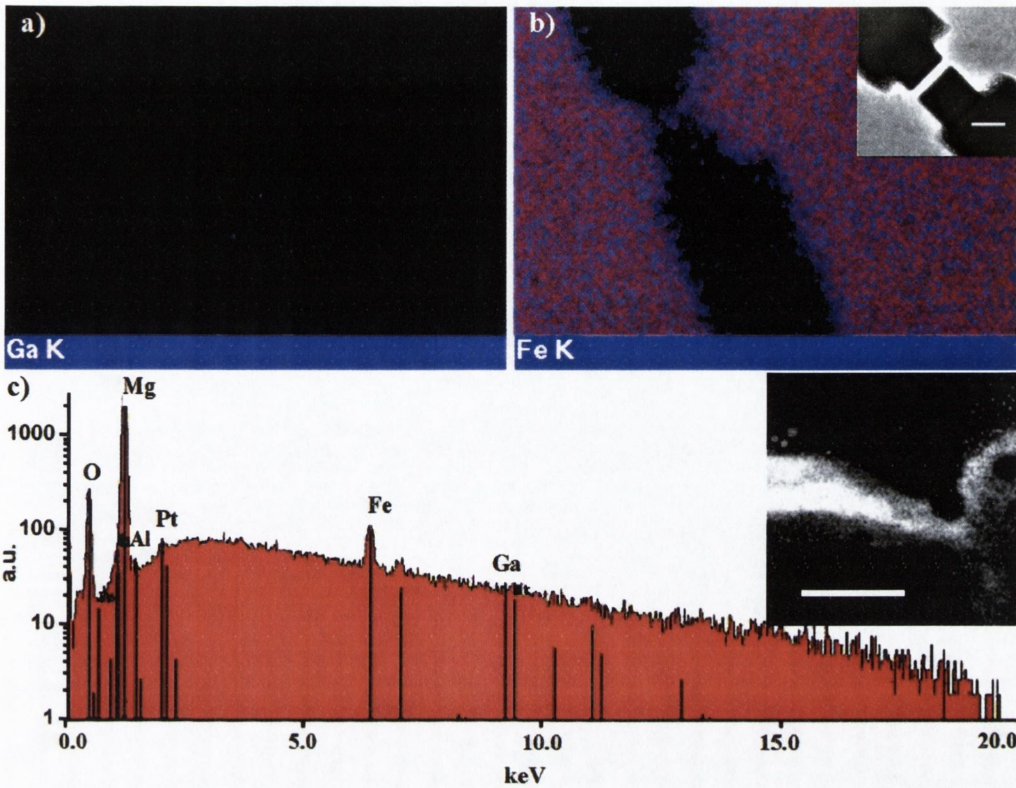

Figure 6.17. Chemical mapping of Ga (0.4 % atm.) a) and Fe (6 % atm.) b) contents in a magnetite nanobridge imaged with an electron-beam and milled with an ion-beam without a cap layer (inset, scale bar 500 nm). c) EDX analysis of a magnetite nanoconstriction (inset, scale bar 200 nm) which had a silver cap layer 50 nm thick. The main elements and peaks are indicated (log scale). The arrows point the current direction.

used (see figure 6.16). This indicates that the origin of the non-linearity is not tunnelling through the insulator substrate, a transport mechanism that would be dependent on the insulating qualities of the substrate (barrier height) as well as on the interface properties and the distance crossed by the electrons in the substrate (barrier width), properties that are not universal but substrate (height) and sample (width) dependent. However, a similar dependence between the barrier width and height has been proved to be an artefact of the Simmons model.

The resistance of most of the samples (in the 10-200 kΩ region) confirms the hypothesis

that the transport is not through an insulator substrate, since magnetic tunnel junctions (free of pin holes and other parallel conduction paths-related problems) have resistances well above 1 MΩ, and that without considering that their cross sections are usually far wider than the scale of the devices here considered.

Most of the MR values fall in the 1-20 % range (unlike in the nickel case) and a way to interpret these results is by assimilating the energy barrier to a hypothetical domain wall trapped at the nanoconstriction. In this case, the highly spin-polarized flow of electrons will have problems to follow the change of magnetization across the narrow domain wall, and the resistance may become voltage-dependent. The common dependence to all the samples of the barrier height with the barrier width can be understood as follows: if the electrons cross a wider domain wall, they can rotate their spin along the nanoconstricted region more easily, and therefore a wider barrier implies a lower barrier height. An applied magnetic field should then eliminate, or at least change the properties of this domain wall-energy barrier.

While it is possible to observe considerable field-induced decreases of resistance (Fig. 6.18a), reversion to the original state is a very slow process, as was the case with the nickel nanocontacts. Mechanical changes should be eliminated by contact with the insulating substrate, so the magnetoresistance is probably due to a change in magnetic configuration of the nanoconstriction, perhaps by the elimination of a domain wall there. The energy involved in the wall itself is Aδ, (being δ the domain wall width and A the exchange parameter $\simeq 10^{-11}$J m^{-1}) $\sim 10^{-19}$ J. But the energy Δ needed to nucleate it must be a little greater since the time τ required is of order $\tau_0 \cdot \exp(\Delta/kT)$ where τ_0^{-1} is an attempt frequency of order 10^{10} s^{-1}. The process is akin to magnetization reversal far from the coercive field in a bulk ferromagnet.

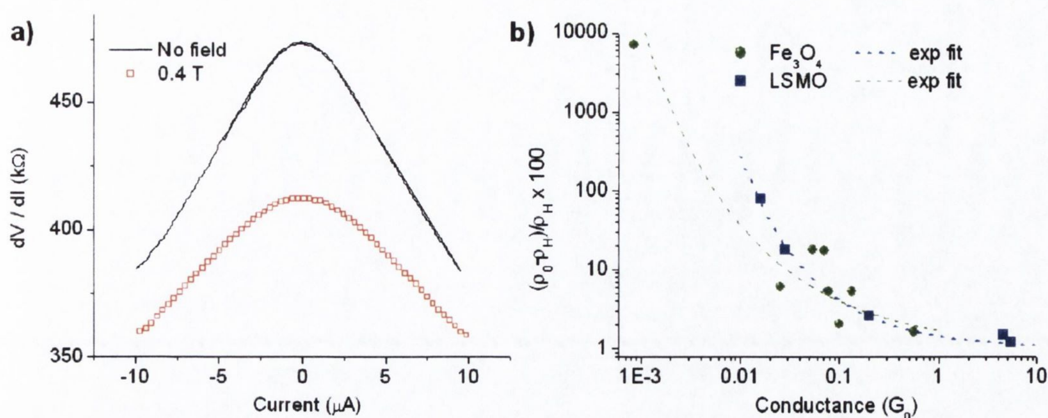

Figure 6.18. a) Magnetic field effect on the resistance of a LSMO nanoconstrictions. b) Scaling of the optimistic MR with the conductance (in units of $G_0 \cong 12.9\ k\Omega^{-1}$) of the samples.

A difference between the MR effect in nickel and LSMO/Fe_3O_4 nanoconstrictions is the dependence with the conductivity. The MR does scale with the conductance, but the relationship is not linear (as it was for nickel nanoconstrictions in a log-log scale), and the huge MR values are obtained for values of conductance one order of magnitude smaller than those of nickel nanoconstrictions (Fig. 6.18b). The former may be due to the different origins of the MR. We cannot talk of oxidised layers which become conducting when a field is applied if we are working with LSMO or Fe_3O_4 structures, which are conducting oxides themselves. However, this does not imply that there is not present a low-conductivity layer, formed by redeposited and/or Ga^+ doped material. The smaller MR values for equal conductivities is probably due to the different conductivity of these materials (and sustains the hypothesis of non ballistic transport).

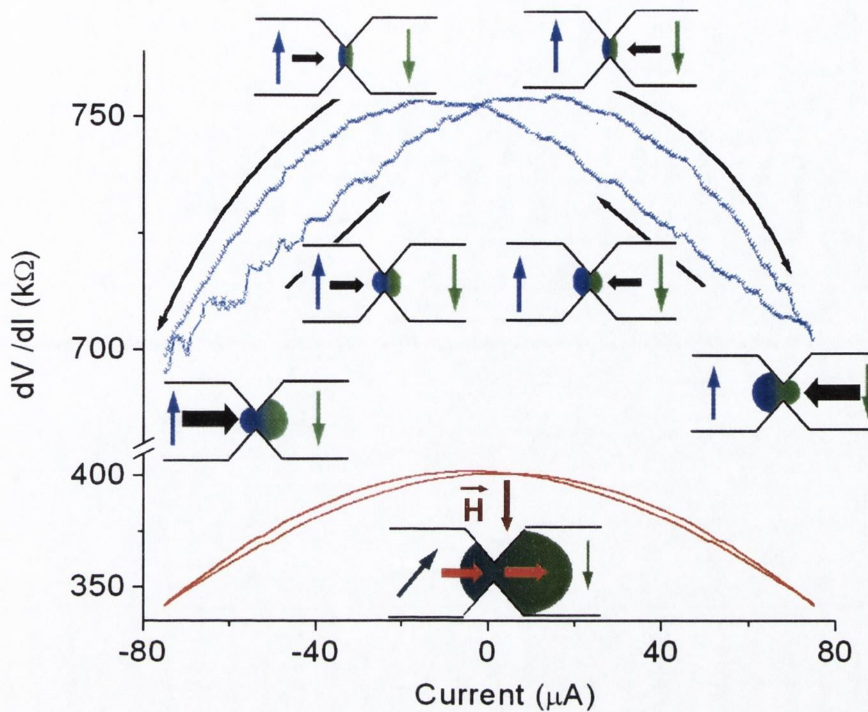

Figure 6.19. $\frac{dV}{dI}$ vs. Current characteristic for a LSMO nanoconstriction before and after a magnetic field is applied. Schematic with a possible explanation based on domain wall deformation. The black, horizontal arrows represent the current, where the colour, vertical arrows represent magnetic moments/field.

The electrical hysteresis found in the samples with higher MR ratios can also be explained in terms of a domain wall trapped at the nanoconstriction. The spin-pressure generated by the spin-polarised current may displace the domain wall to different pinning centers in the vicinity of the constriction where it expands, reducing the resistance. Once it is in one of these pinning centers, a current in the opposite sense is required to move the domain wall back to its original position. A magnetic field can move the domain away from the nanoconstriction (Fig. 6.19) or completely eliminate it (Fig. 6.20), greatly reducing the resistance and annihilating or reducing the electrical hysteresis and non-linearity due to the reduced spin-pressure (we have the same spin-current but over a wider area).

When the domain wall is displaced far from the constriction, but not eliminated, the

non-linear coefficient increases (barrier width increases and barrier height decreases, see next page), and the spin-pressure is exerted over a larger region, reducing domain wall displacement and electrical hysteresis

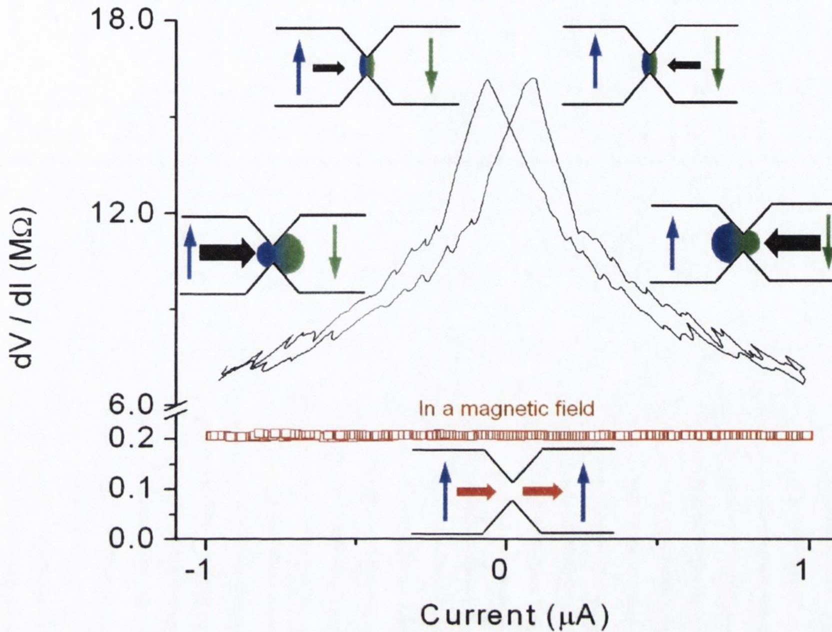

Figure 6.20. Highest effect (~ 8000 %) found in a Fe_3O_4 sample, with total elimination of previous non-linear and electrical (butterfly-like) hysteresis. Horizontal arrows represent once more the electric current.

In the case of LSMO nanoconstrictions this domain wall displacement due to a spin-polarised current would be due to the torque induced by the spin scattering, where in the case of Fe_3O_4, that is a hopping conductor and therefore does not allow for this mechanism, it could be the changes in the spin of the electron population at the nanoconstriction which may induce the change.

This 'domain wall expansion' should be possible to obtain also with magnetic fields. Indeed, the samples which present big changes in the conductivity and non-linear coefficients (β and γ) that saturate at very high fields may be suffering of this magnetically induced

'domain wall expansion' (see Fig. 6.21). Both changes compensate to produce not very big changes of resistance ($\lesssim$ 10 %), but affect qualitatively the I-V characteristic. This can be explained as a expansion of the domain wall (increasing the barrier width) that makes it easier for the electrons to follow the magnetization changes, and therefore to cross it (reducing the barrier energy).

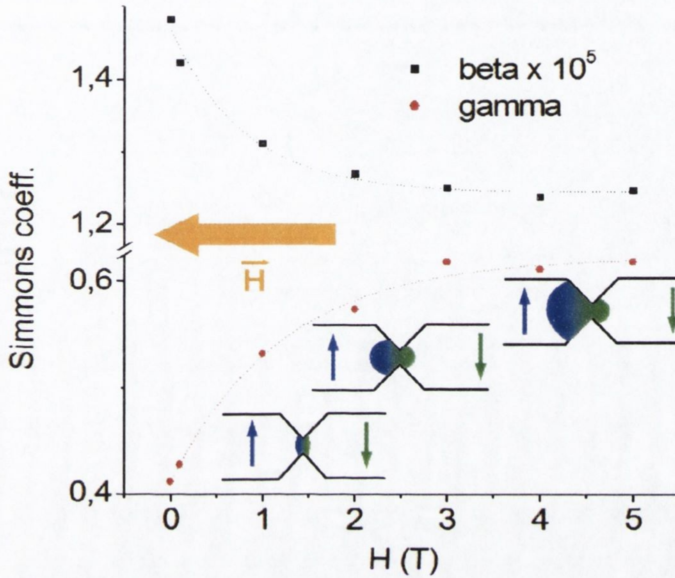

Figure 6.21. Changes on the conductivity and non-linar (β and γ) coefficients of a LSMO nanoconstriction due to high magnetic fields.

We recall that for a I-V characteristic expressed as I = β(V+γV^3), following the Simmons formalism, the barrier width and height can be calculated as:

$$L = \log\left(\frac{4.87 \times 10^{13}}{d \times \beta\gamma^{1/2}}\right) \quad \begin{array}{|l} s \text{ (barrier width in Å)} = 4.94 \cdot \gamma^{1/4} L^{1/2} \\ \phi \text{ (barrier height in eV)} = 0.266 \cdot L/\gamma^{1/2} \end{array} \qquad (1)$$

It was previously discussed the plausible relation between energy barrier and domain wall. Assuming that the barrier width is proportional to the domain wall width, from (1), the changes measured in the figure 6.21 would imply a change in the barrier-domain wall width of 10 %, with changes in the barrier height of 20 % (proportional to $\Delta\gamma^{1/4}$ and $\Delta\gamma^{1/2}$, since

L remains mainly constant due its log dependence with $\Delta\beta\gamma^{1/2}$, which itself do not change more than 5 %).

Interpretation of the results in terms of domain-wall deformation remains however speculative in the absence of precise structural and magnetic characterization of the nanozone. We cannot tell, for example, whether we actually have a tiny zone of insulating Ga-containing oxide at the surface. Electromigration is also a significant factor in these structures, given the electric fields and current densities present at the contact ($\approx 10^9$ V m^{-1} and $\approx 10^{12}$ A m^{-2}), and structural problems can not be discarded, and this could be the origin for the electrical hysteresis present in some of the samples. It is difficult however to find an alternative explanation to why a magnetic field should alter the transport properties of the samples in the reported fashion or why should the transport coefficients give a common behaviour independent of the substrate (MgO, Al_2O_3 and $MgAl_2O_4$) and material (Fe3O4 and LSMO). Magnetostriction is ruled out since the samples are bounded to a substrate, the changes are independent of the field direction and the relaxation times are of the order of hours to days, and other effects, such as cyclotron effect or Hall effect would increase the resistance in the presence of a field, not reduce it.

6.2.2 Magnetite nanobridges

The most peculiar characteristic of the transport across magnetite nanobridges are the oscillations of the Simmons parameter with the magnetic field (Fig. 6.22). These oscillations are variations of about 1 % and damp at high fields. There is also a continuous increase of conductivity of about 0.2 % T^{-1} for fields applied parallel to the bridge or 0.1 % T^{-1} for perpendicular fields. We saw in the chapter 4 that the nanobridges were patterned across regions which showed high contrast in the MFM images, which is believed to be due to the presence of anti-phase boundaries (APBs).

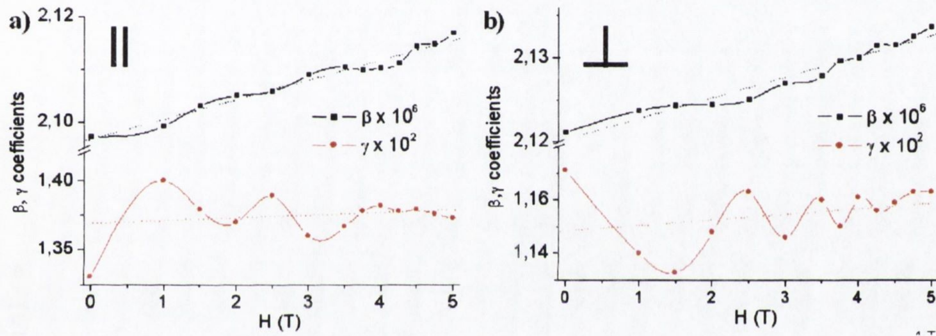

Figure 6.22. Variations in the Simmons coefficients with the magnetic field for a magnetite nanobridge when the field is applied parallel a) and perpendicular b) to it.

The continuous, slow increase of conductivity is probably related to the progressive alignment of the magnetization both sides of the nanobridge, something similar to what happened in the nanoconstrictions, but now the changes are much smaller, due to the strong exchange interactions at the APB higher fields are required (at 5 T the samples give no signal of being saturated). This is in agreement with previous measurements of the saturation fields of APBs, as well as the MR ratios obtained for sharp contacts patterned across APBs [17]. The MR ratios will be different depending on the original alignment of the domains at both

sides of the APB with respect to the applied field, therefore the factor two of difference in the changes of conductivity for fields applied parallel or perpendicular to the nanobridge.

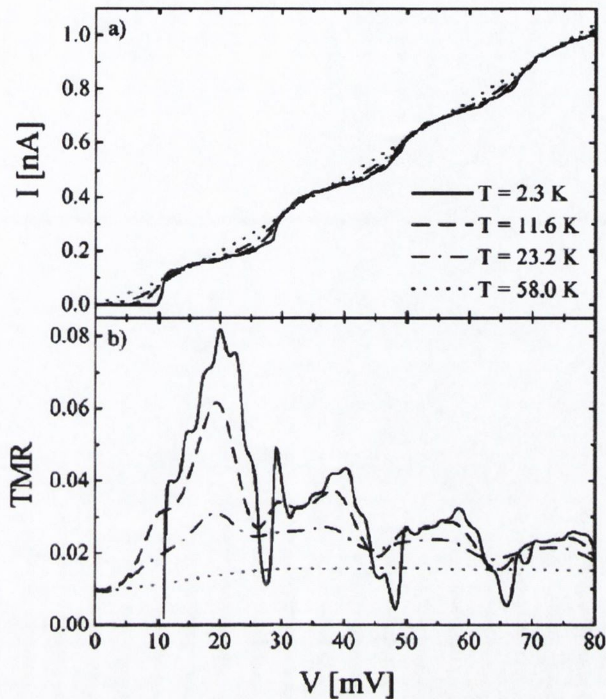

Figure 6.23. Bias dependence of electric current for magnetic tunnel junction in the antiparallel configuration (a) and tunnel magnetoresistance (b) for different temperatures and for $\Delta E/\ k_B = 34.8$ K and Ec / $k_B = 69.9$ K. The junction resistances in the antiparallel configuration are $R_{l\uparrow}$=200 MΩ, $R_{l\downarrow}$=100 MΩ, $R_{r\uparrow}$=2 MΩ, and $R_{r\downarrow}$= 4 MΩ, whereas in the parallel configuration $R_{r\uparrow}$= 4 MΩ, and $R_{r\downarrow}$= 2 MΩ. After [18].

The oscillations of the Simmons coefficients represent a difficult problem. Similar oscillations (but for the MR and not just for the non-linear coefficient) have been predicted for single-electron tunnel junctions due to coulomb blockade charging effects [18]. The oscillations appear when considering a two-dimensional space of states to include the spin, and the influence of discrete energy spectrum of a small central electrode on the tunneling current, charge and spin accumulation and fluctuations (see figure 6.23).

The effect of nonmagnetic impurities and the effective mass on the spin-dependent

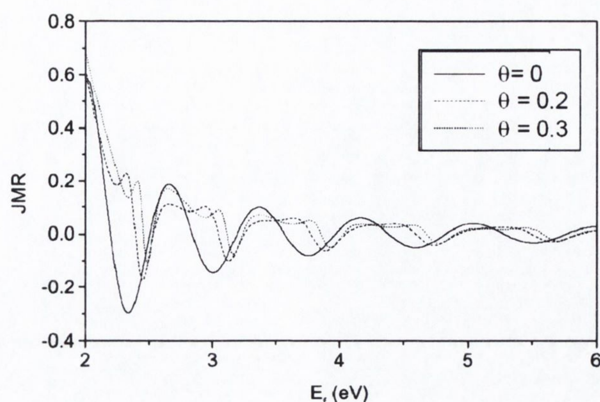

Figure 6.24. Oscillations of the junction magnetoresistance (JMR) with the difference of the Fermi energies between a ferromagnet and a normal metal for different θs. θ represent the impurity potentials at the interface (taken to be equal at both interfaces), see [19] for the full explanation of the figure and the calculations.

transport in a ferromagnet-normal metal-ferromagnet junction can also lead to non-monotonic oscillations of the junction magnetoresistance (JMR) with the incident energy and the thickness of the normal metal (Fig. 6.24). The smaller the difference of the effective masses of electrons in two ferromagnetic electrodes, the larger the amplitude of the JMR oscillation, see [19] for the detailed calculation.

The granular nature of the nanobridges (see the SEM in figure 6.25) can give rise to charging and Coulomb blockade effects. The transport in these nanobridges would represent the charge-spin transport across dozens of single-electron reservoirs in series and parallel (see schematic in the same figure). The combination of the transport characteristics may prevent the measurement of a typical Coulomb staircase and reduce the scale of the oscillations from 50 to 2 %. It is not clear however, why is it still possible to see this effect at room temperature in these devices, when all the theoretical predictions agree that it should not be possible to observe the TMR oscillations at temperatures above 77 K. On the other hand, it is also possible that the transport from one magnetite grain to another may be

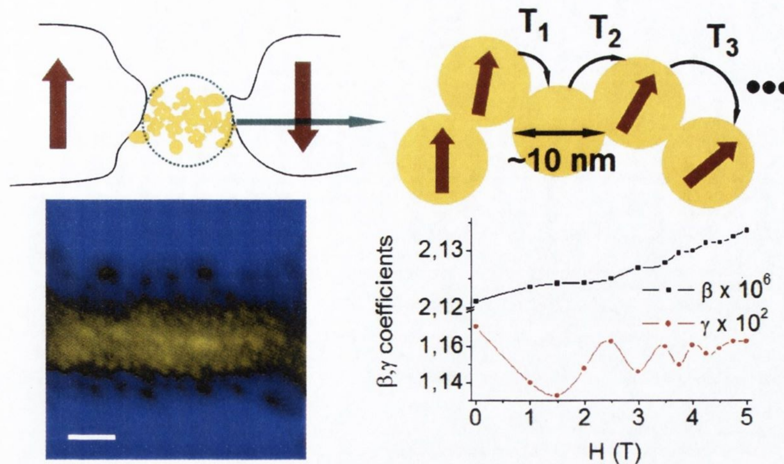

Figure 6.25. SEM (scale bar 50 nm) and schematic of the structure of a nanobridge with the oscillations of the γ coefficient.

impeded by the presence of a non-magnetic (Ga or Ga-Fe_3O_4) material. In this situation, we could obtain transport characteristics similar to those described for ferromagnet-normal metal-ferromagnet junctions, producing oscillations in the conductance (understood as $\beta + \gamma$) with the magnetic field (via variations of the Fermi level with the magnetic field or due to inclusion of the exchange energy between the particles in the Hamiltonian considered by Zhu in [19]), but the explanations remain highly speculative.

6.2.3 Magnetite nanogaps

Finally, in sections 4.2.3 and 4.3.3 we considered the transport across high resistance ($\gtrsim$ 250 kΩ) nanostructures in the field emission regime. Due to the transport characteristic and high resistance of these samples, we considered them as nanogaps between magnetite nanoelectrodes. This nanogap is probably formed by low-conductivity, Ga rich (redeposited or doped) magnetite, and gives us optimum conditions to study the magnetic field effect in

the field emission transport across highly-polarised ferromagnetic electrodes.

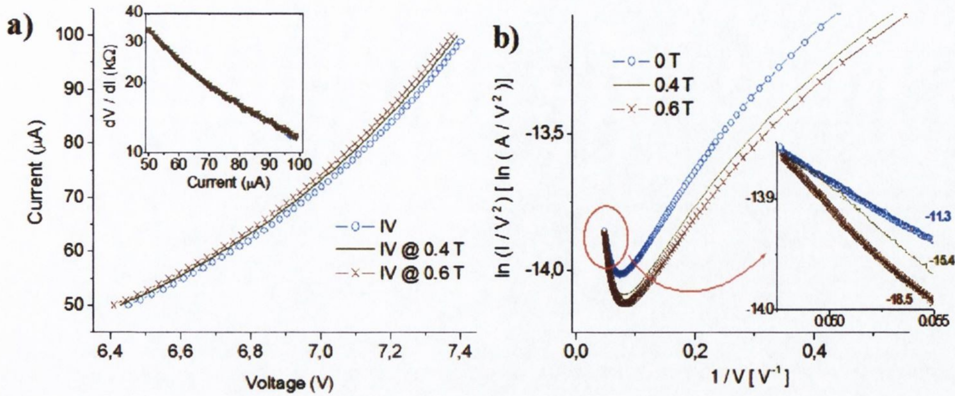

Figure 6.26. Magnetic field effect in the field emission regime. a) I-V and $\frac{dV}{dI}$ (V) characteristic. b) Fowler-Nordheim plot with a zoom on the negative slope (field-emission) region.

The behavior of the nanogap in a magnetic field is puzzling. We can calculate the changes in the energy barrier induced by the magnetic field by looking the changes in the Fowler-Nordheim plot (Fig. 6.26) by taking the voltage ratio at a constant value of ln I/V^2. Thus we eliminate all dimensional uncertainties as thickness or electrically active area [20],[21]. From the field emission equation

$$\mathrm{I} = \frac{a\mathrm{V}^2}{w^2} \exp\left(-\frac{bw}{\mathrm{V}}\right) \tag{2}$$

, with a and b material parameters and w the gap distance, it is easy to deduce that:

$$\left(\frac{\phi_{\mathrm{H}\neq 0}}{\phi_{\mathrm{H}=0}}\right) = \left(\frac{\mathrm{V}_{\mathrm{H}\neq 0}}{\mathrm{V}_{\mathrm{H}=0}}\right)^{2/3}\Bigg|_{\ln\ \mathrm{I}\ /\ \mathrm{V}^2\ =\ \mathrm{const.}} \tag{3}$$

From the equation (3), the deduced changes are of order 100 mVT^{-1} for nanogaps across magnetite electrodes in the field-emission region. This is difficult to explain in terms of Zeeman splitting as was previously done for measurements in the field emission regime [20],[21], since we would need to assume g factors for magnetite of order 1000! Even making

allowances for changes in the effective mass of the electron when crossing a Fe_3O_4-Ga area, which may behave as a semiconductor with a big gap, it seems more reasonable to explain the effect in terms of variations of the exchange energy (which can easily be of that order of magnitude) between both sides of the gap.

As we have seen in the transport across nanoconstrictions, the energy barrier is intimately associated with the magnetization of the nanostructure, and the variations on the exchange energy both sides of the nanogap, could be directly translated in changes of the energy barrier height (Fig. 6.27).

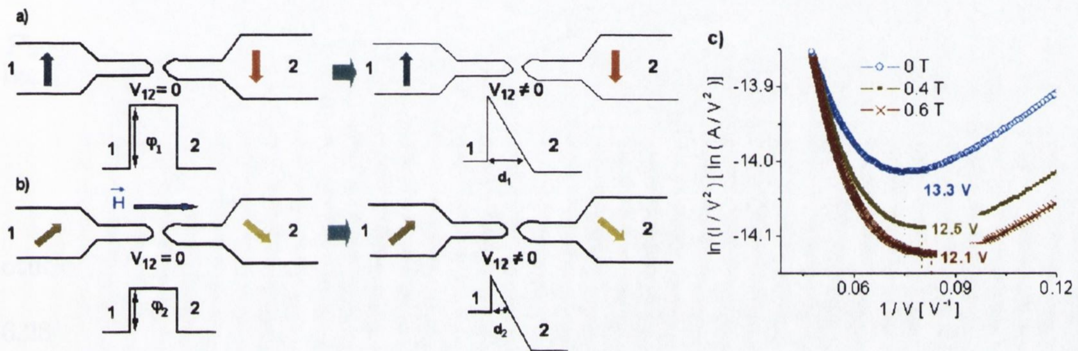

Figure 6.27. Magnetic field effect on the field emission transport between magnetite electrodes. a) The barrier before a field is applied has a height φ_1. When the voltage V_{12} exceeds φ_1 field emission transport occurs. b) When a field is applied the barrier height is reduced to $\varphi_2 < \varphi_1$. The voltage then required then to obtain field emission is smaller, as seen in the data of c) (inflexion points obtained from the change of sign in the differential of the graph).

6.3 Contact induced magnetism in carbon nanotubes

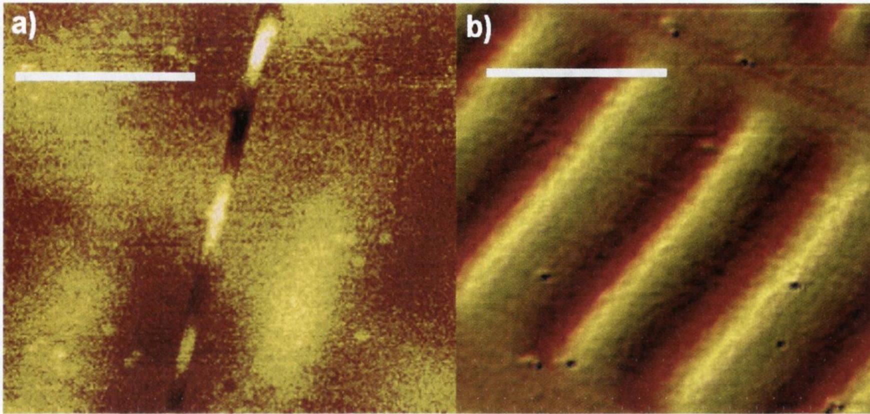

Figure 6.28. a) MFM (50 mV scale) of a CNT laid on a magnetite substrate. The scale bar is 500 nm. b) MFM (400 mV scale) of a floppy disk. The scale bar is 5 μm.

In order to estimate the magnitude of the induced magnetization of the carbon nanotube, we compared our images with those obtained from hard and floppy disks (see figure 6.28). From bits of 1 x 10 μm recorded on γ-Fe_2O_3, we obtain signals that are approximately one order of magnitude greater than those from the carbon nanotubes. The medium has magnetization M 200 kA m^{-1}, and it produces a stray field of order 2 kA m^{-1} around each bit [22]. The dimensions of the recorded bits and nanotubes are similar, so the stray field gradients are expected to scale similarly. The weak dependence on lift height allows us to compare the stray fields generated by the tubes and the bits. The stray field close to the tube will be of order of 0.2 M if it behaves like a bar magnet, so we estimate a tube magnetization of order 1 kA m^{-1}, corresponding to an average carbon moment of order 0.001 μ_B. Finally, allowing for the fact that no more than 1% of the carbon atoms are likely to be in contact with the substrate (Fig. 6.29), the observed magnetization corresponds to a moment of order 0.1 μ_B per contact atom, in agreement with the theoretical prediction (see

Appendix to chapter 5).

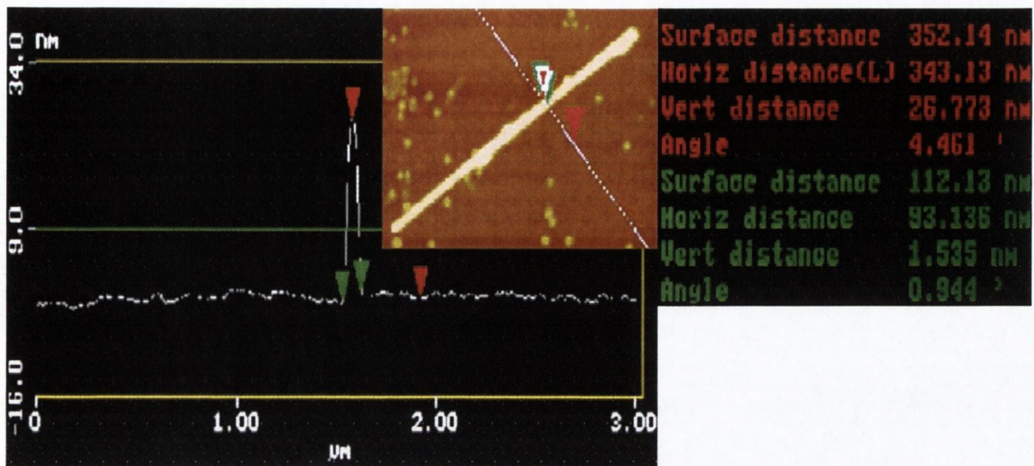

Figure 6.29. Atomic force microscopy section analysis of a carbon nanotube.

An attempt to measure directly the magnetic moment of the tubes was made by measuring the magnetic moment of a cobalt substrate with and without carbon nanotubes laid on it. The film was positioned parallel to the magnetic field both times, and it was not moved from its position in the measuring capsule while spreading the tubes. However, small variations of angle and/or position respect to the applied field or the SQUID coils are likely to happen, and the difference of the signal, 10^{-8}Am^{-2} (the moment is smaller with the tubes on top of the film) is approximately equal to the SQUID precision for these measurements, making very difficult to extract any conclusion from this measurement (see the figure 6.30), and the change of the signal is probably due to a problem of positioning (angle) of the sample with respect the SQUID coil. The nanotubes employed are from the same batch that produced the magnetic measurements of figure 5-6.

Controllable high-temperature magnetism in graphite or carbon nanotubes is a tantalising prospect because of the possibility of combining spin physics [23] with molecular electronics [24]. Graphitic structures have several crucial properties for spin and molecular

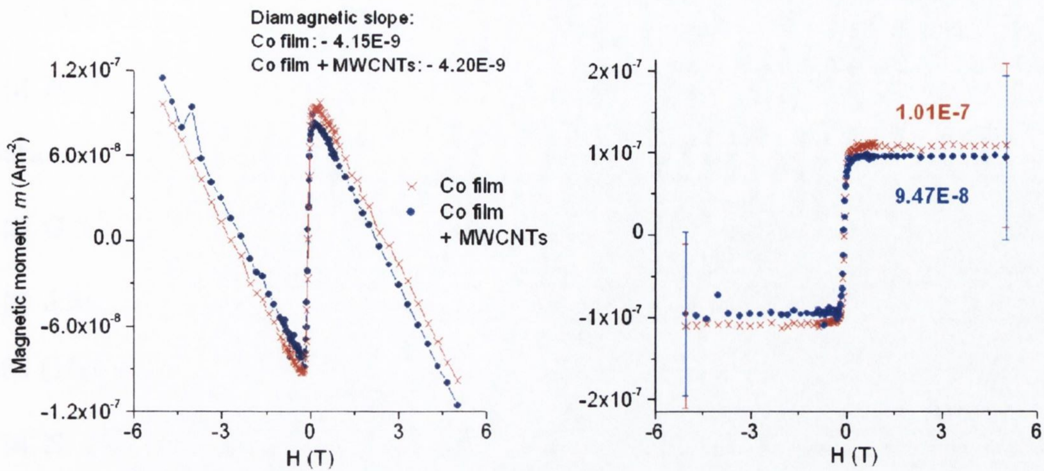

Figure 6.30. SQUID measurements of the magnetic moment of a cobalt film without (red, crosses) and with MWCNTs (blue, circles) laid on its surface. The resolution of the SQUID is about 10^{-8} Am^{-2}

electronics, such as a low effective mass and a long spin diffusion length exceeding 130 nm [25]. Moreover carbon nanotube electronic architectures, such as logic circuits [26]-[28] and non-volatile random access memories have been already demonstrated [29]. The addition of the spin degree of freedom, and the use of the other ferromagnetic nanostructures considered in this work, open many perspectives for spin-based nano-devices, where logic and memory elements are integrated at the molecular level.

Bibliography

[1] A. Rocha and S. Sanvito, Phys. Rev. B 70,094406 (2004);agreement with experimental data: O. Céspedes, A. Rocha, S. Lioret et al., J. Magn. Magn. Mat. 272-76, 1571 (2004)

[2] G.T. Woods, R.J. Soulen, I.I. Mazin et al., Phys. Rev. B 70, 054416 (2004)

[3] J.M. Rowell in'Tunneling Phenomena in Solids', E. Burstein and S. Lundqvist eds., p. 385 (1969)

[4] N. Papanikolau, J.Phys.: Cond. Mat. 15 5049 (2003); N. García, cond-mat/0207323 (2002)

[5] M. Klaui et al., Phys. Rev. Lett. 90, 097202 (2003)

[6] D. Adler and J. Feinleib, Phys. Rev. B 8, 3112 (1970); F.J. Morin, Phys. Rev. 93, 1199 (1954)

[7] P.G. de Gennes, Phys. Rev. 118, 141 (1960)

[8] S.H. Lee, C. E. Tracy and J.R. Pitts, Electrochem. and Sol. St. Lett. 7, A299 (2004); S. Nevill Mott, 'Conduction in Non-Crystalline Materials', Oxford Science publications (1987)

[9] J.T. Richardson, D.I. Yiagas, B. Turk et al., J. App. Phys. 70, 6977 (1991)

[10] S. Nevil Mott, 'Metal-Insulator Transitions', Taylor & Francis eds. (1990)

[11] M.L. Medarde, J. Phys. C: Cond. Matt. 9, 1679 (1997)

[12] S.L. Dudarev, G.A. Botton, S.Y. Savrasov et al., Phys. Rev. B 57, 1505 (1998)

[13] J. Grollier, P. Boulenc, V. Cros et al., App. Phys. Let. 83, 509 (2003)

[14] P. Rottländer, M. Hehn and A. Schuhl, Phys. Rev. B 65, 054422 (2002)

[15] C. P. Hunt, B. M. Moskowitz and S. K. Bannerjee in Rock Physics and Phase Relations, Handbook of Physical Constants J. Ahrens, editor) AGU, Washington 1995

[16] J.J. Versluijs, M.A. Bari and J.M.D. Coey, Phys. Rev. Lett. 87 (2001) 26601

[17] W. Eerenstein, T.T.M. Palstra, S.S. Saxena and T. Hibma, Phys. Rev. Lett. 84, 247204 (2002)

[18] J. Barnás, J. Martinek, G. Michalek et al., Phys. Rev. B 62, 12363 (2000)

[19] Z-G Zhu, G. Su, B. Jin and Q-R Zheng, cond-mat/0210392 (2002)

[20] L. Esaki, P.J. Stiles and S. von Molnar, Phys. Rev. Lett. 19, 852 (1967)

[21] T. Siegrist, S. von Molnar and F. Holtzberg, Appl. Phys. Lett. 47, 1087 (1985)

[22] R.C. O'Handley, 'Modern Magnetic Materials', (Wiley, New York, 2000), pg. 681-3

[23] S.A. Wolf, D.D. Awschalom, R.A. Buhrman, J.M. Daughton. et al., Science 294, 1488 (2001).

[24] C. Joachin, J.K. Gimzewski and A. Aviram, Nature 408, 541 (2000)

[25] K. Tsukagoshi, B.W. Alphenaar and H. Ago, Nature 401, 572 (1999)

[26] A. Bachtold, P. Hadley, T. Nakanishi and C. Dekker, Science 294, 1317 (2001)

[27] Y. Huang, X. Duan, Y. Cui, L.J. Lauhon et al., Science 294, 1313 (2001)

[28] P.G. Collins, M.S. Arnold and P. Avouris, Science 292, 706 (2001)

[29] T. Rueckes, K. Kim, E. Joselevich, G.Y. Tseng et al, Science 289, 94 (2000)

Chapter 7

Conclusion and further work

The asymmetric transport depending on the sense of the voltage applied to nickel nanoconstrictions fabricated by e-beam lithography, FIB and electrochemistry, and the resultant I-V and noise characteristics were unexpected. We associate the asymmetry to tunnelling through the SiO_x substrate and/or through a NiO_x insulating layer present in the nanoconstriction. The later will play a fundamental role in the magnetic properties of the samples.

Our data in nickel nanoconstrictions is not coherent with a ballistic domain wall magnetoresistance, due to the size of the contacts and the polarization of nickel, the MR ratios seen in this work cannot be explained in terms of domain wall scattering. Even in the case of the presence of dead layer at the constriction providing a zero-width domain wall, the MR should not exceed some 40 %. The transport across our structures does not seem to be ballistic either. The Andreev measurements give high Z values more in concordance with diffusive, or even tunnelling transport. Our MR data is not in agreement with magnetostrictive effects either. The samples are bounded to a substrate, the sign of the magnetic effects is independent of the direction of the applied field and the relaxation times are extremely long.

The magnetic field effect in nickel nanoconstrictions can be grouped by the three different MR values obtained. The first one, obtained for samples with high conductance well above G_0, represents an increase of the resistance of a few %, and is probably associated to

the AMR generated by a domain wall. The second one, with an increase of resistance of a few % followed by a drop of 30-50 %, and present in samples with a resistance of 1 to 5 kΩ is related to the annihilation of a domain wall, and the change of the surrounding NiO_x layer from antiferromagnetic-insulating to ferromagnetic-conducting later. Finally, the huge drops of resistance up to 50000 % obtained for samples with a conductance below G_0 are attributed to the constrictions being completely covered by a NiO_x layer which behaviour is also changed from insulating to conducting, opening conduction paths that were not present previously.

We have seen that some samples present evidence for reversible electron wind electromigration. The material displaced to the nanoconstriction may interact magnetically with the NiO_x surrounding the sample. The interaction leads to a two level fluctuation between the antiferromagnetic and the ferromagnetic states in a few NiO_x cells near the displaced material, generating random telegraph noise at room temperature, which increases the noise level by several orders of magnitude. Once the displaced cluster is oxidised, or if a magnetic field is applied, the interaction disappears, and so does the RTN.

Electrical switching and hysteresis was also present in FIB patterned double nanoconstrictions, disappearing in the presence of a magnetic field. This result could be due to domain wall movement (or domain area change in the case of a NiO_x layer) induced by a spin-polarised current.

A metal-insulator transition in NiO_x nanostructures is a strong statement. However, is the only argument we have found which can explain comprehensively (and relate) all the characteristic of the transport in these nanostructures (which are bounded to a substrate):

- The high levels of shot noise, implying a recombination process (tunnelling).
- The random telegraph noise, and its dependence with time, temperature and magnetic field.
- The non-linearity and asymmetry of the I-V, only present for samples patterned on a SiO_x substrate (for Ni and Pt nanoconstrictions).
- The electrical switching and hysteresis.
- The three groups of MR effects, including a huge decrease of resistance for samples with a conductivity $\lesssim G_0$.
- The independence of the magnetic field effect with the direction of the applied field.
- The long relaxation times (up to weeks).
- The Andreev measurements, which show a higher level of polarization than for bulk nickel, with tunnelling transport for most of the samples and highly diffusive for the rest.
- The R(T) characteristic, with a resistance increasing exponentially as the temperature is reduced (two regimes) for samples with a conductivity below G_0 (before a field is applied or for samples which do not show a magnetic field effect), and how this dependence is changed to linear after a field is applied.
- The increased non-linearity and shifting of the resistance peak with the temperature.

A magnetic field effect is also found on the resistance of magnetite and LSMO nanoconstrictions. The MR is present in 15-20 % of the samples, and the values scale with the conductivity. There is good evidence that the large effects found (up to 8000 %) cannot be explained by magnetically-induced strain. As before, the sample is bound to a substrate, and the changes of resistance are negative (resistance is always reduced in a field), independent of the direction of the applied field, and with relaxation times of order of days. The MR values probably reflect the spin-dependent hopping or tunneling probability of the electron across the contact, where a domain wall is likely to form. The data are compatible with transport across a very narrow domain wall and a high degree of spin polarization at room temperature.

Novel effects have been found in magnetite nanobridges and nanogaps. The presence of a APB in the nanobridge is deduced by the variations of conductivity with the magnetic field, with changes of resistance of order 0.2 % T^{-1}. The deduced saturation fields should be well above 5 T, which is the limit of our system. Possible evidence for single electron transport and/or charge accumulation across the magnetite grains which form the nanobridge is present via the oscillation of the Simmons coefficients with the magnetic field.

The effect of a magnetic field in the field-emission regime of nanogaps (mostly ignored in the past) has been studied, finding huge changes in the energy barrier with the magnetic field. This changes in the barrier height we associate with changes in the exchange energy, proving that, for magnetic tunnel junction-like transport, the probability of the electron of crossing the gap (-> energy barrier) is highly dependent of the relative alignment of the magnetic moments both sides of the gap.

A new method to fabricated in-plane edge junctions to measure spin polarization by Andreev reflection was described in this thesis. The success ratio is very low ($\sim$ 5 %) and the fabrication method needs to be perfected, but it has proved to be useful to measure the polarization of $Ni/NiO_x/Nb$ junctions and their transport characteristics (Z parameter).

We have also presented direct evidence for contact-induced magnetism due to spin polarized charge transfer at a contact between a ferromagnet and a carbon nanotube. This magnetic proximity effect is quite distinct from spin-injection. Magnetic proximity produces an equilibrium imbalance of spin density (spin transfer) in a non-magnetic material very close to the contact surface; the length scale is the screening length which in nanotubes may be about one nanometer. Spin-injection is a non-equilibrium spin imbalance of a transport current far from the contacts; the length scale is the spin diffusion length. Although it is difficult to extract quantitative information from MFM images, the data are consistent with a spin transfer of order 0.1 μ_B per contact carbon atom, and an induced magnetization of order 1 kAm^{-1} in multiwalled nanotubes.

Further work

Our results suggest how spin and charge functionalities could be integrated, separating the charge contacts from those producing spin polarization by interface reflection between a CNT and the ferromagnetic substrate, for example, and how this spin flow could be detected by the use of highly polarised ferromagnetic nanoconstrictions. Different geometries may then be used to allow for faster re-nucleation of the magnetic moments.

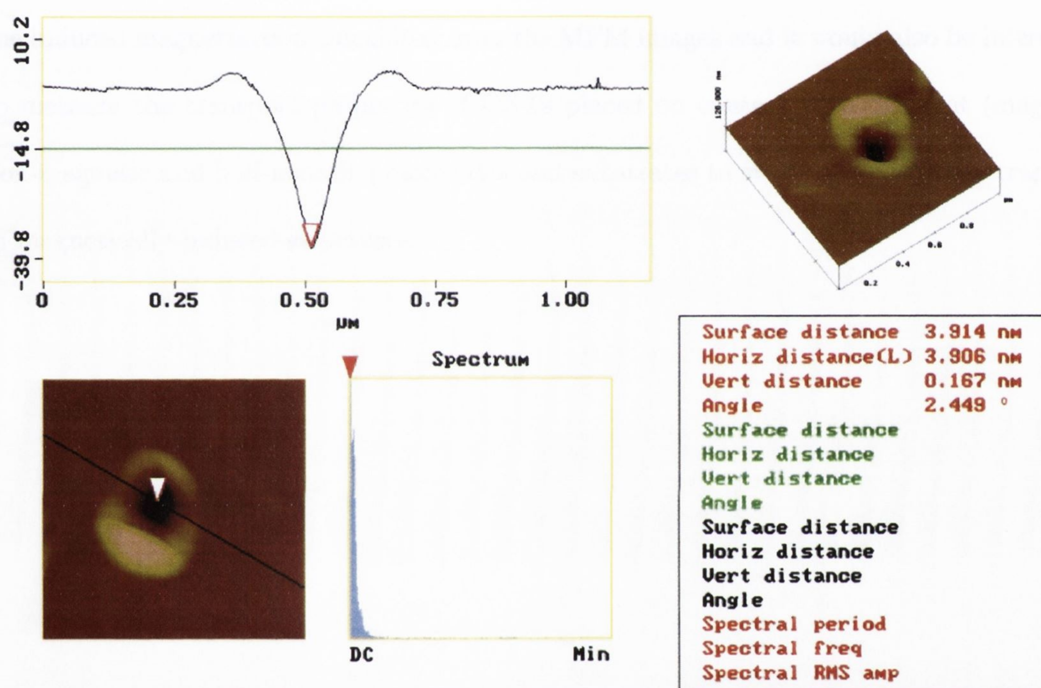

Figure 7.1. AFM of a hole made on a PMMA layer (the hole has been made in the contact mode with the same tip which has scanned the picture in the tapping mode). The diameter of the hole at the bottom is just a few nm.

Other further experiments may include the measurement of the transport properties of sharpened AFM tips fabricated by nickel electrodeposition, or the transport across nanostructures deposited on nano-holes opened with high aspect ratio AFM tips on polymer materials (e.g. PMMA, see figure 7.1) which would prevent or control the oxidation process

by depositing thin Ni layers and heating them up. It would also be possible then to fabricate a stack of multilayers NiO_x/magnetic material (it should be a magnetic material difficult to oxidised, like CoPt, FePt or other $L1_0$ ferromagnetic materials) to enhance the effect and to try to reduce the relaxation time (by studying the dependence of such a relaxation time with the NiO_x/Ni thickness ratio, for example).

The use of a SQUID with a rotatory sample holder may also be possible to confirm the induced magnetization calculated from the MFM images and it would also be interesting to measure the transport properties of CNTs placed on contact with different (magnetic, non-magnetic and half-metallic) electrodes and substrates to study the electronic transport in magnetically-induced structures.